Modes and Propagation in Microstructured Optical Fibres

by

Nader A. Issa

Thesis

Submitted by Nader A. Issa
for fulfillment of the requirements for the Degree of
Doctor of Philosophy

Supervision
Professor Simon C. Fleming
Dr. Martijn A. van Eijkelenborg
Dr. Leon Poladian
Dr. Ian M. Bassett

Optical Fibre Technology Centre
and School of Physics
University of Sydney
Submitted in January, 2005

Modes and Propagation in Microstructured Optical Fibres

Declaration

I declare that this thesis is my own work and has not been submitted in any form for another degree or diploma at any university or other institute of tertiary education. Information derived from the published and unpublished work of others has been acknowledged in the text and a list of references is given.

Nader A. Issa
June 21, 2005

Contents

III APPLICATION 95

Modes and Propagation in Microstructured Optical Fibres

Nader A. Issa
University of Sydney, 2005

Abstract

Microstructured optical fibres (MOFs), also commonly called photonic crystal fibres or holey fibres, describe a type of optical fibre in which continuous channels of (typically) air run their entire length. These ‘holes’ serve to both confine electromagnetic waves within the core of the fibre *and* to tailor its transmission properties. In order to understand and quantify both of these functions, a new computational algorithm was developed and implemented. It solves for the eigenvalues of Maxwell’s wave equations in the two-dimensional waveguide cross-section, with radiating boundary conditions imposed outside the microstructure. This yields the leaky modes supported by the fibre. The boundary conditions are achieved exactly using a novel refinement scheme called the Adjustable Boundary Condition (ABC) method. Two implementations are programmed and their computational efficiencies are compared. Both use an azimuthal Fourier decomposition, but radially, a finite difference scheme is shown to be more efficient than a basis function expansion. The properties of the ABC method are then predicted theoretically using an original approach. It shows that the method is highly efficient, robust, automated and generally applicable to any implementation or to other radiating problems. A theoretical framework for the properties of modes in MOFs is also presented. It includes the use of the Bloch-Floquet theorem to provide a simpler and more efficient way to exploit microstructure symmetry. A new, but brief study of the modal birefringence properties in straight and spun fibres is also included.

The theoretical and numerical tools are then applied to the study of polymer MOFs. Three types of fibres are numerically studied, fabricated and characterised. Each is of contemporary interest. Firstly, fabrication of the first MOFs with uniformly oriented elliptical holes is presented. A high degree of hole ellipticity is achieved using a simple technique relying on hole deformation during fibre draw. Both form and stress-optic birefringence are characterized over a broad scaled-wavelength range, which shows excellent agreement with numerical modelling. Secondly, an analysis of leaky modes in real air core MOFs,

fabricated specifically for photonic band gap guidance, is then used to identify alternative guiding mechanisms. The supported leaky modes exhibit properties closely matching a simple hollow waveguide, weakly influenced by the surrounding microstructure. The analysis gives a quantitative determination of the wavelength dependent confinement loss of these modes and illustrates a mechanism not photonic band gap in origin by which colouration can be observed in such fibres. Finally, highly multimode MOFs (also called 'air-clad' fibres) that have much wider light acceptance angles than conventional fibres are studied. An original and accurate method is presented for determining the numerical aperture of such fibres using leaky modes. The dependence on length, wavelength and various microstructure dimensions are evaluated for the first time for a class of fibres. These results show excellent agreement with published measurements on similar fibres and verify that bridge thicknesses much smaller than the wavelength are required for exceptionally high numerical apertures. The influence of multiple layers of holes on the numerical aperture and capture efficiency are then presented. It shows that a substantial increase in both these parameters can be achieved for some bridge thicknesses. Simple heuristic expressions for these quantities are given, which are based on the physical insight provided by the full numerical models. The work is then supported by the first fabrication attempts of large-core polymer MOFs with thin supporting bridges. These fibres exhibit relatively high numerical apertures and show good agreement with theoretical expectations over a very wide scaled-wavelength range.

Publications

The following publications were generated from research conducted during the period of candidature: March 2001 to September 2004.

Publications in which this author is listed first amongst those who have contributed, have been written by this author. Those publications represent research conducted at the Optical Fibre Technology Centre by the listed authors, who are ordered by greatest relative contribution as estimated by the first author through appropriate discussions. Additional acknowledgements are given in each publication.

This thesis has been based on these publications. The relationship between individual chapters and particular publications is discussed within the preface. The particular contributions of listed authors is also discussed within the preface.

First author publications

Journal publications

1. Nader A Issa and Whayne E Padden, "*Light acceptance properties of multimode microstructured optical fibers: Impact of multiple layers,*" Optics Express, Vol. 12, No. 14, pp. 3224-35 (2004)

2. Nader A Issa, "*High numerical aperture in multimode microstructured optical fibers,*" Applied Optics, Vol. 43, No. 33, pp. 6191-7 (2004)

3. Nader A Issa, Martijn A van Eijkelenborg, Matthew Fellew, Felicity Cox, Geoffrey Henry and Maryanne CJ Large, "*Fabrication and study of microstructured optical fibers with elliptical holes,*" Optics Letters, Vol. 29, No. 12, pp. 1336-8 (2004)

4. Nader A Issa, Alexander Argyros, Martijn A van Eijkelenborg and Joseph Zagari, "*Identifying hollow waveguide guidance in air-cored microstructured optical fibres,*" Optics Express, Vol. 11, No. 9, pp. 996-1001 (2003)

5. Nader A Issa and Leon Poladian, "*Vector wave expansion method for leaky modes of microstructured optical fibres,*" Journal of Lightwave Technology, Vol. 21, No. 4, pp. 1005-12 (2003)

Conference presentations

1. Nader A. Issa, Clemens von Korff Schmising, Whayne E. Padden and Martijn A. van Eijkelenborg, "*High numerical aperture in large-core microstructured polymer optical fibres,*" Proceedings of the international Plastic Optical Fiber (POF) conference, Nürnberg, Germany, pp. 436-43 (2004)

2. Nader A Issa, Martijn A van Eijkelenborg, Matthew Fellew, Felicity Cox, Geoffrey Henry and Maryanne CJ Large, "*Fabrication and characterization of microstructured optical fibres with elliptical holes,*" Proceedings of the Conference of Lasers and Electro-Optics/International Quantum Electronics Conference (CLEO/IQEC), San Francisco, USA, paper CThX3 (2004)

3. Nader A Issa, Martijn A van Eijkelenborg, "*Designing multicore optical fibres with minimal modal dispersion,*" Proceedings of the Conference of Lasers and Electro-Optics/International Quantum Electronics Conference (CLEO/IQEC), San Francisco, USA, paper CTuD2 (2004)

4. Nader A Issa, Alexander Argyros, Martijn A van Eijkelenborg and Joseph Zagari, "*Hollow waveguide guidance in air-cored microstructured optical fibres,*" Proceedings of the Australian Conference on Fibre Optic Technology (ACOFT), Melbourne, Australia, pp. 141-4 (2003)

5. Nader A Issa and Leon Poladian, "*Vector wave equation expansion method for leaky modes in microstructured optical fibres,*" Proceedings of the Australian Conference on Fibre Optic Technology (ACOFT) Sydney Convention Centre, Sydney, Australia, pp. 72-4 (2002)

6. Nader A Issa and Leon Poladian, "*Considerations for an expansion method used to calculate leaky modes in MOFS,*" Proceedings of Australian Optical Society (AOS) conference, Sydney, Australia (2002)

Special presentations

1. Nader A Issa, "*Modelling high numerical aperture MOFs,*" Bath University photonic crystal fibre workshop, Bath, UK (2004)

2. Nader A Issa, "*Numerical methods for holey fibres,*" Commercialisation of MPOF workshop, Polymer Optical Fibre Application Center, Nürnberg, Germany (2004)

3. Nader A Issa, Martijn A van Eijkelenborg, Alexander Argyros, Geoff W Barton, Ian M Bassett, Matthew Fellew, Goeff Henry, Maryanne CJ Large, Steven Manos,

Whayne E Padden, Leon Poladian, Joseph Zagari, "*Recent advances in microstructured polymer optical fibres,*" Poster at FiberComm 2003 trade exhibition, Munich, Germany (2003)

4. Nader A Issa, "*Elliptical hole microstructured polymer optical fibres,*" OFTC departmental seminar, Sydney, Australia (2004)
5. Nader A Issa, "*Multicore optical fibres with minimal modal dispersion,*" OFTC departmental seminar, Sydney, Australia (2003)
6. Nader A Issa, "*Device design for Quasi-Phase-Matched Second Harmonic Generation,*" OFTC departmental seminar, Sydney, Australia (2002)

Jointly authored publications

Journal publications

1. Martijn A van Eijkelenborg, Alexander Argyros, Alexander Bachmann, Geoff W Barton, Maryanne CJ Large, Geoffrey Henry, Nader A Issa, Karl-Freidrich Klein, Hans Poisel, Wilson Pok, Leon Poladian, Steven Manos, Joeseph Zagari, "*Bandwidth and loss measurements of graded-index microstructured polymer optical fibre,*" Electronics Letters, Vol. 40, No. 10, pp. 592-3 (2004)
2. Whayne E Padden, Martijn A van Eijkelenborg, Alexander Argyros and Nader A Issa, "*Coupling in a twin-core microstructured polymer optical fibre,*" Applied Physics Letters, Vol. 84, No. 10, pp. 1689-91 (2004)
3. Joseph Zagari, Alexander Argyros, Geoff W Barton, Geoffrey Henry, Maryanne Large, Nader A Issa, Leon Poladian and Martijn A van Eijkelenborg, "*Small-core single-mode microstructured polymer optical fibre with large external diameter,*" Optics Letters, Vol. 29, No. 8, pp. 818-20 (2004)
4. Alexander Argyros, Nader A Issa, Ian M Bassett and Martijn A van Eijkelenborg, "*Microstructured optical fibres for single-polarisation air-guidance,*" Optics Letters, Vol. 29, No. 1, pp. 20-3 (2004)
5. D. Kácik, I. Turek, I. Martincek, John Canning, Nader A Issa and Katja Lyytikäinen, "*Intermodal interference in a photonic crystal fibre,*" Optics Express, Vol. 12, No. 15, pp. 3465-70 (2004)
6. Martijn A van Eijkelenborg, Alexander Argyros, Geoff W Barton, Ian M Bassett, Matthew Fellew, Goeff Henry, Nader A Issa, Maryanne C J Large, Steven Manos,

Whayne E Padden, Leon Poladian, Joseph Zagari, "*Recent progress in microstructured polymer optical fibre fabrication and characterization,*" Optical Fiber Technology, Vol. 9, No. 4 pp. 199-209 (2003)

7. Leon Poladian, Nader A Issa, and Tanya M Monro, "*Fourier decomposition algorithm for leaky modes of fibres with arbitrary geometry,*" Optics Express, Vol. 10, No. 10, pp. 449-54 (2002)
8. Martijn A van Eijkelenborg, Maryanne C J Large, Alexander Argyros, Joseph Zagari, Steven Manos, Nader A Issa, Ian Bassett, Simon Fleming, Ross C McPhedran, C Martijn de Sterke and Nicolae AP Nicorovici, "*Microstructured polymer optical fibre,*" Optics Express, Vol. 9, No. 7, pp. 319-27 (2001)

Conference presentations

1. John Canning, Whayne E Padden, Leon Poladian, Nader A Issa, "*Imaginary refractive index waveguides and applications,*" Proceedings of the International Microwave and Optoelectronics Conference, Iguazu Falls, Brazil, pp. 443-5(2003)
2. Martijn A van Eijkelenborg, Alexander Argyros, Geoff W Barton, Ian Bassett, Felicity Cox, Matthew Fellew, Simon Fleming, Geoffrey Henry, Nader A Issa, Maryanne CJ Large, Steven Manos, Leon Poladian, Joseph Zagari, "*New possibilities with microstructured polymer optical fibres,*" Proceedings of the international Plastic Optical Fibers (POF) Conference, Tokyo, Japan, pp. 18-20 (2002)
3. Maryanne CJ Large, Martijn A van Eijkelenborg, Alexander Argyros, Joseph Zagari, Steven Manos, Nader A Issa, Ian M Bassett, Simon C Fleming, Geoff W Barton, "*Novel Microstructured Optical Fibres fabricated in Polymer,*" Proceedings of the Australian Conference on Fibre Optic Technology (ACOFT), Sydney, Australia, pp. 78-80 (2002)
4. Maryanne CJ Large, Martijn A van Eijkelenborg, Alexander Argyros, Joseph Zagari, Steven Manos, Nader A Issa, Ian Bassett, Simon Fleming, Ross C McPhedran, C Martijn de Sterke and Nicolae AP Nicorovici, "*Single-mode microstructured polymer optical fibre,*" Proceedings of the Optical Fibre Communication Conference (OFC), Anaheim, USA, pp. 527-8 (2002)
5. Maryanne CJ Large, Martijn A van Eijkelenborg, Alexander Argyros, Joseph Zagari, Steven Manos, Nader A Issa, Ian Bassett, Simon C Fleming, Ross C McPhedran, C Martijn de Sterke and Nicolae AP Nicorovici, "*Microstructured polymer optical fibres: a new approach to POFs,*" Post deadline paper of the Plastic Optical Fiber (POF) conference, Amsterdam, the Netherlands, pp. 27-30 (2001)

Invited conference presentations

1. Martijn A van Eijkelenborg, Alexander Argyros, Alexander Bachmann, Geoff W Barton, Goeffrey Henry, Nader A Issa, Karl-Freidrich Klein, Maryanne CJ Large, Steven Manos, Whayne E Padden, Leon Poladian, Hans Poisel, Yucheng Zhao, "*Applications of microstructured polymer optical fibres,*" Proceedings of the Conference of Lasers and Electro-Optics/International Quantum Electronics Conference (CLEO/IQEC), San Francisco, USA, Paper CThX1 (2004)

2. Maryanne CJ Large, Alexander Argyros, Geoff W Barton, Felicity Cox, Geoffrey Henry, Nader A Issa, Steven Manos, Whayne E Padden, Leon Poladian, Martijn A van Eijkelenborg, Alexander Bachmann, Karl-Freidrich Klein, Hans Poisel, "*Future Directions for Microstructured Polymer Optical Fibres,*" Photonics West, San Jose, USA (2004)

3. Maryanne CJ Large, Alexander Argyros, Geoff W Barton, Ian Bassett, Felicity Cox, Matthew Fellew, Geoffrey Henry, Nader A Issa, Steven Manos, Whayne E Padden, Leon Poladian, Martijn A van Eijkelenborg, Joseph Zagari, "*Microstructured Optical Fibres: Why use polymers?*" Proceedings of the European Conference on Optical Communications (ECOC-IOOC), Vol. 4, paper Th2.7.1, Rimini, Italy, pp. 1014-7 (2003)

4. Geoff W Barton, Martijn A van Eijkelenborg, Geoffrey Henry, Nader A Issa, Karl-Friedrich Klein, Maryanne Large, Steve Manos, Whayne E Padden, Wilson Pok, Leon Poladian, "*Characteristics of Multimode Microstructured POF Performance,*" Proceedings of the international Plastic Optical Fibers (POF) conference, Seattle, USA, pp. 81-4 (2003)

5. Martijn A van Eijkelenborg, Alexander Argyros, Geoffrey Henry, Nader A Issa, Steven Manos, and Jing Xie, "*PMOFTM for high bandwidth transmission*" Proceedings of the international Plastic Optical Fibers (POF) conference, Seattle USA, pp. 26-9 (2003)

6. Martijn A van Eijkelenborg, Alexander Argyros, Geoff W Barton, Ian Bassett, Felicity Cox, Matthew Fellew, Simon Fleming, Geoffrey Henry, Nader A Issa, Maryanne Large, Steven Manos, Whayne E Padden, Leon Poladian, Joseph Zagari, "*Microstructured polymer optical fibres -the exploration of a new class of fibres,*" Proceedings of the Asia-Pacific Polymer Optical Fibre Workshop, Vol. 2, Hong Kong, China, pp. 94-9 (2003)

7. Maryanne Large, Martijn A van Eijkelenborg, Joseph Zagari, Geoff W Barton, Steven Manos, Geoffrey Henry, Nader A Issa, Ian Bassett, Alexander Argyros and

Leon Poladian, "*Microstructured polymer optical fibres, an overview of progress,*" Proceedings of the Microphotonics III Materials and Applications Conference, Boston, USA (2002)

8. Maryanne CJ Large, Martijn A van Eijkelenborg, Alexander Argyros, Joseph Zagari, Steven Manos, Nader A Issa, Ian Bassett, Matt Fellew, Felicity Cox, Leon Poladian, "*Microstructured Polymer Optical Fibres: A State of the Art Review,*" Presented at Photonic Crystals Down-Under as part of the Sir Mark Oliphant Lecture Series, Canberra, Australia (2002)

9. Maryanne CJ Large , Martijn A van Eijkelenborg, Alexander Argyros, Joseph Zagari, Nader A Issa, Ian Bassett, Ross C McPhedran, and Nicolae AP Nicorovici, "*Microstructured Polymer Optical Fibres: Progress and Promise,*" SPIE vol 4616, Photonics West, San Jose (2002)

Journal publications from research prior to candidature but completed during candidature

1. Joseph J Monaghan, Andrew Kos, Nader A Issa, "*Fluid motion generated by impact,*" Journal of waterway, port, coastal and ocean engineering, Vol. 129, No. 6, pp. 250-9 (2003)

Acknowledgments

I have been guilty of underestimating the size of several sections of this thesis. Most of all, that is true of the acknowledgements. There are many individuals that I would like to thank for their support, generosity and friendship over the past four years. However, I wish this section to be a professional acknowledgement and not a personal one. Maybe that is not strictly possible.

Firstly, I would like to thank my supervisor, Simon Fleming, for his guidance in the macro-management of every aspect of this thesis. He has habitually looked out for my best interests and has directed countless deeply-valued opportunities my way, time after time. I am most grateful, for the confidence and liberty he has given me since my first day at the OFTC. It has allowed me to choose and direct my own project, as well as independently attend numerous workshops and conferences to learn, interact and even deliver. All of this has given me a wealth of experience and professional confidence, which is arguably the most valuable inheritance from a graduate degree.

On a day-to-day basis, no other person has been as influential as my associate supervisor Martijn van Eijkelenborg. I thank him for this continuous guidance, tireless support, patient tuition and unwavering confidence. Most of all I thank him for his genuine friendship over the past four years. I consider myself very lucky to have had such a wonderful supervisor.

No simple words can describe the lightning-fast intellect of Leon Poladian. The bulk of this thesis springs from a topic of his initiation. I thank him greatly for taking me on-board and entrusting me with its development. I appreciate his enthusiasm and his numerous insights that have frequently jolted me out of a ditch. Although I may no longer benefit from his supervision, my pilgrimage continues towards his level of algebraic transcendency.

When confronted with a challenging problem, the only source of knowledge at the OFTC with greater breadth than Ian Bassett's personal library is Ian himself. His manner is always gentle, reflective and often profoundly consequential. I thank him deeply for that element in my PhD experience.

In one way or another, every student at the OFTC has some reason to thank Maryanne Large, the student coordinator. For me however, I also have reasons to thank Maryanne, the mPOF researcher. She provides the glue that binds the small mPOF research group together. In doing so, an individual's contribution is magnified, which is both motivating and exciting. I also thank her for nominating me for a number of opportunities that have shaped my PhD.

For every idea that succeeds, a graveyard of incomplete, flawed and muddled ideas is left behind. Although that process is natural, it often seems sluggish and tiresome on your own. I would thank my friend and fellow PhD student, Alex Argyros, for the countless discussions that have made that process easier. I have found that these discussions have only become richer and more fruitful with time. I would also like to thank another friend and fellow PhD student, Steven Manos, his patient advice regarding computer programming, from structure to optimization.

It has been a pleasure to be part of the 'funny fibres' group and meetings. Through the group I have had the opportunity to interact with many wonderful individuals. They have been students at the OFTC, including Felicity Cox and Matt Fellew as well as staff such as Whayne Padden and Geoff Barton. In this respect, the group has been an unequaled source of inspiration and new ideas. Regarding fibre fabrication, the time and efforts of Joseph Zagari and Geoff Henry have been essential. They were advisors, instructors and doers. In particular, I would like to mention an international member of this group, Karl-Friedrich Klein. As an educator and scientist, he has initiated so many stimulating and fruitful discussions. As a mentor, he is always kind, generous and encouraging.

With the administration of Linda Shboul and Patricia Feast it is easy to feel sure-footed in 'getting the job done'. I greatly appreciate their continuous help. Similarly, the IT aid of Alex Henderson and John Freeland has been indispensable.

The generous financial support from Redfern Photonics, both top-up scholarship and equipment expenses, is highly appreciated. I sincerely hope that they find this work beneficial to them in real terms. I also thank Jing Xie of an industry partner, Cactus fibre, for the confident encouragement of some of my work, which has been highly motivating.

I would also like to thank the Australian Centre for advanced Computing and Communications (AC3), for use of supercomputing facilities, as well as the Electron Microscope Unit (EMU), University of Sydney.

Thank you to those who have proof read this thesis and/or other publications. They are: Simon Fleming, Martijn van Eijkelenborg, Leon Poladian, Ian Bassett, Alex Argyros, Dmitrii Stepanov and Whayne Padden.

In conclusion, I thank all of the staff and students at the OFTC and other intimately related organizations for an exceptional PhD experience!

Nader A. Issa

University of Sydney
Submitted in January 2005

Preface

The intentions of this preface are: to outline the structure of this thesis, to identify original findings and to associate some individual chapters with the publications listed on the previous pages. Importantly, the specific contributions of others to this work are explicitly stated here.

Part I

During the period in which this thesis was produced, Microstructured Optical Fibre (MOF) technology had matured at a rapid pace. Research had gradually shifted focus from foundational investigations of the principles of behaviour to more application driven and device based development. This transition has been intimately related to the steady improvement in fabrication quality and reproducibility. A 'speed-of-light' introduction to the background history of this technology is provided in Chapter 1. However, more comprehensive tours can be found in other sources [Russell, 2003, Knight, 2003, Bjarklev et al., 2003]. This author has been fortunate to bear witness *and* assist in the early stages of MOF development at the Optical Fibre Technology Centre (OFTC). Personal contributions have been made on a number of fronts, including the fabrication of Microstructured Polymer Optical Fibre (mPOF), characterisation and a great deal of numerical modelling. Some of this work is summarised in Section 1.3 and by van Eijkelenborg et al. [2003], where many of the jointly authored publications (in which this author is not the first) are described in their context.

A great deal of theoretical/analytic work pertaining to electromagnetic waveguide problems is available in prior literature. However, their application to MOFs sometimes requires some creative adjustment or simply needs to be explicitly stated before they are widely appreciated. Some of these important tools are re-cast in the context of MOFs in Chapter 2. The study of mode-symmetry classes is perhaps more relevant to MOFs than conventional fibres, simply because of the greater geometric freedom they permit. This is introduced in Section 2.1. It begins with the most commonly used reference for this topic and an introduction to its suggested procedure for mode-symmetry classification. However, the classification used throughout this thesis is slightly different and it is presented in Section 2.1.2. The approach, based on the Bloch-Floquet theorem, is a relatively standard one in many numerical problems. Its application specifically to MOF modelling was originally proposed by Leon Poladian [Poladian et al., 2002] and subsequently adopted here. Its implementation is simpler and allows a reduction in the minimum waveguide sector for some mode classes. The benefit for numerical analysis can be enormous, which had been known and used throughout this thesis. Its description in that chapter does include some original findings, such as the procedures for orthogonalisation and the resemblance to circular fibre modes. This full description is believed to be unpublished in an explicit form. Section 2.2 simply summarises the important points relating to the properties of leaky modes, as these modes are used throughout this thesis. With the exception of Eq. (2.8), all other contents can be found in the stated references.

Chapter 3 is composed of two major ingredients. Firstly, the issue of polarization and polarization birefringence in straight MOFs is discussed in sections 3.1 and 3.2. These sections were written in order to address an unanswered question at the time: Can the geometry of a straight MOF be used to induce circular-polarization birefringence? The answer, ‘Not without loss’, seems to be commonly accepted, but an explicit proof is believed not to exist in the literature. Thus the proof is completely original, but it does follow immediately from the fact that transverse field components of a lossless mode can always be made everywhere real. This is commonly stated as a postulate, without proof, in a number of standard texts. The second focus of this chapter is the derivation of the induced circular-polarization birefringence in a spun fibre, using a form of local mode coupling. The derivation is similar to that given in [Bassett, 1988]. However, this alternative approach, which is presented in section 3.3 and 3.4, is shorter but results in the same conclusions. Section 3.4 goes further than this reference by providing the full coupled vector terms in a spun fibre. The expressions are evaluated for the first time for a real MOF.

Part II

While part I of this thesis contains the theoretical aspects of modes in MOFs, part II concentrates on the development of numerical tools, which have been tailored specifically to model the unique properties of these fibres. In particular, the calculation of confinement loss necessitated the development of a new numerical method, which is placed in context of other numerical schemes at the introduction of the chapter. There are two unique and creative aspects to this numerical method: the procedure for determining confinement loss, referred to as the ABC method (section 4.3), and the implementations (sections 4.4 and 4.6). The ABC scheme, of iteratively refining the boundary conditions of the eigenvalue problem, was originally proposed by Leon Poladian and Tanya Monro. It was first implemented by Poladian et al. [2002] within the simpler scalar approximation. However, it is not suited to the accurate study of MOFs that have the refractive index contrasts of air to polymer or glass and is incapable of quantifying polarization effects such as birefringence. The set of basis functions used in this reference was suggested by this author and the same basis functions were used in the first fully vectorial implementation. This implementation is described in Section 4.4, which correlates with the content of journal publication No. 5 ([Issa and Poladian, 2003a]). Having observed the performance of this implementation in the numerical tests given in section 4.5, an alternative, superior implementation was proposed by this author and adopted. It is presented in Section 4.6 and its comparative performance is given in Section 4.7. Both implementations are original, however, the second is unpublished.

It was only after the ABC method had been implemented and its favourable properties been observed, that attempts were made to understand and predict the behaviour of the method. A full theoretical description of its behaviour was completed by this author and shown to accurately predict the actual numerical performance. This analysis is presented in Chapter 5. The findings are completely original, generally applicable to any implementation and currently unpublished in full form. Portions of the derivation, were however, presented in conference presentation No. 6 ([Issa and Poladian, 2002]).

Part III

This part is exclusively devoted to application. In this theme, three separate chapters consider different types of fibres. Each are studied numerically, fabricated and characterised.

Chapter 6 is based on journal publication No. 3 ([Issa et al., 2004d]) and relates to the polarization birefringence induced by elliptical holes in the fibre. Although significant theoretical interest on this topic has appeared in the literature, this work represents the first ever reported fabrication and characterization of MOF with uniformly oriented elliptical holes. The demonstration is thus original, as is the comparison with numerical calculation to identify the relative contributions of stress and form birefringence. Contributors to this work are: Geoffrey Henry, who fabricated the fibres using a new sleeving technique that reduced the hole pitch enough to allow single mode operation. Felicity Cox, who initially discovered this type of hole deformation in similar fibres fabricated for poling purposes. Matthew Fellew who made numerous attempts at fabricating fibres with elliptical holes and carried out some preliminary measurements on other fibres with partial success. Finally, Martijn van Eijkelenborg and Maryanne Large, who supervised and coordinated the efforts of these contributors. New fibre requests, as well as all the characterization measurements, fibre treatments, numerical simulations and analysis presented in this chapter were carried out by this author alone.

The work contained in Chapter 7 was completed after much attention had been given to light guidance in hollow-core mPOFs within the research group at the OFTC. What was initially believed to be photonic band gap guidance in short sections of sample fibres (due to observed colouration at the output of the fibre), was later shown by this author to be the result of another optical effect. The work presented in this chapter is original and novel. It is based on journal publication No. 4 ([Issa et al., 2003b]). Fibre fabrication was performed jointly by Joseph Zagari and Martijn van Eijkelenborg. The first experimental observations and some later experimental characterisation was conducted by Alex Argyros.

Chapter 8 relates to the numerical aperture and capture efficiency in highly multimoded MOFs. Numerical modelling of this problem is highly non-trivial, as standard formulae available for conventional fibres fail. This interesting problem was originally proposed to this author by Karl Klein. The approach presented in Section 8.2 is original and solely developed by this author. As are the results relating to single layer structures in Section 8.3. These two sections are based on journal publication No. 2 ([Issa, 2004a]). Section 8.4 relates to the impact of multiple layers on both numerical aperture and capture efficiency. It is based on journal publication No. 1 ([Issa and Padden, 2004b]). The study of multiple layers was also originally proposed to this author by Karl Klein as an obvious extension to the investigation. Naturally, the simulation method used for single layer structures was applied to the problem of multiple layers. Whayne Padden contributed intellectually to this work during the analysis and understanding of the generated numerical results. The findings in this section quantifying and explaining the increase in numerical aperture for such fibres are completely original. Fabrication of the first polymer MOF with high numerical aperture was carried out jointly by this author and Martijn van Eijkelenborg. Characterisation experiments were completed jointly by this author and Clemens von Korff Schmising. This work is presented in section 8.5, which is based on conference presentation No. 1 ([Issa et al., 2004c]).

Non-represented work

A substantial body of work, conducted during the period of candidature, is not represented in this thesis. The deliberate omission is aimed at preserving the continuity of this thesis and reducing its size. Some of that work has been presented in other forms, such as conference presentation No. 3, special presentation No. 6 and some of the jointly authored publications (journal and conference) listed on previous pages.

Part I

TECHNOLOGY HISTORY AND BACKGROUND THEORY

Chapter 1

Technology history

A remarkable property in optical fibre manufacture, is that the continuity of air channels running the length of a glass preform are preserved when drawn to fibre. This was first reported early on in the history of optical fibre manufacture [Kaiser et al., 1973, Marcatili, 1973, Kaiser and Astle, 1974]. The motivation at that time was to overcome the perceived deficiencies in having different chemical compositions for the core and cladding, a practice which is now standard in conventional fibres. Those perceived deficiencies include the creation of internal stress and losses introduced by scattering at imperfections in the core-cladding interface. While these concerns may be valid for some fabrication processes such as rod-in-tube and core-coating methods, the development of chemical vapor deposition methods, first reported by MacChesney et al. [1974], have largely eliminated such negative effects and provides very pure, low-loss synthetic silica. It has also broadened the versatility in fabrication technology, an overview of which can be found in MacChesney and DiGiovanni [1990]. Present day single-mode optical fibres are highly adapted for long-haul telecommunications and are available in well studied designs, optimized for managing losses, optical nonlinearity, group velocity dispersion and polarization. However, with the diversification in applications for optical fibres, greater demands emerge for particular aspects of their performance. The recent surge of research activity into fibres containing continuous air channels (or holes) was initiated by the report of a fibre containing a multitude of these channels of micrometer dimensions and in a semi-regular arrangement [Knight et al., 1996]. The successes of early reports on these fibres fueled the ambition that they would service the ever growing demands on the performance and functionality of optical fibre technology. Photonic Crystal Fibre (PCF), holey fibre, air-silica fibre and Microstructured Optical Fibre (MOF) are all names given to these fibres in the literature, without a clear distinction between them. However, only the last will be used here. The two major classes of microstructured optical fibre are described below. They are solid-core and hollow-core MOFs. As the core of an optical fibre generally refers to the region in the fibre cross-section containing the majority of guided power, this classification is frequently interchanged with a classification based on the presumed guiding mechanism. However, unlike in conventional fibre where the guiding mechanism is unambiguously total internal reflection, such a classification can be misleading, as will be discussed.

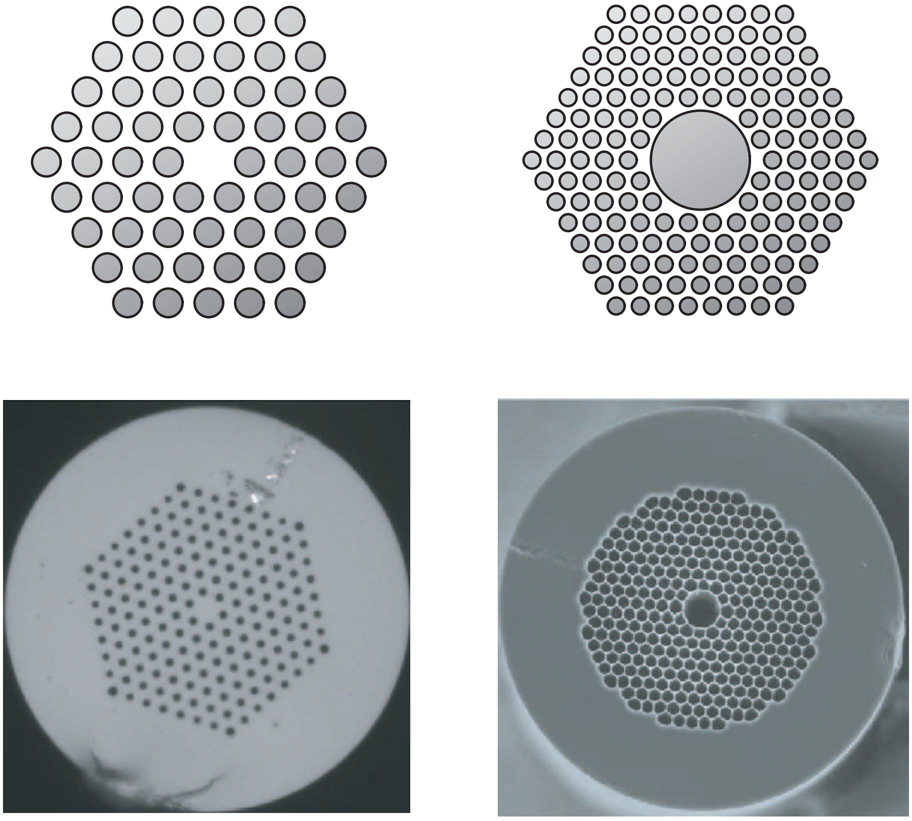

(a) (b)

Figure 1.1: Example of (a) solid core and (b) air core MOFs. Photographs reproduced from Crystal Fiber [CrystalFiber, 2004] and BlazePhotonics [BlazePhotonics, 2004] data sheets respectively.

1.1 Solid core MOFs

These fibres can best be identified by the fact that guided light is mostly localised to a material region of the fibre cross-section. The holes in the fibre may serve to provide light confinement in what is referred to as ‘average-index’ guiding MOFs [Birks et al., 1997, Knight et al., 1998a], and/or be used to tailor particular guiding properties of the fibre. Such properties include dispersion [Hasegawa et al., 2001] and birefringence [Kerbage et al., 2002]. In either situation, the hole shapes and arrangement bear great influence on many optical properties of the fibre. In the average-index model, the highest effective refractive index of the modes propagating in the cladding (called the fundamental space filling mode) is used as the refractive index of the homogenized cladding. It is, however, incorrect to only assume *this* mechanism of guiding in solid core MOFs. When considering a large number of holes in a regular array, there is the prospect for modes to localise in any defect present in the array. The idealised array itself has associated propagating ('conduction') bands of un-localised Bloch modes. The bands may be separated by gaps of forbidden transverse propagation. Defects may introduce modes with effective indices above the highest band, commonly referred to as index guiding modes, or between bands, which should be called Photonic Band Gap (PBG) guided modes, although the light may be localised to a solid region. Some prefer to not distinguish between upper and lower band gaps, referring to all guidance in regular structures as PBG in origin. The subsequent introduction of the average-index concept however, becomes appealing in order to explain the observed guidance of light in a core surrounded by a randomised arrangement of holes [Monro et al., 2000]. Anti-resonance reflection has also been identified as a potential guiding mechanism in solid core MOFs, which rely on high index cylinders surrounding a solid core [White et al., 2002a, Litchinitser et al., 2003]. This ambiguity relating to guiding mechanism motivates the present classification based on the type of core. Additional detail can be found in Ferrando et al. [2000a].

The most common embodiment of a MOF is the structure of a single hole missing in a triangular array of holes, forming a defect where light is confined. This is depicted in Fig. 1.1(a). The optical properties of this particular geometry have been heavily investigated both theoretically and experimentally. The first experimental observation of endlessly single mode behavior in these fibres by Birks et al. [1997] has subsequently been supported by the numerical investigations of Mortensen et al. [2003b] and Kuhlmey et al. [2002a]. These numerical studies show that $V_{\mathrm{PCF}} \simeq \pi$ [1] is needed for significant losses in higher order modes to ensure the fibre is single moded over practical lengths and that a hole diameter to hole pitch ratio of $d/\Lambda \simeq 0.44$ is required for single mode behavior. By realising that the latter condition is independent of wavelength, it demonstrates a valuable advantage of MOFs over conventional fibres, termed endlessly single mode. Unfortunately, this benefit coexists with a fundamental mode cutoff at $V_{\mathrm{PCF}} \simeq 1$ [Kuhlmey et al., 2002b, Nielsen et al., 2003a], which restricts the usefulness of the fibre at very long wavelengths. In addition to this limitation is another constraint imposed by the long wavelength (macro) bend-edge, which results in high losses when $\lambda \gg \Lambda/2$ [Sørensen et al., 2001, Baggett et al., 2003]. Moreover, this type of MOF has been shown to also exhibit a second bend-edge at short wavelengths [Nielsen et al., 2004a], which may be significant for some applications. These combined considerations suggest a very broadband, although finite, spectral window

---

[1] Refer to Nielsen and Mortensen [2003b] for a definition and an empirical expression of V_{PCF}. Very recently an alternative definition has been proposed in which the single mode condition is $V_{\mathrm{PCF}} \simeq 2.405$, as in conventional step index fibres. This definition and a detailed study of the applicability of such conventional fibre parameters to MOFs can be found in Koshiba and Saitoh [2004]. It is important to remember that such definitions are no more than simple heuristic expressions that provide a convenient parallel to the more familiar and established parameters of conventional step index fibres. For this reason it is unused in the remainder of this thesis.

of usefulness for these fibres and presumably those with similar geometry. Other optical properties which have been studied for this particular geometry include the group velocity dispersion [Saitoh et al., 2003, Kuhlmey et al., 2003, Nielsen et al., 2003a], confinement loss [Ferrarini et al., 2002, White et al., 2001], nonlinear effective area [Finazzi et al., 2003a,b], numerical aperture [Mortensen et al., 2002], bandwidth [Nielsen et al., 2004b], polarization properties and classification of modes [Ferrando et al., 2000b, Guobin et al., 2003] and varied material composition [Kiang et al., 2002, van Eijkelenborg et al., 2001, Zagari et al., 2004, Kumar et al., 2002].

These investigations are just a sample of all the studies that have contributed to the diversity in application for this type of MOF. More so, the physical insight they provide is transferrable to the basic understanding of countless other fibre geometries. Some of these alternative geometries, the distant cousins of the triangular array MOF, are the subject of Part III in this thesis. It is by this association that these investigations are indirectly relevant to subsequent chapters. Variations on this structure geometry are now numerous and varying, prohibiting a comprehensive summary. Work which is strongly relevant to a particular structure or an individual chapter will be identified there. The popularity of this particular geometry amongst researchers is due to the fact that it arises naturally via the stacking of capillaries to form the MOF preform - referred to as the capillary stacking technique. Notable MOF examples that utilise this technique include the improved large-mode-area endlessly single mode fibre [Mortensen et al., 2003c], honeycomb cladding fibre for dispersion engineering [Mortensen et al., 2004], dual core fibre for coupling devices [Mangan et al., 2000, Padden et al., 2004], highly birefringent fibre with round holes [Ortigosa-Blanch et al., 2000, Suzuki et al., 2001] and double clad fibres for high power lasers [Furusawa et al., 2001, Bouwmans et al., 2003a, Limpert et al., 2003]. Alternative structural geometries have subsequently been demonstrated which also use the capillary stacking technique in order to provide enhanced performance in particular applications. This diversity in MOF geometry also demonstrates the substantial versatility of the technique.

1.2 Hollow core MOFs

One year after the first solid core PBG guiding fibre was reported by Knight et al. [1998b], the report of light guidance in a hollow core (PBG) guiding fibre appeared [Cregan et al., 1999]. Its design is permissible by the capillary stacking technique when seven central capillaries are removed to create the core. Subsequent reports of light guidance in air have utilised the benefits of a large air fraction, which greatly reduces confinement loss and is responsible for the present low loss record of 1.7 dB/km at a wavelength of 1.55μm by Mangan et al. [2004]. Losses below 1 dB/m had only been reported as late as 2002. Previously, PBG guidance in hollow core MOFs had only been demonstrated in short lengths of fibres and exhibiting high confinement loss. In this situation, care must be taken in order to deduce the guiding mechanism, which is further discussed in Chapter 7. An additional distinction should be made about the guiding mechanism in what are frequently called PBG fibres. In the short wavelength regime, confinement loss may be found to be largely determined by the thickness of the high index elements rather than the period of those elements, as would be expected with PBG or Bragg reflection. Referred to as anti-resonance reflection, it has been shown to provide very low confinement loss with approximately 10 layers. A useful description is given by Litchinitser et al. [2002] and by White et al. [2002a]. It is entirely possible that fibres currently called air-guiding PBG fibre, operate by purely anti-resonance effects or a combination of both.

The commonly fabricated design for hollow core PBG fibres has so far been a triangular lattice of holes, not necessarily circular in shape and sometimes including interstitial holes [Knight, 2003, Russell, 2003]. An example is depicted in Fig. 1.1. The size of the hollow core may also vary by eliminating more of the inner rings of holes. Another design that has been fabricated and has attracted significant attention has been air-guiding Bragg fibres [Kuriki et al., 2004, Vienne et al., 2004, Johnson et al., 2001], in which a Bragg reflector is used to confine light in the hollow core. The concept is a mature one, which originates from the paper by Yeh et al. [1978] and other studies on their practicality in long-haul telecommunications. One unique possibility with Bragg fibres is the realisation of a single mode, single polarization fibre supporting only the TE core mode. This is achieved by ensuring that the incident angle of the mode on the Bragg reflector is close to the Brewster angle, thereby eliminating reflection for TM polarization [Bassett and Argyros, 2002]. An embodiment of this design using circular holes has also been presented [Argyros et al., 2004], however, this principle has not yet been demonstrated experimentally.

There have been a variety of proposed applications for hollow core fibres, whose potentials have not yet been fully explored. While the current loss record in air core fibres is higher than the theoretical limit of ~ 0.2dB/km at 1.55μm for solid core silica fibres, imposed by Rayleigh scattering at nano-scale imperfections in glass, there is potential for air-guiding fibres to surpass that loss. However, the greatest benefits can be derived from reaching such low losses at wavelengths at which the host material of the fibre may not be transparent, particularly for the transmission of CO_2 laser radiation [Temelkuran et al., 2002] or other high energy sources [Shephard et al., 2004, Humbert et al., 2004]. The transport of atoms in hollow core MOFs has been proposed and the transport of micro-particles has been demonstrated [Benabid et al., 2002b]. In addition the interesting possibility of accelerating charged particles has been suggested [Lin, 2001]. After much discussion on the advantages of hollow core PBG fibres over conventional capillary fibres for gas sensing at very low power levels, this concept was recently experimentally demonstrated [Ritari et al., 2004].

Gas-based nonlinear optics is a particularly exciting application of hollow core fibres. Here the ambition is to maximize the interaction of laser light with gases, by tight light confinement and long interaction lengths. It has made possible a 100 fold decrease in the stimulated Raman pulse-energy threshold in hydrogen filled fibre [Benabid et al., 2002a] and the production of very high harmonics in argon filled fibres [Brabec and Krausz, 2000].

In addition to the above mentioned applications, the recent demonstrations of high birefringence in hollow core fibre show that incorporating polarization control is feasible [Bouwmans et al., 2003b, Chen et al., 2004]. Regarding the practicality of handling, the macro bend loss in PBG hollow core fibres is reportedly immeasurable for bend radii as low as 5mm, which is a remarkable result [Bouwmans et al., 2003b, Hansen et al., 2004]. Dispersion, on the other hand, is important for particular nonlinear effects and the short pulse delivery. Fortuitously, a zero dispersion wavelength is commonly found within the band gap windows [Bouwmans et al., 2003b], as well as relatively high anomalous dispersion near the band edges.

Chapter 7 contains work which resulted from numerous attempts at the fabrication of air-core guiding fibres in polymer. To date such attempts have been unsuccessful [Issa et al., 2003b]. However, evidence of PBG or anti-resonance effects have been observed in these fibres for light guided in solid regions of the fibre.

1.3 Microstructured polymer optical fibres

The first reported fabrication of Microstructured Polymer Optical Fibre (mPOF) was by van Eijkelenborg et al. [2001], in which a fibre (single moded at 633nm) was demonstrated. At present, a number of additional research groups have reported the capacity to fabricate mPOF of various fibre quality. They include Choi et al. [2001], Park et al. [2002], Kuzyk [2003] and Huang et al. [2004]. However, little has been published on the advancements of these groups. The development of mPOF has brought about a leap in the diversity of structure geometry by liberating designs from the restriction of close-packed arrangements, as seen in glass MOFs fabricated by the capillary stacking technique, or the simple geometries available through glass extrusion. This is possible through a variety of preform fabrication techniques, including milling, molding, extrusion and casting. Additional potential for functionality arises from the intrinsic tailorability of polymers as well as processing temperatures that are an order of magnitude lower than glass MOFs. These properties can be particularly useful in devices for optical conversion, signal processing and sensing. Development of the potential applications of mPOF is currently at a very early stage. However, the lowest material absorption of PMMA fibre in the visible is approximately 0.2dB/m, which restricts practical communication systems to short distances, such as local area networks, fibre to the home, automotive/aeronautic applications and interconnects for electronic subsystems. In these applications however, better material flexibility in thick fibres is a key advantage. There are some notable examples of the diverse structures achievable with mPOF. These include graded index optical fibres for high bandwidth transmission [van Eijkelenborg et al., 2004a], fibres with elliptical holes for high birefringence [Issa et al., 2004d], fibres with ring structures for approximating Bragg fibres [Argyros et al., 2001, 2004], multi-core fibres for imaging [van Eijkelenborg, 2004b] and flexible large core fibres with high numerical apertures [Issa et al., 2004c].

Subsequent chapters containing either theoretical or numerical investigations are equally applicable to both silica and polymer MOFs, as well as other glasses and materials of similar refractive index. In all applications investigated in Part III, numerical simulation has been supported with at least some experimental demonstration. mPOF has been used exclusively for these demonstrations, due to availability of fabrication facilities and the ability to rapidly prototype.

Chapter 2

Waveguide modes

2.1 Mode symmetries and classification

The symmetry of a waveguide determines the symmetries of its modes, which can be classified into mode classes. It also determines the degeneracies of these classes. However, symmetry analysis not only provides information about the propagation characteristics of the waveguide, it also provides methods for reducing the computational demand of numerical studies on these waveguides by finding the Minimum Waveguide Sector (MWS) that completely describes any mode of a given class.

The context is waveguides which are uniform along their length (translation-invariant), transversely inhomogeneous and whose media are isotropic. Since the waveguide is infinitely long and assuming an $\exp(-i\omega t)$ time dependence, the length variation of a mode is $\exp(i\beta z)$ where β is the propagation constant of the mode and is a function of ω. There are always an infinite number of modes. For waveguides within a closed boundary, the mode spectrum is discrete, while for open boundary waveguides, the spectrum consists of a continuum of radiation modes plus a finite number of discrete bound modes. One can also study the leaky modes of open boundary waveguides, which are also discrete.

One approach to a complete study of symmetry-induced modal characteristics in electromagnetic waveguides was published by McIsaac [1975a, 1975b]. The approach is summarised in Section 2.1.1. Although this study has been widely available for some time, there have recently been a few works that refresh the key findings of this publication in the minds of researchers working on MOFs. They do so by numerically verifying the degeneracy of the fundamental mode of a 6-fold symmetric MOF [Steel et al., 2001b] or numerically demonstrating the modal properties of 6 and 4-fold symmetric MOFs [Ferrando et al., 1999, Guobin et al., 2003].

In Chapter 4, an azimuthal Fourier decomposition is used for the numerical solution of modes in MOFs. Such a decomposition provides a natural method of mode classification that offers several important advantages for numerical modelling. The details are described in Section 2.1.2.

2.1.1 Classification via group representations

A summary of the key findings published by McIsaac [1975a, 1975b] is presented here. A symmetry operation for a figure is a spatial operation that leaves the figure unchanged. For two dimensional figures, only two types of operations exists: rotations about a symmetry axis normal to the plane of the figure and reflections about a line within the plane. If the smallest rotation that leaves the figure unchanged is $2\pi/n$ and the figure has no reflection symmetry, then the figure is said to possess the C_n symmetry group. Note that C_n denotes both the symmetry operation ($2\pi/n$ rotation), as well as the group of operations

$$C_n,\ C_n^2,\ C_n^3, \ldots,\ C_n^{n-1},\ C_n^n \equiv \text{Identity}, \tag{2.1}$$

generated by it. The order of this group is n. Thus a waveguide with n-fold symmetry has n mode classes, where all modes of the same mode class have the same azimuthal symmetry.

If a figure possesses n-fold symmetry and has at least one plane of reflection symmetry, then there are exactly n planes of reflection symmetry. This symmetry group is denoted by $C_{n\nu}$ and is of order $2n$. Similarly, the modes of a waveguide with $C_{n\nu}$ symmetry can be partitioned into $2n$ mode classes containing only modes with the same azimuthal symmetry.

The approach used by McIsaac [1975b] to detail these mode classes is an established group theory tool in quantum mechanics. The symmetry operations of the groups C_n and $C_{n\nu}$ can be represented by distinguishable square matrices that themselves satisfy the same multiplication table as the symmetry group. This set is not unique. The smallest dimension matrices that satisfy this are called the irreducible representations associated with the symmetry group. The irreducible representations for the groups C_n and $C_{n\nu}$ are tabulated in a number of texts (eg. [Tinkham, 1964]) and a key point is that they have either dimension one or two. It so happens that each row of an irreducible representation is associated with one mode class of the waveguide. Thus the total number of mode classes is equal to the total number of rows in all the irreducible representations. A one dimensional irreducible representation is associated with a non-degenerate mode class, while a two dimensional irreducible representation is associated with a doubly-degenerate mode class (the mode classes associated with the first and second rows being degenerate with each other - a degenerate pair).

When a symmetry operation is executed on a mode, the result must also be a mode of the waveguide with the same propagation constant. Thus it must be a linear combination of the original mode and any other modes degenerate to the original. The constants in that combination do in fact make up a column of an irreducible representation. In that way irreducible representations can be constructed from given sets of degenerate modes, called basis modes. This process is outlined briefly by [McIsaac, 1975b]. However, it is the reverse process that was used to identify the mode classes: given the irreducible representations of the symmetry groups C_n and $C_{n\nu}$, the basis modes (one for each mode class) were projected-out from an arbitrary function. The projection operators are given in [Tinkham, 1964, pp.39-41] and the results of this approach are shown in Tables III and IV of McIsaac [1975a].

Table III of this paper is reproduced below in table 2.1 for later reference. It shows the Fourier series expansions for the electric and magnetic fields of modes in waveguides with C_n symmetry. The Fourier expansions of the fields in waveguides with $C_{n\nu}$ symmetry are given in [McIsaac, 1975a, Table IV]. It differs in that sine and cosine functions are used instead of complex exponentials, which allows reflection symmetry to be exploited. The table is not reproduced here.

Given the Fourier expansions for the fields of each mode class, it is then possible to deduce the MWS (with boundary conditions) required to completely describe the mode. What is known about the Fourier expansion can then be discarded when solving for the mode. For waveguides with C_n and $C_{n\nu}$ symmetry, these are provided in [McIsaac, 1975a, Table V plus Fig. 3] and [McIsaac, 1975a, Table VI plus Fig. 4] respectively. A reader knowing the waveguide symmetry and the mode class of interest would then navigate though the relatively complicated tables to determine the appropriate MWS. It would then be noticed that the MWS is greater than $2\pi/n$ for the majority of mode classes. In the worst case scenario, the MWS would be 2π or π for some waveguides with C_n or $C_{n\nu}$ symmetry respectively. For waveguides with multiple modes and a high degree of rotational symmetry, numerical calculations on such waveguide sectors would be computationally prohibitive in both time and memory. Hence a simpler approach has been sought.

2.1.2 Azimuthal Bloch-Floquet solution method

One alternative approach is described here. Its major advantage is that it allows a MWS of $2\pi/n$ for any mode class. It was also recently reported by Fini [2004] that the separation of mode classes created by the MWSs proposed by McIsaac [1975a] was not optimal in another respect. The use of some numerical techniques, such as the multipole method, together with the wide MWSs, makes the method prone to overlook modes in that class without sophisticated searching. Prior to that report, all published numerical schemes for modelling MOFs used the McIsaac [1975a] mode symmetry classes, with the exception of Poladian et al. [2002] and Issa and Poladian [2003a]. In these two methods, the use of an azimuthal Fourier decomposition (originally proposed for optical waveguides by Vassallo [1990]) made an alternative separation a natural choice. It is based on the Bloch-Floquet

n	Mode class index p	$\mathbf{e}_\mathrm{t}(r,\theta),\ \mathbf{h}_\mathrm{t}(r,\theta)$ or $(e_\mathrm{z}(r,\theta), h_\mathrm{z}(r,\theta))$	Mode class index m_0	Degenerate
even, odd	1	$\sum_{\nu=-\infty}^{\infty} \mathbf{f}_\nu(r)e^{in\nu\theta}$	0	No
even, odd	k	$\sum_{\nu=-\infty}^{\infty} \mathbf{f}_\nu(r)e^{i(n\nu+k/2)\theta}$	$\frac{k}{2}$	Yes
even, odd	$k+1$	$\sum_{\nu=-\infty}^{\infty} \mathbf{f}_\nu(r)e^{i(n\nu-k/2)\theta}$	$\frac{-k}{2}$	Yes
even	n	$\sum_{\nu=-\infty}^{\infty} \mathbf{f}_\nu(r)e^{in(\nu-1/2)\theta}$	$\frac{-n}{2}$	No
∞	1	$\mathbf{f}_\nu(r)$	0	No
∞	k	$\mathbf{f}_\nu(r)e^{ik\theta/2}$	$\frac{k}{2}$	Yes
∞	$k+1$	$\mathbf{f}_\nu(r)e^{-ik\theta/2}$	$\frac{-k}{2}$	Yes

Table 2.1: Fourier series expansions for the electric and magnetic fields of modes in waveguides with C_n symmetry. $\mathbf{f}_\nu(r)$ are unknown functions which are usually found numerically. Subscripts ‘t’ and ‘z’ indicate the transverse and longitudinal components of the fields; $\mathbf{e}(r,\theta) = (\mathbf{e}_\mathrm{t}, e_\mathrm{z})$ and $\mathbf{h}(r,\theta) = (\mathbf{h}_\mathrm{t}, e_\mathrm{z})$. The transverse components satisfy the eigenvalue equations Eqs. (B.1) given in appendix B.
NOTE: Mode classes $p = k$ and $p = k+1$ are a degenerate pair and k is always even. Similarly, mode classes $m_0 = k/2$ and $m_0 = -k/2$ are a degenerate pair.

theorem[1] which can be derived purely from symmetry using the tools of group theory. A convenient reference is [Tinkham, 1964, pp.38]. In this approach any reflection symmetries of the waveguide are ignored. Any findings relevant to waveguides with C_n symmetry will equally apply to waveguides with $C_{n\nu}$ symmetry.

Consider a waveguide with C_n symmetry and a pair of field components $\mathbf{f}(r,\theta)$ which may be either $\mathbf{e}_\mathrm{t}(r,\theta)$, $\mathbf{h}_\mathrm{t}(r,\theta)$ or $(e_\mathrm{z}(r,\theta), h_\mathrm{z}(r,\theta))$. All other components can be calculated from any one of these using Eqs. (3.2). By the Bloch-Floquet theorem one can write

$$\mathbf{f}(r,\theta) = \mathbf{u}(r,\theta)e^{im_0\theta}, \tag{2.2}$$

where $\mathbf{u}$ has the same rotational symmetry as the waveguide, ie. C_n, and m_0 is an integer which indexes the mode class. The ranges for m_0 are

$$\begin{array}{lcccc} n \text{ is even:} & \frac{-n}{2} & \leq \; m_0 \; \leq & \frac{n-1}{2} \\ n \text{ is odd:} & \frac{-(n-1)}{2} & \leq \; m_0 \; \leq & \frac{n-1}{2}. \end{array} \tag{2.3}$$

Since $\mathbf{u}$ can be represented by a Fourier expansion containing only the terms $\exp(in\nu\theta)$ (ν is an integer), this approach leads once again to Table 2.1, which lists the expansions for all the possible scenarios. It also allows the reader to relate the mode classes indexed by m_0, with those indexed by p. Here the mode classes m_0 and $-m_0$ are degenerate pairs. A non-degenerate class is clearly $m_0 = 0$ for both even and odd n. However, $m_0 = n/2$ is also a non-degenerate mode class when n is even.

The process for reducing the MWS to $2\pi/n$ for all mode classes is straightforward. Begin by substituting Eq. (2.2) with a chosen value for m_0 into the eigenvalue equation for the fields. Then solve for the function $\mathbf{u}(r,\theta)$ by applying azimuthal periodic boundary conditions on the $2\pi/n$ sector. An azimuthal Fourier decomposition is not necessary for doing this.

For waveguides with $C_{n\nu}$ symmetry, it might appear that efficiency is lost by halving the total number of mode classes. While there may be some situations in which exploiting any reflection symmetries of the waveguide does provide some advantage, the benefit of minimising the waveguide sector to $2\pi/n$ is often the primary concern in numerical simulation. The full potential benefits of this classification are apparent for structures such as those studied in Chapter 8, where the rotational symmetries used are 50, 75 and 100-fold. Without this alternative separation, the computational resources required would have been prohibitive. Furthermore, the conceptual simplicity of this classification makes the explanation of physical effects easier, as discussed below.

---

[1] Bloch's theorem [Bloch, 1928] is commonly used in reference to states in periodic media for generic "wave physics" phenomena. However, in microwave and acoustic wave problems, the theorem has long been called Floquet's theorem [Floquet, 1883] which was developed earlier in the context of linear differential equations.

Orthogonalisation of degenerate bound modes in lossless waveguides

Assume that one has solved for a bound mode in the class $m_0 = k/2$, whose fields will be labeled with P: $\Psi^{\mathrm{P}} = (\mathbf{e}^{\mathrm{P}}, \mathbf{h}^{\mathrm{P}})$. Then one solves for its degenerate counterpart in the class $m_0 = -k/2$, whose fields will be labeled with Q: $\Psi^{\mathrm{Q}} = (\mathbf{e}^{\mathrm{Q}}, \mathbf{h}^{\mathrm{Q}})$. It is clear from Eq. (2.2) that these modes will be linearly independent, however they will generally not be power orthogonal. The orthogonalisation procedure given in Eq. (3.5) is a straightforward way of creating a degenerate mode (labelled $\widetilde{\mathrm{Q}}$) which is power orthogonal to mode P.

Yet a simpler approach exists which does not require one to solve for the degenerate mode Q in a second mode class. Given only Ψ^{P}, a second mode Ψ^{Q} can be constructed using Eq. (3.3). Again it is clear from Eq. (2.2) that these modes will be linearly independent. If both these modes are normalised, then the linear combinations

$$\begin{aligned} &\left(\Psi^{\mathrm{P}} + \Psi^{\mathrm{Q}}\right)/2 \\ &\left(\Psi^{\mathrm{P}} - \Psi^{\mathrm{Q}}\right)/2i \end{aligned} \tag{2.4}$$

will yield an orthonormal pair of degenerate modes. Furthermore, their transverse components will be real, while the longitudinal components will be imaginary.

The two previously mentioned procedures for orthogonalisation are not strictly possible for leaky modes. Notably since leaky modes cannot be made power orthogonal, but are orthogonal in an alternative sense. The difficulty arises from the fact that leaky modes of waveguides with no material absorption contain infinite power in the waveguide cross-section. This is discussed further in section 2.2.

Resemblance to modes of a circular step-index fibre

When the symmetry of a MOF is high (typically 6-fold or higher) and the core of the fibre is 'quasi-circular', then the core modes of the fibre bear some qualitative resemblance to those of a step-index fibre. The MOF shown in Fig. 1.1 is such an example. A study of these resemblances is given by Ferrando et al. [2000b], Guobin et al. [2003] and Section 4.5.1. The aim of this small Section is to associate step-index fibre modes with the mode classes given in Table 2.1. In a step-index fibre the order of the first few modes is HE_{11} (degenerate), TE_{01} (non-degenerate), HE_{21} (degenerate), TM_{01} (non-degenerate) and EH_{11} (degenerate). Their look-alikes can typically be found in mode classes $m_0 = 1, 0, 2, 0$ and 1 respectively and in the same order. While they are not strictly HE, TE or TM, the distribution of intensity and local polarization are alike. The general table of resemblance is given in Table 2.2.

Having found a mode in one of these mode classes, it is then necessary to make the transverse field components real before the local polarizations look like those of a step-index fibre. This is simply done using Eq. (2.4). For example, to find the HE_{11} look-alike

Resemblance to step-index fibre mode	Mode class, m_0
$\mathrm{HE}_{k,l}$-like	$k - jn$
$\mathrm{EH}_{k,l}$-like	$k - jn$
$\mathrm{TE}_{0,l}$-like	0
$\mathrm{TM}_{0,l}$-like	0

Table 2.2: Mode classes of a C_n MOF that contain the modes resembling those of a step-index fibre. The integer j is chosen to fold m_0 back into the allowed ranges given by Eq. (2.3).

mode from mode class $m_0 = 1$, firstly find the fundamental mode of that class then apply Eq. (2.4). It is very important to remember that this is only strictly possible for bound modes. In the case of leaky modes, complex conjugation of modes does not produce a degenerate mode since $\beta^* \neq \beta$.

2.2 Properties of leaky modes

Unlike the truly bound modes in conventional fibres, the modes of MOFs are often leaky. Physically, the light is trapped by an enclosure of air holes and loss arises from small amounts of power leakage between and through the holes. This is termed confinement loss. Light emerging out of the confining holes (microstructure) is radiated into the cladding, which has a refractive index of n_{cl}, that is usually equal to that of the core and all other material regions. Clearly, it is assumed that the microstructure is finite. The cladding of uniform host material is assumed to be non-absorbing and infinite for three reasons. The first reason is that it provides a standardised approach. Although MOFs are often coated with an absorbing outer jacket (usually of higher refractive index than the host material), this is not always the case. Thus any choice for its composition and position would need justification and vary for many different types of problems. The second reason is a trade-off between convenience and physicality. The physical implication of this assumption is that there is no back-reflection from the universe surrounding the MOF. It is a convenient choice because one does not need to account for any more additional objects far from the microstructure, whose influence is assumed to be negligible. The final reason is that it provides a valuable conceptual and mathematical tool which greatly simplifies the study of propagation in MOFs - ie. leaky modes.

In practice, leaky modes introduce a number of mathematical problems while simultaneously simplifying others. A mathematical framework for dealing with leaky modes in waveguides is still underdeveloped. One that deals with issues of power-orthogonality, waveguide perturbations, mode coupling, divergent integrals and lack of completeness. Quantum states in leaky cavities or open boundary problems of other kinds have been topics of research for a long time and remain an area of active research today. It has spawned a few popular approaches such as 'system-and-bath' expansions and leaky mode (also called quasinormal, unbound or improper mode) expansions. Comprehensive reviews have been given by Ching et al. [1998] and Dutra and Nienhuis [2000]. These formulations may one day provide the mathematical framework needed for open boundary waveguide problems. An analysis of the leaky modes supported in planar waveguides [Shevchenko, 1971] and circular fibres [Snyder and Love, 1974, Sammut, 1975, Sammut and Snyder, 1976] first appeared in the 70s. Subsequently, there has been little to no development of the theory in the context of optical fibres. Since leaky modes are used throughout this thesis, this section is devoted to providing the essential background for this concept.

The confinement loss of a waveguide mode can be determined by finding the leaky mode solutions of the vector wave equation. The mode is characterised by a complex effective index $n_{\text{eff}} = \beta/k$. In the cladding, far away from the microstructure, the mode fields must resemble travelling plane waves, with a wave vector (magnitude $n_{\text{cl}}k$) composed of longitudinal and transverse components. Conservation of longitudinal momentum, as the power in the core is lost to radiation, leads to a simple expression for the angle between the direction of radiation and the axis of the fibre [Snyder and Love, 1983, pp.492]

$$\theta = \cos^{-1}(\mathrm{Re}[\mathrm{n_{eff}}]/\mathrm{n_{cl}}). \tag{2.5}$$

This is illustrated graphically in Fig. 2.1. The process of power leakage through the microstructure is commonly referred to as tunneling, since it behaves similarly to the quantum analogue - that attenuation is exponential in length / time. In fact, the imaginary part of the effective index determines the power attenuation by

$$\exp(-2\mathrm{Im}(\mathrm{n_{eff}})\mathrm{kL}), \tag{2.6}$$

where L is the length of the fibre. Thus an expression for loss is

$$\text{loss (dB/m)} = \frac{40\pi}{\lambda \ln(10)} \mathrm{Im}(n_{\text{eff}}). \tag{2.7}$$

An important concept is portrayed in Fig. 2.1. At each reference cross-section through the fibre, the intensity distribution of the mode is haunted by the power radiated at a previous time and position along the fibre. Since the core power grows exponentially as one looks from right to left, the intensity in the reference cross-section must begin to grow at some radius outside the microstructure. As the radius increases, the intensity continues to grow unbounded. This is because the modal solution assumes that the fibre is infinitely long. Thus the total modal power flow through the cross-section is also infinite. In circular fibres, the radius at which the fields change in appearance from evanescent to oscillatory is called the radiation caustic [Sammut and Snyder, 1976a]. It marks the apparent source of

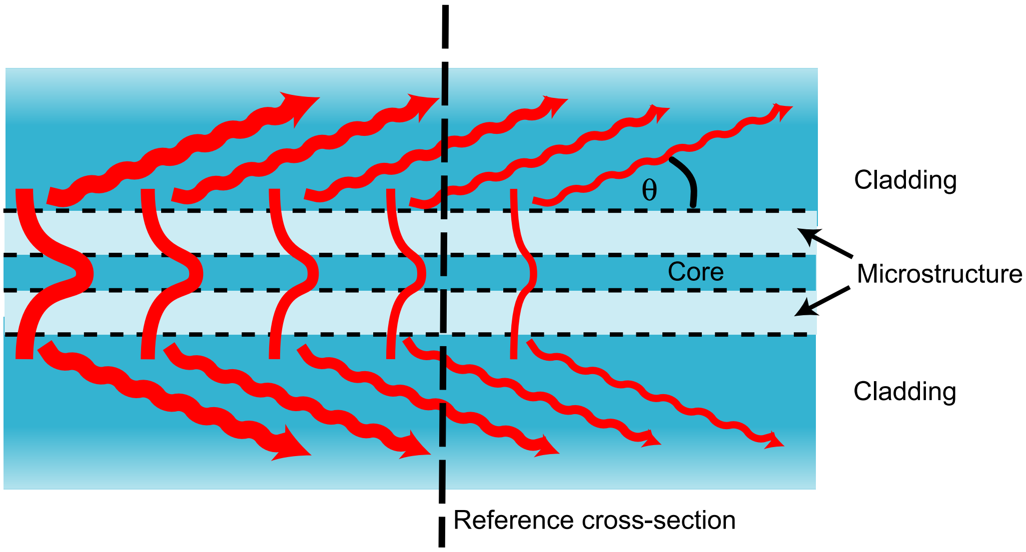

Figure 2.1: Illustration of a leaky mode. The same fraction of the core power is lost in every unit length. It leaks through the microstructure and radiates into the cladding at an angle given by Eq. (2.5).

emission. A similar location exists in MOFs and it is usually found just at the outer edge of the microstructure. These features make leaky modes difficult to model numerically, an issue which is discussed further is Section 4.1.

A useful expression can be obtained which relates the fields of the leaky mode to the imaginary component of the effective index which arises purely from confinement loss. In the case of a waveguide with no material absorption or gain (ie. $n(x, y)$ is real), one can use the conjugated form of the reciprocity theorem supplied in [Snyder and Love, 1983, pp. 602, Eq. 31-4] to derive the expression

$$\mathrm{Im}(n_{\mathrm{eff}}) = \frac{1}{2k}\frac{\displaystyle\oint_{\delta A} \mathbf{S}\cdot\widehat{\mathbf{n}}dl}{\displaystyle\int_{A} \mathbf{S}\cdot\widehat{\mathbf{z}}dA}, \tag{2.8}$$

where $\mathbf{S}$ is the standard Poynting vector, A is some finite region of the waveguide cross-section with boundary δA, $\widehat{\mathbf{n}}$ is the normal to the boundary within the cross-section and $\widehat{\mathbf{z}}$ is the unit vector along the fibre axis. It is emphasised that A is arbitrary and does not need to enclose the microstructure. Although Eq. (2.8) is straightforward to derive from the afore-mentioned reciprocity relation, it has not been found in the known literature. The expression states that in any region of the waveguide cross-section, the ratio of the power flowing out of that region (per unit length) to the power flowing through the region is a constant. It is proportional to the imaginary part of the effective index.

As mentioned previously, electromagnetic propagation in an open waveguide can be completely described using a finite sum of bound modes and an integration over a continuum of radiation modes. However, this integration can be very slowly convergent. For propagation at small angles to the fibre axis, it has been found that leaky modes provide a much more convenient description of propagation. A detailed analysis of how the continuum of radiation modes in a circular step-index fibre can be decomposed into a finite number of leaky modes and the space-wave contribution (the remainder), is provided by Sammut [1975] and an overview by [Snyder and Love, 1983, chapter 26]. For slab waveguides, overviews are provided by Shevchenko [1971] and [Vassallo, 1991, section 3.4].

Of practical importance is the issue of orthogonality for leaky modes. It is shown in [Sammut and Snyder, 1976a] that leaky modes do not obey the usual power orthogonality relation (Eq. (3.4)) for an ideal waveguide. However, when the confinement loss is small, they are approximately power orthogonal in a finite region of the waveguide cross-section containing the microstructure. The unbound fields of leaky modes are the cause of this irregularity. The proposed solution, involves changing the inner product by removing the complex conjugation and changing the integration path. Leaky modes then obey the following orthogonality rule

$$\int\limits_{A'_\infty} \mathbf{e}^{\mathrm{P}} \times \mathbf{h}^{\mathrm{Q}} \cdot \hat{\mathbf{z}}\, \mathrm{d}A = \int\limits_{A'_\infty} \mathbf{e}^{\mathrm{Q}} \times \mathbf{h}^{\mathrm{P}} \cdot \hat{\mathbf{z}}\, \mathrm{d}A = 0 \text{ for } Q \neq P, \tag{2.9}$$

where A'_∞ is defined as

$$\int\limits_{A'_\infty} \mathrm{d}A = \lim_{R\to\infty} \int\limits_0^{2\pi} \mathrm{d}\theta \left(\int\limits_0^d r\ \mathrm{d}r + \int\limits_{L_R} r\ \mathrm{d}r \right). \tag{2.10}$$

In this expression d is some radius enclosing the microstructure and L_R is illustrated in Fig.2.2. The angle γ must be large enough for the integrals to be finite. The asymptotic form for the fields of leaky modes (even for non-circular fibres) is proportional to $\exp\left(-ikr\sqrt{n_{\mathrm{cl}}^2 - n_{\mathrm{eff}}^2}\right)$ (see Eq. (4.10)) as $r \to \infty$. Therefore the angle γ is chosen to make the real part of the exponent negative.

Given a launch / excitation field, the orthogonality relation given in Eq. (2.9) allows one to uniquely determine the relative excitation of each leaky mode in a manner analogous to that for bound modes. In order to do so, one is required to either assume the excitation is zero outside d or know the analytic continuation in this region. It must also be remembered that the set of leaky modes is not complete in the usual sense. The fact that the modes are not power orthogonal does raise the concern that there may be coupling of power between leaky modes during propagation. It has always been assumed that this coupling is negligible, but a satisfactory study has never been conducted nor

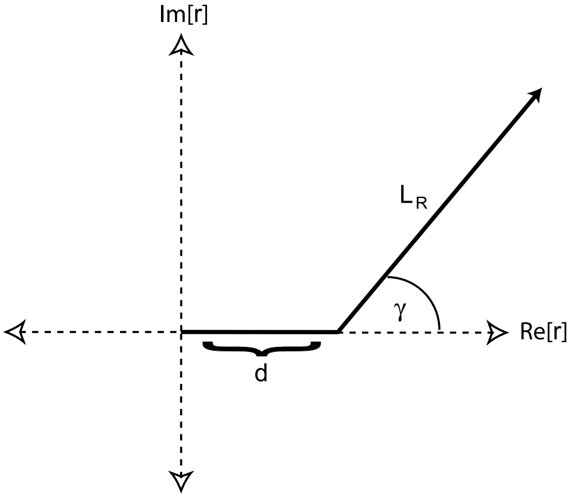

Figure 2.2: The radial integration path (solid line) in the complex r plane.

has a complete interpretation been provided. Sammut and Snyder [1976a] attempts an evaluation of the coupling between truncated leaky modes of a circular step index fibre, which indicates that the coupling is negligible for modes with small confinement losses. A generalization is required which also studies coupling between leaky modes with vastly different confinement loss. It should be noted that this problem is not unique to leaky modes, but that bound modes in absorbing waveguides suffer from a nearly identical issue of coupling. This too is commonly ignored and not completely addressed in the literature.

By using an absorbing outer jacket that encloses the microstructure, it is possible to study confinement loss in MOFs without ever having to introduce the concept of a leaky mode or the related issues such as infinite power in the waveguide cross-section. The modes will however, have some intrinsic loss associated with absorption in the outer jacket. This is unavoidable when the system is non-Hermitian. Furthermore, a small amount of back-reflection from this jacket is to be expected. This approach may be preferable in some situations. In this thesis, the use of leaky modes is motivated purely by pragmatic reasons: A tool was needed to study propagation which was 'mode-like' and where the calculated loss was purely a consequence of the microstructure. That is, to cleanly separate confinement loss from absorption and back-reflection. By assuming that any power escaping the microstructure could not be back-reflected, the resulting solutions are leaky modes. Hence these modes are to be thought of as a descriptor for mode-like propagation which quantifies pure confinement loss.

Chapter 3

Considerations for modal birefringence

There are two major aims of this chapter. Firstly, to provide a more explicit understanding of the meaning of polarization and modal birefringence in fibres such as microstructured fibres which have large refractive index contrasts. Secondly, in the instance of bound modes, to provide clear restrictions on the expected behaviour of polarization in the modes of birefringent fibres. With these aims, one is able to answer open questions such as: 'Can the geometry of a MOF be used to induce circular birefringence in a straight, un-spun fibre?'

Most conclusions that may be only strictly valid for bound modes, are in fact approximately valid for leaky modes with small confinement losses. Note that even when confinement loss is high for practical purposes one usually finds that $\mathrm{Im}(\mathrm{n}_{\mathrm{eff}}) \ll \mathrm{Re}(\mathrm{n}_{\mathrm{eff}})$. Thus the proceeding analysis is approximately applicable to microstructured fibres supporting leaky modes.

3.1 Local polarization

The concept of polarization in optical waveguides is subtle in its difference to the polarization of a freely propagating plane wave. Consider the *reduced* fields **e**, **h** which are obtained from the total fields

$$\begin{aligned}\mathbf{E}(x,y,z,t) &= \mathbf{e}(x,y)e^{i(\beta z-\omega t)} &&= (\mathbf{e}_{\mathrm{t}}(x,y), e_{\mathrm{z}}(x,y))e^{i(\beta z-\omega t)},\\ \mathbf{H}(x,y,z,t) &= \mathbf{h}(x,y)e^{i(\beta z-\omega t)} &&= (\mathbf{h}_{\mathrm{t}}(x,y), h_{\mathrm{z}}(x,y))e^{i(\beta z-\omega t)},\end{aligned} \tag{3.1}$$

by eliminating the dependence on time, t, and the propagating direction, z. They satisfy the vector wave equations [Snyder and Love, 1983, pp. 591]

$$\begin{aligned}
\mathbf{e}_\mathrm{t} &= -\left(\frac{\mu_0}{\varepsilon_0}\right)^{1/2}\frac{1}{kn^2}\hat{\mathbf{z}}\times(\beta\mathbf{h}_\mathrm{t}+i\nabla_\mathrm{t}\,h_\mathrm{z}),\\
\mathbf{h}_\mathrm{t} &= \left(\frac{\varepsilon_0}{\mu_0}\right)^{1/2}\frac{1}{k}\hat{\mathbf{z}}\times(\beta\mathbf{e}_\mathrm{t}+i\nabla_\mathrm{t}e_\mathrm{z}),\\
e_\mathrm{z} &= i\left(\frac{\mu_0}{\varepsilon_0}\right)^{1/2}\frac{1}{kn^2}\hat{\mathbf{z}}\cdot\nabla_\mathrm{t}\times\mathbf{h}_\mathrm{t}=\frac{i}{\beta}(\nabla_\mathrm{t}\cdot\mathbf{e}_\mathrm{t}+(\mathbf{e}_\mathrm{t}\cdot\nabla_\mathrm{t})\ln n^2),\\
h_\mathrm{z} &= -i\left(\frac{\varepsilon_0}{\mu_0}\right)^{1/2}\frac{1}{k}\hat{\mathbf{z}}\cdot\nabla_\mathrm{t}\times\mathbf{e}_\mathrm{t}=\frac{i}{\beta}\nabla_\mathrm{t}\cdot\mathbf{h}_\mathrm{t}.
\end{aligned}\tag{3.2}$$

The refractive index distribution, $n(x, y)$, used to create modes in optical waveguides results in two key differences. Firstly, the magnitude *and* direction of the reduced electric and magnetic field vectors may vary at different points in the waveguide cross-section. Secondly, the orthogonality between the transverse components of electric and magnetic fields are not preserved at all points in the cross-section. However, in the limit of small variation in refractive index (weakly guiding limit) the mode solutions are expected to locally resemble a plane travelling wave. Hence we expect to only deal with these two differences when refractive index contrasts are large. In this latter regime it is the *local* polarization of the electromagnetic field in an arbitrary waveguide mode that has an unambiguous meaning. Birefringence defines the instance where two modes of different effective indices are found which also have *nearly* orthogonal local polarization everywhere in the waveguide cross-section.

3.2 Restrictions on the birefringence of translationally invariant waveguides

An open question is the extent to which waveguide geometry can be used to tailor the local polarization properties of *bound* modes in dielectric waveguides when the materials are assumed to be isotropic, lossless and non-magnetic. Here we show that in such translationally invariant waveguides only modes whose transverse components are everywhere locally linearly polarized can be birefringent. The analysis is completely original, although in retrospect some results may be inferred from statements regarding the transverse and longitudinal field components which are given *without proof* in standard texts such as Snyder and Love [1983] and Vassallo [1991].

Take a bound mode solution, P, of some arbitrary waveguide such as that depicted in Fig. 3.1 and assume there exists at least one point $\mathbf{x}_0$ in the infinite cross-section A_∞ where the fields are not locally linearly polarized. There is some freedom in what

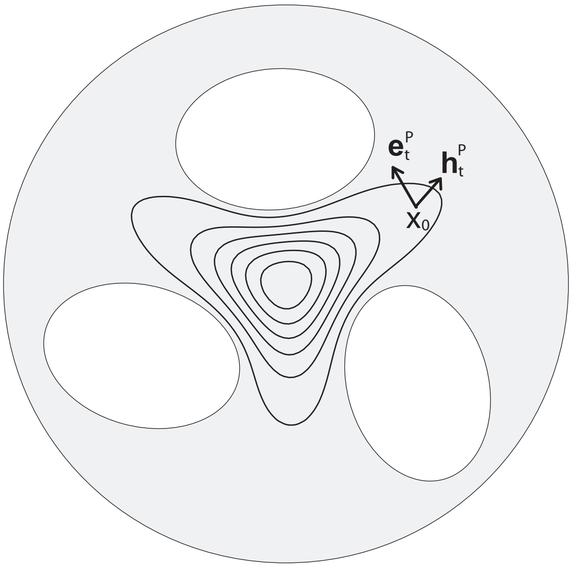

Figure 3.1: Example waveguide geometry with bound mode solution P. Ellipses with depressed refractive index are used in tailoring modal properties.

we mean by the polarization of the field at a point in a bound mode. Here we choose to consider the polarization of only the transverse field components, since they are the dominant components in all glass or polymer based optical fibres. Then this statement can be expressed exactly by saying that $\mathbf{e}_\mathrm{t}^\mathrm{P}$ and $\mathbf{h}_\mathrm{t}^\mathrm{P}$ cannot both be made real valued at $\mathbf{x}_0$ by scaling with a complex constant. This is true since the phase difference between the two components of $\mathbf{e}_\mathrm{t}^\mathrm{P}$ determines the ellipticity of the local polarization.

A mode with label Q can then always be constructed by

$$\begin{array}{rclcl} \mathbf{e}^\mathrm{Q} & = & (\mathbf{e}_\mathrm{t}^\mathrm{Q}, e_\mathrm{z}^\mathrm{Q}) & = & ((\mathbf{e}_\mathrm{t}^\mathrm{P})^*, -(e_\mathrm{z}^\mathrm{P})^*), \\ \mathbf{h}^\mathrm{Q} & = & (\mathbf{h}_\mathrm{t}^\mathrm{Q}, h_\mathrm{z}^\mathrm{Q}) & = & ((\mathbf{h}_\mathrm{t}^\mathrm{P})^*, -(h_\mathrm{z}^\mathrm{P})^*), \end{array} \tag{3.3}$$

which can easily be shown to also satisfy Eqs. (3.2) for the same refractive index profile and equal propagation constant.

Assuming that modes P and Q are not identical, then they are clearly linearly independent modes, but are generally *not* power orthogonal in the sense of Eq. (3.4). However, using a suitable orthogonalisation procedure, provided in Eq. (3.5), an orthogonal and degenerate mode, $\widetilde{\mathrm{Q}}$, can be obtained from modes P and Q so that

$$\int\limits_{A_\infty} \mathbf{e}^\mathrm{P} \times (\mathbf{h}^{\widetilde{\mathrm{Q}}})^* \cdot \hat{\mathbf{z}}\, \mathrm{d}A = \int\limits_{A_\infty} (\mathbf{e}^{\widetilde{\mathrm{Q}}})^* \times \mathbf{h}^\mathrm{P} \cdot \hat{\mathbf{z}}\, \mathrm{d}A = 0, \tag{3.4}$$

where

$$(\mathbf{e}^{\widetilde{\mathrm{Q}}}, \mathbf{h}^{\widetilde{\mathrm{Q}}}) \;=\; (\mathbf{e}^\mathrm{Q}, \mathbf{h}^\mathrm{Q}) - \gamma\, (\mathbf{e}^\mathrm{P}, \mathbf{h}^\mathrm{P}), \tag{3.5}$$

and

$$\gamma = \frac{\displaystyle\int\limits_{A_\infty} \mathbf{e}^{\mathrm{Q}} \times (\mathbf{h}^{\mathrm{P}})^* \cdot \hat{\mathbf{z}}\ \mathrm{d}A}{\displaystyle\int\limits_{A_\infty} \mathbf{e}^{\mathrm{P}} \times (\mathbf{h}^{\mathrm{P}})^* \cdot \hat{\mathbf{z}}\ \mathrm{d}A}. \tag{3.6}$$

Hence we conclude that any mode featuring regions in the waveguide cross-section where the fields are not locally linearly polarized, must be degenerate and power orthogonal with at least one other mode. Furthermore, this mode can easily be constructed by the above procedure involving only complex conjugation and orthogonalisation.

It has been shown [McIsaac, 1975a] and in section 2.1 that the maximum permissible occurrence of non-accidental modal degeneracy in such optical waveguides is two. This property is derived purely from the rotational and reflectional symmetries of the waveguide and in this way degenerate modes often resemble conventional polarization pairs. This is also true of modes P and $\widetilde{\mathrm{Q}}$.

Only in the case where

$$\int\limits_{A_\infty} \mathbf{e}^{\mathrm{P}} \times \mathbf{h}^{\mathrm{P}} \cdot \hat{\mathbf{z}}\ \mathrm{d}A = \int\limits_{A_\infty} \mathbf{e}^{\mathrm{Q}} \times \mathbf{h}^{\mathrm{Q}} \cdot \hat{\mathbf{z}}\ \mathrm{d}A = 0, \tag{3.7}$$

are mode P and Q power orthogonal in the usual sense. The physical significance of this is highlighted in the special case where the fields are everywhere locally circularly polarized. Here modes P and Q are power orthogonal since the fields are locally orthogonally polarized everywhere. That is

$$\mathbf{e}^{\mathrm{P}} \times (\mathbf{h}^{\mathrm{Q}})^* \cdot \hat{\mathbf{z}} = (\mathbf{e}^{\mathrm{Q}})^* \times \mathbf{h}^{\mathrm{P}} \cdot \hat{\mathbf{z}} = 0, \tag{3.8}$$

everywhere in A_∞.

We can equivalently express our findings for bound or approximately bound modes as; only modes which are everywhere linearly polarized in the waveguide cross-section can be non-degenerate. Noting that the orientation of local polarization need not be uniform in the waveguide cross-section. This is the one special case in which the analysis given above fails. That is when $\mathbf{e}_{\mathrm{t}}^{\mathrm{P}}$ and $\mathbf{h}_{\mathrm{t}}^{\mathrm{P}}$ can be made everywhere real with a complex scaling constant and $e_{\mathrm{z}}^{\mathrm{P}}$ would therefore be everywhere imaginary (evident from Eqs.(3.2)). Then mode Q, when constructed with Eq. ((3.3)), would be linearly dependent (if not identical) to mode P, allowing it to be non-degenerate.

3.3 Derivation of local-mode coupling equations for a class of length-dependent perturbations

It is evident from the previous section that translation invariance in optical waveguides (isotropic and lossless) restricts the possible types of non-degenerate bound modes to those with linearly polarized transverse components. We are thus motivated to explore the effects of z-dependent perturbations such as spinning of the local polarization. We use coupled mode theory to investigate this problem with an approach which is parallel to that presented by [Snyder and Love, 1983, Section 31-11] and Bassett [1988].

Take the modes of the unperturbed fibre

$$(\mathbf{E}_{\mathrm{p}}(\mathbf{x},t),\mathbf{H}_{\mathrm{p}}(\mathbf{x},t))=(\mathbf{e}_{\mathrm{p}}(x,y)e^{i(\beta_{\mathrm{p}}z-\omega t)},\mathbf{h}_{\mathrm{p}}(x,y)e^{i(\beta_{\mathrm{p}}z-\omega t)}),\tag{3.9}$$

where $\mathbf{x}=(x,y,z)$ and p$=1,2$ specifies the mode - considering only the coupling between a pair which may resemble a polarization pair with close propagation constants. The corresponding local modes

$$(\widetilde{\mathbf{E}}_{\mathrm{p}}(\mathbf{x},t),\widetilde{\mathbf{H}}_{\mathrm{p}}(\mathbf{x},t))=(\widetilde{\mathbf{e}}_{\mathrm{p}}(\mathbf{x})e^{i(\beta(z)_{\mathrm{p}}z-\omega t)},\widetilde{\mathbf{h}}_{\mathrm{p}}(\mathbf{x})e^{i(\beta(z)_{\mathrm{p}}z-\omega t)}),\tag{3.10}$$

are the solutions for the perturbed waveguide obtained by assuming the waveguide is nearly translationally invariant at each point z_0. This result is an approximation to the exact solution of Maxwell's equations for the z-dependent problem but where coupling of power is expected between local modes [Snyder and Love, 1983, pp. 553-66].

Assume that the actual fields of the perturbed fibre are expressible as some supermode

$$\begin{aligned}(\mathbf{e}^{\mathrm{s}}(\mathbf{x}),\mathbf{h}^{\mathrm{s}}(\mathbf{x}))&=\chi_1\ (\widetilde{\mathbf{e}}_1(\mathbf{x}),\widetilde{\mathbf{h}}_1(\mathbf{x}))+\chi_2\ (\widetilde{\mathbf{e}}_2(\mathbf{x}),\widetilde{\mathbf{h}}_2(\mathbf{x}))\\(\mathbf{E}^{\mathrm{s}}(\mathbf{x},t),\mathbf{H}^{\mathrm{s}}(\mathbf{x},t))&=(\mathbf{e}^{\mathrm{s}}(\mathbf{x}),\mathbf{h}^{\mathrm{s}}(\mathbf{x}))e^{i\beta^{\mathrm{s}}z-i\omega t},\end{aligned}\tag{3.11}$$

over some length, L, of the waveguide containing z_0. We have used the term, supermode, in a context different to its traditional meaning in translationally invariant waveguides. Here it describes the construction of a z-dependent modal distribution $(\mathbf{e}^{\mathrm{s}}(\mathbf{x}),\mathbf{h}^{\mathrm{s}}(\mathbf{x}))$ with a constant-phase travelling wave component $e^{i(\beta^s z-\omega t)}$. Clearly this assumption is strongly dependent on the type of z-dependent perturbation being considered. In order for β^s to be independent of z throughout L two conditions are sufficient; that the propagation constants of the local modes β_1, β_2 and the coupling coefficients between modes (see Eq. (3.17)) are constant throughout L. The types of perturbations that preserve this property include spinning with a constant rate and repeated linear translations. In fact a combination of these perturbations can be used in conjunction, as would be necessary for helically wound spun or un-spun fibre. The relation between the local modes of a spun fibre and the unperturbed fibre is presented in a later section in order to retain the general validity of the proceeding analysis.

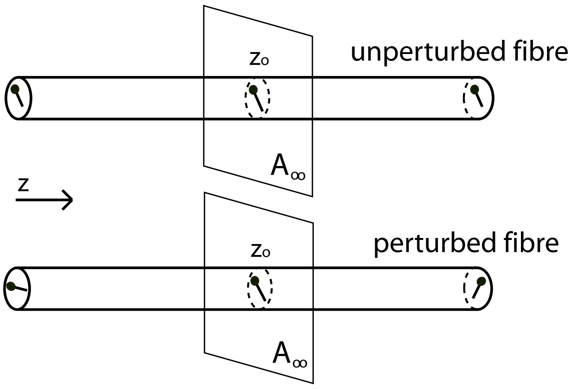

Figure 3.2: Application of the reciprocity theorem on a perturbed and unperturbed waveguide in an infinitesimally thin volume centered at z_0.

In order to evaluate the unknown coefficients, χ_1, χ_2, we use the reciprocity theorem to relate the perturbed and unperturbed waveguides in an infinitesimally thin slice centered at z_0 where the two are identical, as depicted graphically in Fig. 3.2. In this vanishingly thin volume we can readily show [Snyder and Love, 1983, pp. 602-4] that

$$\frac{\partial}{\partial z}\int\limits_{A_\infty} \mathbf{F}_\mathrm{p}\cdot\hat{\mathbf{z}}\;\mathrm{d}A = \int\limits_{A_\infty} \nabla\cdot\mathbf{F}_\mathrm{p}\;\mathrm{d}A = 0, \tag{3.12}$$

where

$$\mathbf{F}_\mathrm{p} = \mathbf{E}^\mathrm{s}\times\mathbf{H}_\mathrm{p}^* + \mathbf{E}_\mathrm{p}^*\times\mathbf{H}^\mathrm{s}. \tag{3.13}$$

and

$$\nabla\cdot\mathbf{F}_\mathrm{p} = -ik\sqrt{\frac{\varepsilon_0}{\mu_0}}\left(n^2-\widetilde{n}^2\right)\mathbf{E}^\mathrm{s}\cdot\mathbf{E}_\mathrm{p}^*. \tag{3.14}$$

The right hand side of Eq. (3.12) is exactly 0 since the difference in refractive index profiles is identically 0 at z_0.

Substituting Eq. (3.11) into Eq. (3.13) then Eq. (3.12) leads to the expression

$$(\beta-\beta_\mathrm{p})\chi_\mathrm{p}N_\mathrm{p} = i(\chi_1\Gamma_{\mathrm{p},1}+\chi_2\Gamma_{\mathrm{p},2}), \tag{3.15}$$

where the normalization constants are

$$N_\mathrm{p} = \int\limits_{A_\infty}\left(\mathbf{e}_\mathrm{p}\times\mathbf{h}_\mathrm{p}^* + \mathbf{e}_\mathrm{p}^*\times\mathbf{h}_\mathrm{p}\right)\cdot\hat{\mathbf{z}}\;\mathrm{d}A \tag{3.16}$$

and the coupling coefficients are

$$\Gamma_{\mathrm{p,q}} = \int\limits_{A_\infty} \left(\frac{\partial \widetilde{\mathbf{e}}_{\mathrm{q}}}{\partial z} \times \mathbf{h}_{\mathrm{p}}^{*} + \mathbf{e}_{\mathrm{p}}^{*} \times \frac{\partial \widetilde{\mathbf{h}}_{\mathrm{q}}}{\partial z} \right) \cdot \hat{\mathbf{z}} \, \mathrm{d}A. \tag{3.17}$$

Note that in obtaining these expressions we used the fact that $\mathbf{e}_{\mathrm{p}} = \widetilde{\mathbf{e}}_{\mathrm{p}}$, $\mathbf{h}_{\mathrm{p}} = \widetilde{\mathbf{h}}_{\mathrm{p}}$ and $\partial \mathbf{e}_{\mathrm{p}}/\partial z \neq \partial \widetilde{\mathbf{e}}_{\mathrm{p}}/\partial z$, $\partial \mathbf{h}_{\mathrm{p}}/\partial z \neq \partial \widetilde{\mathbf{h}}_{\mathrm{p}}/\partial z$ at z_0 and made use of the power orthogonality of modes 1 and 2.

Other than the trivial solution, $\chi_1 = \chi_2 = 0$, to Eq. (3.15) a non-trivial solution can be found by expressing this equation as an eigenvalue equation

$$\begin{gathered} A\chi = \beta\chi, \\ A = \begin{pmatrix} \beta_1 & 0 \\ 0 & \beta_2 \end{pmatrix} + i \begin{pmatrix} \frac{\Gamma_{1,1}}{N_1} & \frac{\Gamma_{1,2}}{N_1} \\ \frac{\Gamma_{2,1}}{N_2} & \frac{\Gamma_{2,2}}{N_2} \end{pmatrix}, \end{gathered} \tag{3.18}$$

where β is the eigenvalue and the eigenvectors are given by $\chi = (\chi_1, \chi_2)$.

As the matrix we have constructed is 2 by 2, we expect 2 supermodes to result from the orthogonal eigenvectors of Eq. (3.18). There are two cases in which valuable simplifications can be made and which provide some physical insight.

Case 1

Where both local modes are locally linearly polarized in the waveguide cross-section and therefore can be scaled so that $\widetilde{\mathbf{e}}_{\mathrm{t\ p}}$ and $\widetilde{\mathbf{h}}_{\mathrm{t\ p}}$ are purely real. Then it is straightforward to show that $\Gamma_{1,1} = \Gamma_{2,2} = 0$ since they are simply the derivative of unity. Furthermore it is possible to show that $\Gamma = \Gamma_{1,2} = -\Gamma_{2,1}$. By making the further assumption that the local modes are normalized and degenerate with propagation constant $\overline{\beta} = \beta_1 = \beta_2$ we find that the solutions to Eq. (3.18) are

$$\begin{gathered} \beta = \bar{\beta} \pm \Gamma, \\ \chi = (\mp i, 1). \end{gathered} \tag{3.19}$$

Thus when any of the perturbations previously discussed are made to a waveguide with degenerate modes, the resulting supermodes of the z-dependent waveguide are locally circularly polarized (as understood in a weakly guiding sense since the local state of polarization is only approximately circularly polarized).

Case 2

Where local modes 1 and 2 are degenerate, orthogonal and satisfy $\widetilde{\mathbf{e}}_{\mathrm{t\ p}} = \widetilde{\mathbf{e}}_{\mathrm{t\ q}}^{*}$ and $\widetilde{\mathbf{h}}_{\mathrm{t\ p}} = \widetilde{\mathbf{h}}_{\mathrm{t\ q}}^{*}$. This case describes the situation when the two modes chosen for the expansion are everywhere locally circular polarized in opposite directions. Then it is possible to show that $\Gamma_{1,2} = \Gamma_{2,1} = 0$, while $\Gamma = -i\Gamma_{2,2} = i\Gamma_{1,1}$ is real and equivalent to that of the case 1. When the modes are normalized we have the solutions

$$\begin{aligned} \beta &= \bar{\beta} \pm \Gamma, \\ \chi &= (0,1), (1,0). \end{aligned} \tag{3.20}$$

This result is formally equivalent to that of case 1 as the supermode propagation constants are equal. Furthermore, the insight we gain is that when the unperturbed modes are approximately locally circularly polarized then the perturbed fields remain so.

3.4 Coupling coefficients for spun fibre

When the pitch length, Ω, of a spun fibre is long enough to assume that the perturbation is adiabatic, we can apply the analysis in the previous section to investigate its polarization properties. This proceeding analysis initially will follow closely that provided in [Bassett, 1988], which uses coupled local modes in the same formulation as that provided in [Snyder and Love, 1983, section 31-14]. The analysis in this reference is formally equivalent to that presented here but the representation is subtly different. Furthermore, the present analysis extends the results of [Bassett, 1988] to a fully vectorial treatment. An alternative and convenient reference which discusses the equivalent straight waveguide of bends and twists is [Vassallo, 1991].

For this type of perturbation we can relate the local modes of the spun fibre with those of the unperturbed fibre using

$$\begin{aligned} \widetilde{\mathbf{e}}_{\mathrm{p}}(\mathbf{x}) &= R_z \mathbf{e}_{\mathrm{p}}(R_{-z}\mathbf{x}), \\ \widetilde{\mathbf{h}}_{\mathrm{p}}(\mathbf{x})) &= R_z \mathbf{h}_{\mathrm{p}}(R_{-z}\mathbf{x})), \end{aligned} \tag{3.21}$$

where the anti-clockwise rotation matrix is given by

$$R_z = \begin{pmatrix} \cos\left(\frac{2\pi z}{\Omega}\right) & -\sin\left(\frac{2\pi z}{\Omega}\right) & 0 \\ \sin\left(\frac{2\pi z}{\Omega}\right) & \cos\left(\frac{2\pi z}{\Omega}\right) & 0 \\ 0 & 0 & 1 \end{pmatrix}. \tag{3.22}$$

Substituting Eq. (3.21) into Eq. (3.17) gives a reduced expression for the coupling coefficients in terms of the fields of the unperturbed fibre at $z = 0$;

$$\begin{aligned} \Gamma_{\mathrm{p,q}} &= \tfrac{2\pi}{\Omega} \int\limits_{A_\infty} \left\{ (T\mathbf{e}_{\mathrm{q}}) \times \mathbf{h}^*_{\mathrm{p}} + \mathbf{e}^*_{\mathrm{p}} \times (T\mathbf{h}_{\mathrm{q}}) \right\} \cdot \hat{\mathbf{z}} \, \mathrm{d}A \, - \\ & \tfrac{2\pi}{\Omega} \int\limits_{A_\infty} \left\{ ([(T\mathbf{x}) \cdot \nabla]\mathbf{e}_{\mathrm{q}}) \times \mathbf{h}^*_{\mathrm{p}} + \mathbf{e}^*_{\mathrm{p}} \times ([(T\mathbf{x}) \cdot \nabla]\mathbf{h}_{\mathrm{q}}) \right\} \cdot \hat{\mathbf{z}} \, \mathrm{d}A \end{aligned} \tag{3.23}$$

where a $\pi/2$ anti-clockwise rotation matrix is defined by

$$T = \frac{\Omega}{2\pi} R'_{z=0} = \begin{pmatrix} 0 & -1 & 0 \\ 1 & 0 & 0 \\ 0 & 0 & 0 \end{pmatrix}, \tag{3.24}$$

and the operator $[(T\mathbf{x}) \cdot \nabla]$ is simply $-y\frac{\partial}{\partial x} + x\frac{\partial}{\partial y}$. The resulting coupling coefficients of Eq. (3.23) are identical to those found in [Bassett, 1988].

If we consider case 1, that is where the modes $\mathbf{e}_{\mathrm{p}}$, $\mathbf{h}_{\mathrm{p}}$ and therefore $\widetilde{\mathbf{e}}_{\mathrm{p}}$, $\widetilde{\mathbf{h}}_{\mathrm{p}}$ are locally linearly polarized and degenerate, then our supermode solutions from Eq. (3.19) are

$$\begin{aligned} (\mathbf{E}^{\mathrm{s}}(\mathbf{x},t), \mathbf{H}^{\mathrm{s}}(\mathbf{x},t)) &= \Big(+i \, (\widetilde{\mathbf{e}}_1(\mathbf{x}), \widetilde{\mathbf{h}}_1(\mathbf{x})) + (\widetilde{\mathbf{e}}_2(\mathbf{x}), \widetilde{\mathbf{h}}_2(\mathbf{x})) \Big) \, e^{i(\overline{\beta} - \frac{2\pi}{\Omega}\gamma)z - i\omega t}, \\ (\mathbf{E}^{\mathrm{s}}(\mathbf{x},t), \mathbf{H}^{\mathrm{s}}(\mathbf{x},t)) &= \Big(-i \, (\widetilde{\mathbf{e}}_1(\mathbf{x}), \widetilde{\mathbf{h}}_1(\mathbf{x})) + (\widetilde{\mathbf{e}}_2(\mathbf{x}), \widetilde{\mathbf{h}}_2(\mathbf{x})) \Big) \, e^{i(\overline{\beta} + \frac{2\pi}{\Omega}\gamma)z - i\omega t}, \end{aligned} \tag{3.25}$$

where $\overline{\beta} = \beta_1 = \beta_2$ and

$$\gamma = \left| \int\limits_{A_\infty} \left\{ ([T + y\frac{\partial}{\partial x} - x\frac{\partial}{\partial y}]\mathbf{e}_2) \times \mathbf{h}_1 + \mathbf{e}_1 \times ([T + y\frac{\partial}{\partial x} - x\frac{\partial}{\partial y}]\mathbf{h}_2) \right\} \cdot \hat{\mathbf{z}} \, \mathrm{d}A \right| . \tag{3.26}$$

In order to understand the behavior of the local polarization we use a simplified, but equivalent, expression for the turning fields in complex notation

$$\begin{aligned} \widetilde{\mathbf{e}}_{\mathrm{p}}(\mathbf{x}) &= \left(\Re \left\{ (\mathbf{e}_{\mathrm{t\ p}}(R_{-z}\mathbf{x}) + iT\mathbf{e}_{\mathrm{t\ p}}(R_{-z}\mathbf{x})) \, e^{-i\frac{2\pi z}{\Omega}} \right\}, e_z(R_{-z}\mathbf{x}) \right), \\ \widetilde{\mathbf{h}}_{\mathrm{p}}(\mathbf{x}) &= \left(\Re \left\{ (\mathbf{h}_{\mathrm{t\ p}}(R_{-z}\mathbf{x}) + iT\mathbf{h}_{\mathrm{t\ p}}(R_{-z}\mathbf{x})) \, e^{-i\frac{2\pi z}{\Omega}} \right\}, e_z(R_{-z}\mathbf{x}) \right), \end{aligned} \tag{3.27}$$

which provides the same pitch as the rotation matrix in Eq. (3.22).

Substituting Eq. (3.27) into Eq. (3.25) gives the following transverse components

$$\begin{aligned}
(\mathbf{E}^{\mathrm{s}}_{\mathrm{t}}(\mathbf{x},t),\mathbf{H}^{\mathrm{s}}_{\mathrm{t}}(\mathbf{x},t)) &= \tfrac{1}{2}\left(i[\mathbf{f}_1 - T\mathbf{f}_2] + [\mathbf{f}_2 + T\mathbf{f}_1]\right) e^{i(\overline{\beta}+\frac{2\pi}{\Omega}[1+\gamma])z-i\omega t} + \\
&\quad \tfrac{1}{2}\left(i[\mathbf{f}_1 + T\mathbf{f}_2] + [\mathbf{f}_2 - T\mathbf{f}_1]\right) e^{i(\overline{\beta}+\frac{2\pi}{\Omega}[-1+\gamma])z-i\omega t}, \\
(\mathbf{E}^{\mathrm{s}}_{\mathrm{t}}(\mathbf{x},t),\mathbf{H}^{\mathrm{s}}_{\mathrm{t}}(\mathbf{x},t)) &= \tfrac{1}{2}\left(i[-\mathbf{f}_1 - T\mathbf{f}_2] + [\mathbf{f}_2 - T\mathbf{f}_1]\right) e^{i(\overline{\beta}+\frac{2\pi}{\Omega}[1-\gamma])z-i\omega t} + \\
&\quad \tfrac{1}{2}\left(i[-\mathbf{f}_1 + T\mathbf{f}_2] + [\mathbf{f}_2 + T\mathbf{f}_1]\right) e^{i(\overline{\beta}+\frac{2\pi}{\Omega}[-1-\gamma])z-i\omega t},
\end{aligned} \tag{3.28}$$

where $\mathbf{f}_p = (\mathbf{e}_{\mathrm{t\ p}}(R_{-z}\mathbf{x}), \mathbf{h}_{\mathrm{t\ p}}(R_{-z}\mathbf{x}))$.

We can gain insight into the meaning of this expression by applying the approximations; $\mathbf{f}_2 \cong -T\mathbf{f}_1$, $\mathbf{f}_1 \cong T\mathbf{f}_2$, which states that the transverse field components of the two modes are approximately orthogonal, which is only strictly true for waveguides with small refractive index contrasts. The resulting supermodes are

$$\begin{aligned}
(\mathbf{E}^{\mathrm{s}}_{\mathrm{t}}(\mathbf{x},t),\mathbf{H}^{\mathrm{s}}_{\mathrm{t}}(\mathbf{x},t)) &\cong (+i\mathbf{f}_1 + \mathbf{f}_2)\, e^{i(\overline{\beta}-\frac{2\pi}{\Omega}[1-\gamma])z-i\omega t}, \\
(E^{\mathrm{s}}_{\mathrm{z}}, H^{\mathrm{s}}_{\mathrm{z}}) &= (+il_1 + l_2) e^{i(\overline{\beta}+\frac{2\pi}{\Omega}\gamma)z-i\omega t}, \\
(\mathbf{E}^{\mathrm{s}}_{\mathrm{t}}(\mathbf{x},t),\mathbf{H}^{\mathrm{s}}_{\mathrm{t}}(\mathbf{x},t)) &\cong (-i\mathbf{f}_1 + \mathbf{f}_2)\, e^{i(\overline{\beta}+\frac{2\pi}{\Omega}[1-\gamma])z-i\omega t}, \\
(E^{\mathrm{s}}_{\mathrm{z}}, H^{\mathrm{s}}_{\mathrm{z}}) &= (-il_1 + l_2) e^{i(\overline{\beta}-\frac{2\pi}{\Omega}\gamma)z-i\omega t},
\end{aligned} \tag{3.29}$$

where $l_{\mathrm{p}} = (e_{\mathrm{z\ p}}(R_{-z}\mathbf{x}), h_{\mathrm{z\ p}}(R_{-z}\mathbf{x}))$. By considering only the transverse components we find that propagation along the spun fibre demonstrates a circular birefringence of magnitude

$$\Delta\beta = \frac{4\pi}{\Omega}(1-\gamma). \tag{3.30}$$

3.4.1 An example

The above analysis is applied to a common MOF to predict the extent of circular birefringence induced by spinning. It is believed to be the first time that such a calculation has been reported. The fibre parameters are $d/\Lambda = 0.43$ (just in the endlessly single mode regime), where the hole pitch is $\Lambda = 1.4\mu$m and the material refractive index is 1.45. The wavelength for this calculation is $\lambda = 1.5\mu$m. The fibre cross-section and mode profile are shown in Fig. 3.3. The mode was found using the finite difference implementation of the ABC method, which is described in Chapter 4. The radial and azimuthal resolutions were 600 and 420 respectively. The field integral for γ was done over a Cartesian mesh of 500 by 500 points.

The evaluation of Eq. (3.30) gives $\gamma = 0.9937$ and therefore a birefringence of

$$\Delta\beta \simeq \frac{7.9 \times 10^{-2}}{\Omega}. \tag{3.31}$$

This corresponds to a beatlength of

$$L_{\mathrm{B}} \simeq 79\Omega. \tag{3.32}$$

It can be seen that the effect is relatively small, despite a large λ/Λ ratio. This is due to a large fraction of mode power being near the spinning axis. An enhancement of circular birefringence can be achieved by spinning off-axis. Such an investigation is reserved for future work.

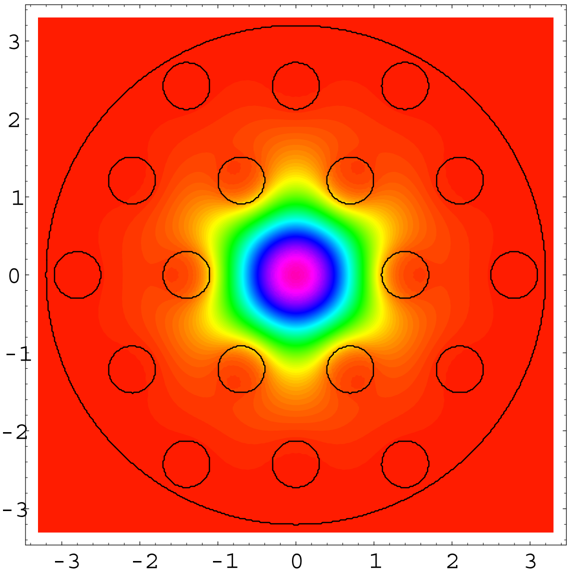

Figure 3.3: Example MOF supporting a degenerate fundamental mode in the straight fibre. A ring of air surrounds the microstructure to ensure that the supported modes are truly bound.

Part II

NUMERICAL MODELLING: THE ABC METHOD

Chapter 4

The Adjustable Boundary Condition method and implementation

4.1 Introduction

The diversity in geometry of Microstructured Optical Fibres (MOF) combined with high refractive index contrasts, enables unique and adjustable optical properties that are very different from conventional fibres. Although the majority of microstructures are fabricated by capillary stacking, which generally produces structures with holes in a hexagonal arrangement, the common photonic band gap fibre depicted in Fig. 1.1 is an example where the capillary stacking technique does not result in circular holes. In addition, various polymer techniques [van Eijkelenborg et al., 2003], and glass extrusion techniques [Kiang et al., 2002] show that a much wider variety of structures have been produced. One example is that of a MOF with elliptical holes (as studied in Chapter 6) and high numerical aperture fibres (as studied in Chapter 8). This variability in structural geometry creates many challenges for numerical modelling.

During development of the numerical method discussed in this chapter, most existing techniques were only able to accurately determine properties such as dispersion, mode size and birefringence. However, another property of great practical importance is confinement loss, which is a central issue to phenomena such as single modedness and photonic band gap guidance in fibres with only a finite number of holes. At the time, only the multipole and beam propagation methods had demonstrated the capability to calculate confinement loss. However, these imposed some limitation, such as being restricted to circular holes or being computationally expensive, respectively. Thus an alternative method was sought, with the intention of eliminating these limitations.

Modal solutions are most frequently sought for translation-invariant waveguides. Even for some length dependent problems, modal solutions are used in conjunction with auxiliary tools such as coupled mode theory. This is because of the great numerical advantage gained by reducing the problem to the two dimensional waveguide cross-section. It is possible to solve for the mode in the infinite cross-section using techniques such as coordinate mapping, infinite elements or multipole expansions. However, it is usually advantageous to restrict the computational domain to some area enclosing the waveguide structure. All information relating to the distant surroundings of the waveguide are then incorporated into the boundary conditions. Some of the actual surroundings of the waveguide may not have any significant physical influence on the guiding properties of the waveguide, thus one boundary condition may be chosen over several contenders solely for mathematical convenience. Truly transparent boundary conditions are an example, since they permit no back-reflection of light escaping the computational domain. It is a convenient assumption, but is realistically only an approximation. Leaky modes, with complex propagation constants, satisfy transparent boundary conditions and are taken to accurately represent the propagation of light in 'leaky' MOFs.

At first thought, the resulting eigenvalue problem should be straightforward to solve for both eigenvalues and eigenvectors. However, complications arise when imposing the desired boundary conditions. This problem is discussed in the following sections and both Chapters 4 and 5 are primarily concerned with its resolution.

4.2 Inventory of methods

As mentioned previously, the waveguide cross-section can be loosely factored into two sections: the computational domain, where the relevant partial differential equations are tackled numerically, and the exterior, for which all relevant information is contained in the boundary conditions. These two factors will be considered separately.

4.2.1 Within the computational domain

A wide variety of numerical schemes can be used to discretise a partial differential equation. Many have been used for the modelling of MOFs. They include; Basis function expansions such as Hermite-Gaussian expansions [Monro et al., 1999, Zhi et al., 2003b], auxilliary mode expansions [Ferrando et al., 1999], plane wave expansions [Ferrando et al., 2000b], polar Fourier expansions [Poladian et al., 2002, Issa and Poladian, 2003a] and multipole expansions [White et al., 2002b, Kuhlmey et al., 2002c]; Finite Difference Methods (FDM) [Zhu and Brown, 2002, Guo et al., 2004, Yu and Chang, 2004]; Finite Element Mehtods (FEM) [Cucinotta et al., 2002, Ferrarini et al., 2002, Saitoh and Koshiba, 2002, Brechet et al., 2000, Uranus and Hoekstra, 2004]; Boundary element methods [Guan et al., 2003, Wang et al., 2004]; and Integral methods [Cheng et al., 2004].

A comprehensive comparison of the advantages and disadvantages of all these methods would be exceedingly detailed. Indeed, there is no clear champion among these methods; one that is able to tackle all MOF problems with the greatest efficiency, ease of implementation, robustness and automation. This is mostly due to the great diversity in MOF geometry. Generally however, methods with flexible meshes or resolutions, such as FEM or FDM, have an added advantage in this respect. In this introduction, the focus is directed towards the execution of boundary conditions rather than the numerical techniques for solving partial differential equations.

4.2.2 Boundary conditions

The calculation of confinement loss is the key interest of this discussion. It requires non-Hermitian boundary conditions that allow power to escape the computational domain with little or ideally no back-reflection. Generally the available numerical techniques that employ basis function expansions (Galerkin techniques) such as plane wave [Ferrando et al., 2000b] and Hermite-Gaussian [Monro et al., 1999, Zhi et al., 2003b] expansions are unable to compute confinement loss since they rely on periodic or zero boundary conditions at the edge of the computational domain and neglect the outward radiating field.

Adding an absorbing boundary layer is a well known technique for solving open region scattering and radiation problems. The introduced artificial absorbing boundary attempts to minimize any back reflection to make the boundary appear as transparent as possible. The choice of refractive index for the absorbing layer requires some skill, as does the position of the layer. This disadvantage, together with the added problem of spurious modes created by the reflections off new boundaries makes the use of absorbing layers undesirable.

Beam propagation methods are able to find confinement loss by dynamically modelling confinement loss, but are numerically intensive and can have difficulty distinguishing modes with similar propagation constants. Attempts to use vector beam propagation on structures with elliptical holes (the subject of Section 4.5) have been unsuccessful for these reasons [Steel and Osgood, 2001a].

More recently, the multipole method [White et al., 2002b, Kuhlmey et al., 2002c] has successfully been used to accurately model radiating boundary conditions. It does so by treating each inclusion (such as holes) in the waveguide as a source of outgoing fields. When the inclusions are circular, a Fourier-Bessel expansion about each inclusion is natural. The conglomeration of inclusions is treated using Graf's addition theorem, which transforms the origins of the Bessel expansions and allows the system to be solved numerically. The method is highly efficient and precise for MOFs with circular inclusion, even in large numbers, and by this metric it is likely to outperform any other methods for such fibres. The extension of the method to arbitrary geometries is somewhat involved, but significant progress has recently been demonstrated with the extension of the method to calculate MOFs with elliptical holes [Campbell et al., 2004]. This method performs searches for modes, as zeros of a matrix determinant, in the complex n_{eff} plane, which can be a disadvantage. Without robust automation of this procedure, the method may be unyielding for highly multimode problems or those requiring rapid solution for new structures. Such automation is currently unavailable.

Perfectly Matched Layers (PML) are a common and highly efficient way to implement radiating boundary conditions with FEM [Cucinotta et al., 2002, Ferrarini et al., 2002, Saitoh and Koshiba, 2002]. It involves the addition of an non-physical boundary layer which simultaneously absorbs all incident light and ideally gives no back reflection. Disadvantages of PML are that some skill is required in choosing the PML parameters for individual applications, as well as the introduction of spurious modes.

Transparent Boundary Conditions (TBC) are also available and have been utilised by some finite difference schemes [Uranus and Hoekstra, 2004]. While they are efficient and relatively user-friendly, they suffer from requiring iteration for each mode solution as well as being *only approximate* to an extent related to the computational domain radius. In the proceeding sections, the Adjustable Boundary Condition (ABC) schemes provides an alternative way for implementing true TBCs. Although the proposed scheme does require similar iteration, convergence is fast and the convergent solution is not approximate for any computational domain.

4.3 Algorithm structure

A new method with two different implementations for calculating leaky modes from the vector wave equation is presented now. One is referred to as the Adjustable Boundary Condition Fourier Decomposition Method (referred to as ABC-FDM), the other as the ABC-Finite Difference Method (also ABC-FDM). A scalar version of the algorithm has been implemented [Poladian et al., 2002], which is only approximately valid when refractive index contrasts are high and is unable to quantify any polarization effects. The ABC method is a refinement scheme that has been devised to correctly and robustly determine the radiating field outside the boundary for most leaky modes. The method exhibits simplicity and speed, while being able to calculate modes and losses of arbitrary hole structures in an automated and reliable manner. The first implementation, founded on Fourier expansion methods, modifies the basis functions to enable non-reflecting boundary conditions on the computational domain. The second implementation employs a general finite difference scheme where the boundary conditions can be adjusted in a straightforward way until the non-reflecting condition is satisfied.

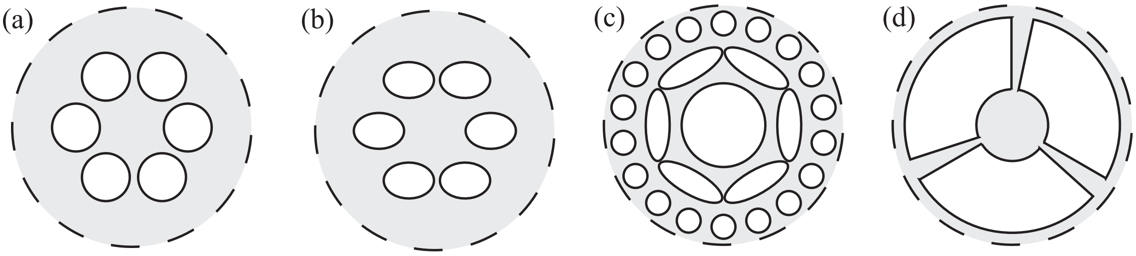

Figure 4.1: Example fibre structures that can be modelled with the ABC-FDM. Air holes are positioned in an otherwise uniform host material extending to infinity. **(a)** Six fold symmetric arrangement in one ring. **(b)** Elliptic perturbation of (a). **(c)** Multiple ring arrangement. **(d)** Solid core suspended by filaments.

4.3.1 Governing equations

A variety of approaches exist to reduce Maxwell's equations to a pair of coupled wave equations representing the vector modes of the optical waveguide. For example, it is possible to eliminate the transverse coordinates and obtain a pair of equations for the longitudinal field components e_z and h_z. However, the propagation constant then appears in the equations in an undesirable way. A desirable formulation would give the effective index in an identifiable linear eigenvalue equation. In addition, when dealing with non-magnetic materials, continuity of the magnetic fields across interfaces eliminates the complication of solving for discontinuous transverse electric field components. These reasons motivate the use of the transverse magnetic field equation

$$\nabla_t^2 \mathbf{h}_t + k^2(n^2 - n_{\text{eff}}^2)\mathbf{h}_t = -\frac{1}{n^2}\nabla_t n^2 \times [\nabla_t \times \mathbf{h}_t], \tag{4.1}$$

where n expresses the refractive index profile of the waveguide. The geometry of the system is best captured in polar coordinates. However, in non-cartesian vectors the field components are coupled on the left of Eq. (4.1). In order to simplify the field solutions outside the computational domain D, this coupling can be removed using the left and right handed fields, which may not be locally linearly polarized

$$\psi^{\pm}(\rho,\theta) = h_r(\rho,\theta) \pm i h_\theta(\rho,\theta), \tag{4.2}$$

where h_r and h_θ are the radial and azimuthal components of the magnetic field in polar coordinates. The radial coordinate is scaled by $\rho = r/R$, where R is a radius chosen to enclose all of the waveguide structure and defines the edge of D, as shown by a dashed line in Fig. 4.1. The resulting equations become

$$\mathcal{L}^{\pm}\psi^{\pm} \mp F^{\pm}(\rho,\theta)G(\rho,\theta) = W^2\psi^{\pm}, \tag{4.3}$$

where

$$\mathcal{L}^{\pm} = \nabla^2 - \frac{1}{\rho^2} \pm \frac{2i}{\rho^2}\frac{\partial}{\partial\theta} + V^2(\rho,\theta) \tag{4.4}$$

and we have identified $V^2(\rho,\theta) = R^2k^2(n^2(\rho,\theta) - n_{\text{cl}}^2)$ and the eigenvalue $W^2 = R^2k^2(n_{\text{eff}}^2 - n_{\text{cl}}^2)$. It is important that the eigenvalue appears only once in this equation. The vectorial corrections are contained in

$$F^{\pm}(\rho,\theta) = \frac{1}{2}\left(\frac{\partial \log(n^2(\rho,\theta))}{\partial\rho} \pm \frac{i}{\rho}\frac{\partial \log(n^2(\rho,\theta))}{\partial\theta}\right), \tag{4.5}$$

while the fields are coupled by $G(\rho,\theta) = G^+ + G^-$ with

$$G^{\pm} = \pm\frac{1}{\rho}\frac{\partial(\rho\psi^{\pm})}{\partial\rho} - \frac{i}{\rho}\frac{\partial\psi^{\pm}}{\partial\theta}. \tag{4.6}$$

4.3.2 Reduction to the scalar wave equation

In the weakly guiding regime [Snyder and Love, 1983, Chapter 32], the scalar equation provides highly accurate modal fields and propagation constants, while greatly reducing computation resources. Reducing Eq. (4.3) to the scalar wave equation is straightforward. One simply removes the vector terms, thereby eliminating coupling between ψ^+ and ψ^-. Now independent, these terms can be represented by a single scalar function ψ, giving

$$\mathcal{L}\psi = W^2\psi, \tag{4.7}$$

where the operator $\mathcal{L}^{\pm}$ can be simplified to

$$\mathcal{L} = \nabla^2 + V^2(\rho,\theta). \tag{4.8}$$

Therefore, the advantage of the scalar simplification is a reduction in the size of the matrix problem by a factor of two. This allows approximately a four fold reduction in memory requirements and an almost eight fold reduction in the time taken to solve for eigenvalues.

4.3.3 Boundary conditions and the refinement technique

External fields

Outside the computational domain ($\rho > 1$) the terms V^2 and $F^{\pm}$ vanish. Thus the fields in this region can be expressed exactly in the form [Snyder and Love, 1983, pp. 491,715]

$$\psi^{\pm}(\rho,\theta) = \sum_m B_m^{\pm} e^{im\theta} K_{m\pm1}(W\rho), \tag{4.9}$$

where the coefficients are unknown and $K_{m\pm1}(W\rho)$ are modified Bessel functions of the second kind with asymptotic behavior ($\rho \to \infty$) given by

$$K_m(W\rho) \cong \left(\frac{\pi}{2W\rho}\right)^{1/2}\left(1+\frac{4m^2-1}{8W\rho}\right)e^{-W\rho}. \tag{4.10}$$

For bound modes W is real and positive, so these fields are evanescent. For leaky modes W is complex and is chosen to be $W = -kRi\sqrt{n_{\mathrm{cl}}^2 - n_{\mathrm{eff}}^2}$ so that the imaginary part is negative. In the absence of material absorption or gain, both real and imaginary parts will be negative [Snyder and Love, 1983, pp. 487-513]. This ensures that the fields are outward radiating for forward propagating modes.

These eigenvalue equations and their corresponding boundary conditions need to be cast in the form of a matrix eigenvalue problem in order to be evaluated numerically. This can be achieved using a number of implementations. Two such implementations are discussed in Sections 4.4 and 4.6.

Refinements

Before the choice of implementation is discussed, it is important to outline how boundary conditions are to be treated in the ABC method. It is clear from Eq. (4.9) that the field expansion outside the computational domain is dependent on only one unknown, the eigenvalue W^2. For this reason, a refinement technique (depicted in Fig. 4.2) is devised to determine the external fields. It has been observed that such a scheme is robust when the fields just outside of the computational domain are a small contribution to the guided mode. This is generally the case for microstructures with low loss, like those of practical interest.

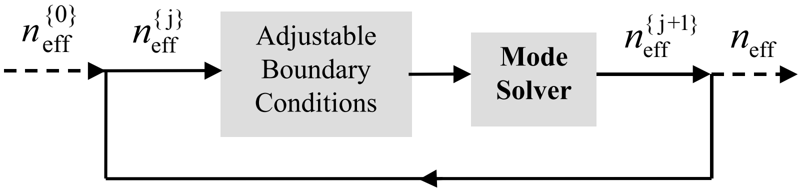

Figure 4.2: The refinement scheme. The mode solver is some generic numerical technique capable of finding modal solutions to specified boundary conditions, such as the FDM.

An initial guess of the effective index, $n_{\mathrm{eff}}^{\{0\}}$, is used to give W in the argument of the external field expansion of Eq. (4.9). This provides an approximate solution to the problem outside the computational domain and continuity of this field and its first derivative with the fields inside provide the boundary conditions. A mode solver finds a solution satisfying these boundary conditions and generates an improved estimate of the effective index. Continued iteration can be used to increase the accuracy of the solution.

By uniqueness it is clear that if the scheme converges then it converges to the correct solution. A detailed derivation of the convergence properties of the refinement scheme is provided in Chapter 5. It supports the observation that the convergence is rapid and correctly predicts an exponential decay in the error of the solution with successive refinements. Convergence is guaranteed for a very wide class of modes, those with the majority of guided power within the computational domain. Most importantly, it can be explicitly shown that the convergence properties are independent of the mode solver used and are simply a property of the ABC refinement scheme. In practice it is found that between one and four refinements are required to achieve convergence to the desired accuracy for most modes and waveguides of interest.

4.4 Implementation by basis function expansion

4.4.1 The matrix equations

Inside the computational domain the fields are expanded in some truncated set of complete basis functions

$$\psi^{\pm}(\rho,\theta) = \sum_{m,n} A^{\pm}_{mn}\psi^{\pm}_{mn}(\rho,\theta) \tag{4.11}$$

with unknown coefficients.

When projected onto another truncated set of complete functions $\phi_{mn}(\rho,\theta)$, a matrix generalized-eigenvalue problem is formulated

$$\begin{bmatrix} [M^+]^{mn}_{\mu\nu} - \left[F^+_+\right]^{mn}_{\mu\nu} & -\left[F^+_-\right]^{mn}_{\mu\nu} \\ \left[F^-_+\right]^{mn}_{\mu\nu} & [M^-]^{mn}_{\mu\nu} + \left[F^-_-\right]^{mn}_{\mu\nu} \end{bmatrix} \begin{bmatrix} A^+_{mn} \\ A^-_{mn} \end{bmatrix}$$

$$= W^2 \begin{bmatrix} [N^+]^{mn}_{\mu\nu} & 0 \\ 0 & [N^-]^{mn}_{\mu\nu} \end{bmatrix} \begin{bmatrix} A^+_{mn} \\ A^-_{mn} \end{bmatrix}, \tag{4.12}$$

where index summations are implied and the matrix elements are given by appropriate inner products

$$\begin{aligned} [M^{\pm}]^{mn}_{\mu\nu} &= \langle \phi_{\mu\nu} \mid \mathcal{L}^{\pm}\, \psi^{\pm}_{mn} \rangle \\ \left[F^{\pm}_+\right]^{mn}_{\mu\nu} &= \langle \phi_{\mu\nu} \mid F^{\pm}(\rho,\theta)G^+ \rangle \\ \left[F^{\pm}_-\right]^{mn}_{\mu\nu} &= \langle \phi_{\mu\nu} \mid F^{\pm}(\rho,\theta)G^- \rangle \\ [N^{\pm}]^{mn}_{\mu\nu} &= \langle \phi_{\mu\nu} \mid \psi^{\pm}_{mn} \rangle\,. \end{aligned} \tag{4.13}$$

Here $\phi_{\mu\nu}(\rho,\theta)$ is some complete set of functions used for weighting and is not necessarily identical to the expansion set. A specific choice is made in Section 4.4.3.

4.4.2 Execution

The refinement scheme needs to be applied to all modes of interest since the radiating boundary conditions are slightly different for each mode. Although this requires additional computational work, manual mode searches in the complex plane are not required, unlike other algorithms capable of calculating leaky modes [Vassallo, 1990, White et al., 2001]. The algorithm consists of two major stages at each refinement of a given mode: computing the matrix elements of Eq. (4.13) and then evaluating the eigenvalue and eigenvector of interest in Eq. (4.12).

Ultimately the matrix operator of Eq. (4.12) must be non-self-adjoint since the leaky modes solutions have complex eigenvalues. The origin of this property lies in the fact that the imposed boundary conditions (Eq. (4.9)) are intrinsically non-self-adjoint. This is in addition to the fact that, unlike the scalar wave equation, the choice of differential operators for the transverse magnetic field in Eq. (4.1) are only adjoint to the complementary equation for the transverse electric field [Silvestre et al., 1998]. Therefore, in the present problem the matrix operators cannot be made self-adjoint by using the same basis functions and weighting functions, ie. $\phi_{mn}(\rho,\theta) = \psi^{\pm}_{mn}(\rho,\theta)$. The weighting functions are thus chosen purely for simplicity and computational efficiency.

For solving the matrix eigenvalue problem Eq. (4.12) the standard inverse iteration technique is used, which is capable of finding only a few eigenvalues closest to an initial estimate. Neighbouring eigenvalues are found by searching in a subspace orthogonal to the modes already found. The corresponding eigenvectors provide the field expansion coefficients and matching with external fields is done in a straightforward way.

4.4.3 The basis functions and boundary conditions

When an expansion technique is used, the boundary conditions are implemented by ensuring that each basis function $\psi^{\pm}_{mn}(\rho,\theta)$ individually satisfies the mixed boundary conditions at the edge of D. This is straightforward when an azimuthal Fourier expansion is used

$$\begin{aligned} \psi^{\pm}_{mn}(\rho,\theta) &= e^{im\theta}\xi_{m\pm1,n}(\rho), \qquad (4.14) \\ \phi_{mn}(\rho,\theta) &= e^{im\theta}\eta_{mn}(\rho). \end{aligned}$$

By matching the internal expansion in Eq. (4.11) with the external field expansion in Eq. (4.9), the requirement at the outer edge of D ($\rho = 1$) becomes

$$K_m(W\rho)\frac{d\xi_{mn}(\rho)}{d\rho} - \frac{dK_m(W\rho)}{d\rho}\xi_{mn}(\rho) = 0, \qquad (4.15)$$

for all m and n. Consequently any linear combination of the above basis functions will also satisfy the desired boundary conditions.

The choice of basis function for the radial expansion is critical for computational efficiency and the robustness of the method. After an investigation of a variety of different basis functions, the following set was chosen

$$\xi_{mn}(\rho) = \frac{\sin(n\pi\rho)}{n\pi} + \alpha_{mn} + \beta_{mn}\,\rho \tag{4.16}$$

$$\eta_{mn}(\rho) = \frac{\sin(n\pi\rho)}{n\pi}, \tag{4.17}$$

where

$$\alpha_{0n} = 1 + \frac{(-1)^n - 1}{WK_0'(W)}K_0(W), \tag{4.18}$$

$$\alpha_{mn} = 0, \quad m \neq 0, \tag{4.19}$$

$$\beta_{0n} = -1, \tag{4.20}$$

$$\beta_{mn} = \frac{(-1)^n K_m(W)}{WK_m'(W) - K_m(W)}, \quad m \neq 0. \tag{4.21}$$

This choice is clearly a variation of the standard Fourier series expansion, with the linear terms providing additional freedom. The values of the coefficients are determined by the matching condition of Eq. (4.15) together with a condition ensuring that each mode has the correct physical behavior at the origin and so that the coordinate singularity appearing in the polar representation of Eq. (4.4) is not problematic, the condition is expressed by

$$\lim_{\rho\to 0}\left[J_m(W\rho)\frac{d\xi_{mn}(\rho)}{d\rho} - \frac{dJ_m(W\rho)}{d\rho}\xi_{mn}(\rho)\right] = 0, \tag{4.22}$$

where $J_m(W\rho)$ are Bessel functions of the first kind with limiting form ($\rho \to 0$) given by $J_m(W\rho) \cong (W\rho/2)^m/m!$.

Amongst the many conceivable variations of the standard Fourier series, we believe those presented in Eq. (4.16) to be the most efficient since the inner product expressions of Eq. (4.13) are greatly simplified. Neglecting the additional terms in the weighting functions further simplifies these expressions. Most importantly, the harmonic nature of this set provides a substantial computational advantage by reducing the total number of distinct trigonometric functions evaluated during computation. Adjusting the arguments of the trigonometric functions in order to match the boundary conditions would be an example where new frequencies will appear in the analytic expressions for the inner product terms.

The inner product in which the standard Fourier series is orthogonal is used for this new basis set:

$$\langle f \mid g\rangle = \int_0^{2\pi}\int_0^1 f^*(\rho,\theta)g(\rho,\theta)d\rho d\theta, \tag{4.23}$$

the weighting set $\phi_{mn}(\rho,\theta)$ is known to be complete for the space of square integrable functions on D.

4.4.4 Calculating inner products

The chosen basis set proves to be highly efficient for the first stage since many expressions involve simple trigonometric functions and therefore can be pre-calculated and tabulated. Inner products involving structure-dependent functions reduce to simple integrals of trigonometric functions over the holes. These integrals are evaluated analytically if the holes are in the shape of annular sectors, while the integrals over holes of other shapes can be evaluated numerically using a functional form of the hole shape and a Simpson's rule numerical integral. An alternative and simpler possibility is to de-construct an arbitrary hole shape into very thin annular sectors and proceed with the analytic expressions for the inner products.

In the case of the field coupling inner products, the derivatives of the discontinuous refractive index profile are not problematic since the following simplification can be made. Noticing that $F^{\pm}(\rho,\theta)$ can be written as

$$F^{\pm}(\rho,\theta) = \nabla \cdot \mathbf{J}^{\pm}(\rho,\theta), \tag{4.24}$$

where $\mathbf{J}^{\pm}(\rho,\theta) = [\frac{1}{2}\log(n^2(\rho,\theta)/n_{\text{cl}}^2), \pm\frac{i}{2\rho}\log(n^2(\rho,\theta)/n_{\text{cl}}^2)]$ and the divergence is Cartesian in coordinates, ie. $\nabla \equiv (\partial/\partial\rho, \partial/\partial\theta)$. Applying a vector identity and using the divergence theorem leads to

$$\begin{aligned} \left\langle \phi_{\mu\nu} \mid F^{\pm}(\rho,\theta) G^{+} \right\rangle = & \oint_{\partial D} \phi_{\mu\nu}^{*} G^{+} \mathbf{J}^{\pm}(\rho,\theta) \cdot \hat{\mathbf{n}} dl \\ & - \iint_{D} \mathbf{J}^{\pm}(\rho,\theta) \cdot \nabla \left(\phi_{\mu\nu}^{*} G^{+}\right) d\rho d\theta \end{aligned} \tag{4.25}$$

$$\begin{aligned} \left\langle \phi_{\mu\nu} \mid F^{\pm}(\rho,\theta) G^{-} \right\rangle = & \oint_{\partial D} \phi_{\mu\nu}^{*} G^{-} \mathbf{J}^{\pm}(\rho,\theta) \cdot \hat{\mathbf{n}} dl \\ & - \iint_{D} \mathbf{J}^{\pm}(\rho,\theta) \cdot \nabla \left(\phi_{\mu\nu}^{*} G^{-}\right) d\rho d\theta, \end{aligned} \tag{4.26}$$

where the first boundary integral around the perimeter of the computational domain, δD, is identically zero since $\mathbf{J}^{\pm} = 0$ there and everywhere outside D and including its boundary. The second integral simply reduces to an integral over the holes.

4.5 Numerical results with basis function expansion

The described algorithm was coded exclusively by this author using the C/C++ programming language, with the exception of the matrix-eigenvalue solution subroutines. The following results were generated by this code using a variety of available computers and software platforms. For an illustration of speed, this author used his desktop computer, which does not accurately represent the usual time taken to produce results on typical desktop workstations, even at the time of writing. Computational efficiency is also highly dependent on the compiler used and speed of individual hardware components such as RAM.

4.5.1 Comparative tests

A direct comparison is made with the published leaky mode solutions to the waveguide depicted in Fig. 4.1(a). The hole diameters are 5.0 μm, the hole separation is 6.75 μm, $\lambda = 1.45$ μm and $n_{\text{cl}} = 1.45$. The table below shows a direct comparison of these solutions with precise results obtained by the multipole method [White et al., 2001].

Number	Mode class	Degeneracy	ABC FDM n_{eff}	Loss dB/m	Multipole n_{eff}
1,2	HE11	2	$1.4453954 + 3.07 \times 10^{-8}i$	1.16	$1.4453952 + 3.19 \times 10^{-8}i$
3	TE01	1	$1.4385890 + 5.43 \times 10^{-7}i$	20.4	$1.4385836 + 5.31 \times 10^{-7}i$
4,5	HE21	2	$1.4384442 + 9.62 \times 10^{-7}i$	36.2	$1.4384448 + 9.73 \times 10^{-7}i$
6	TM01	1	$1.4383643 + 1.38 \times 10^{-6}i$	52.2	$1.4383649 + 1.41 \times 10^{-6}i$

Table 4.1: Comparison of results for the waveguide depicted in Fig. 4.1(a). The ABC-FDM calculations used $n_{\max} = 70$, $m_{\max} = 54$, $R = 9.3$ μm and convergence was achieved in three refinements. An expansion in 15 multipole moments is used in the compared results. Note that the notation used for mode class is only strictly valid for cylindrically symmetric waveguides. In this waveguide the modes are in fact HE, TE or TM like, since they are only loosely identified with this standard mode notation.

Foremost, the comparison above is one of several tests of the correctness of the computer program. Other tests include comparisons with fibre geometries having known analytic solutions, such step index, elliptical core fibres and air ring fibres with leaky modes. In addition each subroutine of the program was checked in isolation for correct operation. The comparison above is not so much intended as a validation of the ABC method, which is validated by the uniqueness principle for solutions of partial differential equations, given a convergent answer. The table shows satisfactory agreement with the multipole method for the limited number of Fourier terms used. A meaningful comparison of the relative merits and disadvantages of the two methods cannot be extracted from only this simple comparison. Indeed, such an undertaking has not been attempted.

Each solution can be qualitatively checked by plotting the modal fields. The fields of modes 1 and 3 are shown in Fig. 4.3. A smooth join of the Fourier expansion to the external fields can be seen across the computational domain boundary.

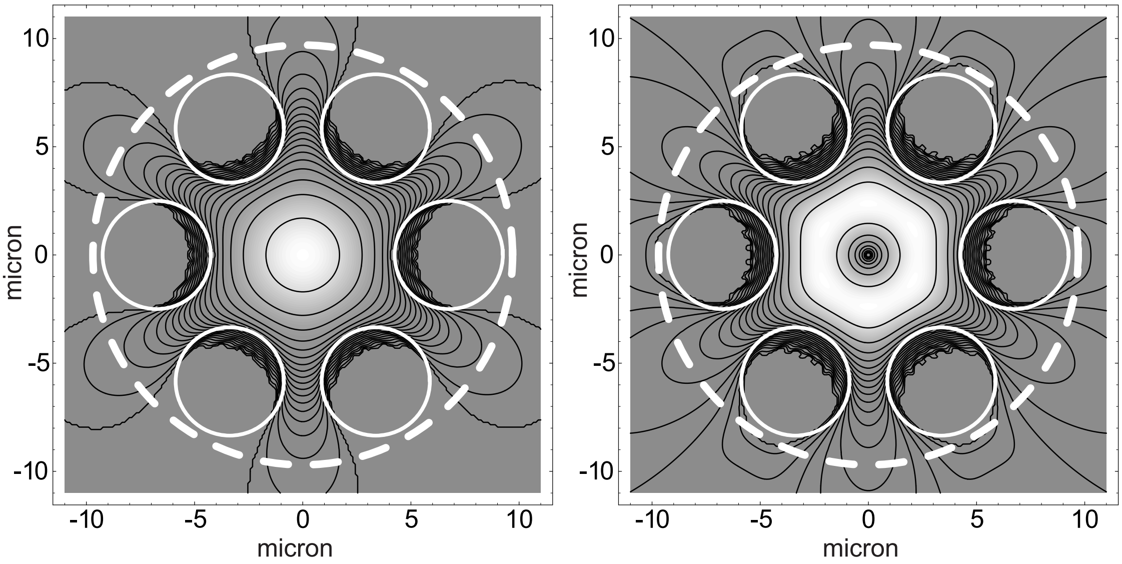

Figure 4.3: Intensity plots of modes 1 and 3. The shading is linear while the contours use a logarithmic scale ranging from 0 dB to -60 dB with 3 dB separation. The holes are shown with a solid white line and the edge of the computational domain is shown with a dashed white line.

The solutions are in excellent agreement for the real parts of the effective index and reasonable agreement is obtained for the imaginary parts, especially when considering how few Fourier components were used. All calculations were run on a standard Pentium III 1GHz desktop, each requiring approximately six hours of computational time. Efficiency considerations are discussed in the next sections. The convergence of the ABC method is shown in Fig. 4.4. It shows an exponential convergence which is typical of the method. The lower bound of machine precision (approximately 10^{-16}) is reached after only three refinements. A full analysis is provided in chapter 5.

4.5.2 Confinement loss and birefringence in elliptical hole MOFs

In order to highlight the key features and advantages of the present algorithm, MOFs with leaky modes that exhibit birefringence were modelled. The holes were elliptically perturbed in order to produce linear birefringence. The ellipticity of the holes is defined by b/a, where a and b are the major and minor hole diameters respectively. It was varied

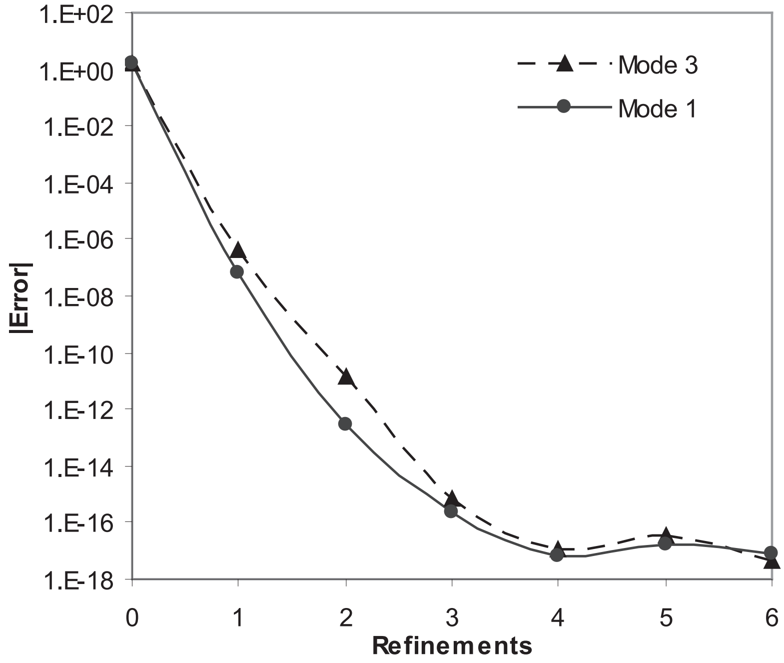

Figure 4.4: Exponential convergence of refinement scheme for modes 1 and 3 over a few refinements. Dashed curves are included to aid the eye.

between 1 and 0.7 while the positions of the holes remained unchanged. Consequently a polarization splitting (birefringence) is induced between modes 1 and 2, removing the degeneracy. Example intensity plots are shown in Fig. 4.5. The intensity plots for the two polarization modes are visually nearly indistinguishable, however the field components are not. The dominant components of Fig. 4.6 and Fig. 4.7 confirm that mode 1 is predominantly x polarized while mode 2 is predominantly y polarized, although both have non-zero longitudinal components.

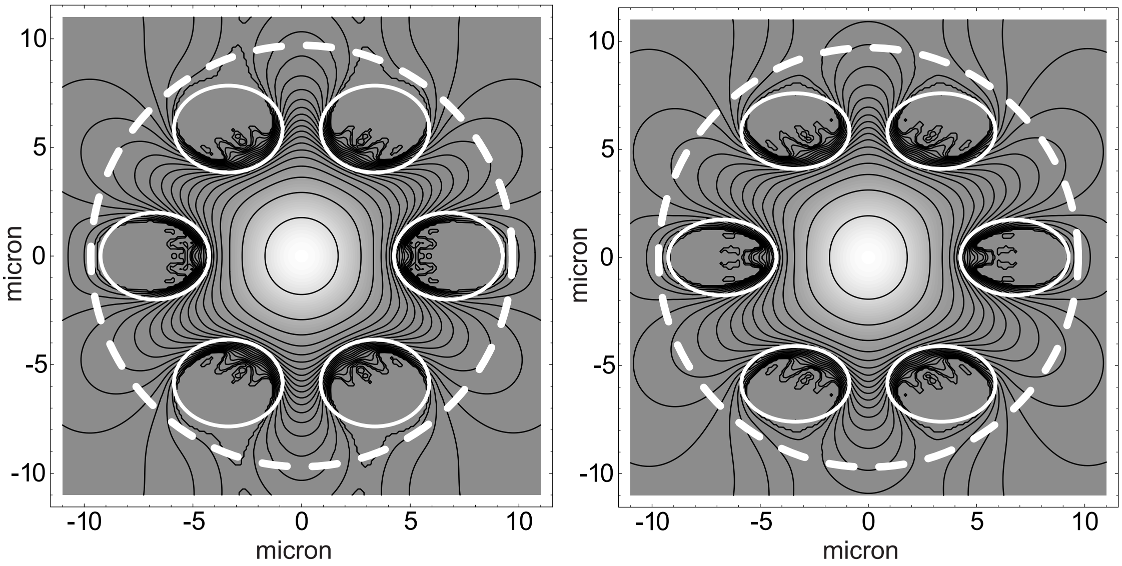

Figure 4.5: Intensity plots of mode 1 for an ellipticity of 0.8 and 0.7. The features of the contour plots are as in Fig. 4.3.

The change in birefringence with ellipticity is shown in Fig. 4.8(a), which grows to a value corresponding to a beat length of 5.6 cm at an ellipticity of 0.6. Only a very small birefringence is demonstrated in this waveguide, due to the relatively large core size. Maybe not practically useful, it does however clearly demonstrate the vectorial nature of the algorithm. The plot of the decrease in loss with ellipticity is shown in Fig. 4.8(b). It demonstrates a polarization dependent loss caused by geometric rather than material properties. The increase in loss can be qualitatively seen in the intensity contour plots as the intensity is spread out from the core region into the microstructure and then out to the cladding. Counting the -3 dB contours along the bridge and out to the computational domain boundary shows that the intensity near the boundary is approximately 6 dB less in the case of higher ellipticity.

The previous example of a MOF with elliptical holes was a perturbation of the circular-hole fibre that was used for comparison with published results. However, a more practical example is shown in Fig. 4.9. The ABC-FDM calculations used $n_{\max} = 85$, $m_{\max} = 30$,

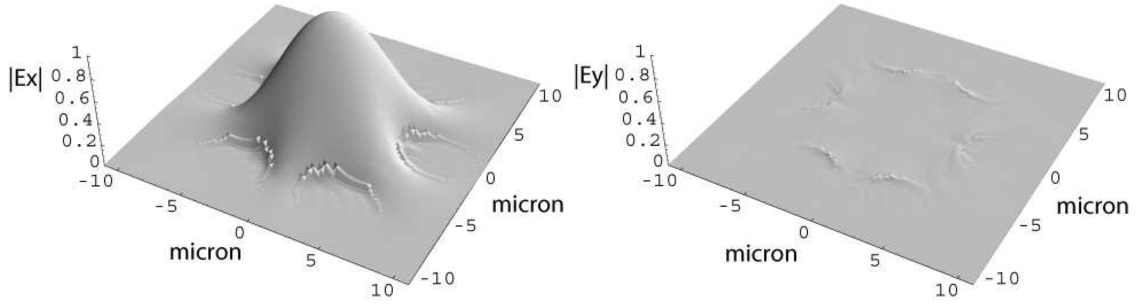

Figure 4.6: x and y components of the scaled electric field for mode 1 with hole ellipticity of 0.7.

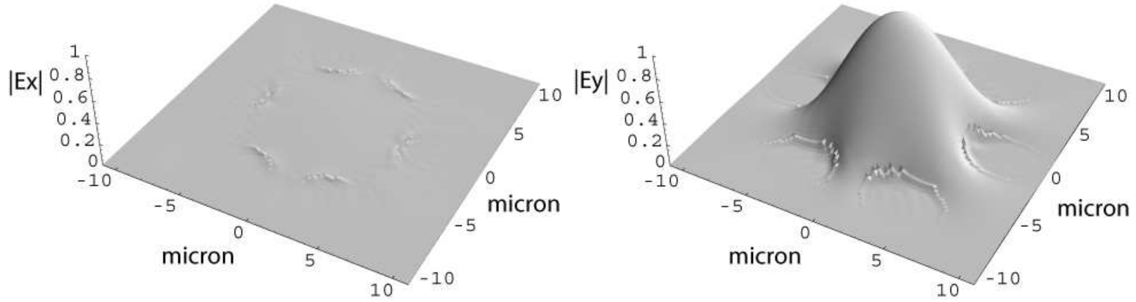

Figure 4.7: x and y components of the scaled electric field for mode 2 with hole ellipticity of 0.7.

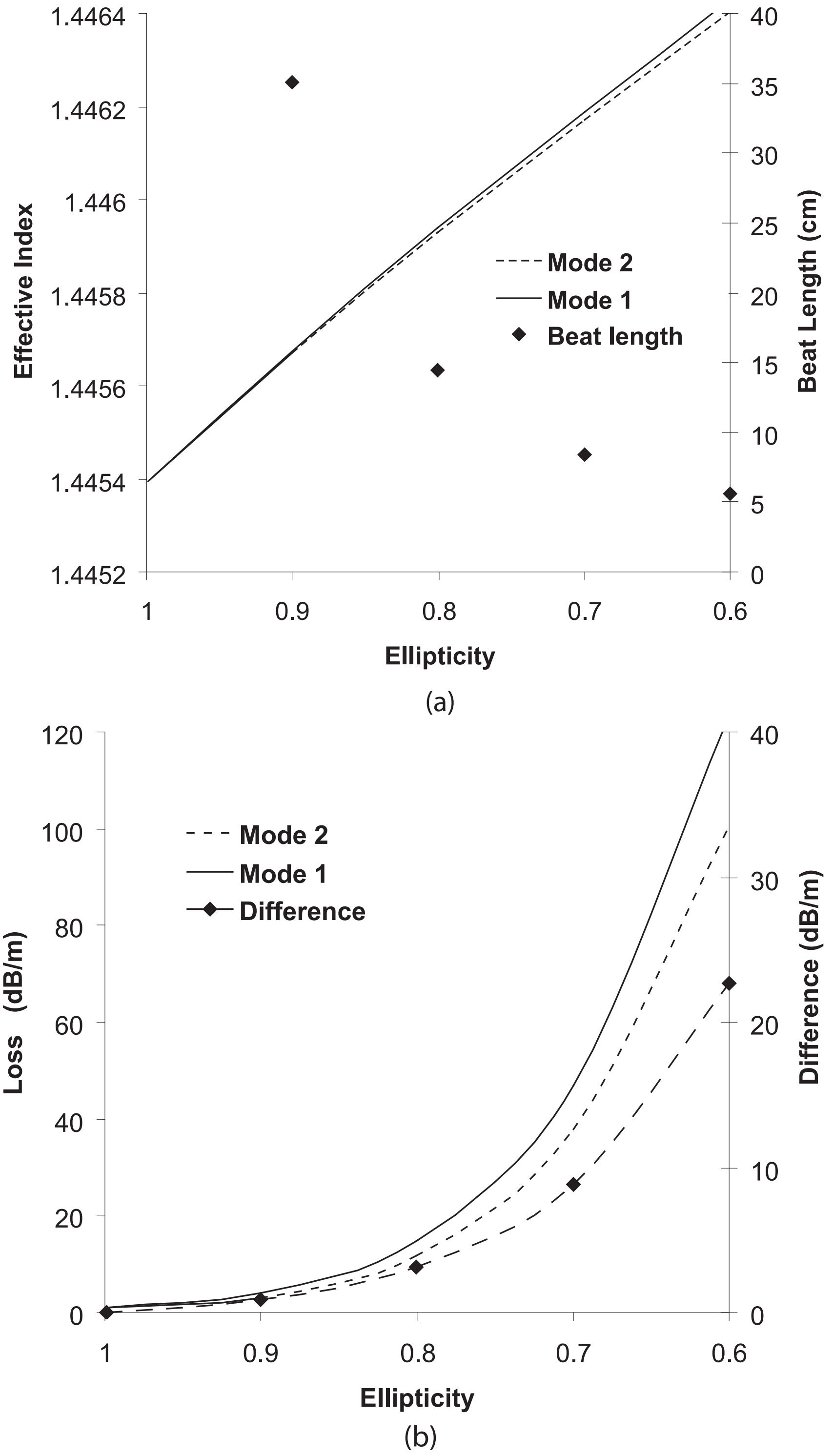

Figure 4.8: Graphs of birefringence as a function of hole ellipticity. The evolution of mode 1 is to an x-like polarization state, while mode 2 becomes y-like, oriented with the symmetry axes of the waveguide. **(a)** Splitting of the degenerate modes. **(b)** Differential loss leading to polarization dependent loss.

$R = 7.1\ \mu\text{m}, \lambda = 1.45\ \mu\text{m}$ and convergence was achieved in two refinements. The structure size is smaller than the previous example which has the effect of increasing birefringence. The addition of a second ring of holes is found to greatly reduce confinement loss to levels of some practical use. This is shown in Fig. 4.10 over a range of wavelengths. It can clearly be seen that at a wavelength of 1.45 μm the beat length is 0.68 cm. This is nearly an order of magnitude greater than that in the structure of Fig. 4.8(a), which is less than half the size. This clearly shows the birefringence is not linearly related to structure scale. In fact, it is shown in Chapter 6 that the dependence is typically a power relation. A explanation is currently unknown.

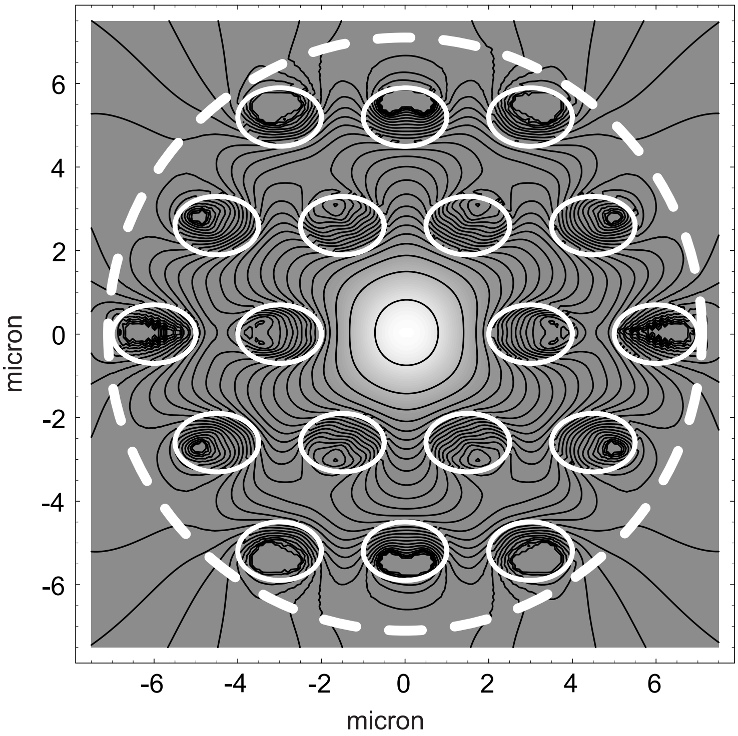

Figure 4.9: Intensity plot of the x polarized mode for two rings of holes with ellipticity of 0.7. Contours range from 0dB to -81dB with 3dB separation. The hole diameters (major direction) are 2.0 μm, the hole separation is 3.0 μm and the host refractive index is that of glass.

4.5.3 Discussion

Much of the behavior of the present algorithm is almost identical to that of standard Fourier expansion methods. A minimum number of angular and radial Fourier components are required to resolve spatial features of the waveguide in these directions. However, an additional requirement arises in the problems considered here as is demonstrated by the

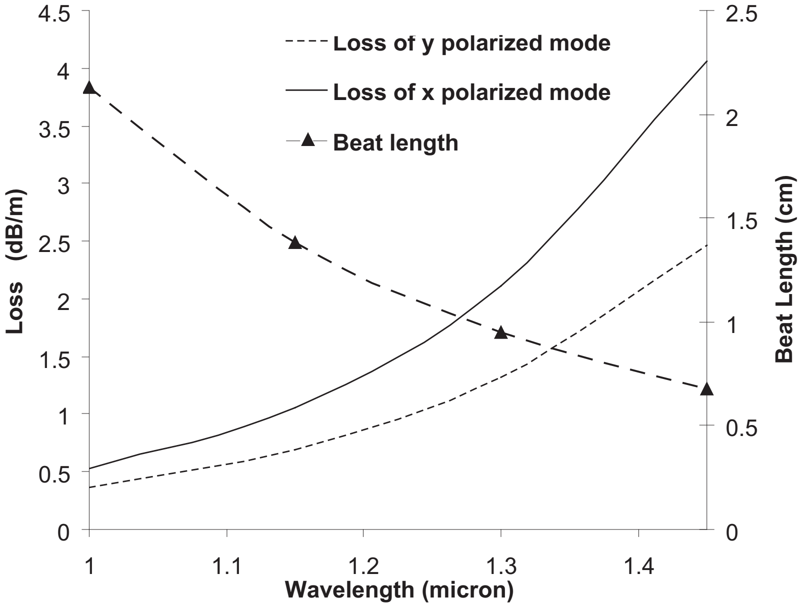

Figure 4.10: Plot of loss and beat length for the birefringent fibre shown in Fig. 4.9.

effective indices of Table 4.1. In order to accurately determine confinement loss, the numerical field solution near the computational domain boundary needs to join smoothly with any external fields. The lower precision in the imaginary parts is due to the difficulty of accurately representing the solutions close to this boundary, where the fields are much smaller than elsewhere in the computational domain (∼-55 dB as seen in Fig. 4.3).

An estimate of the minimum number of azimuthal $m_{\max}$ and radial $n_{\max}$ terms used in the expansion is given by

$$\begin{array}{l} m_{\max} \sim \frac{4\pi}{\Delta\theta} \\ n_{\max} \sim \max\left\{\frac{4R}{\Delta r}, \frac{2\eta}{\pi}\left\langle V(\rho,\theta)\right\rangle_D\right\}, \end{array} \tag{4.27}$$

where $\Delta\theta$ and Δr are *characteristic* angular and radial widths of features in the waveguide. The second radial condition arises from a heuristic derivation of the required number of Fourier components needed to represent the evanescent (assumed exponential) fields that appear in the microstructured region. It supposes that the Fourier expansion is truncated when the amplitudes of the terms become less than approximately $1/\eta$ of the maximum. A value of $\eta \simeq 10$ is found to be appropriate from the derivation and experience shows it to provide adequate accuracy in the imaginary part of n_{eff}. A simple azimuthal average of V over the microstructure is often applicable.

It is shown in Eq. (4.27) that the number of radial components directly increases the precision of confinement loss calculations. For very small confinement loss ($\Im m(n_{\text{eff}}) < O(10^{-9})$) a great improvement in efficiency is achievable by transforming or weighting the solution in such a way that smaller fields are more efficiently represented. There are many possible ways of achieving this, but few preserve the simplicity of the eigenvalue equations.

The present choice of basis functions results in the property that the evaluation of the eigenvalues and vectors is the most computationally intensive stage of the algorithm, rather than the numerical filling of the matrices. For this reason an efficient subroutine for solving for the dominant eigenvalues of dense, complex and non self-adjoint matrices is highly desirable. Current implementations of the algorithm have not utilized optimal matrix subroutines. Such improvements are the subject of future work.

4.6 Implementation by radial finite difference scheme

4.6.1 Motivation

The value of a numerical technique or implementation is often measured by the computational resources (both time and memory) required to achieve a desired accuracy (ie. convergence) for the class of problems being studied. Such is the measure of performance appraising the two implementations presented here, particularly in regard to the calculation of confinement loss. Great value can be derived from the use of basis function expansions for problems in which those functions closely resemble, or mimic, the solution being sought. On first consideration, it would seem highly appropriate to use a Fourier-like expansion for the problem of electromagnetic modes in microstructured fibres, as detailed in section 4.4.3. In retrospect, however, one notices that the computational domain used for the modelling of many microstructured fibres with low confinement loss is in fact mostly occupied by decaying fields. That is, fields that are evanescent within the holes and rapidly decreasing in amplitude between the holes as one looks further away from the core. Under these conditions, a Fourier-like expansion in the radial direction shows poor convergence. As noted previously, the matching of fields within the computational domain to the boundary conditions at the edge of this domain is very important for accurately determining confinement loss. Since the field amplitudes at this edge are extremely small in comparison to the core, poor convergence in the basis function expansion can make the implementation inefficient and unyielding. This inefficiency manifests itself as a blow-out in the required computational resources. The problem is intensified by using non-localised basis functions such as the Fourier set. This is because the operators in Eq. (4.3) will create coupling between each function in the set and every other, even though the set itself may be orthogonal. Ultimately, this results in dense matrices with few, if any, zero elements to exploit for better performance.

In this section the basis set chosen for the radial expansion is replaced by a finite difference scheme. In principle, one could seek alternative basis functions for the radial direction that may better resemble MOF modes. However, the diversity of structures makes it nearly impossible to identify one function set that is both generally efficient at representing mode fields *and* yields compact analytic expressions for the matrix elements. Using localised radial basis functions[1] would then seem more appropriate than other non-localised functions. On the other hand, the azimuthal Fourier expansion is retained for a number of reasons. Firstly, it is generally observed that the number of terms needed in the azimuthal expansion is considerably less than in the radial direction for the desired accuracy. This indicates a relatively efficient performance in the azimuthal representation of the fields. Secondly, the azimuthal Fourier expansion allows easy matching of fields at the computational domain boundary with the exponential-Bessel expansion (Eq. (4.9)) outside. This also substantially simplifies the boundary condition refinement scheme, but is not obligatory. Finally, it is the natural representation in which to select mode classes according to the azimuthal Bloch classification described in Section 2.1. This allows all mode classes to be modelled using the full rotational symmetry of the waveguide and completely separates degenerate mode classes. Finite differences are chosen to replace the radial basis function expansion since they are efficient and versatile in one dimension.

4.6.2 Second order finite differences

It is feasible and very convenient to use the same formalism of sections 4.3.1 and 4.4.3 in order to outline the finite difference implementation. One begins by assuming the following truncated expansion

$$\psi^{\pm}(\rho,\theta) = \sum_m \tilde{A}^{\pm}_m \psi^{\pm}_m(\rho,\theta), \tag{4.28}$$

which is to be only evaluated at particular radii, called radial nodes. These nodes are indexed by n and positioned at ρ_n. Interpolation can later be used to determine the value of the fields between these points.

The analogous expressions to Eqs. (4.14), which are the alternative forms for the basis functions, are only an azimuthal expansion

$$\begin{aligned} \psi^{\pm}_m(\rho,\theta) &= \frac{1}{\sqrt{2\pi}} e^{im\theta} \xi^{\pm}_m(\rho), \\ \phi_m(\theta) &= \frac{1}{\sqrt{2\pi}} e^{im\theta}. \end{aligned} \tag{4.29}$$

In this case the appropriate inner product is simply

$$\langle f \mid g \rangle = \int_0^{2\pi} f^*(\theta) g(\theta) d\theta. \tag{4.30}$$

---

[1] Such as functions that are non-zero only in a small region of the computational domain.

By these definitions, the equation analogous to Eq. (4.12) is

$$\begin{bmatrix} \left[\tilde{M}^{+}\right]_{\mu}^{m} - \left[\tilde{F}_{+}^{+}\right]_{\mu}^{m} & -\left[\tilde{F}_{-}^{+}\right]_{\mu}^{m} \\ \left[\tilde{F}_{+}^{-}\right]_{\mu}^{m} & \left[\tilde{M}^{-}\right]_{\mu}^{m} + \left[\tilde{F}_{-}^{-}\right]_{\mu}^{m} \end{bmatrix} \begin{bmatrix} \tilde{A}_{m}^{+} \\ \tilde{A}_{m}^{-} \end{bmatrix}$$

$$= W^2 \begin{bmatrix} \left[\tilde{N}^{+}\right]_{\mu}^{m} & 0 \\ 0 & \left[\tilde{N}^{-}\right]_{\mu}^{m} \end{bmatrix} \begin{bmatrix} \tilde{A}_{m}^{+} \\ \tilde{A}_{m}^{-} \end{bmatrix}, \tag{4.31}$$

where the summation over only m is implied and the matrix elements are given by these inner products

$$\begin{aligned} \left[\tilde{M}^{\pm}\right]_{\mu}^{m} &= \langle \phi_\mu \mid \mathcal{L}^{\pm}\, \psi_m^{\pm} \rangle \\ \left[\tilde{F}_{+}^{\pm}\right]_{\mu}^{m} &= \langle \phi_\mu \mid F^{\pm}(\rho,\theta) G^{+} \rangle \\ \left[\tilde{F}_{-}^{\pm}\right]_{\mu}^{m} &= \langle \phi_\mu \mid F^{\pm}(\rho,\theta) G^{-} \rangle \\ \left[\tilde{N}^{\pm}\right]_{\mu}^{m} &= \langle \phi_\mu \mid \psi_m^{\pm} \rangle \,. \end{aligned} \tag{4.32}$$

At this point the functions $\xi_m^{\pm}(\rho)$ are discretized and any radial derivatives are then executed using a second order finite difference scheme for unequally spaced nodes. The chosen expressions are provided in Appendix A.1.

When expressed fully in matrix form, Eq. (4.31) becomes precisely Eqs. (4.12), where $A_{mn}^{\pm} = \tilde{A}_m^{\pm} \xi_m^{\pm}(\rho_n)$. This matrix equation is repeated here for convenience

$$\begin{bmatrix} [M^{+}]_{\mu\nu}^{mn} - [F_{+}^{+}]_{\mu\nu}^{mn} & -[F_{-}^{+}]_{\mu\nu}^{mn} \\ [F_{+}^{-}]_{\mu\nu}^{mn} & [M^{-}]_{\mu\nu}^{mn} + [F_{-}^{-}]_{\mu\nu}^{mn} \end{bmatrix} \begin{bmatrix} A_{mn}^{+} \\ A_{mn}^{-} \end{bmatrix}$$

$$= W^2 \begin{bmatrix} [N^{+}]_{\mu\nu}^{mn} & 0 \\ 0 & [N^{-}]_{\mu\nu}^{mn} \end{bmatrix} \begin{bmatrix} A_{mn}^{+} \\ A_{mn}^{-} \end{bmatrix}.$$

The expressions for the elements of these matrices are provided in Appendix A.2. This eigenvalue problem is then solved precisely as described previously.

4.6.3 Boundary conditions

The boundary condition at the origin is expressed by

$$\lim_{\rho \to 0} \left[J_{m\pm 1}(W\rho) \frac{d\xi_m^{\pm}(\rho)}{d\rho} - \frac{dJ_{m\pm 1}(W\rho)}{d\rho} \xi_m^{\pm}(\rho) \right] = 0. \tag{4.33}$$

It ensures that each mode has the correct physical behavior at the origin and also that the coordinate singularity appearing in the polar representation of Eq. (4.3) is not problematic.

Again the limiting form of $J_m(W\rho) \cong (W\rho/2)^m/m!$ as $\rho \to 0$ will be used to simplify the equations to the following conditions:

$$\begin{array}{l} \text{If } m+1=0, \text{ then } \frac{d\xi_m^+}{d\rho}(0)=0, \text{ else } \xi_m^+(0)=0 \\ \text{If } m-1=0, \text{ then } \frac{d\xi_m^-}{d\rho}(0)=0, \text{ else } \xi_m^-(0)=0 \end{array}. \tag{4.34}$$

Matching of the internal and external fields, as given in Eq. (4.9), at the outer edge of D yields the second boundary condition at $\rho = 1$:

$$K_{m\pm1}(W\rho)\frac{d\xi_m^\pm(\rho)}{d\rho} - \frac{dK_{m\pm1}(W\rho)}{d\rho}\xi_m^\pm(\rho) = 0. \tag{4.35}$$

The finite difference forms for both these boundary conditions are provided in Appendix A.3, together with the matrix adjustments that they require.

4.7 Comparison of performance

The new implementation is conceptually simpler, and provides an improvement of approximately $n_{\max}^3/\tilde{n}_{\max}$ in speed and $n_{\max}^2/\tilde{n}_{\max}$ in memory requirement, where $n_{\max}$ and $\tilde{n}_{\max}$ are the radial resolutions used in the calculation. For a Fourier-like expansion, $n_{\max}$ is the number of radial basis functions used, while for the finite difference scheme, $\tilde{n}_{\max}$ is the number of radial nodes. With a simple Nyquist-sampling argument, it is assumed that $\tilde{n}_{\max} \sim 2n_{\max}$ is required for comparable accuracy, particularly because of poor convergence of the radial function expansion. Clearly this is speculative argument, but it is only for instructive purposes. For a typical problem that may require $n_{\max}$ to be between 100 and 200, memory demands are reduced by approximately[2] 50 to 100 times. However, the greatest benefit comes form the reduction in computation time (solving for eigen values/vectors, the dominant time-cost), which can be as much as 5,000 times or 20,000 times respectively. Note also that

$$\left[N^\pm\right]_{\mu\nu}^{mn} \equiv \delta_{m\mu}\delta_{n\nu}, \tag{4.36}$$

which no longer makes Eqs. (4.12) a generalized eigenvalue problem. This further reduces computation time and memory requirements by nearly a factor of 3/2.

A comparison of the two implementations with the multipole method is shown in Table 4.2 for an example MOF studied previously. In order to do so, the required changes were made to the C/C++ computer code. While the function expansion implementation

---

[2] This can only be estimated due to factors such additional overhead programming and the storage of precalculated expressions which are frequently used.

required approximately 6 hours for each mode, the finite difference implementation required nearly 10 seconds on the same desktop Pentium III 1GHz processor. The speed-up factor is approximately 2160, which is close to the predicted value of 2450.

Mode class	ABC with radial function expansion, $n_{\rm eff}$	ABC with radial finite difference scheme, $n_{\rm eff}$	Multipole $n_{\rm eff}$
HE11	$1.4453954 + 3.07 \times 10^{-8} i$	$1.4453941 + 3.26 \times 10^{-8} i$	$1.4453952 + 3.19 \times 10^{-8} i$
TE01	$1.4385890 + 5.43 \times 10^{-7} i$	$1.4385873 + 5.58 \times 10^{-7} i$	$1.4385836 + 5.31 \times 10^{-7} i$
HE21	$1.4384442 + 9.62 \times 10^{-7} i$	$1.4384433 + 9.89 \times 10^{-7} i$	$1.4384448 + 9.73 \times 10^{-7} i$
TM01	$1.4383643 + 1.38 \times 10^{-6} i$	$1.4383671 + 1.42 \times 10^{-6} i$	$1.4383649 + 1.41 \times 10^{-6} i$

Table 4.2: Comparison of results for the waveguide depicted in Fig. 4.1(a) results given in Table 4.1. The ABC-FDM calculations used: $n_{\rm max} = 70$, $m_{\rm max} = 54$ for the implementation with radial function expansion and $\tilde{n}_{\rm max} = 140$, $m_{\rm max} = 54$, for the radial finite difference implementation. $R = 9.3\ \mu$m and convergence was achieved in three refinements.

An arbitrary hole shape is easiest to incorporate by simply de-constructing the hole into many very thin annular sectors. Hundreds of annular sectors can be used for each arbitrary hole with negligible increase to computation time. Similarly, graded-index and other exotic inclusions can be incorporated in a variety of ways.

In both implementations, rotational symmetries in the waveguide structure can easily be exploited by including only azimuthal components which increase by multiples of the symmetry of the waveguide. The background theory is given in Section 2.1.

Any implementation of the ABC method can solve for mode types other than leaky modes with no further alterations. They include bound modes, modes in absorbing waveguides and leaky modes in photonic band gap structures. Only, care should be taken when choosing the sign of $W(n_{\rm eff})$ used in the external fields for bound and leaky modes. Convergence of the ABC scheme is not guaranteed for some extreme modes such as those with very poor confinement ($\Im m(n_{\rm eff}) > O(10^{-1})$). However, in the case of bound modes it can be shown that a suitable choice of R can always be made to ensure convergence. It is generally advisable that the choice of R should be as small as possible while still containing all the waveguide structure, as indicated in the previous results. This provides better accuracy for a given $n_{\rm max}$, which is shown to grow linearly with R in Eq. (4.27). On the other hand, reducing R will in principle require more refinements to bring the solution within acceptable error. However, as shown in Fig. 4.4 the decay in error is very rapid for a typical fibre and acceptable error is achieved in only a few refinements. It is believed that the rapid convergence of the ABC refinement scheme to be completely independent of the expansion set used and therefore a valuable tool for modelling such radiating systems. A detailed theoretical study follows.

Chapter 5

Properties of the Adjustable Boundary Condition method

Physical systems with open boundaries have long been known to be a mathematical challenge, both in analytic formulation and numerical solution. The concept is still one of active research today, particularly in ‘leaky’ optical systems. The motivation for developing the Adjustable Boundary Condition (ABC) refinement scheme for leaky modes in optical waveguides was outlined in chapter 4. The key points are re-emphasised: The solution of a partial differential equation (PDE) is sought within a computational domain that must satisfy the boundary conditions at the edge of this domain. The problem is an eigenvalue/eigenvector one, where the additional complication comes from the fact that the boundary conditions are dependent on the eigenvalue in a *non-linear* way. A refinement scheme was proposed whereby the eigenvalue is initially guessed and used for the boundary conditions, allowing the PDE to be solved. This provides a new eigenvalue which is then used again for a new boundary condition. The process is repeated and generates a sequence of eigenvalues. The questions that naturally arise are: Would the sequence converge? Would it converge to the correct physical solution? How rapid is the convergence? The answer to the second question is relatively simple; since the solution to a PDE with specific boundary conditions is unique, a convergent solution is necessarily the correct one. However, providing the conditions which guarantee convergence and determining the rate of convergence is a more difficult but very rewarding investigation. The suggested refinement scheme is not claimed to be the only or even optimal method of solution. On the other hand, its characteristics are highly favorable, as will be demonstrated here. This has motivated its development and use throughout this thesis.

This chapter contains an original study of the convergence properties of the ABC method. Expressions will be derived that state the conditions necessary to ensure convergence for both bound and leaky modes. In addition, the rate of convergence of the mode effective index will be predicted and confirmed with numerical simulation. It demonstrates that an exponential decay in the error is expected, which allows convergent solutions to be found very rapidly (ie. within only a few iterations).

The derivation presented is shown to be completely independent of the numerical scheme (or implementation) used within the computational domain. This suggests very broad and general validity, as the convergence properties and conditions would be identical for finite element, finite difference, function expansion or many other numerical schemes that employ the ABC method at their boundary. The combined attributes of; robust conditions for convergence, rapid convergence and general validity to many numerical schemes make the ABC method potentially valuable for more than just the modelling of bound and leaky modes in optical fibres, but also for many other radiating (or even non-radiating) systems, such as antennae, planar waveguides and microstrip waveguides.

5.1 Convergence equations

An investigation into the convergence properties of the ABC method was made possible by one major realisation. That is, at each iteration or refinement the numerical solution to the approximate boundary conditions is in fact the correct solution of a *perturbed* waveguide with a slightly different refractive index outside the computational domain. This index will be called $n_{\overline{D}}$ and it is anticipated that as the boundary conditions converge with successive refinements, then $n_{\overline{D}} \to n_{\mathrm{cl}}$, where n_{cl} is the correct refractive index. In this general treatment, the computational domain, D, need not be circular but *must* contain all the waveguide structure, as depicted in Fig. 5.1. The region outside the computational domain, $\overline{D}$, is precisely the complement of D.

The diagram in Fig. 4.2 shows that during the j th refinement of the effective index $n_{\mathrm{eff}}^{\{j\}}$, the fields in $\overline{D}$ are

$$\psi^{\pm}(\rho,\theta) = \sum_{m} B_m^{\pm} e^{im\theta} K_{m\pm1}(W^{\{j\}}\rho), \tag{5.1}$$

where $\left(W^{\{j\}}\right)^2 = R^2k^2\left((n_{\mathrm{eff}}^{\{j\}})^2 - n_{\mathrm{cl}}^2\right)$. Initially, neither n_{eff} nor the coefficients $B_m^{\pm}$ are known.

When the refined solution $n_{\mathrm{eff}}^{\{j+1\}}$ is found by the mode solver, an adjustment is defined by

$$\eta^{\{j+1\}} = \left(n_{\mathrm{eff}}^{\{j\}}\right)^2 - \left(n_{\mathrm{eff}}^{\{j+1\}}\right)^2. \tag{5.2}$$

The corresponding modal fields, $(\mathbf{h}^{\{j+1\}}, \mathbf{e}^{\{j+1\}})$ of the $(j+1)$ th approximate solution, can then be considered the precise solution to a waveguide with refractive index

$$n_{\overline{D}}^{\{j+1\}} = \left(n_{\mathrm{cl}}^2 - \eta^{\{j+1\}}\right)^{1/2} \tag{5.3}$$

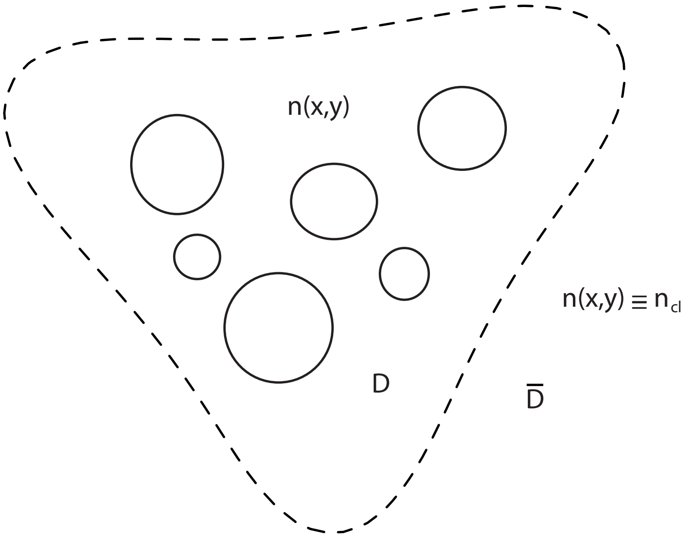

Figure 5.1: Depiction of computational domain D and its compliment $\overline{D}$. The boundary is given by the dotted line and $A_\infty = D + \overline{D}$. All waveguide structure, depicted with solid lines, is contained within D. The refractive index is assumed constant in $\overline{D}$.

in $\overline{D}$, since the fields in that region are given by Eq. (5.1), with

$$\left(W^{\{j\}}\right)^2 = R^2k^2\left((n_{\text{eff}}^{\{j+1\}})^2 - (n_{\overline{D}}^{\{j+1\}})^2\right). \tag{5.4}$$

An original reciprocity relation which is derived in Appendix B can then be applied to the consecutive j th and $j+1$ th refinements of the modes. Remembering that these modes are correct modes supported by the 'perturbed' waveguides of those refinements

$$\left(n_{\text{eff}}^{\{j\}}\right)^2 - \left(n_{\text{eff}}^{*\{j+1\}}\right)^2 = \frac{\int\limits_A \left(\left(n^{\{j\}}\right)^2 - \left(n^{*\{j+1\}}\right)^2\right)\widetilde{\mathbf{S}}\cdot\widehat{\mathbf{z}}dA}{\int\limits_A \widetilde{\mathbf{S}}\cdot\widehat{\mathbf{z}}dA} + \widetilde{M} + \widetilde{L}, \tag{5.5}$$

where

$$
\begin{aligned}
\widetilde{\mathbf{S}} &= \mathbf{e}_t^{\{j\}} \times \mathbf{h}_t^{*\{j+1\}} + \mathbf{e}_t^{*\{j+1\}} \times \mathbf{h}_t^{\{j\}} \\
\widetilde{M} &= \frac{\int\limits_D \left(\mathcal{E}^{\{j\}} \times \mathbf{h}_t^{*\{j+1\}} - \mathcal{E}^{*\{j+1\}} \times \mathbf{h}_t^{\{j\}}\right) \cdot \widehat{\mathbf{z}} dA}{k^2 \int\limits_A \widetilde{\mathbf{S}} \cdot \widehat{\mathbf{z}} dA} \\
&\quad + \frac{\int\limits_D \left(\mathbf{e}_t^{*\{j+1\}} \times \mathcal{H}^{\{j\}} - \mathbf{e}_t^{\{j\}} \times \mathcal{H}^{*\{j+1\}}\right) \cdot \widehat{\mathbf{z}} dA}{k^2 \int\limits_A \widetilde{\mathbf{S}} \cdot \widehat{\mathbf{z}} dA} \\
\widetilde{L} &= \frac{\oint\limits_{\delta A} \left[\left(\widehat{\mathbf{n}} \cdot \nabla_t \mathbf{e}_t^{\{j\}}\right) \times \mathbf{h}_t^{*\{j+1\}} - \left(\widehat{\mathbf{n}} \cdot \nabla_t \mathbf{e}_t^{*\{j+1\}}\right) \times \mathbf{h}_t^{\{j\}}\right] \cdot \widehat{\mathbf{z}} dl}{k^2 \int\limits_A \widetilde{\mathbf{S}} \cdot \widehat{\mathbf{z}} dA} \\
&\quad + \frac{\oint\limits_{\delta A} \left[\mathbf{e}_t^{*\{j+1\}} \times \left(\widehat{\mathbf{n}} \cdot \nabla_t \mathbf{h}_t^{\{j\}}\right) - \mathbf{e}_t^{\{j\}} \times \left(\widehat{\mathbf{n}} \cdot \nabla_t \mathbf{h}_t^{*\{j+1\}}\right)\right] \cdot \widehat{\mathbf{z}} dl}{k^2 \int\limits_A \widetilde{\mathbf{S}} \cdot \widehat{\mathbf{z}} dA} \\
\mathcal{E}^{\{j\}} &= -\nabla_t \left(\mathbf{e}_t^{\{j\}} \cdot \nabla_t \ln \left(n^{\{j\}}\right)^2\right) \\
\mathcal{H}^{\{j\}} &= \left(\nabla_t \times \mathbf{h}_t^{\{j\}}\right) \times \nabla_t \ln \left(n^{\{j\}}\right)^2 .
\end{aligned}
$$

A is some region of integration with boundary δA. It is assumed that A completely contains the computational domain D. The region of integration in the numerators of $\widetilde{M}$ has been reduced to D since the refractive index outside the computational domain is constant.

In addition, the refractive index profile of the waveguide in Eq. (5.5) satisfies

$$
(n^{\{j\}})^2 - (n^{*\ \{j+1\}})^2 = 2i\mathrm{Im}[\mathrm{n}^2] + \begin{cases} (n_{\overline{D}}^{\{j\}})^2 - (n_{\overline{D}}^{*\ \{j+1\}})^2 - 2i\mathrm{Im}[\mathrm{n}_{\mathrm{cl}}^2] & \text{outside D} \\ 0 & \text{inside D} \end{cases} . \quad (5.6)
$$

Eqs. (5.5) and (5.6) are exact, however an approximation is now made using the fact that the integrals of the modal solution are nearly constant relative to $(n_{\mathrm{eff}}^{\{j\}})^2$ during refinements. Justifying these replacements

$$\begin{aligned}
&\mathbf{e} \simeq \mathbf{e}^{\{j\}} \simeq \mathbf{e}^{\{j+1\}} \\
&\mathbf{h} \simeq \mathbf{h}^{\{j\}} \simeq \mathbf{h}^{\{j+1\}} \\
&\mathbf{S} \simeq \widetilde{\mathbf{S}} \simeq \mathbf{e}\times\mathbf{h}^{*} + \mathbf{e}^{*}\times\mathbf{h},
\end{aligned} \tag{5.7}$$

where $\mathbf{S}$ is four times the time averaged Poynting vector. Substituting these approximations and Eq. (5.6) into Eq. (5.5) gives

$$\left(n_{\text{eff}}^{\{j\}}\right)^{2} - \left(n_{\text{eff}}^{*\{j+1\}}\right)^{2} = \left\{\left(n^{\{j\}}\right)^{2} - \left(n^{*\{j+1\}}\right)^{2} - 2i\mathrm{Im}[\mathrm{n}_{\mathrm{cl}}^{2}]\right\} I + M_1 + M_2 + L, \tag{5.8}$$

where

$$\begin{aligned}
I &= \frac{\displaystyle\int_{\bar{D}} \mathbf{S}\cdot\widehat{\mathbf{z}}dA}{\displaystyle\int_{A} \mathbf{S}\cdot\widehat{\mathbf{z}}dA} \\
M_1 &= \frac{\displaystyle\int_{A} 2i\mathrm{Im}[\mathrm{n}^2]\mathbf{S}\cdot\widehat{\mathbf{z}}\mathrm{dA}}{\displaystyle\int_{A} \mathbf{S}\cdot\widehat{\mathbf{z}}dA} \\
M_2 &= \frac{\displaystyle\int_{D} (\mathcal{E}\times\mathbf{h}_t^{*} - \mathcal{E}^{*}\times\mathbf{h}_t)\cdot\widehat{\mathbf{z}}dA}{\displaystyle k^2\int_{A} \mathbf{S}\cdot\widehat{\mathbf{z}}dA} + \frac{\displaystyle\int_{D} (\mathbf{e}_t^{*}\times\mathcal{H} - \mathbf{e}_t\times\mathcal{H}^{*})\cdot\widehat{\mathbf{z}}dA}{\displaystyle k^2\int_{A} \mathbf{S}\cdot\widehat{\mathbf{z}}dA} \\
L &= \frac{\displaystyle\oint_{\delta A} [(\widehat{\mathbf{n}}\cdot\nabla_t\mathbf{e}_t)\times\mathbf{h}_t^{*} - (\widehat{\mathbf{n}}\cdot\nabla_t\mathbf{e}_t^{*})\times\mathbf{h}_t]\cdot\widehat{\mathbf{z}}dl}{\displaystyle k^2\int_{A} \mathbf{S}\cdot\widehat{\mathbf{z}}dA} \\
&\quad + \frac{\displaystyle\oint_{\delta A} [\mathbf{e}_t^{*}\times(\widehat{\mathbf{n}}\cdot\nabla_t\mathbf{h}_t) - \mathbf{e}_t\times(\widehat{\mathbf{n}}\cdot\nabla_t\mathbf{h}_t^{*})]\cdot\widehat{\mathbf{z}}dl}{\displaystyle k^2\int_{A} \mathbf{S}\cdot\widehat{\mathbf{z}}dA}
\end{aligned}$$

$$\begin{aligned}
\mathcal{E} &= -\nabla_t\left(\mathbf{e}_t\cdot\nabla_t\ln n^2\right) \\
\mathcal{H} &= (\nabla_t\times\mathbf{h}_t)\times\nabla_t\ln n^2
\end{aligned}$$

Finally, substituting expressions Eqs. (5.3) and (5.2), which relate the waveguide refractive index in $\overline{D}$ to the modal effective index, yields this recurrence relation

$$\begin{aligned}\left(n_{\text{eff}}^{*\{j+1\}}\right)^2 - \left(n_{\text{eff}}^{\{j\}}\right)^2 &= \left\{\left(n_{\text{eff}}^{*\{j+1\}}\right)^2 - \left(n_{\text{eff}}^{\{j\}}\right)^2 - \left(n_{\text{eff}}^{*\{j\}}\right)^2 + \left(n_{\text{eff}}^{\{j-1\}}\right)^2\right\} I \\ &\quad + M_1 + M_2 + L. \end{aligned} \tag{5.9}$$

It is clear that I is purely real, positive and between 0 and 1, while M_1, M_2 and L are purely imaginary. Thus the real and imaginary components of the recurrence relation Eq. (5.9) are uncoupled and can be solved separately.

Upon closer inspection, it can been seen that I, M_1, M_2 and L are constant with respect to the refinements indexed by j. Particularly M_2, since the region of integration in the numerator is only over the computational domain, in which n is independent of j. All these facts are emphasised since they will be important in simplifying the subsequent solutions of this recurrence relation.

It is fortuitous that a very simple and physically intuitive understanding of the convergence properties of this algorithm is available for bound modes. These expressions are derived in the following section. Unfortunately, the expressions for leaky modes do not provide the same physical insight. For this reason the derivations for both classes of modes are treated separately, although they both originate from Eq. (5.9).

5.2 Convergence for bound modes

For bound modes the fields decay sufficiently rapidly to set $A \equiv A_\infty$, ie. the entire waveguide cross-section, and neglect the boundary integral, ie. $L = 0$. The cases of waveguides with and without material absorption (or gain) will be treated separately, in order to highlight the significance of the individual terms in Eq. (5.9).

5.2.1 Without material absorption or gain

By setting $n_{\text{eff}} = n_{\text{eff}}^{\{j+1\}} = n_{\text{eff}}^{\{j\}} = n_{\text{eff}}^{\{j-1\}}$ in Eq. (5.9) and knowing that n_{eff} is purely real for a bound mode in a waveguide with no material absorption or gain it becomes clear that $M_1 = M_2 = 0$. The simplified recurrence relation (which is the real component of Eq. (5.9)) then becomes

$$\left(n_{\text{eff}}^{\{j+1\}}\right)^2 - \left(n_{\text{eff}}^{\{j\}}\right)^2 = \left\{\left(n_{\text{eff}}^{\{j+1\}}\right)^2 - 2\left(n_{\text{eff}}^{\{j\}}\right)^2 + \left(n_{\text{eff}}^{\{j-1\}}\right)^2\right\} I. \tag{5.10}$$

The general solution to this equation is

$$(n_{\text{eff}}^{\{j\}})^2 = C_1 \left(\frac{-I}{1-I}\right)^j + C_2, \tag{5.11}$$

where C_1 and C_2 are unknown constants.

The particular solution with initial condition $n_{\mathrm{eff}}^{\{1\}}$ at $j = 1$, as well as asymptotic behaviour $n_{\mathrm{eff}}^{\{j\}} \to n_{\mathrm{eff}}$ as $j \to \infty$ leads to

$$\text{Error} = (n_{\mathrm{eff}}^{\{j\}})^2 - (n_{\mathrm{eff}})^2 = \left((n_{\mathrm{eff}}^{\{1\}})^2 - (n_{\mathrm{eff}})^2\right)\left(\frac{-I}{1-I}\right)^{j-1}. \tag{5.12}$$

Solution (5.12) completely specifies the convergence properties of bound mode solutions in lossless waveguides using the adjustable boundary condition method. Firstly it shows that a value of $I < 1/2$ guarantees convergence. Physically this signifies that more than half of the *total* mode power must be within the computational domain, since $\mathbf{S}$ is proportional to the Poynting vector. Secondly, it demonstrates an exponential decay in the error, with a decay constant of $\ln(I/(1-I))$. This is extremely rapid since $I \ll 1$ can be *easily arranged* for any bound mode by increasing the size of D.

The solution is verified with a simple numerical example. The finite difference implementation of the ABC method described in sections 4.3 and 4.6 is applied to find the fundamental mode of a very thin cylindrical glass rod surrounded by air. The refractive index of the rod is 1.45, the diameter is 1μm and the wavelength is 1.55μm. These parameters are relatively extreme in the sense that much of the mode intensity is located *outside* the glass rod. The computational domain is circular and has a radius of 1.1μm, which means that the value of I will be relatively larger than in most common waveguide problems and thus the ABC convergence will be slower - allowing better verification of our model. This is shown in Fig. 5.2.

The agreement between predicted and simulation error is excellent over many refinements. For this example $I = 0.0167$ and the exponential decay is clearly verified. Within a few refinements, convergence is below the numerical error in n_{eff} due to the resolution of the numerical scheme inside the computational domain ($n_{\max} = 600$ and $m_{\max} = 0$). After 7 refinements, convergence is limited by the machine precision error. Clearly the level of resolution error must be greater than that due to machine precision. However, both numerical errors are dependent on resolution, since an increase in resolution demands more floating point operations are performed, which accumulates error from truncations in the representation of numbers. An estimate is indicated by dashed lines in the graphs of convergence.

5.2.2 Anticipating the sequence

Most readers will notice that the initial guess $n_{\mathrm{eff}}^{\{0\}}$ was not used when the unknown constants of Eq (5.11) were determined. Rather, the asymptotic behaviour of the sequence was used instead, which lead to the finding that $C_2 = (n_{\mathrm{eff}})^2$. Had this constant been

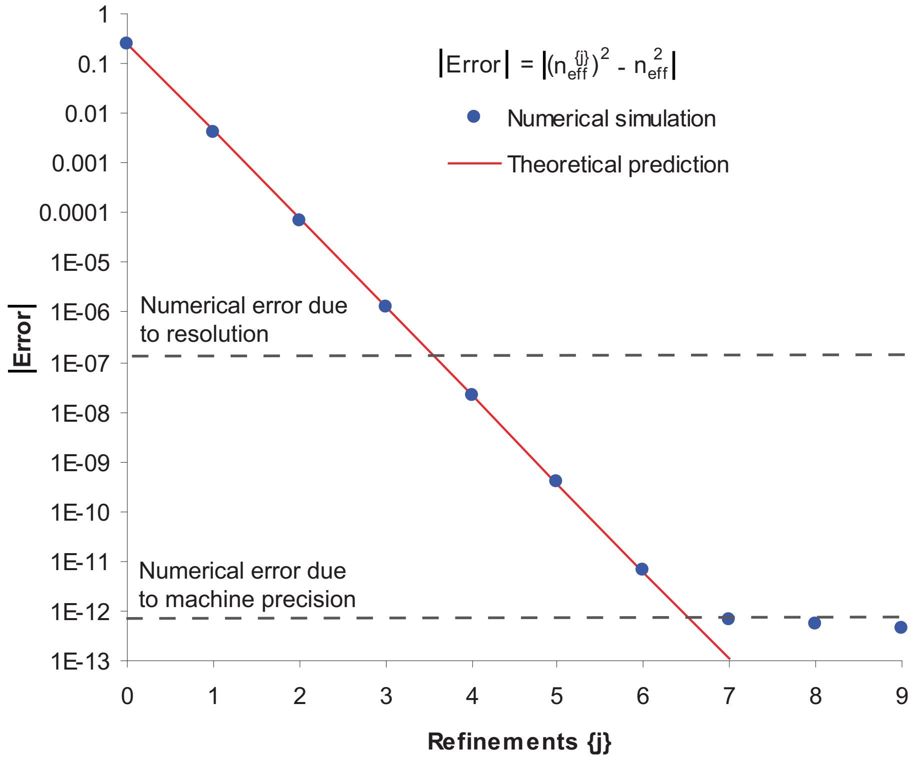

Figure 5.2: ABC convergence for a bound mode in a lossless waveguide. The predicted (Eq. (5.12)) and simulation error in modal effective index through subsequent refinement. The initial guess was $n_{\text{eff}}^{\{0\}} = 1.45$ and the final solution was $n_{\text{eff}} = 1.358714\ldots$.

found using only $n_{\text{eff}}^{\{0\}}$ and $n_{\text{eff}}^{\{1\}}$, the inevitable conclusion would be that

$$(n_{\text{eff}})^2 = C_2 = \frac{\left(\frac{I}{1-I}\right)(n_{\text{eff}}^{\{0\}})^2 + (n_{\text{eff}}^{\{1\}})^2}{1+\left(\frac{I}{1-I}\right)}. \tag{5.13}$$

At first glance it would appear that this formula provides a means by which the convergent solution can be found using only one refinement - in all waveguide circumstances. In practice, the prediction offered by Eq. (5.13) is not sufficiently accurate. Numerous techniques exist that extrapolate the later elements of a sequence given two or more initial elements. While these can be used to speed up the refinement scheme, they are beyond the scope of this chapter. Note however, that at *any* location in the sequence, the final answer can also be predicted by

$$(n_{\text{eff}})^2 = \frac{\left(\frac{I}{1-I}\right)(n_{\text{eff}}^{\{j-1\}})^2 + (n_{\text{eff}}^{\{j\}})^2}{1+\left(\frac{I}{1-I}\right)}, \tag{5.14}$$

which becomes increasingly accurate as $j \to \infty$. These expression also hold for the study of lossy and leaky modes.

5.2.3 With material absorption or gain

In this case, by setting $n_{\text{eff}} = n_{\text{eff}}^{\{j+1\}} = n_{\text{eff}}^{\{j\}} = n_{\text{eff}}^{\{j-1\}}$ in Eq. (5.9) the following identity is revealed

$$\mathrm{Im}[\mathrm{n}_{\mathrm{eff}}^2] = \frac{\mathrm{M}_1 + \mathrm{M}_2}{-2\mathrm{i}}, \tag{5.15}$$

remembering that $A \equiv A_\infty$.

The real and imaginary components of the recurrence relation Eq. (5.9) are then

$$\begin{aligned} \mathrm{Re}\left[\left(\mathrm{n}_{\mathrm{eff}}^{\{\mathrm{j+1}\}}\right)^2 - \left(\mathrm{n}_{\mathrm{eff}}^{\{\mathrm{j}\}}\right)^2\right] &= \left(\mathrm{Re}\left[\left(\mathrm{n}_{\mathrm{eff}}^{\{\mathrm{j+1}\}}\right)^2 - 2\left(\mathrm{n}_{\mathrm{eff}}^{\{\mathrm{j}\}}\right)^2 + \left(\mathrm{n}_{\mathrm{eff}}^{\{\mathrm{j-1}\}}\right)^2\right]\right) I \\ \mathrm{Im}\left[\left(\mathrm{n}_{\mathrm{eff}}^{\{\mathrm{j+1}\}}\right)^2 + \left(\mathrm{n}_{\mathrm{eff}}^{\{\mathrm{j}\}}\right)^2\right] &= \left(\mathrm{Im}\left[\left(\mathrm{n}_{\mathrm{eff}}^{\{\mathrm{j+1}\}}\right)^2 - \left(\mathrm{n}_{\mathrm{eff}}^{\{\mathrm{j-1}\}}\right)^2\right]\right) I + 2\mathrm{Im}[\mathrm{n}_{\mathrm{eff}}^2]. \end{aligned} \tag{5.16}$$

The general solution to these equations are

$$\begin{aligned} \mathrm{Re}\left[(\mathrm{n}_{\mathrm{eff}}^{\{\mathrm{j}\}})^2\right] &= C_1\left(\frac{-I}{1-I}\right)^j + C_2 \\ \mathrm{Im}\left[(\mathrm{n}_{\mathrm{eff}}^{\{\mathrm{j}\}})^2\right] &= C_3\left(\frac{-I}{1-I}\right)^j + C_4(-1)^j + \mathrm{Im}\left[(\mathrm{n}_{\mathrm{eff}})^2\right], \end{aligned} \tag{5.17}$$

where C_1 to C_4 are unknown constants.

With the same initial condition, $n_{\text{eff}}^{\{1\}}$, as well as asymptotic behaviour $n_{\text{eff}}^{\{j\}} \rightarrow n_{\text{eff}}$ as $j \rightarrow \infty$, the particular solutions are

$$\begin{aligned}
\text{Re[Error]} = \text{Re}\left[(\text{n}_{\text{eff}}^{\{\text{j}\}})^2 - (\text{n}_{\text{eff}})^2\right] &= \left(\text{Re}\left[(\text{n}_{\text{eff}}^{\{1\}})^2 - (\text{n}_{\text{eff}})^2\right]\right)\left(\frac{-I}{1-I}\right)^{j-1} \qquad (5.18) \\
\text{Im[Error]} = \text{Im}\left[(\text{n}_{\text{eff}}^{\{\text{j}\}})^2 - (\text{n}_{\text{eff}})^2\right] &= \left(\text{Im}\left[(\text{n}_{\text{eff}}^{\{1\}})^2 - (\text{n}_{\text{eff}})^2\right]\right)\left(\frac{-I}{1-I}\right)^{j-1}
\end{aligned}$$

These solutions go further than the previous solution by completely specifying the convergence properties of all bound modes in any waveguide. It shows that having more than half the modal power ($I < 1/2$) within the computational domain ensures convergence for both the real and imaginary components of the effective index. Again, the decay in error is exponential with a rate of $\ln(I/(1-I))$. These expressions are tested on the same waveguide detailed in the previous section, but where a small amount of loss[1] is introduced to the glass rod. Thus the rod has a refractive index of $1.45 + 0.02i$.

Again it is verified that the decay in error is exponential until the threshold of machine precision error is reached, as seen in Fig. 5.3. This holds true for both real and imaginary components of the mode effective index. One additional feature is visible in the plot of the imaginary component: the trend is not obeyed at $j = 0$. This is to be expected in some circumstances, since the recurrence relations are second order and are therefore the only strictly valid for $j \geq 1$.

5.3 Convergence for leaky modes

Leaky modes do not have decaying fields outside the computational domain, rather, the fields continue to grow in amplitude the further one looks from the core. Thus, in the infinite cross-section, it is not generally true that the boundary integral L of reciprocity relation Eq. (5.8) tends to zero as $A \rightarrow A_\infty$. Neither are the denominators of any of the constants finite when $A = A_\infty$. The consequence, at first glance, would be to seek a replacement for Eq. (5.9). However, this relation can be revived with some abstract adjustments inspired by the approach suggested by Sammut and Snyder [1976a].

For application with leaky modes, the limit $A \rightarrow A_\infty$ is taken subject to a change in the integration path. For integration in the radial direction, rather than keeping ρ purely real, it is allowed to be complex outside the computational domain. The actual integration path taken is depicted in Fig. 5.4. In this path ρ is real within the computational domain, but becomes complex outside. Such a change in integration path is possible because the fields outside the computational domain are given analytically by Eq. (5.1) and it is straightforward to substitute a complex number into the argument of the Bessel functions.

---

[1] This loss is numerically small compared to the real part of the refractive index. The value is chosen purely for demonstration purposes. In reality, such a material loss would be considered extremely high.

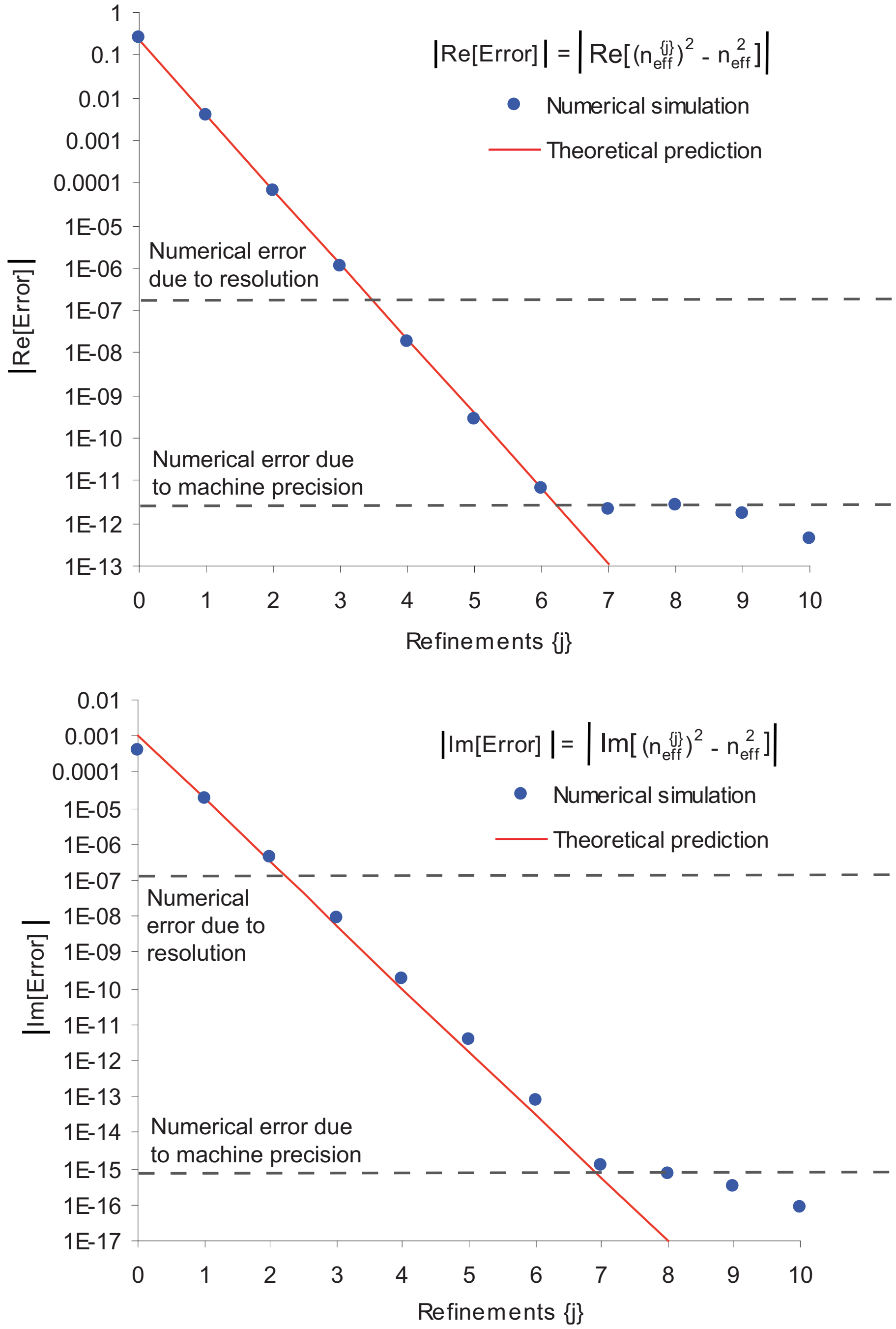

Figure 5.3: ABC convergence for a bound mode in a waveguide with material loss. The predicted (Eq. (5.18)) and simulation error in modal effective index through subsequent refinement. The initial guess was $n_{\text{eff}}^{\{0\}} = 1.45 + 0.0i$ and the final solution was $n_{\text{eff}} = 1.358637\ldots + 0.020209\ldots i$.

There are two important issues relating to this process. Firstly, the change in integration path does not rely on the integrand being analytic, since the intention here is not to carry out a contour deformation in the complex plane that preserves the value of the integral. Instead, since the choice of integration domain A is arbitrary, it is equally justified to simply choose a complex integration for A. In doing so however, some physical interpretation is lost, such as the simple understanding that convergence is governed by the fraction of mode power within the computational domain. Secondly, there is good reason for this particular choice of integration path. Making ρ complex in $\overline{D}$ has the effect of making the fields there decay nearly exponentially, with a rate dictated by Im[W], which is the dominant component. This can be easily seen in the asymptotic form of the Bessel function K, given in Eq. (4.10). This situation is most like that in the bound mode case and where I can be assumed to be largely constant with respect to the refinements. Indeed, this is the most important property that makes the recurrence relations solvable.

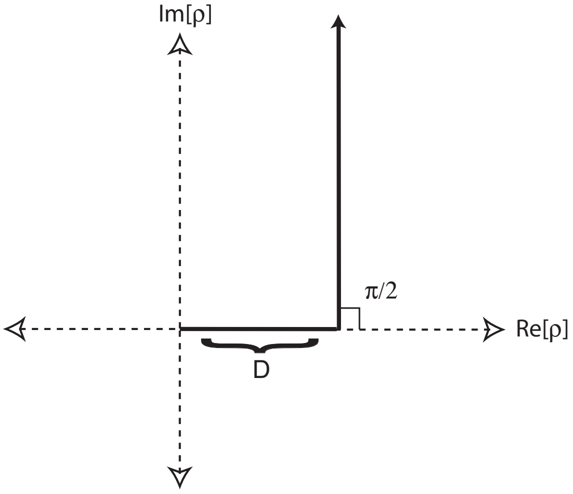

Figure 5.4: The radial integration path (solid line) in the complex ρ plane.

Once the new integration path is adopted, the boundary integral at infinity can be dropped since the fields decay sufficiently rapidly far away from D. However, $L \neq 0$ since the integration variable has changed on the boundary of D. The correct expression is then

$$\begin{aligned} L = & \frac{\oint_{\delta D^+} [(\widehat{\mathbf{n}} \cdot \nabla_t \mathbf{e}_t) \times \mathbf{h}_t^* - (\widehat{\mathbf{n}} \cdot \nabla_t \mathbf{e}_t^*) \times \mathbf{h}_t] \cdot \widehat{\mathbf{z}} dl}{k^2 \int_A \mathbf{S} \cdot \widehat{\mathbf{z}} dA} \\ & + \frac{\oint_{\delta D^+} [\mathbf{e}_t^* \times (\widehat{\mathbf{n}} \cdot \nabla_t \mathbf{h}_t) - \mathbf{e}_t \times (\widehat{\mathbf{n}} \cdot \nabla_t \mathbf{h}_t^*)] \cdot \widehat{\mathbf{z}} dl}{k^2 \int_A \mathbf{S} \cdot \widehat{\mathbf{z}} dA} \\ & - \frac{\oint_{\delta D^-} [(\widehat{\mathbf{n}} \cdot \nabla_t \mathbf{e}_t) \times \mathbf{h}_t^* - (\widehat{\mathbf{n}} \cdot \nabla_t \mathbf{e}_t^*) \times \mathbf{h}_t] \cdot \widehat{\mathbf{z}} dl}{k^2 \int_A \mathbf{S} \cdot \widehat{\mathbf{z}} dA} \\ & - \frac{\oint_{\delta D^-} [\mathbf{e}_t^* \times (\widehat{\mathbf{n}} \cdot \nabla_t \mathbf{h}_t) - \mathbf{e}_t \times (\widehat{\mathbf{n}} \cdot \nabla_t \mathbf{h}_t^*)] \cdot \widehat{\mathbf{z}} dl}{k^2 \int_A \mathbf{S} \cdot \widehat{\mathbf{z}} dA}, \end{aligned} \tag{5.19}$$

where δD^+ and δD^- represent the boundary of D when approached from within or from outside respectively.

The recurrence relations describing ABC convergence for leaky modes are subsequently identical to those for bound modes with material absorption, Eq. (5.16). However, in this case

$$\mathrm{Im}[\mathrm{n}_{\mathrm{eff}}^2] = \frac{\mathrm{M}_1 + \mathrm{M}_2 + \mathrm{L}}{-2\mathrm{i}}. \tag{5.20}$$

The solutions are therefore identical to Eq. (5.18). Again the condition $I < 1/2$ is necessary for convergence, but without an interpretation in terms of mode power. The rate of convergence is now verified for a more complicated waveguide that supports a fundamental leaky mode. The geometry of the microstructured fibre is described in Fig. 5.5, where the mode is also shown.

The decay in error of this waveguide is shown in Fig. 5.6. In this example $I = 0.0204$ and once again the decay is exponential. Very good agreement between numerical simulation and the predicted errors is seen over many refinements. Although the arguments leading to this result have been highly abstract, this exciting confirmation not only delivers information about ABC convergence for leaky modes, but also suggests a valuable tool for studying leaky modes. In addition, one notices that for leaky modes it is not always

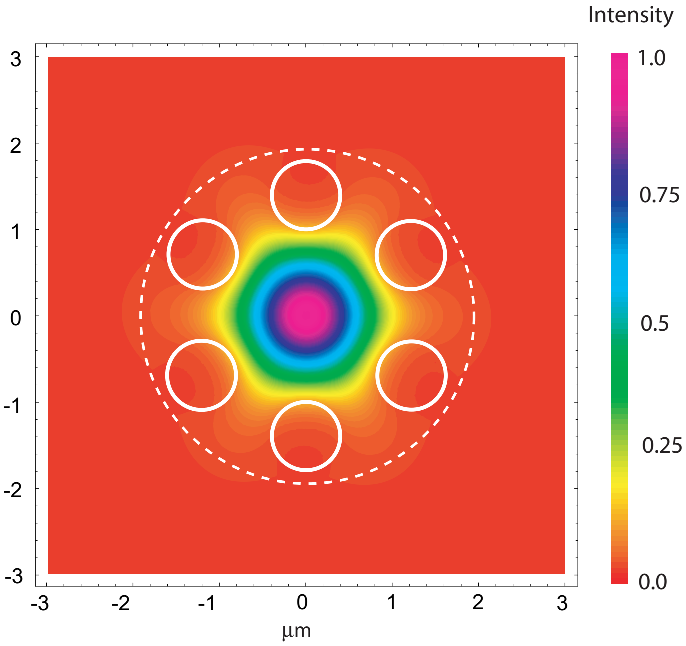

Figure 5.5: The intensity distribution of the leaky mode used to study ABC convergence. The air holes are indicated by the solid line and the computational domain is indicated with the dashed line. The holes have a radius of 0.4μm and are positioned 1.4μm from the origin. The computational domain is circular, with a radius of 1.9μm. The wavelength is 1.55μm and the host material refractive index is 1.45. The resolution is $n_{\max} = 550$ and $m_{\max} = 162$.

possible to choose a computational domain that gives $I < 1/2$, unlike the bound mode case.

5.4 Discussion

A number of alternative reciprocity equations have been tried, particularly those provided in [Snyder and Love, 1983, Chapter 31]. However, these resulted in nonlinear recurrence relations that were difficult to solve analytically without making additional assumptions that worsened the agreement with numerical simulation. Furthermore, they did not provide a physical interpretation as clear as that outlined in this chapter. While it may be possible to study the convergence of the ABC method with a different reciprocity equation or even by an entirely different approach, the present approach seems to be clear, effective and efficient. This study has been kept as general as possible so that it may apply to a wide variety of waveguide problems and numerical schemes. Consequently, it has been shown that the property of robust and rapid convergence is generally valid. This makes the investigation rewarding and may motivate others to use the ABC method in conjunction with other numerical mode solvers. In particular situations of slow convergence, this study may also allow the user to predict the convergent solution after several refinements.

5.4.1 Multimode waveguides

The process of applying the ABC method to many modes of a multimode waveguide is straight forward and is shown in Fig 5.7. At the initial iteration ($j = 0$), the initial guess $n_{\text{eff}}^{\{0\}}$ is used in the boundary conditions to find as many modes as desired - generating a list of new guesses. These are then individually refined to the appropriate level of convergence. Since each converged solution is descendant from the same initial guess, it is consistent that the solutions to the recurrence relations are predictive from $j = 1$ and not $j = 0$.

5.4.2 Scalar approximation

All the analysis above correctly applies to waveguides with small refractive index contrasts, and where the scalar wave equation is used. Simply make the substitution

$$\psi \equiv \mathbf{h}_t \equiv \left(\frac{\varepsilon_0}{\mu_0}\right)^{1/2} n\hat{\mathbf{z}} \times \mathbf{e}_t \tag{5.21}$$

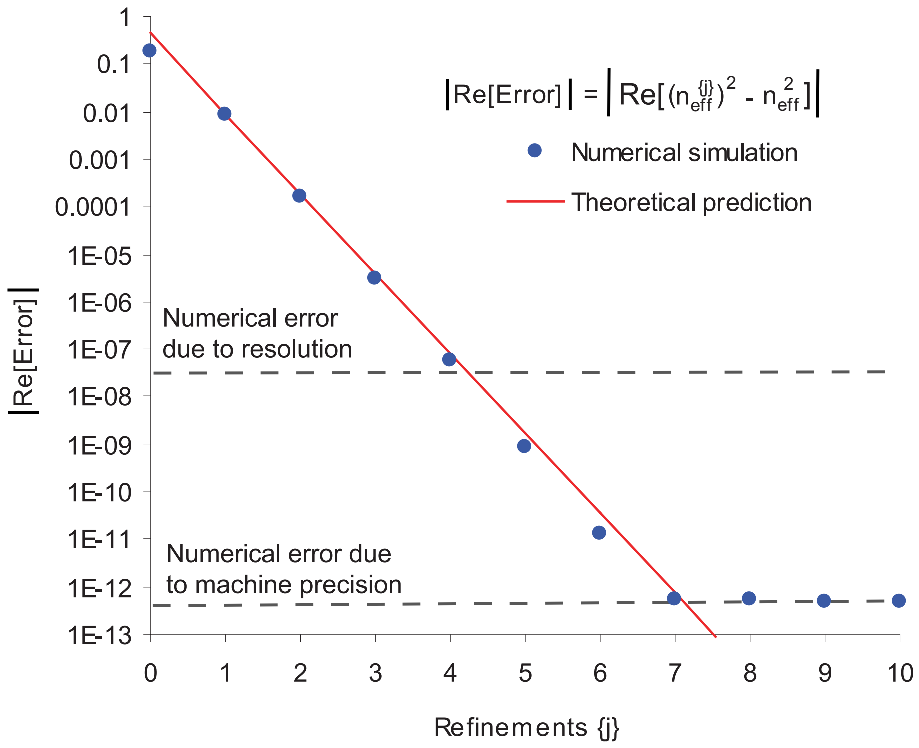

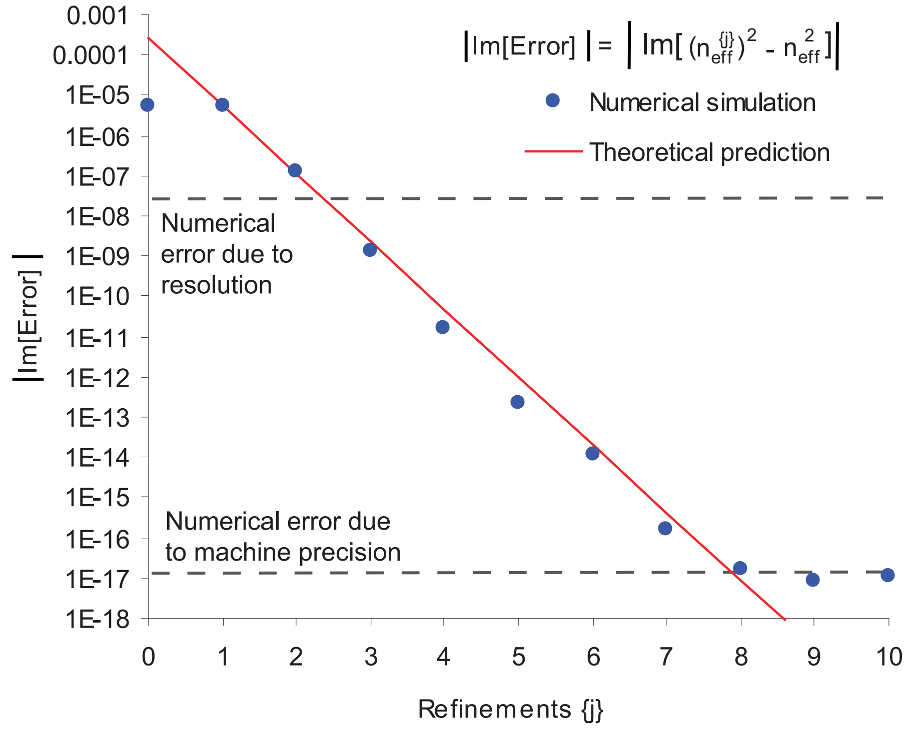

Figure 5.6: ABC convergence for a leaky mode. The predicted (Eq. (5.18)) and simulation error in modal effective index through subsequent refinement. The initial guess was $n_{\text{eff}}^{\{0\}} = 1.45 + 0.0i$ and the final solution was $n_{\text{eff}} = 1.384353\ldots + 0.002307\ldots i$.

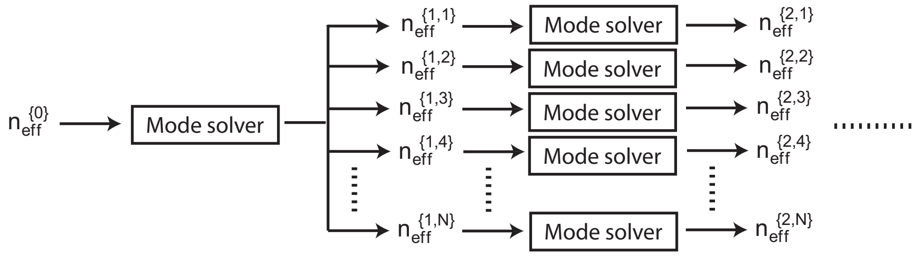

Figure 5.7: Illustration of ABC refinements for a multimode waveguide.

into all of the above equations. After the approximation $n \cong n_{\mathrm{cl}}$ is made, the only relevant expression is

$$I = \frac{\displaystyle\int_{\bar{D}} \psi\psi^* dA}{\displaystyle\int_{A_\infty} \psi\psi^* dA}, \tag{5.22}$$

which is also the fraction of modal power outside the computational domain.

5.4.3 The unknown coefficients

The advantages of the azimuthal Fourier decomposition (used here for the mode solver) have been thoroughly discussed in section 4.6.1. However, one additional advantage is highlighted by the investigation of convergence in the ABC method. Given that Eq. (5.1) describes the fields outside the computational domain, in order to impose this as boundary conditions one does not need to know the value of the coefficients $B_m^{\pm}$ when an azimuthal Fourier decomposition is used. After several refinements, when the error in the mode effective index is below some desired threshold, these coefficients can found from the eigenvector generated by the mode solver in a straightforward way. The procedure for dealing with these coefficients in other numerical schemes, or where the computational domain is not circular is important.

For other types of numerical schemes used for the mode solver, one approach would be to make an initial guess for these unknown coefficients. For example $B_m^{\pm} = 0$, for all m. At each refinement the fields within the computational domain can be used to find an improved estimate of these coefficients which are then applied to the boundary conditions during the next refinement. The convergence study given in this chapter should then still apply after the first refinement. The simplest way to do this, would be if D enclosed some circle, of radius R, centred at the origin and which also completely enclosed the waveguide structure. The coefficients would then be given by

$$B_m^{\pm\{j\}} = \frac{1}{2\pi} \frac{1}{K_{m\pm1}\left(W^{\{j-1\}}R\right)} \int_0^{2\pi} \psi^{\pm\{j-1\}}\left(R,\theta\right) e^{-im\theta} d\theta, \tag{5.23}$$

which can be evaluated numerically and depends on the scheme used.

However, this approach is not elegant. A greatly preferable solution would be to encode the numerical scheme in such a way as to avoid guessing the unknown coefficients, as is the case for an azimuthal Fourier decomposition. This should be possible for most numerical schemes, but the details do greatly depend on the scheme being used. Therefore, the issue is not explored further here.

5.4.4 Extension to external objects

The absence of structure outside the computational domain means that only one kind of Bessel function is found in the expansion of Eq. (5.1) - those representing outward radiating fields. It is possible however, to use the ABC method when some structure lies outside the computational domain. This can be achieved by including another type of Bessel function in this expansion, one which can account for back-reflection from the external objects. The new expansion

$$\psi^{\pm}(\rho,\theta) = \sum_m A_m^{\pm} e^{im\theta} I_{m\pm1}(W\rho) + B_m^{\pm} e^{im\theta} K_{m\pm1}(W\rho), \tag{5.24}$$

or alternatively

$$\psi^{\pm}(\rho,\theta) = \sum_m A_m^{\pm} e^{im\theta} J_{m\pm1}(-iW\rho) + B_m^{\pm} e^{im\theta} H_{m\pm1}^{(1)}(-iW\rho), \tag{5.25}$$

is valid in the regions between the computational domain (which clearly must include the origin) and the external objects. This needs to include the boundary of D.

Now the number of unknown coefficients in this expansion has doubled. To *reduce* this, either Chew's method [Chew, 1990, Chapter 3] can be used in the case of external cylindrical layers or a variation of the multipole method [White et al., 2002b, Kuhlmey et al., 2002c] in the case of external circular inclusions. Matching of the fields inside the computational domain to the *reduced* expansion provides the boundary conditions and the ABC refinements are executed as before. All findings presented in this chapter are then still expected to apply to this situation. This approach may prove to be highly advantageous in studying the influence of an external jacket which is far away from the microstructure. A situation in which enlarging D to include this jacket is computationally prohibitive. Verification of this approach will be the topic of future work.

Part III

APPLICATION

“You use the boogie man as follows:”

- Richard P. Feynman

Chapter 6

MOFs with elliptical holes

6.1 Introduction

Microstructured Optical Fibres (MOF) with *elliptical* holes have received significant theoretical analysis because of their polarization dependent interaction with guided electromagnetic waves. In addition to the high-birefringence and polarization maintaining characteristics of these fibres [Steel and Osgood, 2001a, Mogilevtsev et al., 2001], a number of properties such as photonic band gap guidance [Qiu and He, 1999] and dispersion [Steel and Osgood, 2001a] have been investigated. Furthermore, the addition of an elliptical hole in the core region of MOFs has also been studied [Mogilevtsev et al., 2001, Zhi et al., 2003a] for the prospect of enhancing birefringence even beyond the exceptionally high levels demonstrated in MOFs to date [Ortigosa-Blanch et al., 2000, Suzuki et al., 2001]. Fabrication of the first MOFs with uniformly oriented elliptical holes is reported here. Composed of polymer [van Eijkelenborg et al., 2003], these fibres provide the first steps at realizing the variety of elliptical hole structures presented in the literature.

The difficulty in fabricating MOFs with non-circular holes is due to the action of surface tension, viscous stresses, heating and pressure effects during the fibre draw. These effects typically result in either non-uniformly oriented hole deformations or hole re-circularization when the holes are non-circular in the preform stage. It is shown here that with an appropriate geometry some of these effects can be advantageously employed to create oriented elliptical holes.

6.2 Fabrication

The hole pattern shown in Fig. 6.1(a) was drilled into a commercially available extruded polymethylmethacrylate (PMMA) preform of diameter 8cm. This was subsequently drawn to a structured cane of diameter 6mm, sleeved in a PMMA jacket with outer diameter of 12mm and drawn again to fibre of three different outer diameters. The deformed hole pattern in the resulting fibre is shown in the electron microscope image of Fig. 6.1(b).

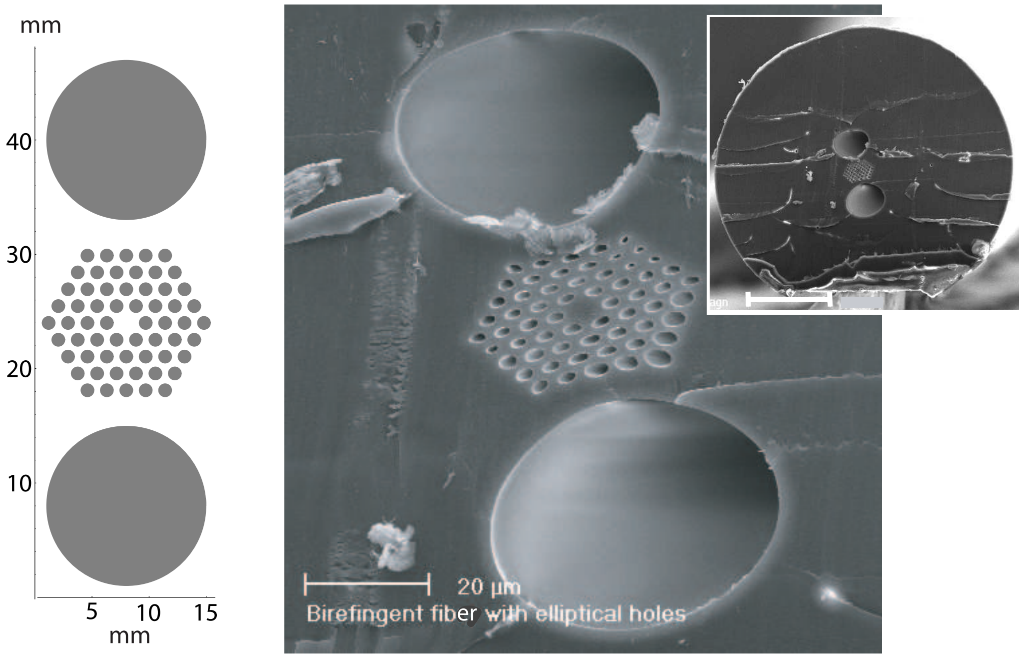

(a) (b)

Figure 6.1: (a) Schematic showing drilled hole pattern in PMMA preform. (b) Scanning electron microscope (SEM) image of resulting sleeved fibre after drawing, $\Lambda_a = 5.12\ \mu$m. Despite appearances, the cleave is perpendicular to the fibre axis and the image is taken end-on to the cleave (less than roughly 10 degrees).

The major hole pitch, Λ_a, as indicated in Fig. 6.2(a) for the three different diameter fibres are 5.12, 3.82 and 3.14 μm. The ellipticity of the cores, defined as the ratio of minor to major pitches, Λ_b/Λ_a, are 0.61, 0.61 and 0.59 respectively. The averaged hole major diameters, d_a, of the inner ring are 3.0, 2.1 and 1.6 μm for these three fibres, with average hole ellipticity $d_b/d_a = 0.59$, 0.54 and 0.48 respectively. The reproducibility of these measurements over several perpendicular cleaves the accuracy is estimated to be ±5%.

By studying these measurements of structural sizes at various fibre diameters, the process of hole deformation has been understood as follows; during fibre draw the phenomenon of hole collapse drives the preferential collapse of the holes along the line joining the two giant deforming voids on either side of the microstructure. The interplay between surface tension, viscous stresses and pressure differentials is believed to be the cause of partial hole collapse observed in many MOFs [Fitt et al., 2002]. Thus, pressurization of the air holes may provide some control on such deformations [Lyytikäinen et al., 2003, Yoshida and Morikawa, 1996]. However, such collapse is impeded by the viscosity of the material while in its glassy state. For the structure shown in Fig. 6.1(a), the absence of material in

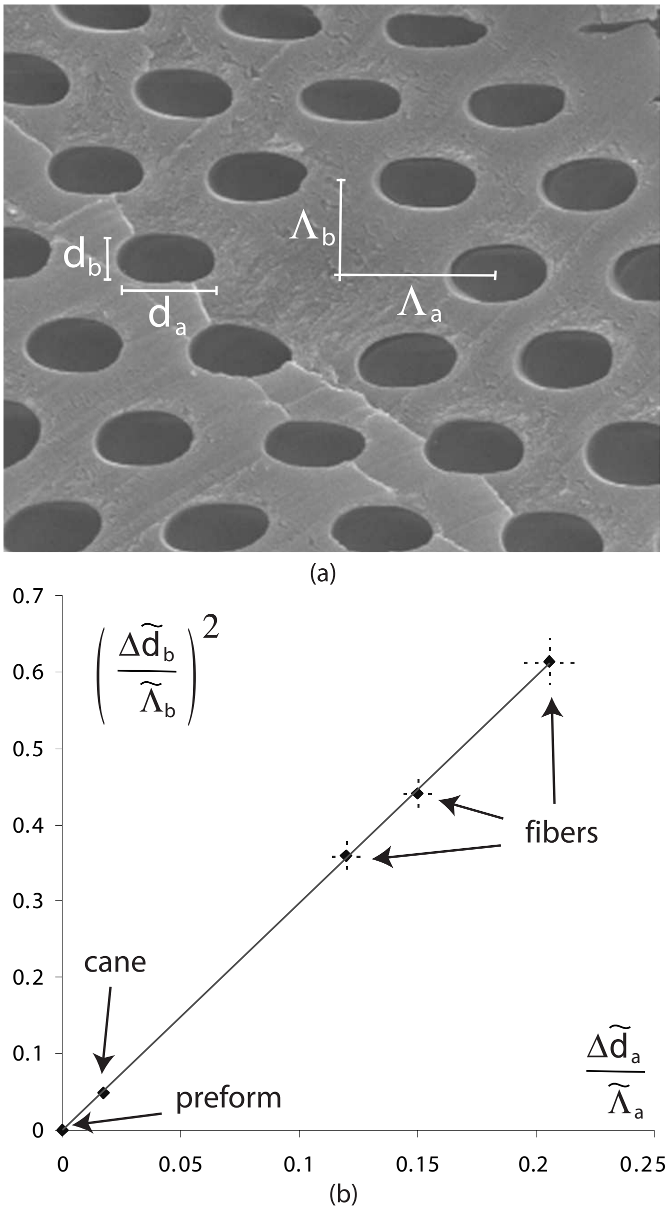

Figure 6.2: (a) SEM image of inner rings of elliptical holes ($\Lambda_a = 5.12\ \mu$m). (b) Comparison of deformation formula Eq. (6.1) (solid line) with measured dimensions (points).

the deforming voids provides less resistance to deformation and the resultant asymmetric stresses deform the smaller holes to ellipses. It is worthwhile to note that the type of deformation described above is qualitatively reproducible from similar initial preforms. However, a quantitative investigation of such reproducibility has not been attempted.

An empirical formula was found by considering appropriate dimensionless quantities to accurately describe the deformation process in the inner ring of holes. It is given by

$$\left(\frac{\Delta\widetilde{d}_b}{\widetilde{\Lambda}_b}\right)^2 = 2.98\,\frac{\Delta\widetilde{d}_a}{\widetilde{\Lambda}_a}, \tag{6.1}$$

where the notation $\widetilde{x} = x/D$ is used to indicate that these quantities have been scaled by the outer fibre/preform diameter, D, and where $\Delta\widetilde{d}_{a,b} = \widetilde{d}_{a,b} - \widetilde{d}$ represents the change in these scaled quantities from the initial preform dimensions, $\widetilde{d}$.

An important finding is that Λ_a *scales geometrically* with the outer fibre diameter, ie. $\Lambda_a \propto D$, and in that sense undergoes no deformation. It is therefore used to represent the structure scale throughout this paper. The term $\Delta\widetilde{d}_a/\widetilde{\Lambda}_a \propto \Delta\widetilde{d}_a$ can be simply understood as the magnitude of hole collapse. Measurements taken from the three fibres, initial preform and intermediate cane are compared against Eq. (6.1) in Fig. 6.2(b) and show excellent agreement. It demonstrates that an uncomplicated relation exists between hole collapse (right hand side of Eq. (6.1)) and the two measures of deformation in the minor direction (left hand side). An understanding of this relation may be possible through a rheological analysis, but is beyond the scope of this thesis.

6.3 Birefringence

Polarized light from a broadband light source is launched at 45° to the principal axes of the birefringent MOF of known length. The output polarization state is analyzed with a second polarizer also at 45° to the MOF principle axes. An intensity modulation is observed over the broad wavelength range (see Fig. 6.3) which can be used to characterize the wavelength dependent modal birefringence, $B(\lambda) = n_x - n_y = \lambda/L_{\mathrm{B}}(\lambda)$, where n_x, n_y are the effective indices of the dominantly polarized modes and L_{B} is the polarization beat length. The light source used for the measurements was a high brightness white light source. However, for fibres with very short modulation periods, a tunable Ti:sapphire laser operating from 700 to 860nm was used. Measurements at longer wavelengths were impossible due to very high material absorption, thus measurements were limited to the transparency windows in the visible and near-infrared. All fibres were experimentally found to be single moded. However, the fibre with $\Lambda_a = 5.12$ μm was only single moded for lengths over two meters, after which higher order leaky modes are significantly attenuated. The smallest test length used was 30cm while the longest was 3m.

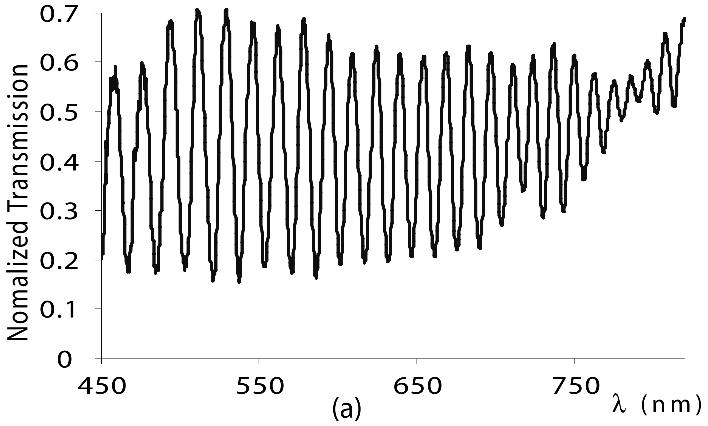

Figure 6.3: Example transmission spectrum. The effects of a PMMA absorption peak near 770nm are observable. The length of fibre in this example was 50cm and the modulation depth is determined by such factors as mode coupling due to scattering centers in the fibre and imperfect alignment of the polarizers with the polarization axis of the fibre.

The relative phase difference, ϕ, between the two polarization modes after a length, L, is given by $\phi(\lambda) = 2\pi LB/\lambda$. By making the assumption that $B \propto (\lambda/\Lambda_a)^{k_0}$, which is suggested in the literature and is strongly supported here [Ortigosa-Blanch et al., 2000, Suzuki et al., 2001], the use of $\Delta\phi = \phi(\lambda(1 + \Delta\lambda/\lambda)) - \phi(\lambda)$ gives

$$B(\lambda) = \frac{\Delta\phi\ \lambda}{2\pi L}\left[\left(1 + \frac{\Delta\lambda}{\lambda}\right)^{k_0 - 1} - 1\right]^{-1}, \tag{6.2}$$

which is accurate for small $\Delta\lambda/\lambda$. When λ is centered on a peak and $\Delta\lambda$ represents the distance to a nearby peak, then $\Delta\phi = 2\pi n$, where n is an integer. Alternatively, a peak-to-node reading corresponds to $\Delta\phi = 2\pi(n + 1/2)$. In this way several measurements can be averaged at each sample wavelength to statistically reduce the overall errors. The unknown power, k_0, can be determined efficiently by iteration. That is, once the measured data is graphed with an initial guess for k_0, its value can then be accurately refined by a power law fit to the trend.

The resulting birefringence measurements on the three fibres are overlayed in Fig. 6.4, where the wavelength has been scaled with the major pitch of the fibres. In good accordance with the size-wavelength scaling law for electromagnetism [Sakoda, 2001, pp. 21-23], the three measurements piecewise construct a distinct functional dependence of birefringence on wavelength. The small discontinuities between measurements are the result of the slightly different deformations at different microstructure sizes and are approximately the same magnitude as the ±5% errors in the data. The measured values of $k_0 \simeq 2.8$ are in excellent agreement between fibres and support the appropriateness of the power law fit over a very broad wavelength range.

Numerical modelling of the real MOF was carried out using the fully vectorial mode solver described in Chapter 4, employing the finite difference implementation. The confinement losses of the fundamental modes were found to be negligible in comparison to the material losses. Only waveguide-induced (form) birefringence was calculated and the stress-optic contribution neglected. Importantly, the form birefringence was found to be weakly dependent on the variation of the measured deformations. The fast polarization axis is in the minor direction of the core, Λ_b.

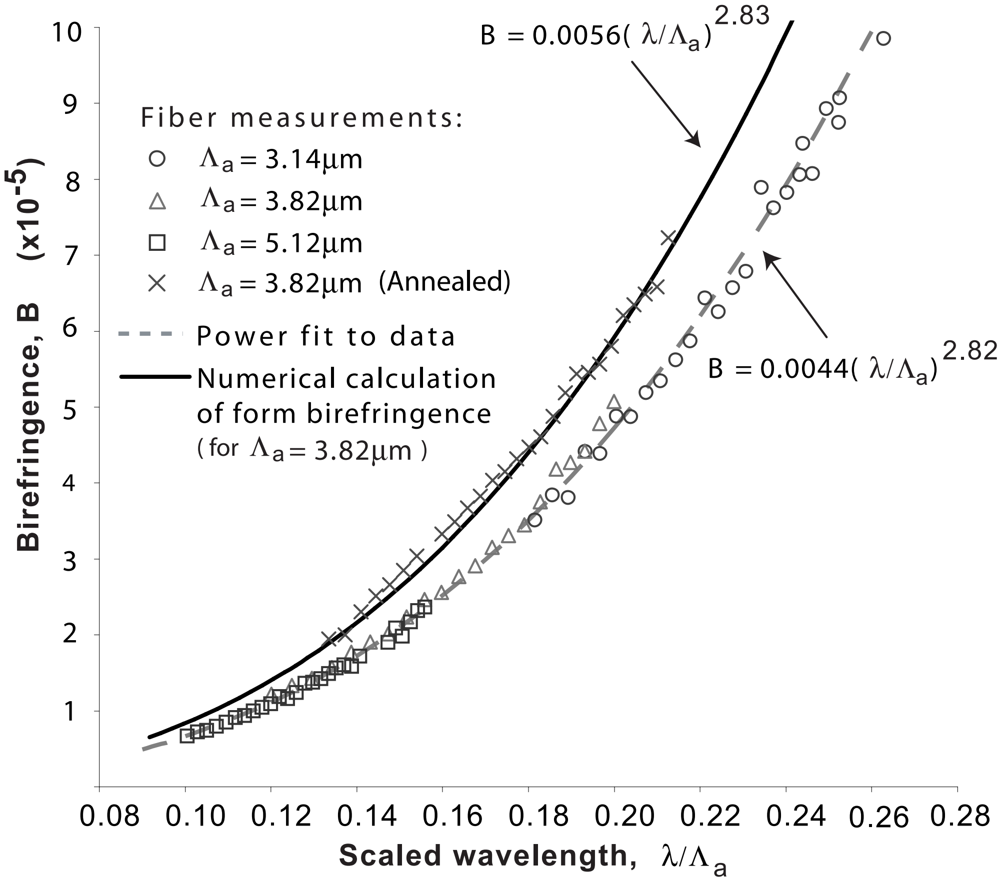

Figure 6.4: Measured and numerically calculated birefringence. The stated power law for the numerical calculation is obtained from a fit with $R^2 > 0.999$ in this range.

The numerical results for the MOF with $\Lambda_a = 3.82$ μm are plotted in Fig. 6.4 and show a deviation from agreement with the initial measurements. Subsequently, this fibre was annealed at 90°C (~ 20°C below the glass transition temperature) for 25min to alleviate any material stresses and the birefringence measurement retaken (shown in Fig. 6.4). The annealed results show excellent agreement with numerical modelling and prove that a non-zero stress-optic birefringence was latent in the material in opposition to the form birefringence.

The experimental results indicate that the increase in measured birefringence by eliminating stress was $\sim 25\%$, which is wavelength independent. The birefringence for these fibres increases strongly with wavelength and beyond 850nm is comparable in magnitude with conventional polarization maintaining fibres, for which birefringence is nearly wavelength independent. SEM images of the annealed fibre confirm no discernible change in the microstructure and thus the purely form birefringence of the type investigated here is expected to be largely independent of temperature. This has recently been demonstrated numerically by Szpulak et al. [2002] and experimentally by Michie et al. [2004]. It is highly desirable in a number of sensing applications, such as fibre optic gyroscopes, which are limited by temperature effects in highly stressed birefringent fibres.

Chapter 7

Guidance in air-core MOFs

7.1 Introduction

One particular sub-class of microstructured fibres, the photonic band gap (PBG) fibre, has received considerable attention, particularly because of its ability to guide light in air [Cregan et al., 1999, West et al., 2000], which is instrumental for many applications such as gas sensing [Monro et al., 2001], enhanced Raman scattering [Benabid et al., 2002a], CO_2 laser guidance [Temelkuran et al., 2002] or particle transport [Benabid et al., 2002b]. In addition, it could potentially provide a reduction of the fibre losses when material absorption is large [van Eijkelenborg et al., 2001, Temelkuran et al., 2002].

The bands of peak transmission found in the spectral response of PBG fibres is a distinctive feature caused by the Bragg reflection of light from the microstructure surrounding the central air core. Therefore colouration of the modes at the output of the fibre when illuminated by a very broadband or white-light source is a common first test for photonic band gap guidance [Cregan et al., 1999, West et al., 2000, van Eijkelenborg et al., 2002]. However, it is important to understand all processes that can lead to colouration in optical fibres before any conclusions are drawn about the PBG nature of the guidance. A number of additional colouration effects in MOFs have already been observed and reported. Each has a unique origin unrelated to PBG effects, such as those associated with anti-resonant optical waveguides [White et al., 2002a], fibre bending [Birks et al., 1997], and bending of MOFs with a depressed index core [Mangan et al., 2001] or with an off-center core [van Eijkelenborg et al., 2000]. In this chapter we identify and explain one additional mechanism by which colouration can arise in straight sections of air-cored MOFs. Unlike in the cited articles, the obtained transmission spectra are insensitive to the surrounding microstructure. That is, structural disorder results in the transmission properties of the MOF being dominated by the reflection of light off the first air/solid interface.

A number of guiding mechanisms are possible in air-cored microstructured fibres. Since guidance by total internal reflection is impossible in an air core fibre, the modes supported by the waveguide must be leaky. Confinement losses arise from partial reflections off air/solid interfaces and the leakage of light through the microstructure. Modes in hollow waveguides are also an example of such leaky modes, a detailed analysis of which can be found in [Marcatili and Schmeltzer, 1964]. They are legitimate eigen-solutions to the standard wave-equations for a waveguide consisting of simply one air hole in a uniform host material. Guidance is achieved only by partial reflection off the single air/material interface, commonly referred to as external reflection. When microstructure surrounds the air core the leaky mode solution describes the net reflection from the microstructured region. The MOF investigated here belongs to a common class of air-cored fibre where the features of roughly uniform size are air holes in a host material. Such fibres first demonstrated approximately 35% transmission through *only* 30mm of fibre [Cregan et al., 1999] and more recently a loss as low as 13dB/km has been reported [Venkataraman et al., 2002].

7.2 Experimental observation

Air-cored PBG polymer fibres have been fabricated, and evidence of PBG guiding through short lengths of fibre has been observed [van Eijkelenborg et al., 2002]. Unfortunately, these initial results have proved difficult to reproduce, a fact that has been attributed to non-uniformities in the fibre structure, both in the transverse and longitudinal direction, which led to a closing of the band gap [West and Allan, 2002].

Despite the absence of a PBG in the current fibre under study, colouration was still observed, as shown in Fig. 7.1. The first fibre has a 6-layer hexagonal structure similar to a PBG fibre, while the second is a simple single-hole hollow waveguide. The core sizes of these two fibres are comparable; 17.5μm for the PBG fibre and 22μm for the hollow waveguide, and both display similar characteristics. The three pictures next to the fibre images in Fig. 7.1 show the length-dependent output when diffuse white light is launched into the core by coupling with a multimode, high NA glass fibre. The shortest lengths show essentially white light transmission. Intermediate lengths show mixed colouration and blue transmission is observed around 45mm lengths. Longer lengths show no observable transmission in the core. The pictures are taken by cutting back one piece of fibre in both cases.

Quantitatively it can bee seen that the observation of colouration is very sensitive to the length of the fibre. Furthermore the same trend towards predominantly blue transmission is observed in both cases, suggesting that the surrounding microstructure may not contribute substantially to the dominant guiding mechanism. An important fact is that the intensity profiles closely resemble that of the common (Gaussian like) fundamental mode with *uniform phase*. It motivates an analysis of the leaky modes supported by the

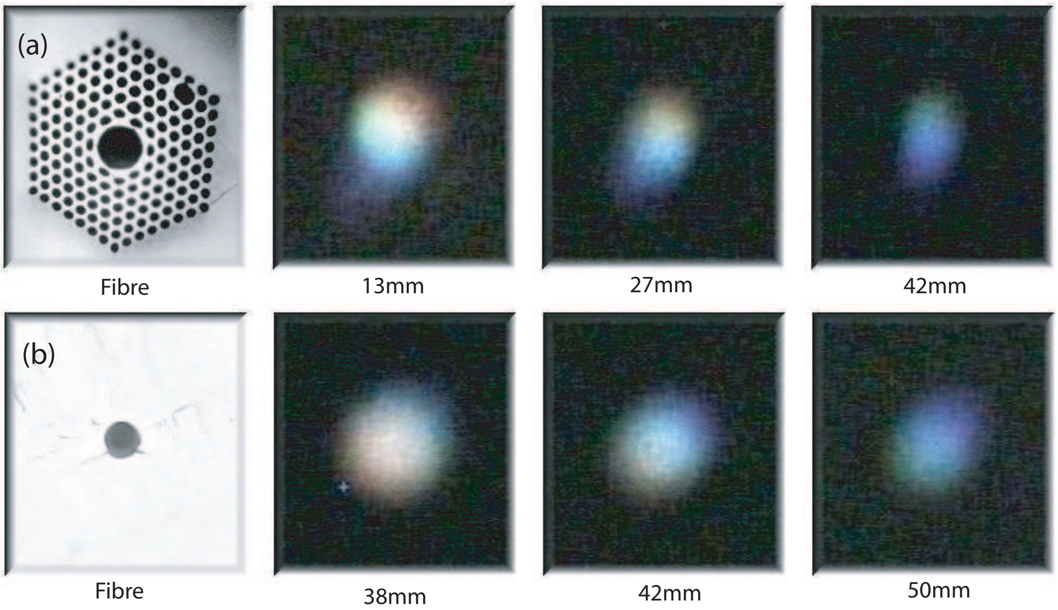

Figure 7.1: Two polymer (PMMA) fibres. **(a)** PBG MOF with a 17.5μm core diameter, hole diameters of 4.3μm $\pm$ 7% and hole spacings of 6μm $\pm$ 5%. **(b)** Hollow waveguide with a 22μm core diameter. The three pictures next to the fibres show the length dependent output when diffuse white light is launched into the core.

waveguide in order to best describe the observed phenomena. This is presented in the following sections.

7.3 Identifying the dominant guiding mechanism

Since the confinement losses of various modes may differ by orders of magnitude it is convenient, although not strictly true, to attribute a particular guiding mechanism to the size of the confinement loss. Furthermore, since the power in the core decays exponentially, the length of a tested fibre is crucial in determining the dominant guiding mechanism responsible for the observed mode. Due to the considerable technical difficulty in fabricating microstructured fibres (at the time of this work) with sufficient uniformity along their length, the optical characterisation of fibres was often done with very short lengths, sometimes no more than a few centimetres. In such cases care must be taken when interpreting observation, since a number of guiding mechanisms are likely to contribute. Recently however, much greater lengths of air-guiding fibre are commercially available. Thus this chapter serves particularly to instruct those in the early stages of fibre fabrication (as this author is) or those using very short lengths of fibre.

The measured optical transmission spectra for the MOFs presented in Fig. 7.1 (a) are given in Fig. 7.2 for 2 different core sizes. No sharp PBG transmission peaks are observed over this broad wavelength range, although some features are visible, which are relatively small when compared to the overall trend. These are mainly attributed to the wavelength dependent interaction of light with the surrounding microstructure.

Both core sizes permit greater transmission at shorter wavelengths, resulting in predominantly blue colouration. Due to the similarities in transmission for both fibres shown in Fig. 7.1 a theoretical comparison is made with the expected transmission of a hollow waveguide with equal diameter. Since ray-optics approximations are invalid for the small core/cavity size of the hollow waveguide, the transmission spectrum was determined from the confinement losses of leaky-mode solutions. The diffuse (spatially incoherent) light source used here is expected to approximately equally excite every leaky mode supported by the waveguide [Snyder and Love, 1983, pp. 436-41]. Thus to simulate transmission though all leaky modes, 210 leaky modes were used in all the results presented. This number was convergent in the sense that exciting a greater number of modes did not significantly change the resulting transmission curve.

It is well understood that a large increase in reflectivity can occur at an interface as the glancing angle of incidence approaches zero degrees. Accordingly the large variation in confinement loss of modes supported by a hollow waveguide results from the effective reduction of the glancing angle at shorter wavelengths [Marcatili and Schmeltzer, 1964]. The numerical results over a broad spectral range for the hollow waveguide are superimposed in Fig. 7.2. It is clear that the hollow waveguide model correctly approximates the experimental data over orders of magnitude in transmission. A secondary finding is that the contribution to transmission of higher order leaky modes cannot be neglected when the core diameter is very large or the fibre length is short. In those cases the analysis provides better agreement with the experimental data when the higher order modes are taken into account.

7.4 Comparison through numerical modelling

The Adjustable Boundary Conditions (ABC) method with finite difference implementation that has been described in Chapter 4 is used for the present calculations. The complex effective indices, n_{eff}, of the leaky modes are found and confinement loss is determined from its imaginary part using Eq. (2.7).

In Fig. 7.3 (a) is shown the overall trend of chromatic dispersion for the modelled MOF as compared to the hollow waveguide. The two trends are in excellent agreement over a broad wavelength range apart from small deviations due to Kramers-Kronig like features that are coincident with dominant peaks in confinement loss. In Fig. 7.3 (b) the overall trend in confinement loss is made clearer by using a running average of transmission over 20nm about each point. This is expected to simulate experimental effects such as the finite resolution of the optical spectrum analyser (10nm) and random perturbations from

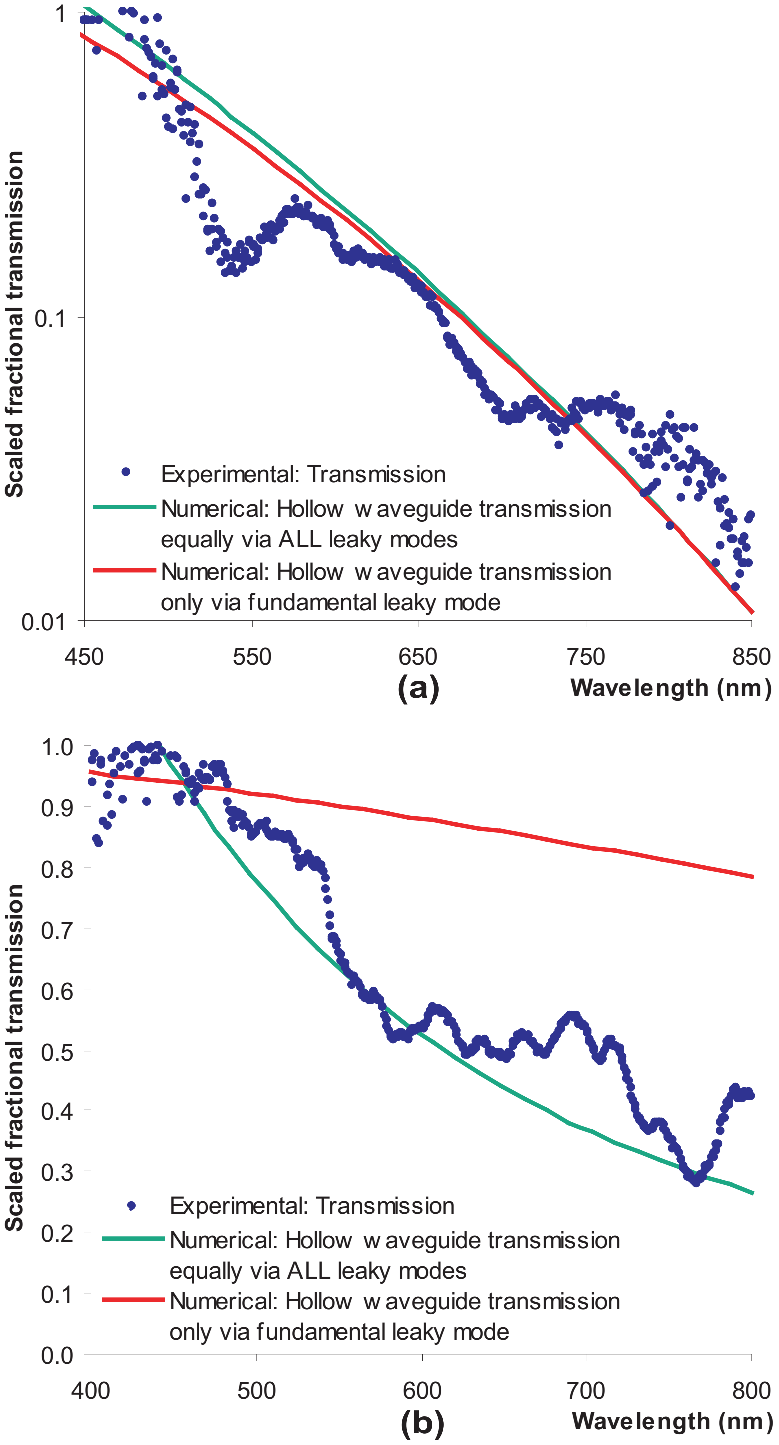

Figure 7.2: A comparison of the measured transmission spectrum of two 13mm long pieces of air core MOF with the expected transmission for a hollow waveguide with equal diameter. The core diameters are **(a)** 17.5μm and **(b)** 48.0μm. The spectra have been normalised to a spectrum of the light source.

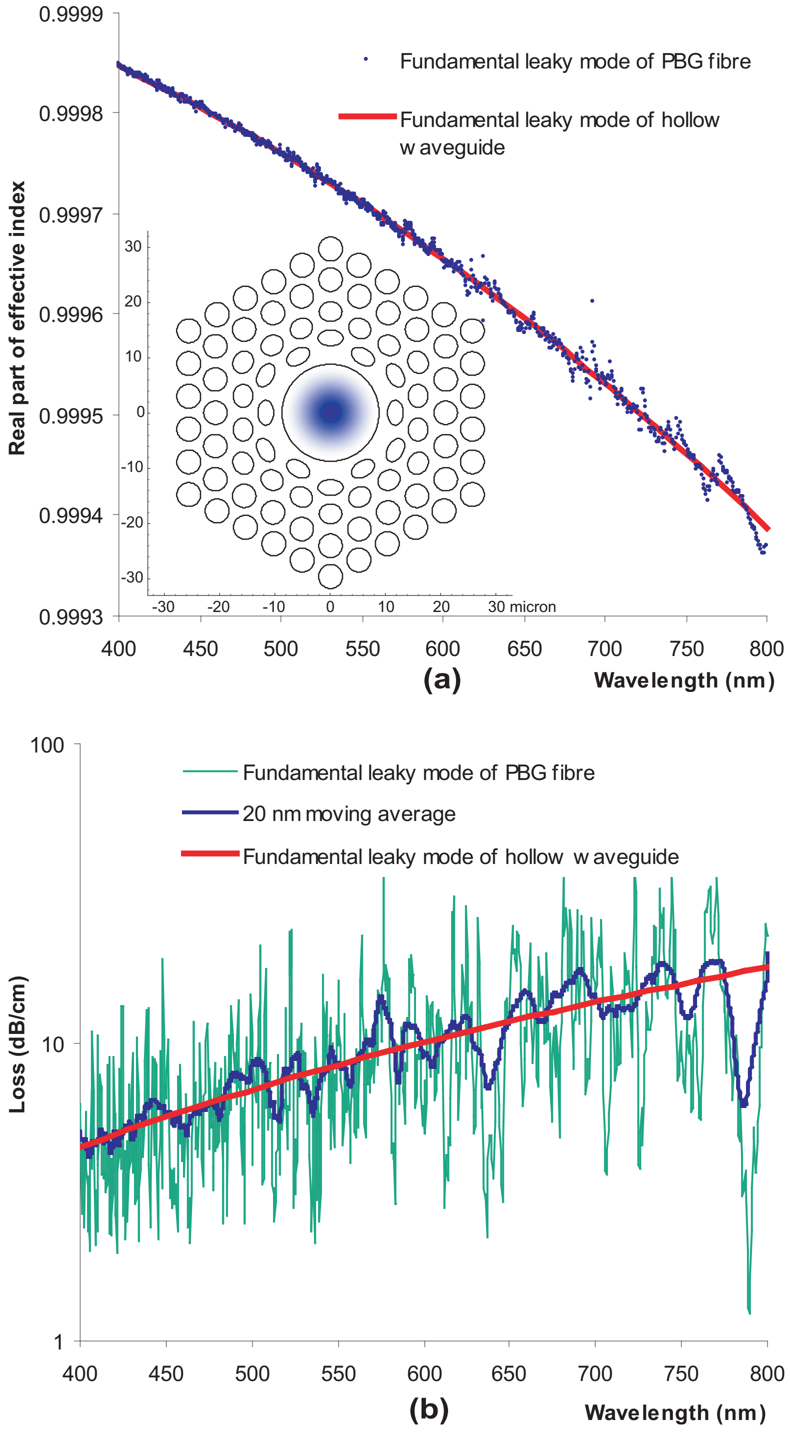

Figure 7.3: Numerical propagation characteristics for the MOF shown in the inset - a 6-fold symmetric idealization of the fibre in Fig. 7.1 (a), including the measured ellipticity of the first ring of holes. The intensity profile of the fundamental (HE11 like) leaky mode solution is superimposed to demonstrate the similarity with experimental observation. **(a)** The real part of n_{eff} and **(b)** confinement loss are compared with the fundamental mode solution of the hollow waveguide model.

the idealized microstructure, whose effects are difficult to quantify. Structural disorder of only $4 - 8\%$ in the range of hole positions and radii has been shown to completely close a typical PBG [West and Allan, 2002]. This places stringent tolerances on the fabrication of MOFs that have not been reached here. It is clear that the spectral features of this MOF are especially narrow in the visible wavelength range (i.e. $< 3\%$ of the central wavelength). It is highly likely that structural disorder has contributed to the destruction of evidence of PBG guidance in the fibres tested. However, another contributor is surface modes, which are discussed later.

7.5 Surface modes

The apparent similarity between the properties of core modes in a hollow core MOF and those of a simple hollow waveguide of the same core diameter can also be explained using the concept of surface modes [West et al., 2004, Saitoh et al., 2004, Digonnet et al., 2004, Kim et al., 2004]. The term refers to modes that are localised to the thin material bridges that encircle the core and comprise the microstructure. This concept emerged in the literature later than the production of the results above. In this model, the dispersion curve (effective index against wavelength) of the fundamental core mode has the underlying trend of the smooth curve of a fundamental mode in a simple hollow waveguide. However, additional features are added by avoided-crossings between the core mode and surface modes. That is, whenever the dispersion curve of the core mode is intersected by that of a surface mode, an avoided crossing takes place that disconnects both curves. Fig. 7.4 illustrates this phenomena graphically and shows features that can be recognised in Fig. 7.3(a) in the wavelength range 700-800 nm. Also, the reader is referred to [West et al., 2004] for a convenient reference.

It is appreciated that surface modes commonly have a convenient avenue for leakage through the microstructure and are relatively lossy. This results in a sharp increase in loss close to the avoided crossing between core and surface modes. Thus *two criteria* are necessary for a very low confinement loss at a given wavelength; not only must the mode be located within the band gap of the microstructure, but also there must be an absence of surface modes with propagation constant close to that of the core mode. For the fibre studied here, the material bridges are thick and support many surface modes. Thus the dispersion curve is afflicted with numerous intersections. The result is high confinement losses at all visible wavelengths, without any significantly wide bands of low loss. Using a reference chart recently published by Mortensen and Nielsen [2004b], one can also infer that the fundamental band gap of the MOF studied here is in the far-infrared (>4 μm) and very narrow ($<3\%$ center wavelength). Thus any band gaps in the visible would be higher order. It is clear from those calculations that much higher air filling fractions ($>90\%$) and a smaller hole pitch (~ 1 μm) are required to achieve a fundamental PBG in the visible.

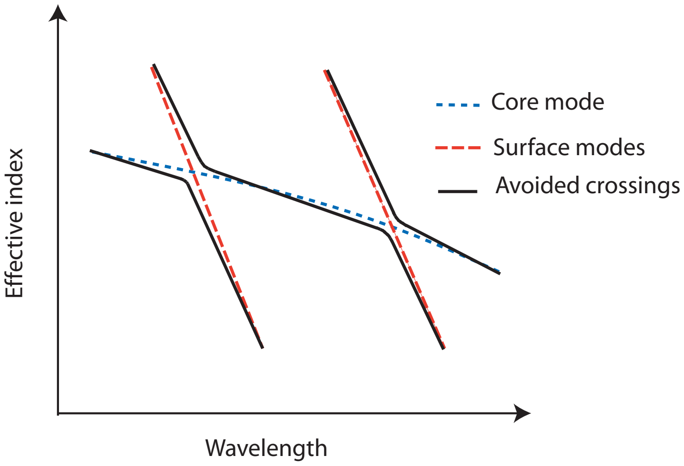

Figure 7.4: Dispersion curve showing avoided crossings between the surface modes (where the intensity is localised to the thin material bridges) and core mode of a simple hollow waveguide. The resulting solid curve represents the dispersion curve of the apparent core mode in a hollow-core MOF. At the avioded crossings, the mode field is closely approximated by a linear superposition of both core and surface modes. A coupled-mode analysis is provided by West et al. [2004].

While surface modes provide a convenient model for the dispersion curve, it contributes little to the understanding of confinement loss. Particularly the key observation reported in this chapter, that the trend in confinement loss also follows that of a simple hollow waveguide, largely uninfluenced by the surrounding microstructure, remains valid.

7.6 Reference charts for air-core waveguides

This section provides useful reference charts in Fig. 7.5 for identifying hollow waveguide type guidance in air-cored MOFs.

Although it is known [Marcatili and Schmeltzer, 1964] that the loss of each mode in a simple hollow waveguide is proportional to λ^2/D^3, the combined losses of all the modes are provided in Fig. 7.5. It shows that a range of λ/D and lengths exist where the guidance of light in the hollow waveguide is dominated by transmission properties of the fundamental mode. In this regime one can then expect the intensity distribution of the transmitted light to appear similar to that of a typical fundamental mode. Such is the case of the MOF considered in Fig. 7.2 (a) with core diameter 17.5μm and length of 1.3cm. While outside this regime the results reveal that the blue colouration is enhanced by considering the loss contributions of higher order modes, as experimentally demonstrated using a core diameter of 48.0μm in Fig. 7.2 (b). Roughly speaking, Fig. 7.5 indicates that in order to confirm PBG guidance in fibres with core diameters smaller than 40μm, a length larger than 50cm is required for the full attenuation (> 40dB) of hollow waveguide modes.

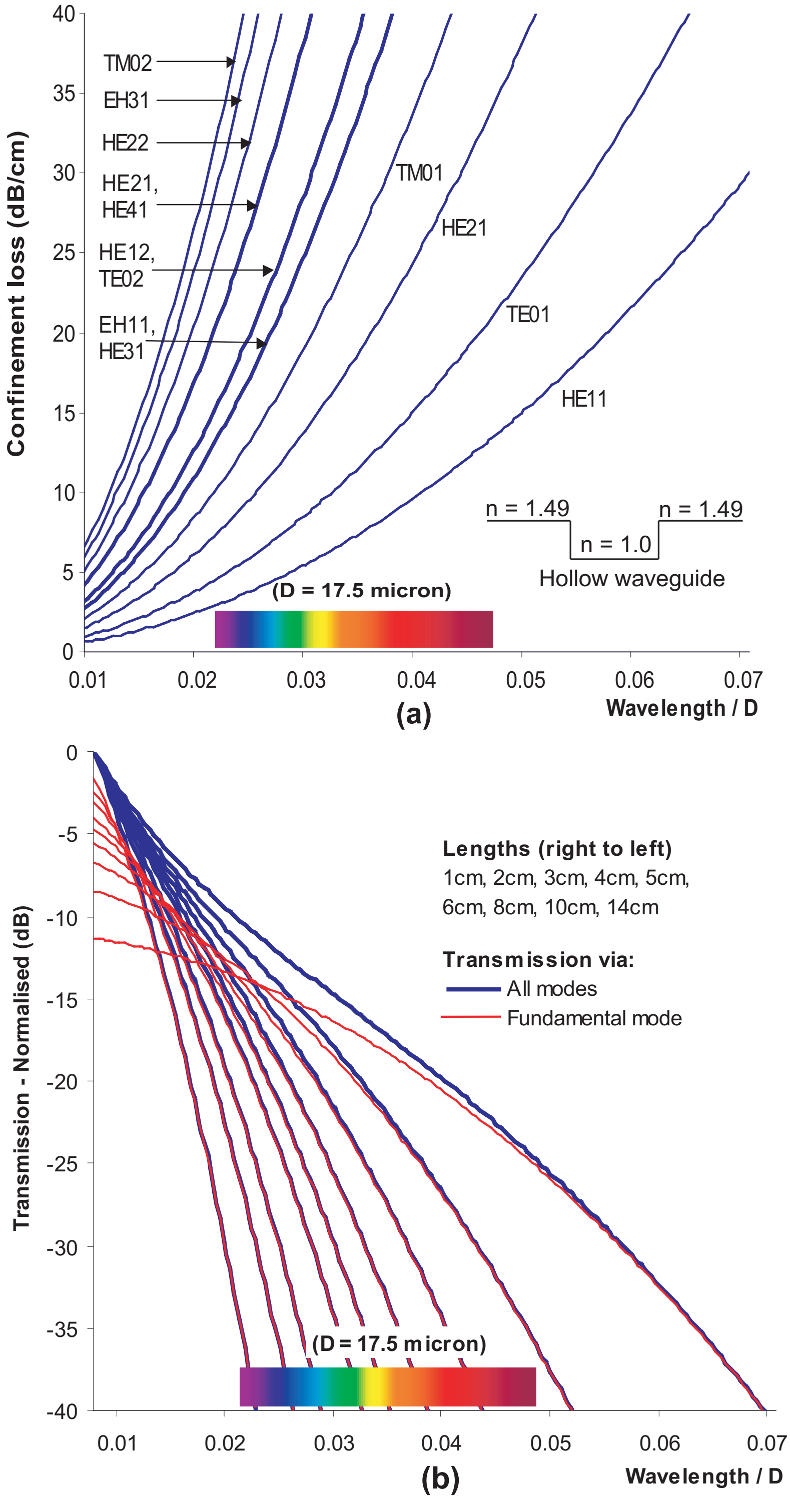

Figure 7.5: Transmission characteristics for hollow waveguides. **(a)** Mode dependent confinement loss of the 13 least lossy leaky modes and **(b)** overall transmission via all leaky modes for various fibre lengths. A colour bar indicates the visible spectrum range for the core diameter ($D = 17.5\mu$m) of the MOF in Fig. 7.1 (a).

Chapter 8

Light collection properties of multimode MOFs

8.1 Introduction

The utility of optical fibres with wide light acceptance angles and high trapping efficiency has a long history in a variety of applications. In recent years they have become increasingly important in such fields as the detection of charged particles and ionizing radiation [Achenbach and Cobb, 2003], multi-object spectroscopy [Mediavilla et al., 1998] and most notably for cladding pumped fibre lasers [Sahu et al., 2001]. Their application in short distance communication has a long history due to their ease of connectivity and high launching efficiency. More recently, however, their usefulness in the interconnection of electronic systems over very short distances is being recognised [Mortensen et al., 2003a].

In order to quantify the capture of light from large area, broad-beam sources, or the trapping of light emissions from within the fibre core, the common definition of numerical aperture (NA, also referred to as nominal NA) for optical fibres is

$$\mathrm{NA} = \sin(\theta_{\mathrm{max}}), \tag{8.1}$$

where θ_{max} is the maximum angle at which a *meridional* ray entering the fibre will be guided. It is measured from the half angle at which the far-field angular intensity distribution has decreased to a standard 5% of its maximum value.

High NA values ranging from 0.37 in doped silica fibre to 0.66 in teflon coated fibres [Feuermann et al., 2002] are not uncommon. Yet, these values can be considerably lower than the NAs achievable in multimode microstructured optical fibres, also called ‘air-clad fibres’. The concept of air-clad optical fibres is an old one [Marcatili, 1973] and has historically provided a valuable alternative for achieving high NAs. They are named so due to the discontinuous jacket of air which provides a large refractive index contrast with the core material. The practical requirement for insensitivity of the fibre to its environment necessitates a solid outer jacket. Numerous fibre designs involving variations on the bridges which support the core in its air cladding have tried to balance fabrication constraints, mechanical stability and optical performance. While the mechanical properties of thick supporting bridges are desirable, these bridges provide core light with an avenue for leakage. In this respect, recent designs of microstructured fibre which possess bridges of sub-wavelength thickness have proven to be a substantial improvement in terms of both quality of fabrication and optical performance. Such fibres, with NAs in the range of 0.6 to 0.9 [Sahu et al., 2001, Wadsworth et al., 2003, Bouwmans et al., 2003a, Furusawa et al., 2001, Limpert et al., 2003] have significantly exceeded the NAs obtainable by conventional alternatives. To our knowledge however, few studies on the dependence of optical performance on bridge thickness and geometry, or fibre length have been conducted. The classes of air-clad fibre that are studied in this chapter are shown in Fig. 8.2 and Fig. 8.8. The NA is determined from an analysis of leaky modes supported by the fibre, providing accurate solutions with a simple physical interpretation.

Conventional multimode fibres have accurately been modelled by the ray method [Achenbach and Cobb, 2003, Feuermann et al., 2002, Potter, 1961]. This method however, is incapable of correctly describing the scattering of light off sub-wavelength features nor optical tunnelling through short evanescent regions (Frustrated Total Internal Reflection - FTIR). A local-plane-wave approach can supplement this method by solving for the reflection matrices of the ‘flattened’ microstructured array. The overall fibre transmission is dictated then by the total number of reflections along the fibre length. While this approach has the merit of simple conceptual understanding, it is no less computationally demanding than the leaky mode approach proposed here. In fact, excellent agreement between these two approaches is shown here for the simplified problem of a continuous air ring of finite radial width w. A disadvantage of the local-plane-wave method is highlighted here by the small disagreement when $w/\lambda \ll 1$, where the number of guided modes in a given length becomes small. In this extreme, the modal nature of the waveguide is not represented by plane wave approximations.

Another method models the radiation of power into free space from the end-face of the fibre. This has been successfully applied to the NA of single mode microstructured fibres [Mortensen et al., 2002], but for multimode fibres knowledge of the final distribution of power amongst the modes is of greatest importance. This requires the calculation of confinement losses. Beam propagation can be used to quantify confinement losses during propagation, however given the large dynamic range of confinement losses, such computations are usually prohibitive.

An alternative, but heuristic estimate of NA can be obtained by a form of local mode coupling. It assumes that core modes efficiently couple to fictitious but transient modes localized in the microstructured bridges (or cladding) when their effective indices match.

Once these bridge modes are excited they quickly propagate power into the outer jacket. The fundamental bridge mode, with effective index $n_{\rm b}$, then provides the cut-off condition for guidance in the core, rather than the cladding index in conventional fibres. The NA is subsequently defined by $\widetilde{\rm NA} = (n_{\rm co}^2 - n_{\rm b}^2)^{1/2}$. This highly simplified technique has been shown to provide an excellent estimate of the experimentally measured NA in fibres by Bouwmans et al. [2003a] and very recently by Wadsworth et al. [2004]. Furthermore, it is shown here to be consistent with present full calculations. Wadsworth et al. make a comparison of this simplified model with the numerical aperture as determined solely by the fictitious cladding-mode in the 'flattened' microstructured cladding. While these simplifications are highly convenient for many structures, they remain heuristic and are limited to fibres which either have an obvious choice for a localised bridge mode or a relatively wide cladding. In addition, they provide no information on the dependence of NA on fibre or bridge length.

8.2 Outline of method

Unlike the truly bound modes of conventional fibres, the propagated power in microstructured and air-clad fibres is often only via leaky modes. Physically, light is confined by the enclosure of air holes and loss arises from power leakage between and through the holes. Leaky modes provide a highly effective description of the propagation process in such waveguides (see section 2.2). They are eigen-solutions of the vector wave equation and are characterised by a complex longitudinal component of the wave vector, $\beta = kn_{\rm eff}$, where $k = 2\pi/\lambda$ and $n_{\rm eff} = n_{\rm eff}^{\rm r} + in_{\rm eff}^{\rm i}$ is the complex mode effective index. Power attenuation due to confinement loss is given simply by $\exp(-2n_{\rm eff}^{\rm i}kL)$, where L is the length of the fibre. Leaky modes are chosen as the analytic tool for this study because they arise naturally from the simplest boundary conditions that can be imposed on the waveguide problem; that no light radiated from the microstructured region is reflected back. In this study the excitation of groups of leaky modes is addressed with a simplified physical approach, however in order to calculate the precise excitation of individual leaky mode fields, a more sophisticated mathematical process is required [Sammut and Snyder, 1976a]. A highly absorbing outer jacket, similar to the coatings used in real optical fibres, may be used in numerical calculations. This may serve the purpose of avoiding the use of leaky modes, potentially at the cost of greatly increasing the computation domain and therefore computational resources. Furthermore, the choice of jacket position and constitution would then require justification and introduce spurious modes into the calculation. It is assumed here that the back reflection from such a jacket is negligible, so that losses are closely approximated by confinement loss, as predicted by the leaky mode solutions.

Within the core, the wave vector of a mode is decomposed into its longitudinal and transverse components [see Fig. 8.1(a)]. Thus an effective index uniquely specifies an

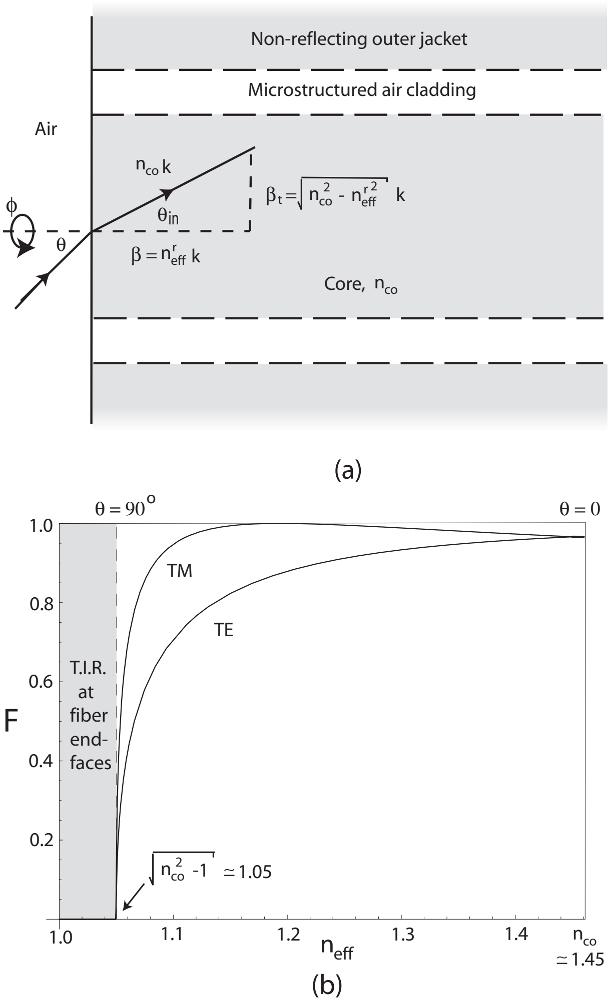

Figure 8.1: (a) Cross section along optical fibre axis. The core refractive index, $n_{\rm co} = 1.45$, is assumed equal to the index of the infinite jacket. Both are lossless. (b) Fresnel reflection at fibre end-faces for TE and TM polarized light. Total internal reflection (TIR) occurs at the fibre end faces when $n_{\rm eff} \leq \sqrt{n_{\rm co}^2 - 1}$ or $\theta_{\rm in} \geq \arcsin(1/n_{\rm co})$.

internal angle, θ_{in}, and the external angle

$$\theta = \sin^{-1}\left(\sqrt{n_{\mathrm{co}}^2 - n_{\mathrm{eff}}^{\mathrm{r}\,2}}\right), \tag{8.2}$$

can be derived using Snell's law. Similarly, the neighbourhood of any external angle, $\theta \pm \Delta\theta/2$, maps to an interval of effective index, $n_{\mathrm{eff}}^{\mathrm{r}}(\theta) \pm \Delta n_{\mathrm{eff}}^{\mathrm{r}}(\theta)/2$, within which a typical fibre will support only a finite number of leaky modes, M.

Now consider a source of area A which is much smaller than the fibre core. When placed close to the fibre end face and centered within the core, such a source is expected to launch only near-meridional rays. The power radiated by the source within a narrow angular range $\theta \pm \Delta\theta/2$ is given by [Potter, 1961] and [Snyder and Love, 1983, Chapers 4 and 20]

$$P(\theta) = A \int_0^{2\pi} \int_{\theta-\Delta\theta/2}^{\theta+\Delta\theta/2} I(\theta')\sin(\theta')d\theta' d\phi \;\simeq\; 2\pi A I(\theta)\sin(\theta)\Delta\theta, \tag{8.3}$$

for both TE and TM polarizations and where $I(\theta)$ is the angular intensity distribution. For a diffuse source which obeys Lambert's (cosine) law, $I(\theta) = I_o\cos(\theta)$. Apart from Fresnel reflections at the end faces, the only remaining source of loss is confinement loss. For this it is assumed that this power is transmitted equally and only via the leaky modes with $n_{\mathrm{eff}}^{\mathrm{r}}$ in the range $n_{\mathrm{eff}}^{\mathrm{r}}(\theta) \pm \Delta n_{\mathrm{eff}}^{\mathrm{r}}(\theta)/2$ determined from Eq. (8.2). Thus, for a normalised source the *far-field* angular transmission, or intensity distribution (power per unit solid angle), upon exiting the fibre becomes

$$\begin{aligned} T(\theta) &\simeq \frac{P(\theta)\left(\frac{F_{\mathrm{TE}}(\theta)+F_{\mathrm{TM}}(\theta)}{2}\right)^2 \alpha(\theta)}{2\pi A\sin(\theta)\Delta\theta} \\ &= I(\theta)\left(\frac{F_{\mathrm{TE}}(\theta)+F_{\mathrm{TM}}(\theta)}{2}\right)^2 \alpha(\theta), \end{aligned} \tag{8.4}$$

where

$$\alpha(\theta) = \frac{1}{M}\sum_{m=1}^{M} \exp(-2\{n_{\mathrm{eff}}^{\mathrm{i}}\}_m kL), \tag{8.5}$$

is the averaged transmission via leaky modes in the range $n_{\mathrm{eff}}^{\mathrm{r}}(\theta) \pm \Delta n_{\mathrm{eff}}^{\mathrm{r}}(\theta)/2$. The terms F_{TE} and F_{TM} account for the angular and polarization dependence of Fresnel reflective losses entering *and* leaving the fibre. Its importance at large angles is obvious from Fig. 8.1(b) as it prevents the NA from being theoretically greater than 1. In fact, when the measured NA is 1, it is possible for an air-clad silica fibre ($n_{\mathrm{co}} \simeq 1.45$) to support modes with $1 < n_{\mathrm{eff}}^{\mathrm{r}} < (n_{\mathrm{co}}^2 - 1)^{1/2} \simeq 1.05$. These modes experience total internal reflection even at the end-faces of the fibre and therefore cannot be excited by external launching. When an application requires the efficient detection of light generated from within the fibre core, it may be important to provide index matching between the fibre end-face and detector to extract the light in these modes.

The simple interpretation of Eq. (8.4) is that far-field transmission for an incident angle is evaluated by averaging the transmission via modes that are excited in a narrow range about that angle. Such averaging is necessary since confinement losses are strongly dependent on the polarization of the mode (or mode class) at large θ_{in}. Recall that the definition of NA is for meridional rays only. In a modal picture, this implies that the only relevant mode class to consider is the TE_{0n}-like and TM_{0n}-like modes, which are only strictly TE or TM for cylindrically symmetric fibres. However, HE_{mn}-like and EH_{mn}-like mode classes have also been included in the analysis of Section 8.3.4 since they play a dominant role in power propagation in real fibre systems, as well as having the property of nearly zero skewness when m is a small integer. That is, $\mid \beta_\phi \mid^2 \ll (n_{\text{co}}k)^2$, where the transverse component of the wave vector is decomposed in polar coordinates $\beta_t^2 = \beta_{\text{r}}^2 + \beta_\phi^2$ [Buck, 1995]. Depending on the numerical method used for the calculation of leaky modes, these mode classes can be selected in different, but straight-forward ways. On the other hand, modes with large skewness behave quite differently. Fortuitously, these modes are generally difficult to launch, partially due to their distance from the fibre center as well as the higher Fresnel reflection they experience at end-faces. The current definition therefore remains useful for practical purposes [Achenbach and Cobb, 2003, Feuermann et al., 2002, Gallawa, 1982], but it is important to note that the inclusion of skew rays will generally increase numerical aperture.

By evaluating Eq. (8.4) at numerous sample angles (or equivalently at sample $n_{\text{eff}}^{\text{r}}$ in the range $1 \leq n_{\text{eff}}^{\text{r}} \leq n_{\text{co}}$) a typical far-field transmission profile like Fig. 8.3 or Fig. 8.5(b) is obtained. These curves are usually quite smooth when using a sufficient number of samples, which allows the 5% transmission angle to be easily determined. The NA is then found using Eqs. (8.1) and (8.2).

8.2.1 Internal sources

Consider an internal source, or one in contact with the end-face of the fibre, with intensity distribution $I(\theta_{\text{in}})$ for each polarization. The source is assumed to be small in comparison to the fibre core and centred so as to excite only near-meridional rays. The transmission within the fibre after a given length L is then

$$T_{\text{in}}(\theta_{\text{in}}) \simeq I(\theta_{\text{in}})\alpha(\theta_{\text{in}}), \tag{8.6}$$

where

$$\alpha(\theta_{\text{in}}) = \frac{1}{M}\sum_{m=1}^{M} \exp(-2\{n_{\text{eff}}^{\text{i}}\}_m kL), \tag{8.7}$$

is the averaged transmission via the M leaky modes in the range $n^{\mathrm{r}}_{\mathrm{eff}}(\theta_{\mathrm{in}}) \pm \Delta n^{\mathrm{r}}_{\mathrm{eff}}/2$ and where $k = 2\pi/\lambda$.

Similarly, the far field intensity distribution in air (power per unit solid angle) for a source internal to the fibre is then given by

$$T(\theta) \simeq \frac{1}{n_{\mathrm{co}}}\frac{d\theta_{\mathrm{in}}}{d\theta} I(\theta_{\mathrm{in}}) \left(\frac{F_{\mathrm{TE}}(\theta) + F_{\mathrm{TM}}(\theta)}{2}\right) \alpha(\theta_{\mathrm{in}}), \tag{8.8}$$

where F_{TE}, F_{TM} are the Fresnel reflection coefficients leaving the fibre and Snell's law relates the internal and external angles by $n_{\mathrm{co}} \sin\theta_{\mathrm{in}} = \sin\theta$. It is straightforward to show that $(d\theta_{\mathrm{in}}/d\theta) I(\theta_{\mathrm{in}})/n_{\mathrm{co}} = I(\theta)/n^2_{\mathrm{co}}$ for a Lambertian source.

While the transmission distributions of many fibres are simply such that the NA provides a good measure of light acceptance, the transmission distributions of more complicated fibres are not. The fibres with multiple layers presented below are an example, as they may display more than one sharp feature in transmission. In such situations a more representative measure of light acceptance is the capture efficiency.

Capture efficiency

The meridional capture efficiency ϵ is defined as the fraction of emitted photons in forward propagation that remain after a length L. It is given by

$$\epsilon = \frac{1}{P_o} \int\limits_{\phi=0}^{2\pi} \int\limits_{\theta_{\mathrm{in}}=0}^{\pi/2} T_{\mathrm{in}}(\theta_{\mathrm{in}}) \sin(\theta_{\mathrm{in}}) d\theta_{\mathrm{in}} d\phi, \tag{8.9}$$

where $P_o = 2\pi I_o$ for an isotropic source ($I(\theta_{\mathrm{in}}) \equiv I_o$) or $P_o = \pi I_o$ for a Lambertian source ($I(\theta_{\mathrm{in}}) = I_o \cos\theta_{\mathrm{in}}$). Clearly the capture efficiency is a length dependent quantity. If the materials comprising the waveguide are assumed lossless, then ϵ provides an estimate for the aggregate confinement loss in a multimode fibre for a specified length.

An approximate and simple relation can be obtained between capture efficiency and NA for an internal source, if the attenuation due to Fresnel reflection leaving the fibre is neglected. Under the simplifying assumption that internal transmission obeys a unit-step-function U which is independent of polarization, ie. $T_{\mathrm{in}}(\theta_{\mathrm{in}}) \simeq I(\theta_{\mathrm{in}}) U(\theta_{\mathrm{in}} - \theta^{\mathrm{max}}_{\mathrm{in}})$, one can easily show using Eq. (8.9) that

$$\mathrm{NA_L} \simeq n_{\mathrm{co}} \sqrt{\epsilon_{\mathrm{L}}}, \tag{8.10}$$

$$\mathrm{NA_i} \simeq n_{\mathrm{co}} \sqrt{\epsilon_{\mathrm{i}}(2 - \epsilon_{\mathrm{i}})}, \tag{8.11}$$

for Lambtertian and isotropic sources respectively. Since any attenuation due to Fresnel reflection has been omitted, these expressions are only valid for NA $\lesssim 1$. It is important to emphasise that the capture efficiency is sensitive to the choice of angular intensity distribution of the source, while NA is usually not, particularly when the fibre transmission function has a distinct cut-off analogous to a step function. This allows us to approximately relate the capture efficiency from these two sources by the useful expression

$$\epsilon_{\mathrm{L}} \sim \epsilon_{\mathrm{i}}(2-\epsilon_{\mathrm{i}}). \tag{8.12}$$

8.3 Single layer structures

The class of structures investigated here is shown schematically in Fig 8.2. The key dimensions are defined in the caption.

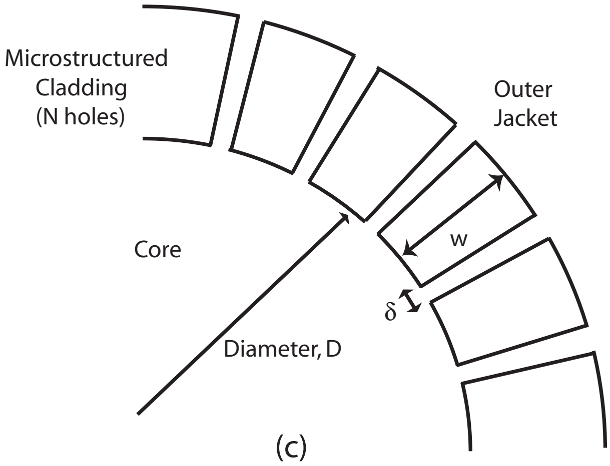

Figure 8.2: Schematic of air-clad fibre geometry studied here. There are N holes separated by bridges of thickness δ and length w. The core diameter D is measured up to the beginning of the bridges.

8.3.1 Implementation

The Adjustable Boundary Condition (ABC) method was used for the calculation of leaky modes in this chapter. The unique treatment of boundary conditions in this method correctly determines the outward radiating fields of leaky modes without difficult (sometimes manual) searches in the complex n_{eff} plane. This high degree of automation, robustness and versatility was crucial to the sampling of over 80,000 modes for section 8.3. The radial finite difference implementation (see Chapter 4) was used here due to its superior performance. The typical resolution of a calculation involves 4000 radial nodes and $10 \times N$ azimuthal Fourier components, where N is the number of bridges and symmetry of the waveguide. The waveguide symmetry is fully exploited to improve computational speed by including only Fourier components that are multiples of N. Thus the computational domain effectively looks like a *very* thin slice of pie.

Thus, over 1600 near-meridional modes were found in the interval $1.0 \leq n^{\mathrm{r}}_{\mathrm{eff}} \leq 1.45$ in order to generate the far-field transmission curve. They were equally sampled from TE_{0n}, TM_{0n}, $\mathrm{HE/EH}_{1n}$, $\mathrm{HE/EH}_{2n}$ and $\mathrm{HE/EH}_{3n}$ -like mode classes, using the labels of section 2.1.2. Note that the last three are doubly-degenerate. Additional near-skew mode classes have been shown to negligibly influence the proceeding results. Fixed fibre parameters were: core diameter $D = D_{\mathrm{o}} = 150\mu\mathrm{m}$, $n_{\mathrm{co}} = 1.45$ and $\lambda = 1.0\mu\mathrm{m}$. An advantage of this method is that from the modal solutions of a given fibre geometry, the length dependence of numerical aperture can be found without further computation. It is emphasised that the number of meridional modes is a small fraction of the total modes. Here $I(\theta) \equiv 1$ is assumed for an isotropic or rotated *external source.* While it may overestimate the transmission at large angle in some practical situations, the choice is clearly dependent on the system under consideration. However, its influence on the calculated NA has been tracked and found to be not substantial. Therefore, this intensity distribution was adopted to emphasize the influence of other physical factors in the far-field transmission. The major source of inaccuracy in the far field transmissions, such as Figs. 8.3 and 8.5, is in fact the size of the interval $\Delta n^{\mathrm{r}}_{\mathrm{eff}}(\theta)$ used and the discrete number of modes sampled within. The latter consideration is due to the strong polarization dependence of confinement loss. This error typically translates to less than ±2% in the calculated NA.

The calculation of each far-field transmission curve required approximately 50 hours on a AMD 64bit-Opteron 1.6GHz processor. Using several processors, the data required for the graph of Fig. 8.7 was generated within one week, since 18 different bridge thicknesses and 3 different values for N were used. The raw data of confinement losses was processed into far-field transmissions and NAs in a fully automated way using a Mathematica code of the equations given in Section 8.2.

8.3.2 Dependence of numerical aperture

When considering microstructured fibres with complex geometries, it is prudent to firstly consider the variables on which NA depends. In comparison to the wavelength dependence of the refractive index in the host material, the refractive index contrast with air is very large. This permits a highly profitable simplification due to wavelength-scale equivalence [Sakoda, 2001]. Without further assumptions, a functional form for a mode effective index is $n_{\mathrm{eff}}(D/\lambda, w/\lambda, \delta/\lambda, N)$, where D is the core diameter, w is the radial width of the hole, δ is the bridge thickness and N is the number of bridges. Highly multimode fibres generally lie in the extreme of $D/\lambda \gg 1$, where the NA is intuitively weakly dependent on this variable. This was checked and allows this variable to be dropped. However, the appearance of L/λ in Eq. (8.5) presents an additional variable, which can be equally represented by the more traditional term L/D. It is proportional to the total number of reflections experienced by a meridional ray. Therefore, the functional form of numerical aperture becomes simply NA$(L/D, w/\lambda, \delta/\lambda, N)$. This smaller parameter space is now explored in two different regimes of operation, which give insight into the design of high NA fibres.

8.3.3 An upper bound on numerical aperture

Firstly, the idealised case of a cylindrically symmetric core surrounded by a continuous air ring ($\delta \to 0$, $N = 0$) of radial extent, w, is considered. Here optical tunnelling (FTIR) is the only loss mechanism, so the purpose of this investigation is two-fold. Not only is it instructive of the workings and accuracy of the method in comparison to an alternative method, but it also provides an upper bound on the NA achievable in any air-clad fibre whose microstructured cladding is contained within an annulus of width w.

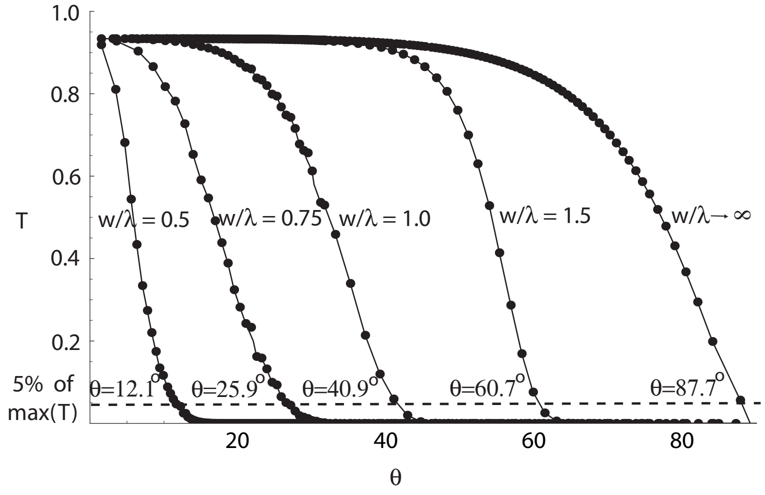

Figure 8.3: Typical far-field transmission calculation for a core surrounded by a continuous air ring. $L = 10$ m.

Typical transmission distributions of the leaky mode method are shown in Fig.8.3. As $w/\lambda \to \infty$ the shape of the transmission curve is dominated by the Fresnel reflections entering and leaving the fibre. For $w/\lambda \lesssim 2$ confinement loss dominates the shape of the far-field transmission and the curves slope gently.

A reference chart for the NA in such fibres is given in Fig. 8.4. Solutions of the local-plane-wave approach are compared with the leaky mode method. The angular dependence of the plane wave reflection coefficients in the former method can be found in standard textbooks [Hecht, 1998]. It shows good agreement mostly for large numerical apertures, where the fibre is highly multimode. An important attribute of the NA in these fibres is the strong length dependence, particularly when $w/\lambda \simeq 1$. The upper bounds on NA it provides are valuable for choosing the radial width of air-clad designs. It suggests that when $w/\lambda > 4$ the role of optical tunnelling in influencing the NA can be neglected for all practical lengths.

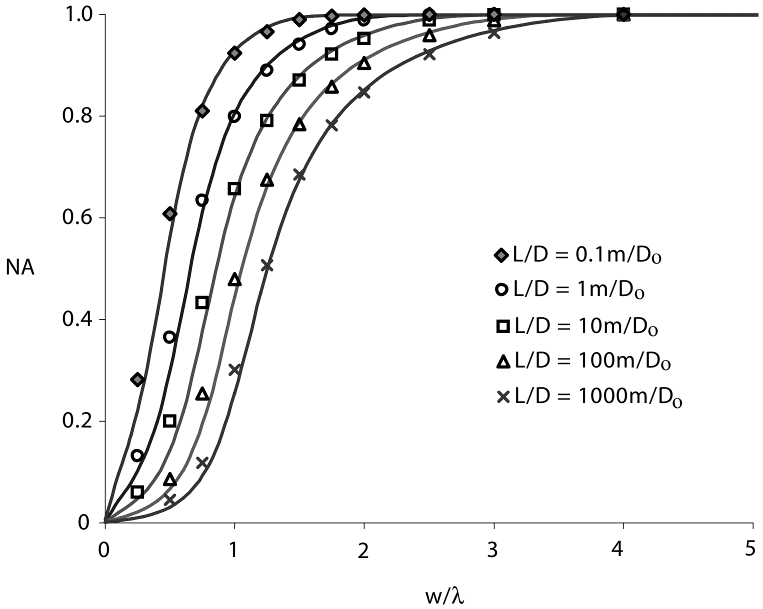

Figure 8.4: Numerical aperture of a circular core with continuous air ring of radial width w. Results are obtained by a leaky mode analysis (points) and the local-plane-wave approach (solid lines). Both show strong length dependence.

8.3.4 Dependence on bridge thickness, number of bridges and fibre length

The fibre with bridged cladding is considered here. In order to separate the leakage mechanisms of loss via the bridges from that of optical tunnelling, the extreme situation of $w/\lambda \gg 1$ is assumed. Referring to Fig. 8.4, a choice of $w/\lambda = 8$ is more than adequate for this purpose.

The important loss characteristics for different mode classes in these fibres are shown in the example of Fig. 8.5(a). It shows two well-defined knees in confinement loss, which are not present in the case of a continuous air ring. The TM-like mode class, as well as the HE and EH-like mode classes, display a knee which coincides with the effective index of the fundamental mode $n_{\mathrm{b}}^{\mathrm{TE}}$ of a slab waveguide of equivalent thickness to the bridges. It is highest solution to the following equation [Snyder and Love, 1983, pp. 243]

$$W = U \tan(U), \tag{8.13}$$

where $W = k\delta\sqrt{(n_{\mathrm{b}}^{\mathrm{TE}})^2 - n_{\mathrm{holes}}^2}$ and $U = k\delta\sqrt{n_{\mathrm{co}}^2 - (n_{\mathrm{b}}^{\mathrm{TE}})^2}$. The slab waveguide representing a bridge is assumed to be oriented radially outward to the fibre. In that sense, the fundamental mode is TE with respect to this orientation. Similarly, the loss curve for the TE-like mode class shows a knee which coincides with the effective index of the second mode of the slab waveguide $n_{\rm b}^{\rm TM}$, which is TM with respect to slab orientation. This value is the highest solution to this alternative equation [Snyder and Love, 1983, pp. 243]

$$W = \frac{n_{\rm holes}^2}{n_{\rm co}^2} U \tan(U), \tag{8.14}$$

where $W = k\delta\sqrt{(n_{\rm b}^{\rm TM})^2 - n_{\rm holes}^2}$ and $U = k\delta\sqrt{n_{\rm co}^2 - (n_{\rm b}^{\rm TM})^2}$. The explanation for this behaviour is revealed by considering the local polarizations at the entrance of the bridge; TM-like core modes couple preferentially to TE bridge modes because the polarizations are locally parallel. Similarly for TE-like core modes and TM bridge modes. Evidently, cross coupling between orthogonal polarizations is greatly suppressed. HE and EH-like core modes on the other hand, are hybrid and couple efficiently into both bridge modes, yet their loss curve closely follows that of the TM-like core modes.

The direction of power propagation in bridge modes can, in general, have radial and longitudinal components. In the limit of $w/\lambda \to \infty$ a continuum of these modes exist with effective indices (proportional to the longitudinal component of the wave vector) in the range between 1 and $n_{\rm b}^{\rm TE}$. The effective index $n_{\rm b}^{\rm TE}$ is therefore an upper bound for all such localised bridge modes that have a radial component to power propagation. These are expected to rapidly channel power out of core modes with $n_{\rm eff}^{\rm r} < n_{\rm b}^{\rm TE}$ and prevent significant transmission beyond the critical angle dictated by this inequality.

A typical far-field transmission profile is shown in Fig. 8.5(b). Indicated on the curve is the 5% of maximum transmission point, which is taken after the first sharp drop. Partial transmission after this point is solely due to modes of the TE-like class that continue to possess low confinement loss at angles just beyond this transition. However, since the TE-like modes constitute a small fraction of the total modes, they make a negligible contribution to transmission as more mode classes are included. The choice of 5% transmission at the first sharp drop is therefore justified.

To investigate the evolution of the leaky mode solutions in the neighbourhood of this transition, four locations were chosen and the mode intensities are plotted in Fig. 8.6. The plots confirm that the transitions in loss seen in Fig. 8.5(a) signal the efficient launching of power into local bridge modes. Strong coupling between TM-like core modes and the TE bridge mode is seen while TE-like core modes remain well confined until a TM bridge mode is supported. Often the difference in loss between TE and TM-like core modes can be orders of magnitude for nearly equal $n_{\rm eff}^{\rm r}$. This effect disappears for thicker bridges which support many closely spaced TE and TM modes.

Finally a chart showing the dependence of numerical aperture on bridge thickness and fibre length is given in Fig. 8.7. It shows that NA is strongly dependent on bridge

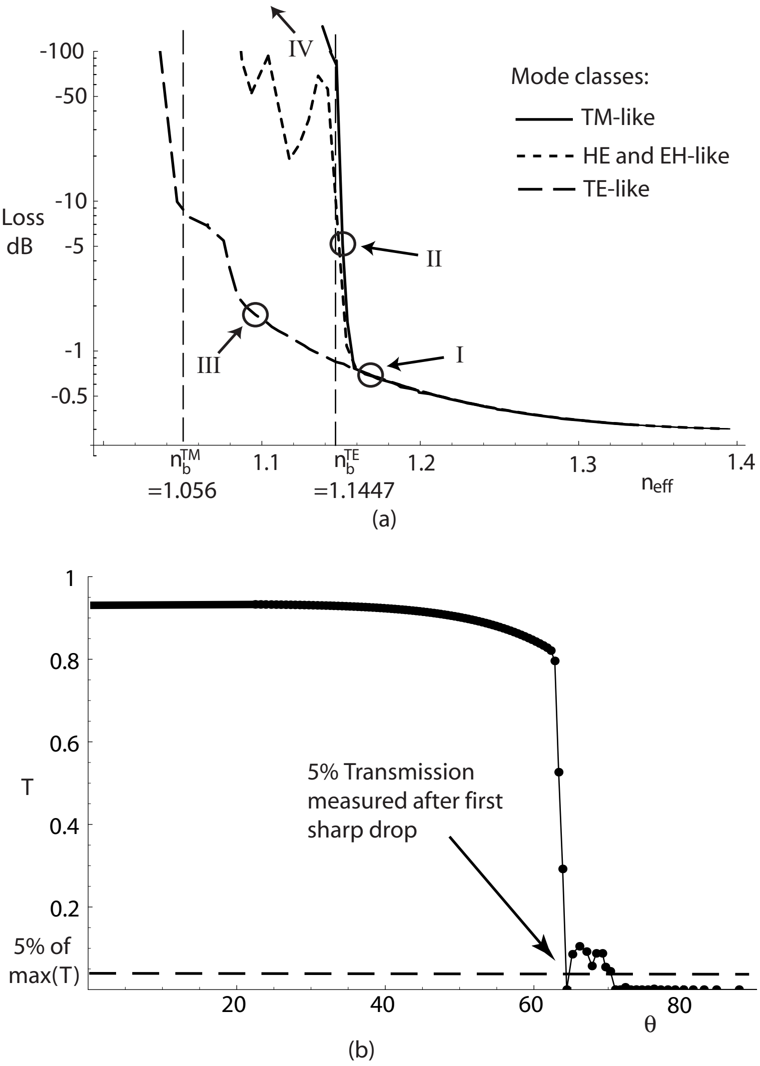

Figure 8.5: Example far field transmission for bridged air-clad fibre. $\delta/\lambda = 0.2$, $N = 75$, $w/\lambda = 8$ and $L/D = 10\text{m}/D_\text{o}$. (a) Shows the total loss, $-10\log[T(\theta)]$, as a function of n_eff for three mode classes. n_b^TE is the effective index of the fundamental bridge mode, calculated for the equivalent slab waveguide of thickness 0.2. It is a TE mode with respect to the orientation of the slab. n_b^TM is the effective index of the second bridge mode, which is a TM mode with respect to the orientation of the slab. (b) Shows a typical far field transmission curve. Partial transmission after the first sharp drop is due to low loss TE-like modes and is neglected when measuring the 5% level.

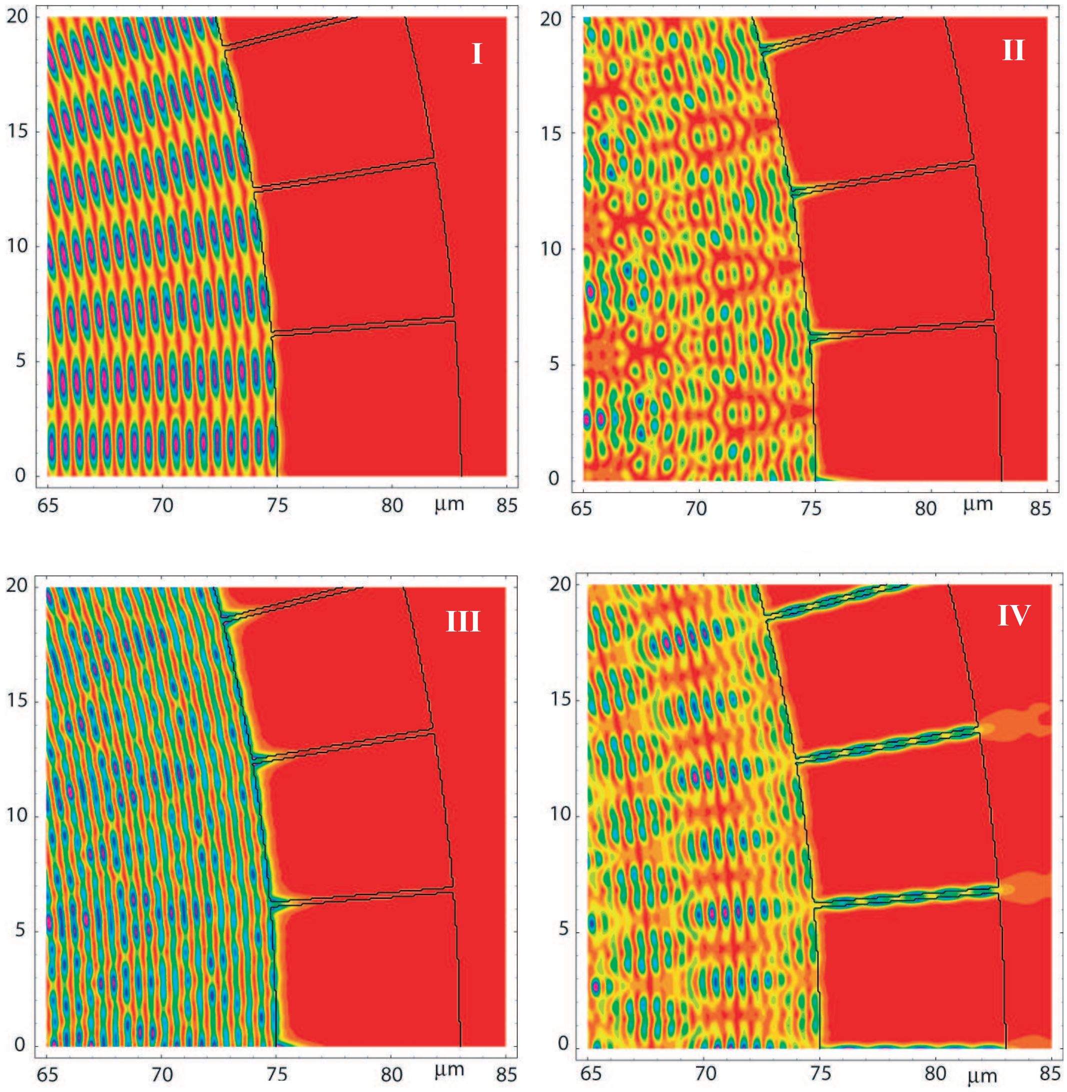

Figure 8.6: Example intensity plots of sample core modes in regions I ($n_{\rm eff}^{\rm r} \simeq 1.175 > n_{\rm b}^{\rm TE}$ TM-like mode), II ($n_{\rm eff}^{\rm r} \simeq 1.1412 \simeq n_{\rm b}^{\rm TE}$ TM-like mode), III ($n_{\rm eff}^{\rm r} \simeq 1.1 < n_{\rm b}^{\rm TE}$ TE-like mode) and IV ($n_{\rm eff}^{\rm r} \simeq 1.1 < n_{\rm b}^{\rm TE}$ TM-like mode).

thickness and that $\delta/\lambda \ll 1$ is required for NAs close to 1. On the other hand, the length dependence is very weak for all practical lengths and only becomes significant for small NA. The number of bridges also proved to be a weak dependence. For N =50, 75 and 100 the calculated NA differed by less than a few percent for all lengths. Both these findings are consistent with the qualitative observation of a very sharp increase in confinement loss at a particular angle. Also plotted is the heuristic expression $\widetilde{\mathrm{NA}} = (n_{\mathrm{co}}^2 - n_{\mathrm{b}}^{\mathrm{TE}\ 2})^{1/2}$, obtained from the fundamental bridge mode. As expected, it provides a close upper bound on the calculated NA. The asymptotic for of this expression for when $V = k\delta\sqrt{n_{\mathrm{co}}^2 - n_{\mathrm{holes}}^2} \gg 1$ is [Snyder and Love, 1983, pp. 243]

$$\mathrm{NA} \simeq \frac{\pi}{2}\frac{1}{\mathrm{k}\delta}(1 - \frac{1}{\mathrm{V}+1}). \tag{8.15}$$

8.3.5 Comparison with published measurements

Most importantly, the published results of NA measurements on similar fibres are compared. The fibre presented by Bouwmans et al. [Bouwmans et al., 2003a] is the closest in geometry and shows excellent agreement with calculations. The fibres of Wadsworth et al. [Wadsworth et al., 2003, 2004] and Limpert et al. [Limpert et al., 2003] (fibres 1 and 2) differ slightly in that they also contain microstructure in the core and have a hexagonally shaped cladding. Nevertheless, the agreement is good to fair, which suggests the results may be applicable to a wider class of fibre geometries.

A measurable length dependence of NA has been reported. When values are given, the quoted range of measured NA is indicated in Fig. 8.7 with a vertical bar. However, the magnitude of NA variation with length exceeds numerical predictions. This is likely due to the inevitable launching of skew rays which will generally increase the measured NA for short lengths of fibre but quickly degrade to the meridional NA. The rapid loss of skew rays is due to the relatively larger number of reflections experienced along their helical path. Alternatively, coupling between modes as a result of fibre non-uniformities and surface scattering is another contributing factor. The influence of such effects is beyond the scope of this chapter and has been so far neglected. Measurement error is another important factor in determining the significance of such discrepancies. Sources of error may include fibre non-uniformity, improper launching and inaccuracy in the measurement of bridge thickness or NA. These errors have so far not been discussed or quantified in the literature.

8.4 Multiple layer structures

Here it is demonstrated that the simplistic use of the most fundamental cladding or bridge mode will generally underestimate the NA of fibres with multiple layers. A more suitable expression is hence sought. The class of structures investigated here is shown schematically

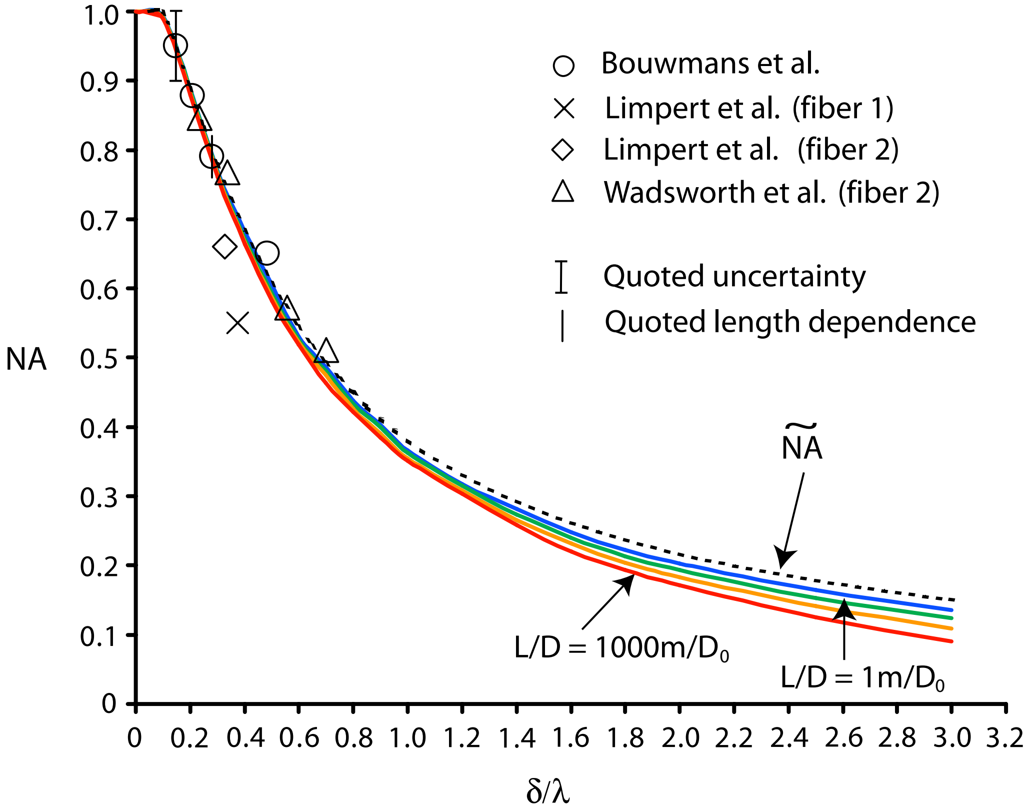

Figure 8.7: Full calculation of NA and comparison with measured values. The vertical bar through experimental data indicate the range of measured values for different fibre lengths (when quoted). Shown are $L/D = 1\mathrm{m}/D_\mathrm{o}$, $10\mathrm{m}/D_\mathrm{o}$, $100\mathrm{m}/D_\mathrm{o}$ and $1000\mathrm{m}/D_\mathrm{o}$ for $w/\lambda = 8$. Calculations for $N = 50$, 75 and 100 are nearly indistinguishable. The $\widetilde{\mathrm{NA}} = \sqrt{n_\mathrm{co}^2 - n_\mathrm{b}^{\mathrm{TE}\ 2}}$ curve is obtained from the fundamental bridge mode.

in Fig 8.8. The key dimensions are defined in the caption. All bridges are of equal thickness.

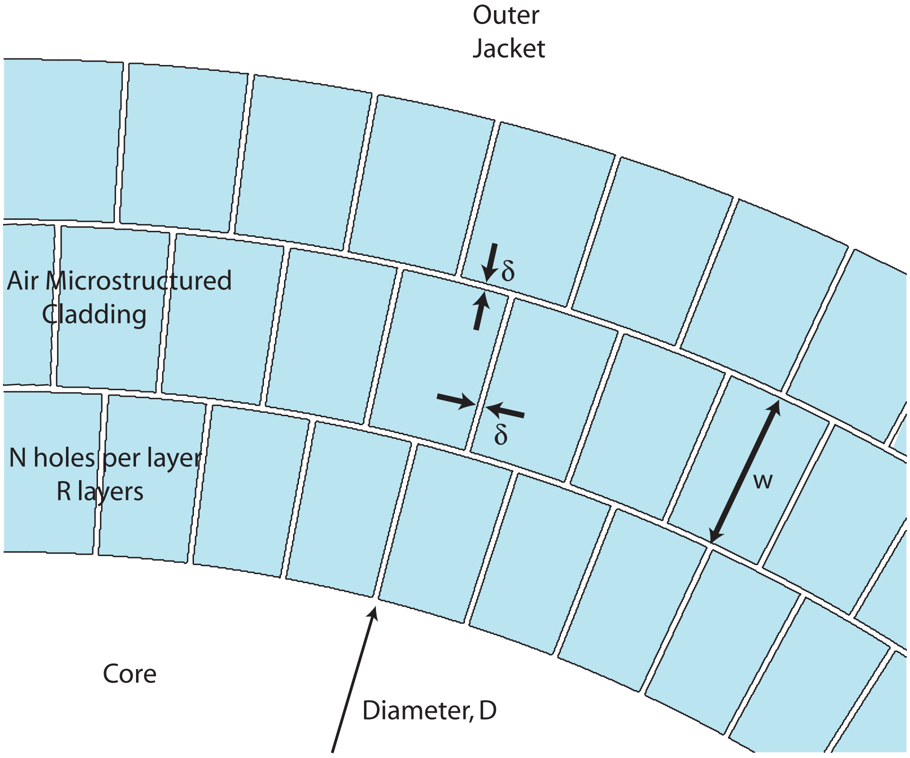

Figure 8.8: Schematic illustrating the class of air-clad fibre geometry studied here. All bridges have equal thickness δ and width w. N denotes the number of bridges in each layer while R denotes the number of layers.

8.4.1 Implementation

The fixed parameters for calculations were: core diameter $D = D_o = 150\mu$m, core refractive index $n_{co} = 1.45$ and $\lambda = 1.0\mu$m. Furthermore, an *internal isotropic source* $I(\theta_{in}) \equiv 1$ is assumed for all subsequent calculations of far field transmission and capture efficiency. Note that an external isotropic source was used for the calculations in Section 8.3.

The radial and angular resolutions employed up to 4000 radial nodes and $20 \times N$ azimuthal Fourier components respectively, where N denotes the number of bridges in each layer. For each fibre structure the angular transmissions of Eq. (8.7) were obtained from 1600 near-meridional leaky modes in the interval $1.0 \leq n^{r}_{\mathrm{eff}} \leq 1.45$. They were equally sampled from TE_{0n}, TM_{0n}, $\mathrm{HE/EH}_{1n}$, $\mathrm{HE/EH}_{2n}$ and $\mathrm{HE/EH}_{3n}$ like mode classes (see section 2.1.2), where the last three are doubly degenerate. All are meridional or near-meridional as is required for the calculation of NA. It is important to note that the HE and EH mode classes play a dominant role in power propagation in real fibre systems and must be included in the analysis for realistic results, as in Section 8.3.

In this section the calculation of each far-field transmission curve required approximately 160 hours on a AMD 64bit-Opteron 1.6GHz processor. The generation of all subsequent graphs required such a calculation for 204 different fibres. Using the supercomputing facilities at the Australian Centre of Advanced Computing and Communication (AC3), the calculations were distributed and managed between 40 and 130 processors, completing the results within 2 weeks. Once again, the raw data of confinement losses was processed into far-field transmissions, NAs and capture efficiencies in a fully automated way using a Mathematica code.

8.4.2 Dependence of capture efficiency and numerical aperture

The microstructured fibres considered here possess a substantial number of independent parameters that specify a particular fibre. In order to reduce the parameter space under consideration while still providing a systematic study, it has already been prescribed that all bridge thicknesses and widths are equal. Since the refractive index contrast between the host material and air is very large in comparison to its wavelength dependence, wavelength-scale equivalence [Sakoda, 2001] is assumed, which results in this most general dependence of capture efficiency $\epsilon(L/D, D/\lambda, w/\lambda, \delta/\lambda, N, R)$. This parameter space is reduced by first noting that these multimode fibres necessarily lie in the extreme of $D/\lambda \gg 1$, where ϵ is weakly dependent on this variable. In addition it has been shown that values of N between 50 and 100 provide no discernable change in the calculated NA in single layer fibres (see Section 8.3). This has been checked and confirmed for the multiple layer structures presented here, and so $N = 100$ is fixed for all calculations. Finally, in order to discount the influence of confinement loss due to frustrated total internal reflection (optical tunnelling) the condition that $w/\lambda \gg 1$ is enforced on the air holes. Our choice of $w/\lambda = 8$ is more than adequate for this purpose at all practical lengths and wavelengths (see Section 8.3). Thus the dependence of capture efficiency is reduced to $\epsilon(L/D, \delta/\lambda, R)$. By identical arguments, the dependence of numerical aperture is also $\mathrm{NA}(L/D, \delta/\lambda, R)$. This parameter space in explored in the following sections.

8.4.3 Heuristic expressions

It is rewarding to firstly investigate the typical characteristics of confinement loss in these fibres and determine their physical origins. The aim is to derive simple heuristic expressions for capture efficiency and NA that can be directly compared with full numerical simulation.

It has previously been shown that the condition for high confinement loss in a single layer fibre is $n_{\mathrm{eff}}^{\mathrm{r}} \lesssim n_{\mathrm{b}}^{\mathrm{TE}}$, where $n_{\mathrm{b}}^{\mathrm{TE}}$ is the effective index of the fundamental TE mode in a slab waveguide of equivalent thickness to the bridge (see Section 8.3 and [Wadsworth et al., 2004]). It is referred to as the TE local bridge mode, or just TE bridge mode for convenience, but such modes are not actual modes of the waveguide. The dispersion relations for these modes are available in many standard texts [Snyder and Love, 1983, Chapter 12]. When satisfying this inequality, core light can efficiently couple to at least this local bridge mode, which quickly radiates power into the outer jacket, depending on the radial component of propagation in the bridge. This leads to one heuristic expression for numerical aperture

$$\mathrm{NA}_{\mathrm{b}}^{\mathrm{TE}} = \sqrt{n_{\mathrm{co}}^2 - n_{\mathrm{b}}^{\mathrm{TE}\ 2}}, \tag{8.16}$$

which has been proven to accurately estimate the NA of single layer structures. Using Eq. (8.11), the capture efficiency for an isotropic source can be estimated by

$$\epsilon_{\mathrm{b}}^{\mathrm{TE}} = 1 - \frac{n_{\mathrm{b}}^{\mathrm{TE}}}{n_{\mathrm{co}}}, \tag{8.17}$$

which is also suitable for single layer fibres.

Our attention so far has focused solely on the most fundamental local mode of the bridge, which is TE with respect to the slab orientation. Consider now the second mode supported by a slab waveguide, which is TM with respect to the slab orientation and has an effective index denoted by $n_{\mathrm{b}}^{\mathrm{TM}}$. It has been shown that it is only the TE-like core modes that do not strongly couple power into the TE bridge modes, since their polarizations are largely orthogonal. Only when the condition $n_{\mathrm{eff}}^{\mathrm{r}} \lesssim n_{\mathrm{b}}^{\mathrm{TM}}$ was satisfied did the confinement loss of TE-like core modes sharply increase. However, since the TE-like mode class constitute a small fraction of the power carrying modes, the influence of this TM bridge mode on the NA was shown to be insignificant for single layer fibres. In stark contrast, this mode plays a very important role in determining both NA and capture efficiency of multiple layer fibres. In anticipation an alternative expression is defined for the heuristic NA and capture efficiency similar to Eqs. (8.16) and (8.17)

$$\begin{aligned} \mathrm{NA}_{\mathrm{b}}^{\mathrm{TM}} &= \sqrt{n_{\mathrm{co}}^2 - n_{\mathrm{b}}^{\mathrm{TM}\ 2}}, && (8.18) \\ \epsilon_{\mathrm{b}}^{\mathrm{TM}} &= 1 - \frac{n_{\mathrm{b}}^{\mathrm{TM}}}{n_{\mathrm{co}}}. && (8.19) \end{aligned}$$

8.4.4 Numerical aperture and capture efficiency

The usefulness of these expressions are first evident in Fig. 8.9, which shows how typical far-field angular transmission distributions, Eq. (8.8), behave as additional layers are added to the fibre. Transmission in the window $\theta_{\mathrm{b}}^{\mathrm{TE}} < \theta < \theta_{\mathrm{b}}^{\mathrm{TM}}$ is greatly enhanced by the use of 3 or 4 rings, for which a new sharp cut-off is formed at the new angle determined by the TM bridge mode.

A deeper insight is gained from Figs. 8.10 and 8.11, which illustrate the evolution of loss for the four major mode classes. In the range $n_{\mathrm{eff}}^{\mathrm{r}} > n_{\mathrm{b}}^{\mathrm{TE}}$, the bridges support no

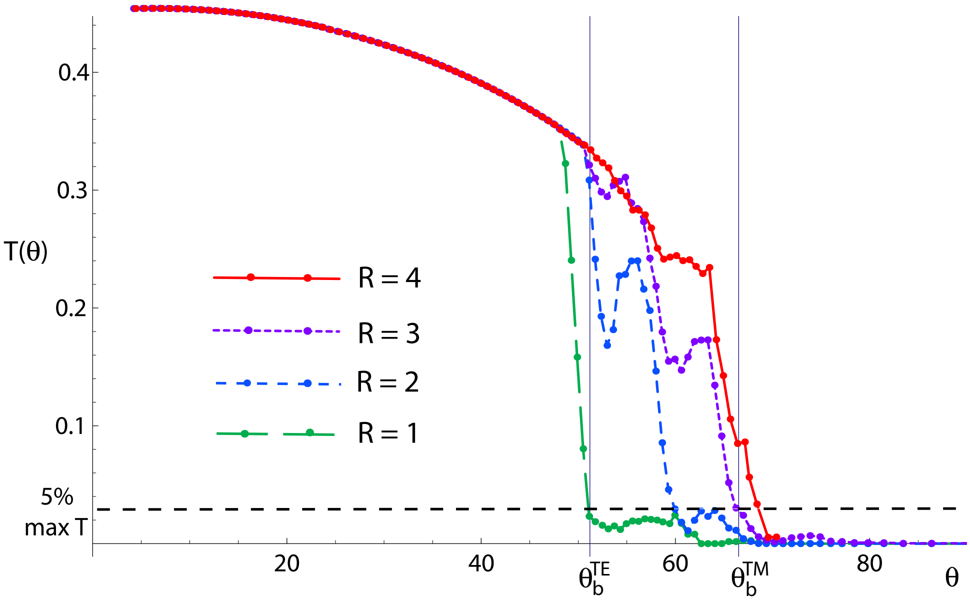

Figure 8.9: Example external angular transmission distribution used to determine NA, showing dependence on the number of rings. Increasing the number of rings results in a shift in the transition from near $\theta_\mathrm{b}^\mathrm{TE}$ to near $\theta_\mathrm{b}^\mathrm{TM}$, where $\theta_\mathrm{b}^\mathrm{TE/TM} = \sin^{-1}(\mathrm{NA}_\mathrm{b}^\mathrm{TE/TM})$. The values $\delta/\lambda = 0.3$, $N = 100$, $w/\lambda = 8$ and $L/D = 20\mathrm{m}/D_\mathrm{o}$ were used in the calculation.

modes and core light is tightly confined regardless of polarization. This is demonstrated in Fig. 8.11 I and II. As previously discussed for $n_\mathrm{eff}^\mathrm{r} < n_\mathrm{b}^\mathrm{TE}$, the behaviour of light at the first layer of bridges has a simple explanation; TM-like core modes preferentially couple light into the TE bridge mode when it is supported by the bridge, since their polarizations are largely parallel. As do HE and EH modes, since their hybrid nature allows relatively efficient coupling between core and bridge modes regardless of polarization. TE-like core modes, do not couple efficiently to the fundamental TE bridge mode, but do couple to the TM bridge mode. However, in a multiple layer cladding, the radial bridges terminate at a 90 degree 'T' intersection of bridges of equal thickness. At these intersections the orientation of the TE and TM polarizations swap with the orientation of the bridge.

In the window $n_\mathrm{b}^\mathrm{TM} < n_\mathrm{eff}^\mathrm{r} < n_\mathrm{b}^\mathrm{TE}$ core light may only couple to a TE mode in the radial bridges which are incapable of efficiently coupling to a TE mode in the azimuthal bridges since their polarizations are largely orthogonal. This is clearly demonstrated in Fig. 8.11 III and IV, where the cladding penetration of the TE and TM-like core modes is different, but their losses are relatively close. In fact, TM-like core modes are found to abruptly terminate at the end of the first radial bridges. As the number of layers and the number of intersections traversed by light escaping to the outer jacket increases, the total loss reduces for all mode classes that are capable of coupling to the TE bridge mode at the first layer.

For $n_{\text{eff}}^{\text{r}} \lesssim n_{\text{b}}^{\text{TM}}$ a new knee in the loss curve is formed for all mode classes. In this range, power is coupled into both TE and TM modes at the first radial bridges. At each subsequent intersection, TE or TM modes in radial bridges are then able to preferentially couple to TM or TE modes respectively in the azimuthal bridges. Thus core light of all mode classes can penetrate deep into the microstructured cladding and radiate power to the outer jacket. This is also clearly shown in Fig. 8.11 V and VI, where due to the full penetration of light throughout the cladding the losses of TE and TM-like core modes become extreme.

A number of sharp peaks and minor transitions are visible in both these loss curves. They have been attributed to various resonances associated with the bridges such as the choice of w/λ or N. Specifically one can match most of these minor features, such as that at $n_{\text{eff}}^{\text{r}} \simeq 1.16$, with radial (standing wave) resonances in the bridges. They typically occur at $n_{\text{eff}}^{\text{r}} = n_{\text{b}}^{\text{TE/TM}} - (p/4)\lambda/w$, for $p = 1, 2, 3....$ Further analysis is complex, without providing additional value to the present analysis.

What has so far been revealed about the physical processes, suggests that while Eqs. (8.16) and (8.17) are applicable for single layer fibres, Eqs. (8.18) and (8.19) are more appropriate for multiple layered fibres. These expressions are directly compared against full numerical calculations for a wide range of δ/λ in Figs. 8.12 and 8.13. They serve as a convenient reference for a common practical fibre length and are expected to show robust agreement with a variety of air-clad fibre designs. The charts show that both NA and ϵ are well approximated by $\text{NA}_{\text{b}}^{\text{TE}}$ and $\epsilon_{\text{b}}^{\text{TE}}$ for single layer fibres, but become increasingly better represented by $\text{NA}_{\text{b}}^{\text{TM}}$ and $\epsilon_{\text{b}}^{\text{TM}}$ as more layers are added. The heuristic expressions for NA reach a maximum value of $(n_{\text{co}}^2 - 1)^{1/2}$, which is an un-physical result caused by neglecting the Fresnel reflections upon leaving the fibre to air. The insets display the potential improvement that can be achieved through the addition of multiple layers. They are simply estimations obtained from the heuristic models, but predict significant improvements in both the NA and the capture efficiency, reaching a maximum of $\sim 20\%$ and $\sim 50\%$ respectively. It is important for practical purposes to note that for high NAs or capture efficiencies exceeding 0.9 or 0.25 respectively, the addition of multiple layers allows one to more than double the bridge thickness and sill maintain this high performance.

8.4.5 Aggregate confinement loss

Finally Fig. 8.14 illustrates the dependence of capture efficiency on fibre length L/D, number of layers and bridge thickness δ/λ. The results are presented in terms of relative capture efficiency

$$\Delta\epsilon = \epsilon - \epsilon_{\text{b}}^{\text{TE}}, \tag{8.20}$$

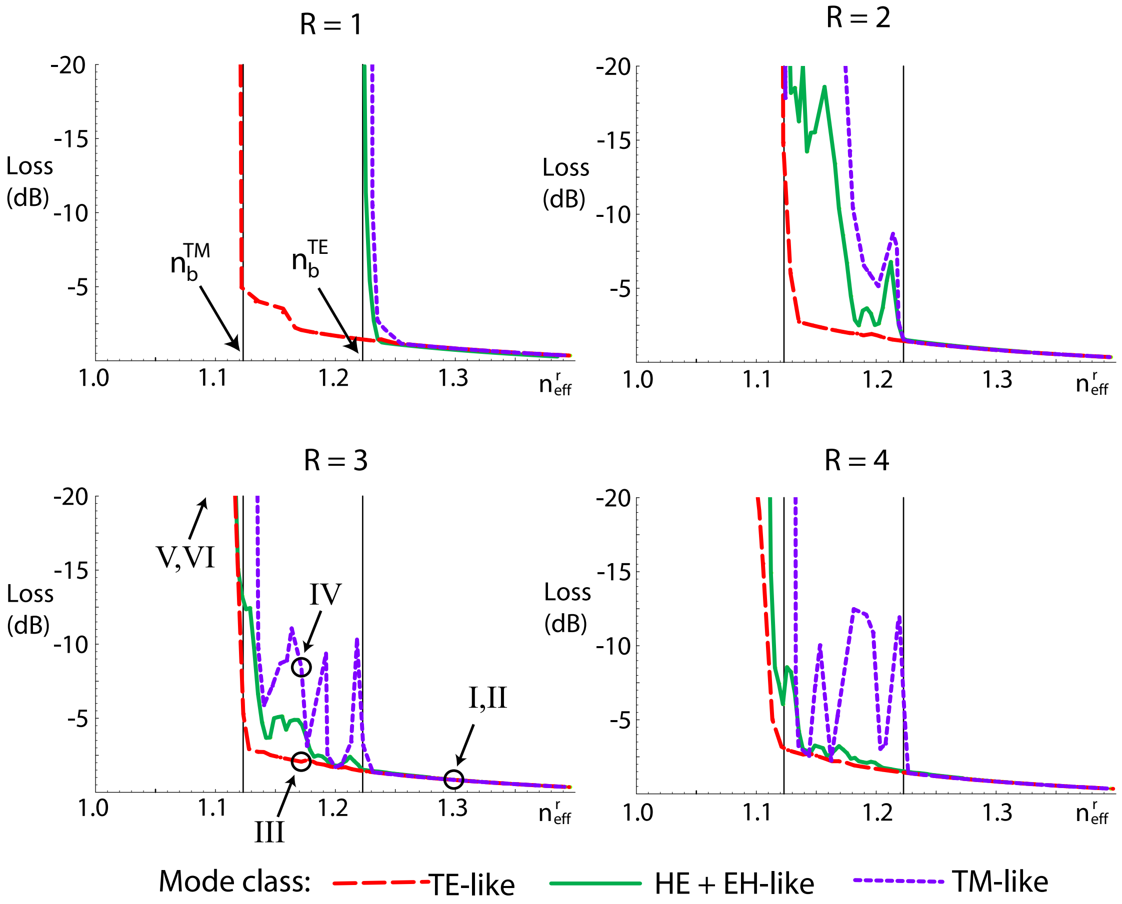

Figure 8.10: Total loss, $-10\log[T(\theta)]$, for three mode classes clearly showing a shift in the loss knee for TE and HE + EH mode classes as the number of rings is increased. The vertical lines indicate n_b^TE and n_b^TM, which are the effective indices of the TE fundamental and TM second order bridge modes. They are calculated for the equivalent slab waveguide of thickness 0.3 and the polarizations are prescribed with respect to the orientation of radial bridges. The values $\delta/\lambda = 0.3$, $N = 100$, $w/\lambda = 8$ and $L/D = 20\mathrm{m}/D_\mathrm{o}$ were used in the calculation.

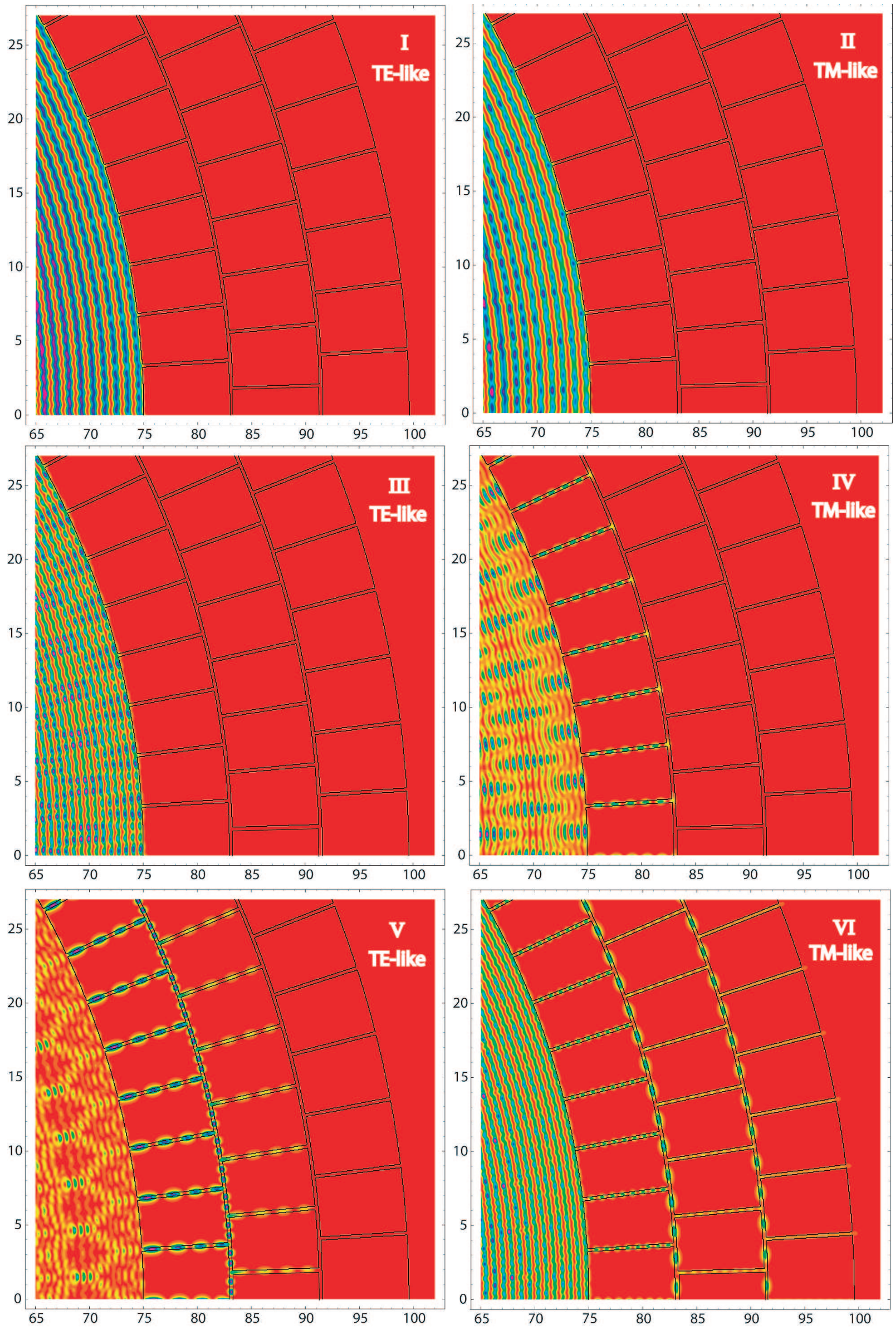

Figure 8.11: Example intensity plots of sample TE and TM-like modes in regions I, II ($n^{\mathrm{r}}_{\mathrm{eff}} \simeq 1.3 > n_{\mathrm{b}}^{\mathrm{TE}}$), III, IV ($n^{\mathrm{r}}_{\mathrm{eff}} \simeq 1.172$ between $n_{\mathrm{b}}^{\mathrm{TE}}$ and $n_{\mathrm{b}}^{\mathrm{TM}}$), and V, VI ($n^{\mathrm{r}}_{\mathrm{eff}} \simeq 1.104 < n_{\mathrm{b}}^{\mathrm{TM}}$). The extent of light penetration is shown to correlate with confinement loss which is similarly strongly polarization dependent.

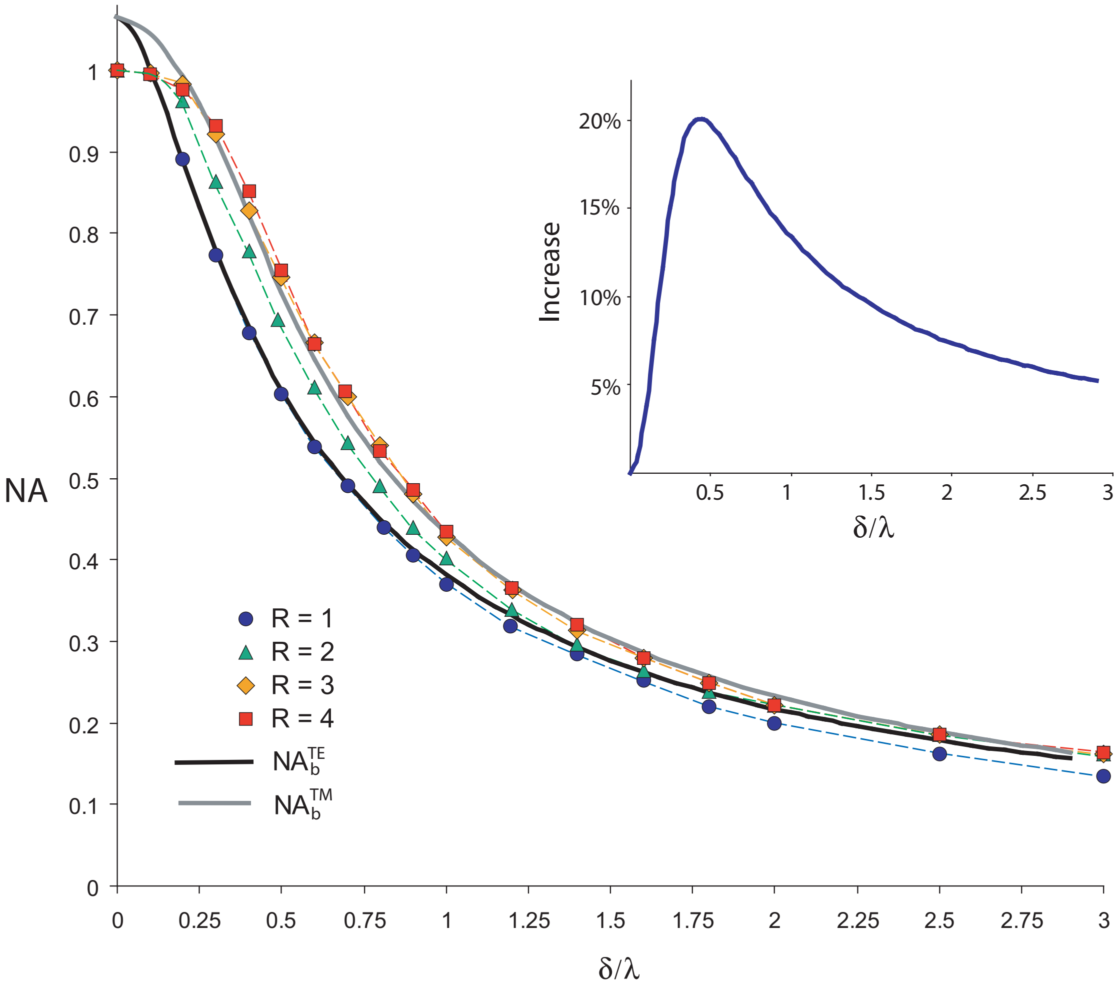

Figure 8.12: Numerical aperture as a function of δ/λ and number of layers, full numerical results (data points) are compared to the heuristic estimates. Largely independent of source intensity distribution and weakly length dependent. $L/D = 10\text{m}/\text{D}_\text{o}$. *Inset*: Percentage increase in NA by adding multiple layers, $100 \times (\text{NA}_\text{b}^\text{TM} - \text{NA}_\text{b}^\text{TE})/\text{NA}_\text{b}^\text{TE}$.

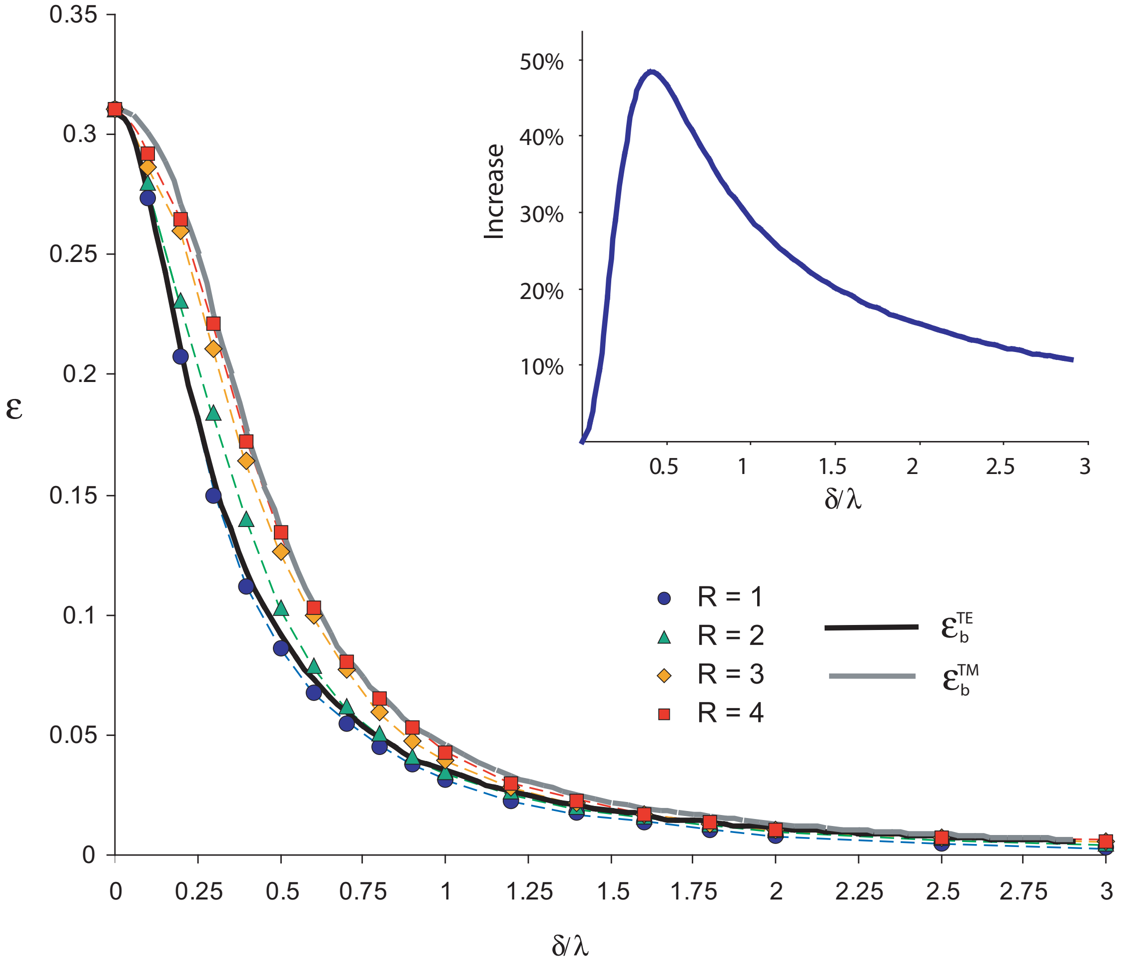

Figure 8.13: Capture efficiency as a function of δ/λ and number of layers for an isotropic source. $L/D = 10\mathrm{m/D_o}$. *Inset*: Percentage increase in capture efficiency by adding multiple layers, $100 \times (\epsilon_b^{TM} - \epsilon_b^{TE})/\epsilon_b^{TE}$.

in order to simplify the illustration. The small scale ripples in the curves are due to numerical error as well as actual fibre properties associated with radial and azimuthal bridge resonances. Evidently, the addition of multiple layers results in the trend $\epsilon \to \epsilon_b^{TM}$.

The aggregate confinement loss for an isotropic source in these fibres can be directly determined from Fig. 8.14. To estimate the fraction of power at a length L_1 which is lost during propagation between lengths L_1 and L_2, one would simply use $|\Delta\epsilon(L_2/D) - \Delta\epsilon(L_1/D)|/\epsilon(L_1/D)$.

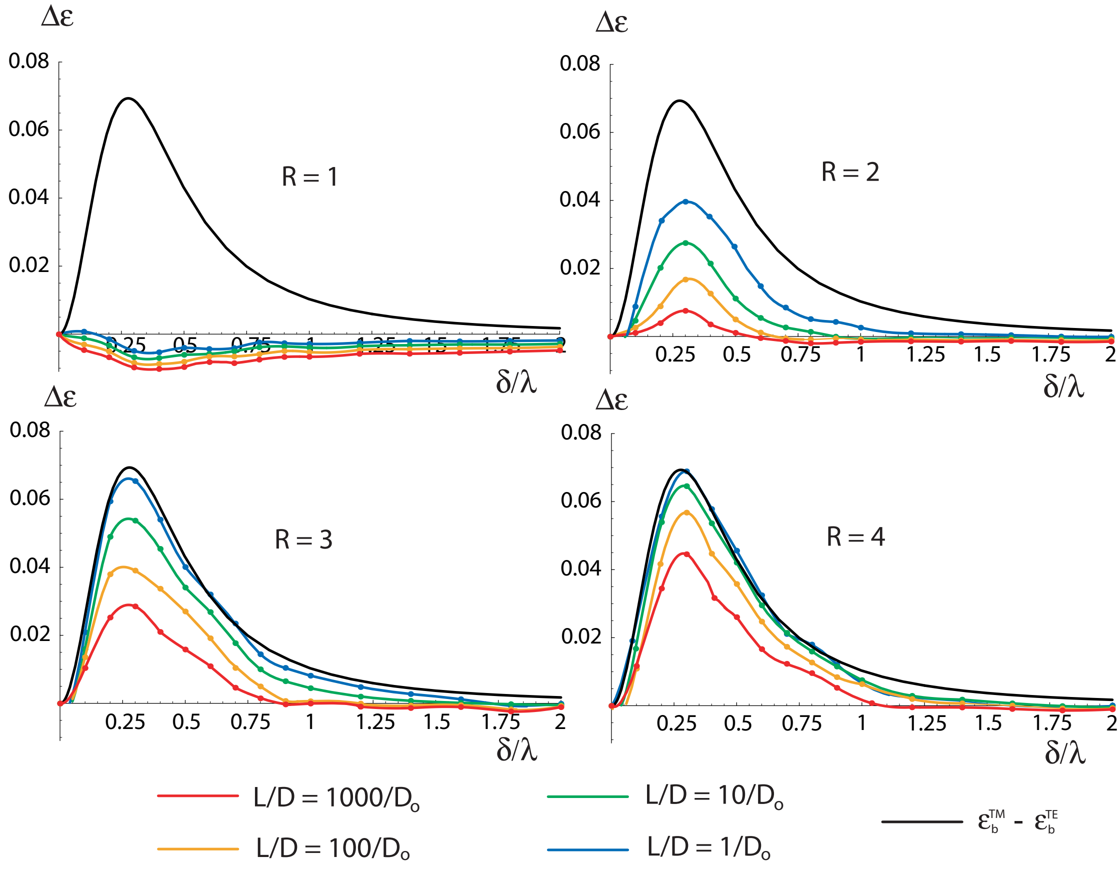

Figure 8.14: Relative capture efficiency as a function of δ/λ, L/D and number of rings.

8.4.6 Impact of variation in bridge thickness

In this section the usefulness of the physical insight gained thus far is demonstrated by applying it to the situation of a multiple layer structure where the radial and azimuthal bridges are unequal. The four effective indices of interest are $n_{\text{b radial}}^{\text{TE}}$, $n_{\text{b radial}}^{\text{TM}}$, $n_{\text{b azimuthal}}^{\text{TE}}$ and $n_{\text{b azimuthal}}^{\text{TM}}$ for the TE and TM modes found in the radial and azimuthal bridges. In the scenario where the azimuthal bridges are thicker than the radial bridges, it can be easily verified that $n_{\text{b radial}}^{\text{TE}} < n_{\text{b azimuthal}}^{\text{TE}}$ and $n_{\text{b radial}}^{\text{TM}} < n_{\text{b azimuthal}}^{\text{TM}}$. In a similar manner to the previous section, core light is able to penetrate to the outer jacket by coupling to the TE modes in the radial bridges and the TM modes in the azimuthal bridges. Thus $n^{\mathrm{TM}}_{\mathrm{b\ azimuthal}}$ is the cut-off index in this scenario, except when $n^{\mathrm{TE}}_{\mathrm{b\ radial}} < n^{\mathrm{TM}}_{\mathrm{b\ azimuthal}}$, where the cut-off index is then given by $n^{\mathrm{TE}}_{\mathrm{b\ radial}}$. In the alternative scenario where the azimuthal bridges are thinner than the radial bridges, the inequalities $n^{\mathrm{TE}}_{\mathrm{b\ radial}} > n^{\mathrm{TE}}_{\mathrm{b\ azimuthal}}$ and $n^{\mathrm{TM}}_{\mathrm{b\ radial}} > n^{\mathrm{TM}}_{\mathrm{b\ azimuthal}}$ are true. Here core light can escape to the outer jacket by coupling between TM modes in the radial bridges and TE modes in the azimuthal bridges. Therefore in this scenario $n^{\mathrm{TM}}_{\mathrm{b\ radial}}$ is the cut-off index, except when $n^{\mathrm{TM}}_{\mathrm{b\ radial}} > n^{\mathrm{TE}}_{\mathrm{b\ azimuthal}}$, where the cut-off index is then given by $n^{\mathrm{TE}}_{\mathrm{b\ azimuthal}}$. The numerical apertures and capture efficiencies can then be approximated from the cut-off indices using either Eqs. (8.16) and (8.17) or Eqs. (8.18) and (8.19).

8.5 Fabrication and characterization of high numerical aperture polymer MOFs

The purpose of this section is to demonstrate for the first time a high numerical aperture multimode mPOF and make comparisons with numerical calculations. Thus three Microstructured Polymer Optical Fibres (mPOF) were fabricated using a two stage draw process with sleeving [van Eijkelenborg et al., 2003]. The three fibres were drawn from the same initial preform to different outer diameters. Thus their geometry was nearly identical, apart from scale. The bridge thicknesses in the inner layer of these three fibres were $\delta = 0.66$ μm, $\delta = 0.99$ μm and $\delta = 1.59$ μm, which have been numbered in that order. The bridge thickness is measured from the thinnest portion of the bridge. When the bridge length is long and the length of the thinnest portion, l, satisfies the condition $l/\lambda > 4$ (as discussed in Section 8.3.3), then the use of this measure of thickness to compare with numerical calculations is justifiable. This condition is nearly satisfied for the fibre samples used.

The pictures of fibre 2 are shown in Fig. 8.15, which are similar to those of fibres 1 and 3. The satellite holes seen beyond the two layers of holes are due to imperfect sleeving before the second fibre draw.

Measurements of the NA were taken for the three fibres by launching white light with a 60× (NA = 0.8) microscope objective and recording the far field transmission for many wavelengths in the range of 450nm to 850nm. This was achieved with a multimode silica fibre connected to an OSA, which was swept in an arc about the end-face of the microstructured fibre in increments of 1 degree. Thus the solid angle of detection remained constant for all angles and wavelengths. The measured NA is shown in Fig. 8.16 and compared with numerical simulation. Sources of measurement error (as indicated by the size of the data points) include fibre non-uniformity and inaccuracy in the measurement of bridge thickness or angle.

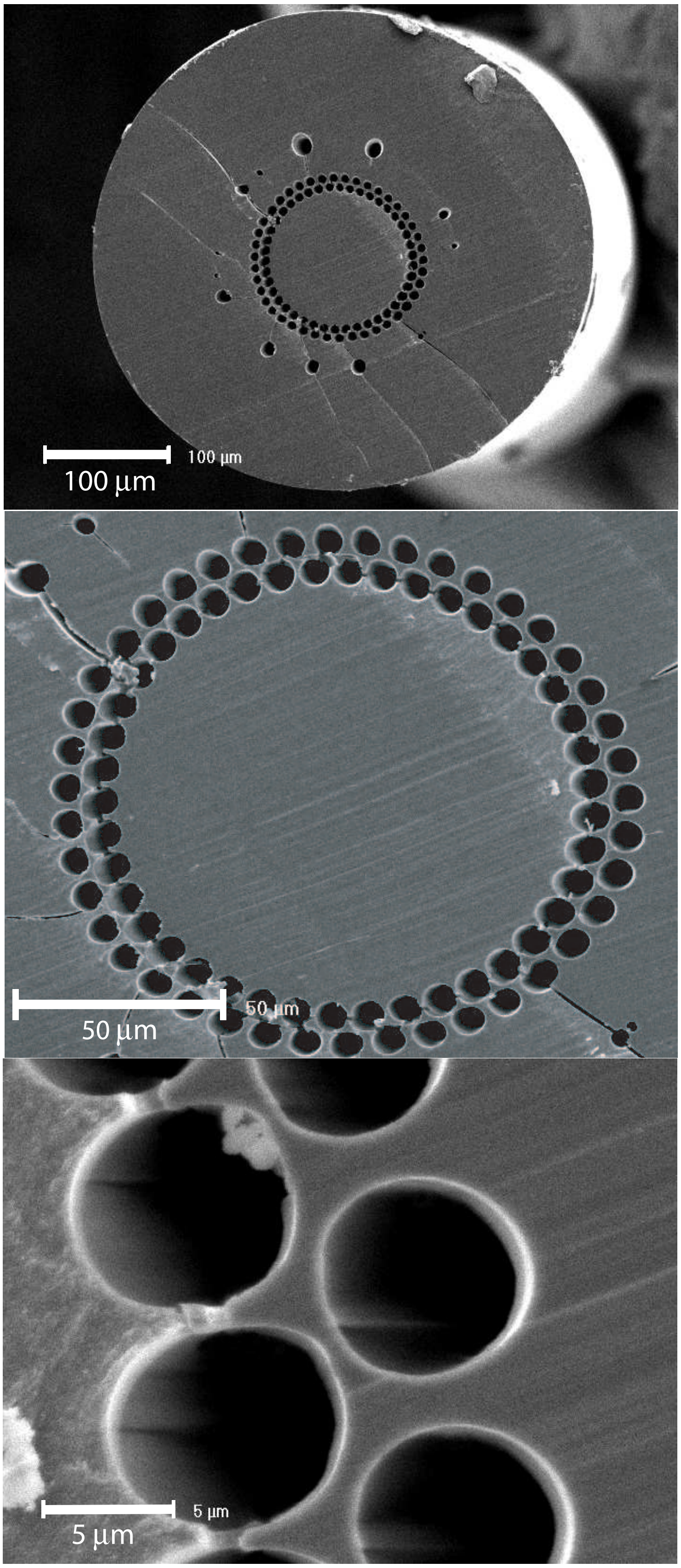

Figure 8.15: Scanning electron microscope images of fibre 2.

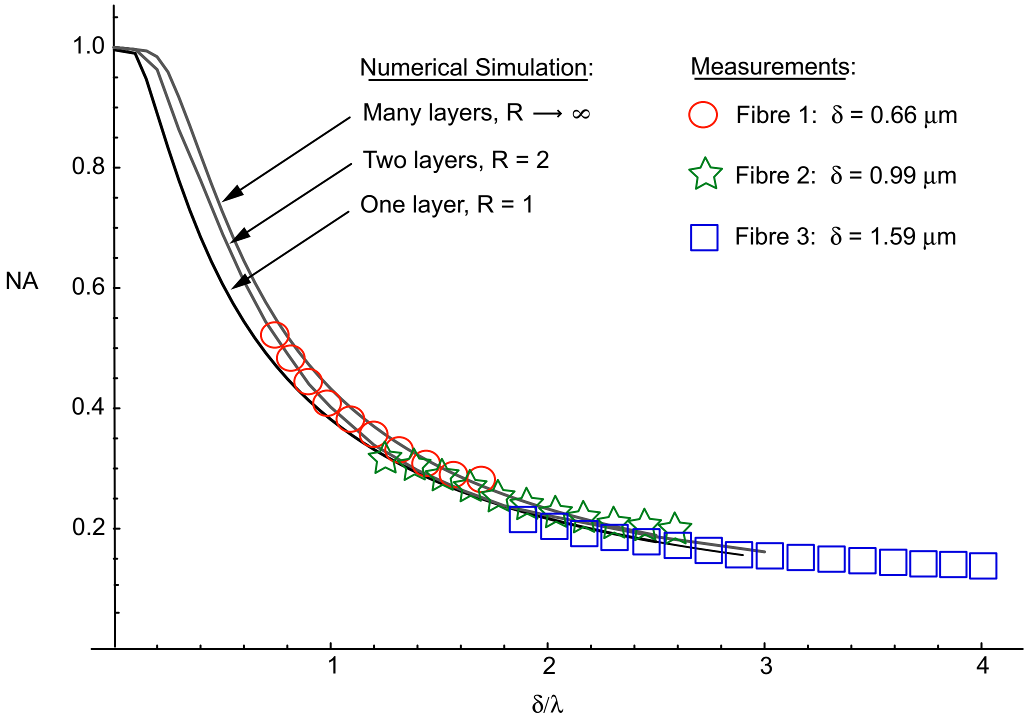

Figure 8.16: Comparison of the numerically simulated and measured numerical aperture. The size of the symbols used in this figure are representative of errors.

While the measurement error is not small enough to discriminate clear agreement with either the single layer or two-layer numerical results, the overall agreement is very good over a wide parameter range. Further support is thus given for the accuracy of our numerical approach.

Summation and Conclusions

A combination of analytical and numerical tools have been developed, then effectively applied to the study of modes and propagation in MOFs of contemporary interest. The analysis reveals some of the physical processes governing light propagation in MOFs and demonstrates the potential usefulness of these tools in this growing field.

Part I began with the history of MOF technology, which motivates the study of the fibre's optical properties. The review highlighted the recent and rapid development in fabrication capability as well as discussed key experimental milestones which illustrate the unique properties of MOFs. The development of polymer MOFs is placed in context, a technology which this author has contributed to and used for part III of this thesis. The future potential for polymer MOFs to meet the demands of diverse functionality and performance is discussed. Chapters 2 and 3 introduced some analytic tools that aid in the understanding and classification of modal properties in MOFs. Some notable findings include the following: In chapter 2 the use of the Bloch-Floquet theorem enables a reduction of the minimum waveguide sector to $2\pi/n$ rad of the waveguide and a relationship between confinement loss and the modal fields was discussed. In chapter 3 it was shown that the local polarization of non-degenerate lossless modes in straight fibres must be everywhere linearly polarized. This precludes the possibility of achieving circular birefringence through the tailoring of geometry in straight MOFs when confinement loss is low. However, a calculation based on local mode coupling is used to provide the full vector fields in a spun fibre, where circular birefringence is possible. A simple example is also provided. Each of these analytic tools help to describe the physical and mathematical properties of modes in general MOFs. Some have a great impact on improving the efficiency of numerical calculations, while others aid in fibre design.

A fully vectorial algorithm for modelling leaky modes in microstructured optical fibres was presented in Part II. At the time of development, the algorithm was distinct from available algorithms in that it is capable of exactly calculating the leaky modes of fibres with arbitrary structure. This provides a valuable numerical tool for studying modal properties of MOFs which also possess confinement loss. It uses a novel refinement scheme, called the ABC method, by which the boundary conditions are sequentially adjusted to correctly determine the outward radiating fields external to the computational domain. Thus transparent boundary conditions are achieved without approximation. A key advantage of this refinement scheme is that it eliminates the need for artificial boundary conditions or the need to perform mode searches in the complex n_{eff} plane, which are often difficulties associated with current leaky mode algorithms. It is simple to implement, efficient, robust and automated. Furthermore, it is broadly applicable to many mode solvers, which makes it a worthwhile alternative to current methods of treating open waveguide problems.

Two implementations of the ABC method were presented in chapter 4. One was based on a two-dimensional polar Fourier decomposition, while the other used a hybrid scheme composed of an azimuthal Fourier decomposition and radial finite differences. The latter implementation proved to be several thousand times more efficient in terms of computational speed and several hundred times more efficient in terms of memory requirement. Numerical examples were given to highlight the key features of the algorithm for both structures already studied in the literature and structures previously not modelled. They show polarization effects associated with elliptical hole shapes, such as birefringence and polarization dependent confinement loss. A comparison of the two implementations was also presented. A comparison with a finite element implementation of the ABC method would be valuable future study.

Chapter 5 gives a detailed study of the behavioural properties of the ABC method, which is in fact a solution method for a non-linear eigenvalue problem. The convergence properties are predicted theoretically and in an original manner. These predictions were then shown to compare very well with the actual numerical behaviour. It was found that convergence was guaranteed when the majority of mode power is contained within the computational domain, that the decay in error is always exponential and that convergence is usually very rapid. This knowledge allows a user to more effectively use the ABC method and appreciate its limitations. It also encourages wider acceptance of the method.

Part III contains more than just applications of the numerical tools presented in the previous chapters. Numerical calculations are presented alongside experimental demonstrations using polymer MOFs. Each of the three chapters concentrates on different phenomena occurring in MOFs of contemporary interest.

A technique employing hole deformation during fibre draw was presented in Chapter 6 for the fabrication of microstructured optical fibres with uniformly oriented elliptical holes. The process of deformation is qualitatively understood through the process of hole collapse (a commonly observed phenomenon) and results in a high degree of ellipticity (~ 0.5). An empirical formula has been accurately fitted to the measured deformations, which relates the minor direction deformations to the magnitude of hole collapse. The birefringence of three fibres having different structure sizes were measured and show consistent agreement in their scaled-wavelength trends. Annealing the fibres alleviated a non-zero stress-optic component to birefringence, which increased the measured birefringence by $\sim 25\%$. The subsequent birefringence measurements show excellent agreement with numerical calculations of form birefringence. The use of elliptical holes may one day provide a practical means of controlling both polarization and mode shape in stress-free fibres.

In Chapter 7, the predominantly blue colouration of light transmitted though real air-cored microstructured optical fibres was examined and compared with hollow waveguide guidance in short lengths of fibre. Experimental and theoretical spectral trends have been presented to identify the core interface reflection as the main guiding mechanism. This was understood using the wavelength dependent confinement loss of the leaky modes supported by the fibre. A full numerical simulation of the microstructured fibre demonstrated that the experimental test is incapable of resolving the narrow photonic bandgap features of the fibre. This is due to structural disorder and a recently introduced concept of surface modes. Hence the dispersion curve and confinement loss of this air-core MOF behaves macroscopically as a simple hollow waveguide. The analysis provides a useful reference for others trying to interpret the spectral properties of light transmission though short lengths of air core MOFs.

The calculated numerical apertures and capture efficiencies for a class of multimode microstructured fibres with thin supporting bridges forming an air-cladding was presented in chapter 8. The calculations are performed using an original and accurate method that employs the leaky modes supported by the fibre. A study of the light acceptance properties of single layer structures shows that exceptionally high NA can only be achieved for bridge thicknesses much smaller than the wavelength. This is due to the conditions that allow core light to efficiently couple to the fundamental TE bridge mode, which then radially propagates power into the outer jacket. Thus for single layer structures, the numerical aperture and capture efficiency is best approximated by $\mathrm{NA}_{\mathrm{b}}^{\mathrm{TE}}$ and $\epsilon_{\mathrm{b}}^{\mathrm{TE}}$ respectively. The situation for multiple layer structures however, is significantly different. Here the condition for light acceptance is largely dictated by the second order TM bridge mode. This is understood in terms of the efficient transmission of light through numerous bridge 'T' intersections in the microstructured cladding. Since the orientation of the local polarization of TE and TM bridge modes swap between radial and azimuthal bridges, both bridge modes are needed for light to penetrate deep into the cladding. The alternative heuristic expressions for both NA and capture efficiency are then $\mathrm{NA}_{\mathrm{b}}^{\mathrm{TM}}$ and $\epsilon_{\mathrm{b}}^{\mathrm{TM}}$. When compared with full numerical calculations, they show good agreement. These physical principles governing numerical aperture and capture efficiency were then used to predict the influences of some perturbations to the structure. Preliminary attempts at the fabrication of large-core, polymer microstructured optical fibres with thin supporting bridges are presented. These fibres exhibit high numerical apertures which are strongly scale/wavelength dependent. Measurements show good agreement with theoretical expectations over a very wide scaled-wavelength range, with a highest NA measured to be approximately 0.5 at 850nm. It is believed that the use of microstructure in polymer optical fibres can potentially provide tailorable numerical apertures, up to extreme values, with superior bending flexibility in comparison to their silica counterparts. Multiple layers of holes can then be used to increase the NA further in applications that require it.

APPENDICES

Appendix A

Finite difference implementation

A.1 Finite difference expressions

After the functions $\xi_m^{\pm}(\rho)$ are discretized, the notation $\xi_n^{\pm} = \xi_m^{\pm}(\rho_n)$ is introduced. Clearly, the dependence on m is implicit on the left hand side, but the index has been dropped for clarity in the proceeding equations. The equations are stated in an minimalist manner that allows the method to be easily re-implemented and coded efficiently.

When a second order finite difference scheme (for unequally spaced nodes) is applied, the inner products of Eq. (4.32) become

$$\begin{aligned}
\langle \phi_\mu \mid \mathcal{L}^{\pm}\, \psi_m^{\pm} \rangle \quad &= \quad \tfrac{2}{\Delta\rho_n + \Delta\rho_{n-1}} \left(\tfrac{\xi_{n+1}^{\pm} - \xi_n^{\pm}}{\Delta\rho_n} - \tfrac{\xi_n^{\pm} - \xi_{n-1}^{\pm}}{\Delta\rho_{n-1}} \right) + \\
&\quad\quad \tfrac{1}{\rho_n} \tfrac{1}{\Delta\rho_n + \Delta\rho_{n-1}} \left(\Delta\rho_{n-1} \tfrac{\xi_{n+1}^{\pm} - \xi_n^{\pm}}{\Delta\rho_n} + \Delta\rho_n \tfrac{\xi_n^{\pm} - \xi_{n-1}^{\pm}}{\Delta\rho_{n-1}} \right) - \\
&\quad\quad \tfrac{(m\pm1)^2}{\rho_n^2} \xi_n^{\pm} + \xi_n^{\pm} \mathfrak{V}_{m\mu n}, \\
\langle \phi_\mu \mid F^{\pm}(\rho,\theta) G^{+} \rangle \quad &= \quad \mathfrak{F}_{m\mu n}^{\pm} \left[\tfrac{+1}{\Delta\rho_n + \Delta\rho_{n-1}} \left(\Delta\rho_{n-1} \tfrac{\xi_{n+1}^{+} - \xi_n^{+}}{\Delta\rho_n} + \Delta\rho_n \tfrac{\xi_n^{+} - \xi_{n-1}^{+}}{\Delta\rho_{n-1}} \right) + \tfrac{(m+1)}{\rho_n} \xi_n^{+} \right], \\
\langle \phi_\mu \mid F^{\pm}(\rho,\theta) G^{-} \rangle \quad &= \quad \mathfrak{F}_{m\mu n}^{\pm} \left[\tfrac{-1}{\Delta\rho_n + \Delta\rho_{n-1}} \left(\Delta\rho_{n-1} \tfrac{\xi_{n+1}^{-} - \xi_n^{-}}{\Delta\rho_n} + \Delta\rho_n \tfrac{\xi_n^{-} - \xi_{n-1}^{-}}{\Delta\rho_{n-1}} \right) + \tfrac{(m-1)}{\rho_n} \xi_n^{-} \right], \\
\langle \phi_\mu \mid \psi_m^{\pm} \rangle \quad &= \quad \delta_{m\mu} \xi_n^{\pm},
\end{aligned} \tag{A.1}$$

where $\Delta\rho_n = \rho_{n+1} - \rho_n$ is the distance between nodes n and $n+1$.

The two undefined terms relating to the refractive index profile are

$$\begin{aligned}
\mathfrak{V}_{m\mu n} &= \tfrac{1}{2\pi}\int\limits_0^{2\pi} e^{i(m-\mu)\theta}V^2(\rho_n,\theta)d\theta, \\
\mathfrak{F}^{\pm}_{m\mu n} &= \tfrac{1}{2\pi}\int\limits_0^{2\pi} \tfrac{e^{i(m-\mu)\theta}}{\Delta\rho_n+\Delta\rho_{n-1}}\left(\Delta\rho_{n-1}\tfrac{\ln[n(\rho_{n+1},\theta)]-\ln[n(\rho_n,\theta)]}{\Delta\rho_n}+\Delta\rho_n\tfrac{\ln[n(\rho_n,\theta)]-\ln[n(\rho_{n-1},\theta)]}{\Delta\rho_{n-1}}\right)d\theta \\
&\quad \pm\tfrac{1}{2\pi}\tfrac{i}{\rho_n}\int\limits_0^{2\pi} e^{i(m-\mu)\theta}\left(\tfrac{\partial\ln[n(\rho_n,\theta)]}{\partial\theta}\right)d\theta,
\end{aligned} \tag{A.2}$$

where using integration by parts, the second term of $\mathfrak{F}^{\pm}_{m\mu n}$ can be simplified to

$$(1-\delta_{m\mu})\frac{1}{2\pi}\frac{m-\mu}{\rho_n}\int\limits_0^{2\pi} e^{i(m-\mu)\theta}\ln\left[n(\rho_n,\theta)\right]d\theta. \tag{A.3}$$

For a given waveguide both $\mathfrak{V}_{m\mu n}$ and $\mathfrak{F}^{\pm}_{m\mu n}$ should be precalculated and stored, which saves a great deal of time as they are frequently used in the matrix elements and do not change as the boundary conditions are adjusted. The integral expressions can be trivially calculated when the holes are annular sectors. Arbitrary hole shapes can be deconstructed into hundreds of very thin annular sectors. The result is an increase in the time required to precalculate expressions $\mathfrak{V}_{m\mu n}$ and $\mathfrak{F}^{\pm}_{m\mu n}$, but this is a negligible fraction of total computation time.

A.2 Matrix elements

For the finite difference implementation, the elements of Eqs. (4.12) are given by

$$\begin{aligned}
\left[M^{\pm}\right]^{mn}_{\mu\nu} &= \delta_{m\mu}L_{mn\nu}-\tfrac{(m\pm1)^2}{\rho_n^2}\delta_{m\mu}\delta_{n\nu}+\mathfrak{V}_{m\mu n}\delta_{n\nu} \\
\left[F^{\pm}_{+}\right]^{mn}_{\mu\nu} &= \begin{cases} n=\nu+1; & \mathfrak{F}^{\pm}_{m\mu\nu}\tfrac{1}{\Delta\rho_\nu+\Delta\rho_{\nu-1}}\tfrac{\Delta\rho_{\nu-1}}{\Delta\rho_\nu} \\ n=\nu; & \mathfrak{F}^{\pm}_{m\mu\nu}\left[\tfrac{1}{\Delta\rho_\nu+\Delta\rho_{\nu-1}}\left(\tfrac{\Delta\rho_\nu}{\Delta\rho_{\nu-1}}-\tfrac{\Delta\rho_{\nu-1}}{\Delta\rho_\nu}\right)+\tfrac{(m+1)}{\rho_n}\right] \\ n=\nu-1; & -\mathfrak{F}^{\pm}_{m\mu\nu}\tfrac{1}{\Delta\rho_\nu+\Delta\rho_{\nu-1}}\tfrac{\Delta\rho_\nu}{\Delta\rho_{\nu-1}} \end{cases} \\
\left[F^{\pm}_{-}\right]^{mn}_{\mu\nu} &= \begin{cases} n=\nu+1; & -\mathfrak{F}^{\pm}_{m\mu\nu}\tfrac{1}{\Delta\rho_\nu+\Delta\rho_{\nu-1}}\tfrac{\Delta\rho_{\nu-1}}{\Delta\rho_\nu} \\ n=\nu; & \mathfrak{F}^{\pm}_{m\mu\nu}\left[\tfrac{-1}{\Delta\rho_\nu+\Delta\rho_{\nu-1}}\left(\tfrac{\Delta\rho_\nu}{\Delta\rho_{\nu-1}}-\tfrac{\Delta\rho_{\nu-1}}{\Delta\rho_\nu}\right)+\tfrac{(m-1)}{\rho_n}\right] \\ n=\nu-1; & \mathfrak{F}^{\pm}_{m\mu\nu}\tfrac{1}{\Delta\rho_\nu+\Delta\rho_{\nu-1}}\tfrac{\Delta\rho_\nu}{\Delta\rho_{\nu-1}} \end{cases} \\
\left[N^{\pm}\right]^{mn}_{\mu\nu} &= \delta_{m\mu}\delta_{n\nu}
\end{aligned} \tag{A.4}$$

where

$$L_{mn\nu} = \begin{cases} n = \nu + 1; & \frac{1}{\Delta\rho_\nu + \Delta\rho_{\nu-1}} \left(\frac{2}{\Delta\rho_\nu} + \frac{1}{\rho_\nu} \frac{\Delta\rho_{\nu-1}}{\Delta\rho_\nu} \right) \\ n = \nu; & \frac{1}{\Delta\rho_\nu + \Delta\rho_{\nu-1}} \left(\frac{-2}{\Delta\rho_\nu} - \frac{2}{\Delta\rho_{\nu-1}} - \frac{1}{\rho_\nu} \frac{\Delta\rho_{\nu-1}}{\Delta\rho_\nu} + \frac{1}{\rho_\nu} \frac{\Delta\rho_\nu}{\Delta\rho_{\nu-1}} \right) \\ n = \nu - 1; & \frac{1}{\Delta\rho_\nu + \Delta\rho_{\nu-1}} \left(\frac{2}{\Delta\rho_{\nu-1}} - \frac{1}{\rho_\nu} \frac{\Delta\rho_\nu}{\Delta\rho_{\nu-1}} \right) \end{cases} . \tag{A.5}$$

These result from Eqs. (4.31) using the inner product expressions given in Eqs. (A.1). Note that $L_{mn\nu}$ is only dependent on m due to the boundary conditions.

A.3 Boundary conditions

According to the boundary conditions discussed in section 4.6.3, changes need to be made to a few of the above equations.

At the origin

For this boundary condition and where the first node is placed at the origin $\rho_0 = 0$, the boundary condition of Eq. (4.34) is expressed as:

$$\begin{array}{l} \text{If } m+1=0, \text{ then } \xi_0^+ = \xi_1^+, \text{ else } \xi_0^+ = 0 \\ \text{If } m-1=0, \text{ then } \xi_0^- = \xi_1^-, \text{ else } \xi_0^- = 0 \end{array} . \tag{A.6}$$

Note that these expressions are not strictly second order accurate at the origin. However, it is the most simple to implement and the accuracy can be regained by reducing $\Delta\rho_0$. Only the following replacements then need to be made

$$L_{111} = L_{-111} = \frac{1}{\Delta\rho_1 + \Delta\rho_0} \left(\frac{-2}{\Delta\rho_1} - \frac{1}{\rho_1} \frac{\Delta\rho_0}{\Delta\rho_1} \right) . \tag{A.7}$$

For all other instances of m, L_{m11} and L_{m21} are given by the general expressions above.

Similarly if $m+1=0$ or $m-1=0$, then

$$\begin{array}{lcl} \left[F_+^+\right]_{\mu 1}^{-11} & = & \mathfrak{F}_{-1\mu 1}^+ \left(\frac{-1}{\Delta\rho_1 + \Delta\rho_0} \frac{\Delta\rho_0}{\Delta\rho_1} \right) \\ \left[F_+^-\right]_{\mu 1}^{11} & = & \mathfrak{F}_{1\mu 1}^- \left(\frac{-1}{\Delta\rho_1 + \Delta\rho_0} \frac{\Delta\rho_0}{\Delta\rho_1} + \frac{2}{\rho_1} \right) \\ \left[F_-^+\right]_{\mu 1}^{-11} & = & \mathfrak{F}_{-1\mu 1}^+ \left(\frac{1}{\Delta\rho_1 + \Delta\rho_0} \frac{\Delta\rho_0}{\Delta\rho_1} - \frac{2}{\rho_1} \right) \\ \left[F_-^-\right]_{\mu 1}^{11} & = & \mathfrak{F}_{1\mu 1}^- \left(\frac{1}{\Delta\rho_1 + \Delta\rho_0} \frac{\Delta\rho_0}{\Delta\rho_1} \right) \end{array} . \tag{A.8}$$

For all other instances of m and μ, $\left[F_\pm^\pm\right]_{\mu 1}^{m1}$ and $\left[F_\pm^\pm\right]_{\mu 1}^{m2}$ are given by the general expressions above.

At the computational domain boundary

This boundary condition applies to the last three radial nodes, $N-1$, N and $N+1$. Node N is assumed to be located precisely on the computational domain boundary $\rho_N = 1$. In this case, the boundary condition of Eq. (4.35) is discretized as

$$\frac{1}{\Delta\rho_N + \Delta\rho_{N-1}} \left(\Delta\rho_{N-1} \frac{\xi^{\pm}_{N+1} - \xi^{\pm}_{N}}{\Delta\rho_N} + \Delta\rho_N \frac{\xi^{\pm}_{N} - \xi^{\pm}_{N-1}}{\Delta\rho_{N-1}} \right) = \frac{WK'_{m\pm1}(W)}{K_{m\pm1}(W)} \xi^{\pm}_{N}, \tag{A.9}$$

for all m.

The implication for the matrix elements are that for all instances of m and μ, the following replacements need to be made

$$\begin{array}{lcl} L_{mNN} & = & \frac{2}{\Delta\rho_N+\Delta\rho_{N-1}} \frac{1}{\Delta\rho_{N-1}} \left(\frac{1}{\Delta\rho_N+\Delta\rho_{N-1}} \frac{WK'_{m\pm1}(W)}{K_{m\pm1}(W)} - \frac{\Delta\rho_N}{\Delta\rho_{N-1}} - 1 \right) \\ & & + \frac{1}{\Delta\rho_N} \frac{WK'_{m\pm1}(W)}{K_{m\pm1}(W)} \\ L_{mN-1N} & = & \frac{2}{\Delta\rho_N+\Delta\rho_{N-1}} \frac{1}{\Delta\rho_{N-1}} \left(1 + \frac{\Delta\rho_N}{\Delta\rho_{N-1}} \right) \end{array} . \tag{A.10}$$

As well as

$$\begin{array}{lcl} \left[F^{\pm}_{+}\right]^{mN}_{\mu N} & = & \mathfrak{F}^{\pm}_{m\mu N} \left(\frac{WK'_{m\pm1}(W)}{K_{m\pm1}(W)} + \frac{(m+1)}{\rho_N} \right) \\ \left[F^{\pm}_{-}\right]^{mN}_{\mu N} & = & \mathfrak{F}^{\pm}_{m\mu N} \left(-\frac{WK'_{m\pm1}(W)}{K_{m\pm1}(W)} + \frac{(m-1)}{\rho_N} \right) \\ \left[F^{\pm}_{+}\right]^{mN-1}_{\mu N} & = & 0 \\ \left[F^{\pm}_{-}\right]^{mN-1}_{\mu N} & = & 0 \end{array} . \tag{A.11}$$

Appendix B

Reciprocity theorem

A reciprocity theorem relates two distinct electromagnetic situations. In this case they are two distinct homogeneous waveguides, $n(x, y)$ and $\widetilde{n}(x, y)$, together with their respective modes. All field quantities contain the implicit time dependence $\exp(-i\omega t)$, where ω is the angular frequency. The permeability is constant and equal to the free space value μ_0. The following reciprocity expression and its derivation has not been found any reference. It is used in the ABC convergence study of chapter 5.

The transverse field components obey the following equations [Snyder and Love, 1983, section 30-7]

$$\left(\nabla_t^2 + n^2k^2 - \beta^2\right) \mathbf{e}_t = \mathcal{E} \tag{B.1}$$

$$\left(\nabla_t^2 + n^2k^2 - \beta^2\right) \mathbf{h}_t = \mathcal{H} \tag{B.2}$$

where

$$\mathcal{E} = -\nabla_t \left(\mathbf{e}_t \cdot \nabla_t \ln n^2\right)$$

$$\mathcal{H} = \left(\nabla_t \times \mathbf{h}_t\right) \times \nabla_t \ln n^2$$

Consider a different waveguide, which is denoted with a tilde. The complex conjugate of the analogous expressions are

$$\left(\nabla_t^2 + (\widetilde{n}^*)^2k^2 - (\widetilde{\beta}^*)^2\right) \widetilde{\mathbf{e}}_t^* = \widetilde{\mathcal{E}}^* \tag{B.3}$$

$$\left(\nabla_t^2 + (\widetilde{n}^*)^2k^2 - (\widetilde{\beta}^*)^2\right) \widetilde{\mathbf{h}}_t^* = \widetilde{\mathcal{H}}^* \tag{B.4}$$

where

$$\widetilde{\mathcal{E}}^* = -\nabla_t \left(\widetilde{\mathbf{e}}_t^* \cdot \nabla_t \ln(\widetilde{n}^*)^2\right)$$

$$\widetilde{\mathcal{H}}^* = \left(\nabla_t \times \widetilde{\mathbf{h}}_t^*\right) \times \nabla_t \ln(\widetilde{n}^*)^2$$

Now the following operations are made

$$[\text{Eq. (B.1)}] \times \widetilde{\mathbf{h}}_t^* + \widetilde{\mathbf{e}}_t^* \times [\text{Eq. (B.2)}]$$

to give

$$\nabla_t^2 \mathbf{e}_t \times \widetilde{\mathbf{h}}_t^* + \widetilde{\mathbf{e}}_t^* \times \nabla_t^2 \mathbf{h}_t + \left(n^2 k^2 - \beta^2\right) \widetilde{\mathbf{S}} = \mathcal{E} \times \widetilde{\mathbf{h}}_t^* + \widetilde{\mathbf{e}}_t^* \times \mathcal{H} \tag{B.5}$$

and

$$\mathbf{e}_t \times [\text{Eq. (B.4)}] + [\text{Eq. (B.3)}] \times \mathbf{h}_t$$

to give

$$\mathbf{e}_t \times \nabla_t^2 \widetilde{\mathbf{h}}_t^* + \nabla_t^2 \widetilde{\mathbf{e}}_t^* \times \mathbf{h}_t + \left((\widetilde{n}^*)^2 k^2 - (\widetilde{\beta}^*)^2\right) \widetilde{\mathbf{S}} = \mathbf{e}_t \times \widetilde{\mathcal{H}}^* + \widetilde{\mathcal{E}}^* \times \mathbf{h}_t \tag{B.6}$$

where $\widetilde{\mathbf{S}}$ is defined by

$$\widetilde{\mathbf{S}} = \mathbf{e}_t \times \widetilde{\mathbf{h}}_t^* + \widetilde{\mathbf{e}}_t^* \times \mathbf{h}_t.$$

Subtracting Eq. (B.6) from Eq. (B.5) gives

$$\begin{aligned} &\left(\nabla_t^2 \mathbf{e}_t \times \widetilde{\mathbf{h}}_t^* - \mathbf{e}_t \times \nabla_t^2 \widetilde{\mathbf{h}}_t^*\right) + \left(\widetilde{\mathbf{e}}_t^* \times \nabla_t^2 \mathbf{h}_t - \nabla_t^2 \widetilde{\mathbf{e}}_t^* \times \mathbf{h}_t\right) \\ &\quad + k^2 \left(n^2 - (\widetilde{n}^*)^2\right) \widetilde{\mathbf{S}} - \left(\beta^2 - (\widetilde{\beta}^*)^2\right) \widetilde{\mathbf{S}} \\ &= \left(\mathcal{E} \times \widetilde{\mathbf{h}}_t^* - \widetilde{\mathcal{E}}^* \times \mathbf{h}_t\right) + \left(\widetilde{\mathbf{e}}_t^* \times \mathcal{H} - \mathbf{e}_t \times \widetilde{\mathcal{H}}^*\right) \end{aligned} \tag{B.7}$$

Finally, by taking a dot product with the unit vector $\widehat{\mathbf{z}}$ and integrating over a portion A of the waveguide cross-section, the result is the reciprocity expression

$$n_{\text{eff}}^2 - (\widetilde{n}_{\text{eff}}^*)^2 = \frac{\displaystyle\int_A \left(n^2 - (\widetilde{n}^*)^2\right) \widetilde{\mathbf{S}} \cdot \widehat{\mathbf{z}} dA}{\displaystyle\int_A \widetilde{\mathbf{S}} \cdot \widehat{\mathbf{z}} dA} + \widetilde{M} + \widetilde{L} \tag{B.8}$$

where

$$\widetilde{M} = \frac{\int\limits_A \left(\mathcal{E}\times\widetilde{\mathbf{h}}_t^* - \widetilde{\mathcal{E}}^* \times \mathbf{h}_t\right) \cdot \widehat{\mathbf{z}} dA}{k^2 \int\limits_A \widetilde{\mathbf{S}} \cdot \widehat{\mathbf{z}} dA} + \frac{\int\limits_A \left(\widetilde{\mathbf{e}}_t^* \times \mathcal{H} - \mathbf{e}_t \times \widetilde{\mathcal{H}}^*\right) \cdot \widehat{\mathbf{z}} dA}{k^2 \int\limits_A \widetilde{\mathbf{S}} \cdot \widehat{\mathbf{z}} dA}$$

$$\begin{aligned}
\widetilde{L} &= \frac{\int\limits_A \left(\nabla_t^2 \mathbf{e}_t \times \widetilde{\mathbf{h}}_t^* - \mathbf{e}_t \times \nabla_t^2 \widetilde{\mathbf{h}}_t^*\right) \cdot \widehat{\mathbf{z}} dA}{k^2 \int\limits_A \widetilde{\mathbf{S}} \cdot \widehat{\mathbf{z}} dA} + \frac{\int\limits_A \left(\widetilde{\mathbf{e}}_t^* \times \nabla_t^2 \mathbf{h}_t - \nabla_t^2 \widetilde{\mathbf{e}}_t^* \times \mathbf{h}_t\right) \cdot \widehat{\mathbf{z}} dA}{k^2 \int\limits_A \widetilde{\mathbf{S}} \cdot \widehat{\mathbf{z}} dA} \\
&= \frac{\oint\limits_{\delta A} \left[(\widehat{\mathbf{n}} \cdot \nabla_t \mathbf{e}_t) \times \widetilde{\mathbf{h}}_t^* - \mathbf{e}_t \times \left(\widehat{\mathbf{n}} \cdot \nabla_t \widetilde{\mathbf{h}}_t^*\right)\right] \cdot \widehat{\mathbf{z}} dl}{k^2 \int\limits_A \widetilde{\mathbf{S}} \cdot \widehat{\mathbf{z}} dA} \\
&\qquad + \frac{\oint\limits_{\delta A} \left[\widetilde{\mathbf{e}}_t^* \times (\widehat{\mathbf{n}} \cdot \nabla_t \mathbf{h}_t) - (\widehat{\mathbf{n}} \cdot \nabla_t \widetilde{\mathbf{e}}_t^*) \times \mathbf{h}_t\right] \cdot \widehat{\mathbf{z}} dl}{k^2 \int\limits_A \widetilde{\mathbf{S}} \cdot \widehat{\mathbf{z}} dA} \\
&= \frac{\oint\limits_{\delta A} \left[(\widehat{\mathbf{n}} \cdot \nabla_t \mathbf{e}_t) \times \widetilde{\mathbf{h}}_t^* - (\widehat{\mathbf{n}} \cdot \nabla_t \widetilde{\mathbf{e}}_t^*) \times \mathbf{h}_t\right] \cdot \widehat{\mathbf{z}} dl}{k^2 \int\limits_A \widetilde{\mathbf{S}} \cdot \widehat{\mathbf{z}} dA} \\
&\qquad + \frac{\oint\limits_{\delta A} \left[\widetilde{\mathbf{e}}_t^* \times (\widehat{\mathbf{n}} \cdot \nabla_t \mathbf{h}_t) - \mathbf{e}_t \times \left(\widehat{\mathbf{n}} \cdot \nabla_t \widetilde{\mathbf{h}}_t^*\right)\right] \cdot \widehat{\mathbf{z}} dl}{k^2 \int\limits_A \widetilde{\mathbf{S}} \cdot \widehat{\mathbf{z}} dA}.
\end{aligned}$$

Note that for $\widetilde{L}$ a divergence theorem based on [Snyder and Love, 1983, Pg. 712, Eq. (37-58)] is used to convert the surface integral into a line integral along the boundary of A. It is verified in a straight-forward way.

References

Achenbach, C. P. and Cobb, J. H. [2003]. Computational studies of light acceptance and propagation in straight and curved multimode active fibers, *Journal of Optics A* **5**: 239–49. (Cited on pages 112, 113 and 117.)

Argyros, A., Bassett, I. M., van Eijkelenborg, M. A., Large, M. C. J., Zagari, J., Nicorovici, N. A. P., McPhedran, R. C. and Martijn de Sterke, C. [2001]. Ring structures in microstructured polymer optical fibres, *Optics Express* **9**(13): 813–20.
URL: `http://www.opticsexpress.org/abstract.cfm?URI=OPEX-9-13-813` (Cited on page 29.)

Argyros, A., Issa, N. A., Bassett, I. M. and van Eijkelenborg, M. A. [2004]. Microstructured optical fibres for single-polarisation air-guidance, *Optics Letters* **29**(1): 20–3. (Cited on pages 27 and 29.)

Baggett, J. C., Monro, T. M., Furusawa, K., Finazzi, V. and Richardson, D. J. [2003]. Understanding bending losses in holey optical fibers, *Optics Communications* **227**: 317–5. (Cited on page 25.)

Bassett, I. M. [1988]. Design principle for circularly birefringent optical fiber, *Optics Letters* **13**(10): 844–6. (Cited on pages 19, 45, 48 and 49.)

Bassett, I. M. and Argyros, A. [2002]. Elimination of polarization degeneracy in round waveguides, *Optics Express* **10**(23): 1342–6.
URL: `http://www.opticsexpress.org/abstract.cfm?URI=OPEX-10-23-1342` (Cited on page 27.)

Benabid, F., Knight, J. C., Antonopoulos, G. and Russell, P. S. J. [2002a]. Stimulated raman scattering in hydrogen-filled hollow-core photonic crystal fiber, *Science* **298**: 375–99. (Cited on pages 28 and 103.)

Benabid, F., Knight, J. C. and Russell, P. S. J. [2002b]. Particle levitation and guidance in hollow-core photonic crystal fiber, *Optics Express* **10**(21): 1195–203.
URL: `http://www.opticsexpress.org/abstract.cfm?URI=OPEX-10-21-1195` (Cited on pages 27 and 103.)

Birks, T. A., Knight, J. C. and Russell, P. S. J. [1997]. Endlessly single-mode photonic crystal fiber, *Optics Letters* **22**(13): 961–3. (Cited on pages 24, 25 and 103.)

Bjarklev, A., Broeng, J. and Bjarklev, A. S. [2003]. *Photonic crystal fibres*, Kluwer academic publishers, Boston, USA. (Cited on page 18.)

BlazePhotonics [2004]. Hollow core photonic band gap fibre, product hc-1550-02.
URL: `http://www.blazephotonics.com/pdf/HC-1550-02.pdf` (Cited on page 24.)

Bloch, F. [1928]. Über die quantenmechanik der electron in kristallgittern, *Z. phys.* **52**: 555–600. (Cited on page 34.)

Bouwmans, G., Luan, F., Knight, J. C., Russell, P. S. J., Farr, L., Mangan, B. J. and Sabert, H. [2003b]. Properties of a hollow-core photonic bandgap fiber at 850 nm wavelength, *Optics Express* **11**(14): 1613–20.
URL: `http://www.opticsexpress.org/abstract.cfm?URI=OPEX-11-14-1613` (Cited on page 28.)

Bouwmans, G., Percival, R. M., Wadsworth, W. J., Knight, J. C. and Russell, P. S. J. [2003a]. High-power Er:Yb fiber laser with very high numerical aperture pump-cladding waveguide, *Applied Physics Letters* **83**: 817–8. (Cited on pages 26, 113, 114 and 126.)

Brabec, T. and Krausz, F. [2000]. Intense few-cycle laser fields: Frontiers of nonlinear optics, *Reviews of Modern Physics* **72**(2): 545–91. (Cited on page 28.)

Brechet, F., Marcou, J., Pagnoux, D. and Roy, P. [2000]. Complete analysis of the characteristics of propagation into photonic crystal fibers by finite element method, *Optical Fiber Technology* **6**: 181–91. (Cited on page 54.)

Buck, J. A. [1995]. *Fundamentals of optical fibers*, John Wiley & sons, New York. (Cited on page 117.)

Campbell, S., McPhedran, R. C., Martijn de Sterke, C. and Botten, L. C. [2004]. Differential multipole method for microstructured optical fibers, *Journal of the Optical Society of America* **21**(11): 1919–28. (Cited on page 56.)

Chen, X., Li, M. J., Venkataraman, N., Gallagher, M. T., Wood, W. A., Crowley, A. M., Carberry, J. P., Zenteno, L. A. and Koch, K. W. [2004]. Highly birefringent hollow-core photonic bandgap fiber, *Optics Express* **12**(16): 3888–93.
URL: `http://www.opticsexpress.org/abstract.cfm?URI=OPEX-12-16-3888` (Cited on page 28.)

Cheng, H., Crutchfield, W. Y., Doery, M. and Greengard, L. [2004]. Fast, accurate integral equation methods for the analysis of photonic crystal fibers i: Theory, *Optics*

Express **12**(16): 3791–805.
URL: `http://www.opticsexpress.org/abstract.cfm?URI=OPEX-12-16-3791` (Cited on page 54.)

Chew, W. C. [1990]. *Waves and fields in inhomogeneous media*, Van Nostrand Reinhold, New York. (Cited on page 94.)

Ching, E. S. C., Leung, P. T., Maassen van den Brink, A., Suen, W. M., Tong, S. S. and Young, K. [1998]. Quasinormal-mode expansion for waves in open systems, *Review of modern physics* **70**: 1545–54. (Cited on page 37.)

Choi, J., Kim, D. Y. and Paek, U. C. [2001]. Fabrication and properties of polymer photonic crystal fibers, *Proceedings of the Plastic Optical Fibres Conference*, Amsterdam, Netherlands, pp. 335–60. (Cited on page 28.)

Cregan, R. F., Mangan, B. J., Knight, J. C., Birks, T. A., Russell, P. S. J., Roberts, P. J. and Allan, D. C. [1999]. Single-mode photonic band gap guidance of light in air, *Science* **285**: 1537–9. (Cited on pages 26, 103 and 104.)

CrystalFiber [2004]. Large mode area photonic crystal fiber, product lma-8.
URL: `http://www.crystal-fibre.com/Products/large_mode_area/datasheets/LMA-8.pdf` (Cited on page 24.)

Cucinotta, A., Selleri, S., Vincetti, L. and Zoboli, M. [2002]. Holey fiber analysis through the finite element method, *IEEE Photonics Technology Letters* **14**: 1530–2. (Cited on pages 54 and 56.)

Digonnet, M. J. F., Kim, H. K., Shin, J., Fan, S. and Kino, G. S. [2004]. Simple geometric criterion to predict the existence of surface modes in air-core photonic-bandgap fibers, *Optics Express* **12**(9): 1864–72.
URL: `http://www.opticsexpress.org/abstract.cfm?URI=OPEX-12-9-1864` (Cited on page 109.)

Dutra, S. M. and Nienhuis, G. [2000]. Quantized mode of a leaky cavity, *Physical Review A* **62**(063805): 1–13. (Cited on page 37.)

Ferrando, A., Silvestre, E., Miret, J. J., Andres, P. and Andres, M. V. [2000a]. Donor and acceptor guided modes in photonic crystal fibers, *Optics Letters* **25**(18): 1328–30. (Cited on page 25.)

Ferrando, A., Silvestre, E., Miret, J. J., Andres, P. and Andres, M. V. [2000b]. Vector description of higher-order modes in photonic crystal fibers, *Journal of the Optical Society of America A* **17**(7): 1333–40. (Cited on pages 26, 35, 54 and 55.)

Ferrando, A., Silvestre, E., Miret, J. J., Andres, P. and Andres, V. [1999]. Full vector analysis of a realistic photonic crystal fiber, *Optics Letters* **24**: 276–8. (Cited on pages 30 and 54.)

Ferrarini, D., Vincetti, L. and Zoboli, M. [2002]. Leakage properties of photonic crystal fibers, *Optics Express* **10**(23): 1314–9.
URL: `http://www.opticsexpress.org/abstract.cfm?URI=OPEX-10-23-1314` (Cited on pages 26, 54 and 56.)

Feuermann, D., Gordon, J. M. and Huleihil, M. [2002]. Light leakage in optical fibers: Experimental results, modelling and the consequences for solar collectors, *Solar Evergy* **72**: 195–204. (Cited on pages 112, 113 and 117.)

Finazzi, V., Monro, T. M. and Richardson, D. J. [2003a]. Small-core silica holey fibers: nonlinearity and confinement loss trade-offs, *Journal of the Optical Society of America B* **20**(7): 1427–36. (Cited on page 26.)

Finazzi, V., Monro, T. M. and Richardson, D. J. [2003b]. The role of confinement loss in highly nonlinear silica holey fibers, *IEEE Photonics Technology Letters* **15**(9): 1246–8. (Cited on page 26.)

Fini, J. [2004]. Improved symmetry analysis of many-moded microstructured optical fibers, *Journal of the Optical Society of America* **21**(8): 1431–6. (Cited on page 32.)

Fitt, A. D., Furusawa, K., Monro, T. M., Please, C. P. and Richardson, D. J. [2002]. The mathematical modelling of capillary drawing for holey fiber manufacture, *Journal of Engineering Mathematics* **43**: 201–227. (Cited on page 97.)

Floquet, G. [1883]. Sur les équations différentielles linéaries à coefficients périodique, *Ann. École Norm. Sup.* **12**: 47–88. (Cited on page 34.)

Furusawa, K., Malinowski, A., Price, J. H. V., Monro, T. M., Sahu, J. K., Nilsson, J. and Richardson, D. J. [2001]. Cladding pumped ytterbium-doped fiber laser with holey inner and outer cladding, *Optics Express* **9**(12): 714–20.
URL: `http://www.opticsexpress.org/abstract.cfm?URI=OPEX-9-13-714` (Cited on pages 26 and 113.)

Gallawa, R. L. [1982]. On the definition of fiber numerical aperture, *Electro-Optical Systems Design* **14**: 46–54. (Cited on page 117.)

Guan, N., Habu, S., Takenaga, K., Himeno, K. and Wada, A. [2003]. Boundary element method for analysis of holey optical fibers, *Journal of Lightwave Technology* **21**: 1787–92. (Cited on page 54.)

Guo, S., Wu, F., Albin, S., Tai, H. and Rogowski, R. S. [2004]. Loss and dispersion analysis of microstructured fibers by finite-difference method, *Optics Express* **12**(15): 3341–52.
URL: `http://www.opticsexpress.org/abstract.cfm?URI=OPEX-12-15-3341` (Cited on page 54.)

Guobin, R., Zhi, W., Shuqin, L. and Shuisheng, J. [2003]. Mode classification and degeneracy in photonic crystal fibers, *Optics Express* **11**(11): 1310–21.
URL: `http://www.opticsexpress.org/abstract.cfm?URI=OPEX-11-11-1310` (Cited on pages 26, 30 and 35.)

Hansen, T. P., Broeng, J., Jakobsen, C., Vienne, G., Simonsen, H. R., Nielsen, M. D., Skovgaard, P. M. W., Folkenberg, J. R. and Bjarklev, A. [2004]. Air-guiding photonic bandgap fibers: spectral properties, macrobending loss, and practical handling, *Journal of Lightwave Technology* **22**(1): 11–5. (Cited on page 28.)

Hasegawa, T., Sasaoka, E., Onishi, M., Nishimura, M., Tsuji, Y. and Koshiba, M. [2001]. Hole-assisted lightguide fiber for large anomalous dispersion and low optical loss, *Optics Express* **9**(13): 681–6.
URL: `http://www.opticsexpress.org/abstract.cfm?URI=OPEX-9-13-681` (Cited on page 24.)

Hecht, E. [1998]. *Optics*, third edn, Addison-Wesley, Massachusetts, USA. (Cited on page 121.)

Huang, C. W., Ho, M. C., Yu, C. P., Chang, H. C., Yang, C. C., Chien, H. H., Ma, K. J. and Zheng, Z. P. [2004]. Fabrication and characterization of microstructured polymer optical fibres, *Proceedings of the Conference on Lasers and Electro Optics*, San Francisco, USA, p. CThX21. (Cited on page 28.)

Humbert, G., Knight, J. C., Bouwmans, G., Russell, P. S. J., Williams, D. P., Roberts, P. J. and Mangan, B. J. [2004]. Hollow core photonic crystal fibers for beam delivery, *Optics Express* **12**(8): 1477–84.
URL: `http://www.opticsexpress.org/abstract.cfm?URI=OPEX-12-8-1477` (Cited on page 27.)

Issa, N. A. [2004a]. High numerical aperture in multimode microstructured optical fibers, *Applied Optics* **43**(33): 6191–7. (Cited on page 21.)

Issa, N. A., Argyros, A., van Eijkelenborg, M. A. and Zagari, J. [2003b]. Identifying hollow waveguide guidance in air-cored microstructured optical fibres, *Optics Express* **11**(9): 996–1001.
URL: `http://www.opticsexpress.org/abstract.cfm?URI=OPEX-11-9-996` (Cited on pages 20 and 28.)

Issa, N. A. and Padden, W. E. [2004b]. Light acceptance properties of multimode microstructured optical fibers: Impact of multiple layers, *Optics Express* **12**(14): 3224–35.

URL: `http://www.opticsexpress.org/abstract.cfm?URI=OPEX-12-14-3224` (Cited on page 21.)

Issa, N. A. and Poladian, L. [2002]. Considerations for an expansion method used to calculate leaky modes in mofs, *Proceedings of Australian Optical Society*, Sydney, Australia. (Cited on page 20.)

Issa, N. A. and Poladian, L. [2003a]. Vector wave expansion method for leaky modes of microstructured optical fibres, *Journal of Lightwave Technology* **21**: 1005–12. (Cited on pages 20, 32 and 54.)

Issa, N. A., van Eijkelenborg, M. A., Fellew, M., Cox, F., Henry, G. and Large, M. C. J. [2004d]. Fabrication and study of microstructured optical fibers with elliptical holes, *Optics Letters* **29**(12): 1336–8. (Cited on pages 20 and 29.)

Issa, N. A., von Korff Schmising, C., Padden, W. E. and van Eijkelenborg, M. A. [2004c]. High numerical aperture in large-core microstructured polymer optical fibres, *Proceedings of the Polymer Optical Fibre Conference*, Nürnberg, Germany, pp. 135–8. (Cited on pages 21 and 29.)

Johnson, S. G., Ibanescu, M., Skorobogatiy, M., Weisberg, O., Engeness, T. D., Soljacic, M., Jacobs, S. A., Joannopoulos, J. D. and Fink, Y. [2001]. Low-loss asymptotically single-mode propagation in large-core omniguide fibers, *Optics Express* **9**(13): 748–79. **URL:** `http://www.opticsexpress.org/abstract.cfm?URI=OPEX-9-13-748` (Cited on page 27.)

Kaiser, V. P. and Astle, H. W. [1974]. Low-loss single-material fibers made from pure fused silica, *Bell System Technical Journal* **53**: 1021–39. (Cited on page 23.)

Kaiser, V. P., Marcatili, E. A. and Miller, S. E. [1973]. A new optical fiber, *Bell System Technical Journal* **52**(2): 265–9. (Cited on page 23.)

Kerbage, C., Steinvurzel, P., Reyes, P., Westbrook, P. S., Windeler, R. S., Hale, A. and Eggleton, B. J. [2002]. Highly tunable birefringent microstructured optical fiber, *Optics Letters* **27**(10): 842–4. (Cited on page 24.)

Kiang, K. M., Frampton, K., Monro, T. M., Moore, R., Tucknott, J., Hewak, D. W., Richardson, D. J. and Rutt, H. N. [2002]. Extruded single mode non-silica glass holey optical fibres, *Electronics Letters* **38**(12): 546–7. (Cited on pages 26 and 53.)

Kim, H. K., Digonnet, M. J. F., Kino, G. S., Shin, J. and Fan, S. [2004]. Simulations of the effect of the core ring on surface and air-core modes in photonic bandgap fibers, *Optics Express* **12**(15): 3436–42.
URL: `http://www.opticsexpress.org/abstract.cfm?URI=OPEX-12-15-3436` (Cited on page 109.)

Knight, J. C. [2003]. Photonic crystal fibres, *Nature* **424**: 847–51. (Cited on pages 18 and 27.)

Knight, J. C., Birks, T. A., Russell, P. S. J. and Atkin, D. M. [1996]. All-silica single mode optical fiber with photonic crystal cladding, *Optics Letters* **21**(19): 1547–9. (Cited on page 23.)

Knight, J. C., Birks, T. A., Russell, P. S. J. and Sandro, J. [1998a]. Properties of photonic crystal fibres and the effective index model, *Journal of the Optical Society of America A* **15**: 748–52. (Cited on page 24.)

Knight, J. C., Broeng, J., Birks, T. A. and Russell, P. S. J. [1998b]. Photonic band gap guidance in optical fibers, *Journal of the Optical Society of America A* **282**: 1476–8. (Cited on page 26.)

Koshiba, M. and Saitoh, K. [2004]. Applicability of classical optical fiber theories to holey fibers, *Optics Letters* **29**(15): 1739–41. (Cited on page 25.)

Kuhlmey, B. T., McPhedran, R. C. and Martijn de Sterke, C. [2002a]. Modal cutoff in microstructured optical fibers, *Optics Letters* **27**(19): 1684–6. (Cited on page 25.)

Kuhlmey, B. T., McPhedran, R. C., Martijn de Sterke, C., Robinson, P. A., Renversez, G. and Maystre, D. [2002b]. Microstructured optical fibers: Where's the edge?, *Optics Express* **10**(22): 1285–90.
URL: `http://www.opticsexpress.org/abstract.cfm?URI=OPEX-10-22-1285` (Cited on page 25.)

Kuhlmey, B. T., Renversez, G. and Maystre, D. [2003]. Chromatic dispersion and losses of microstructured optical fibers, *Applied Optics* **42**: 634–9. (Cited on page 26.)

Kuhlmey, B. T., White, T. P., Renversez, G., Maystre, D., Botton, L. C., Martijn de Sterke, C. and McPhedran, R. C. [2002c]. Multipole method for microstructured optical fibers ii: Implementation and results, *Journal of the Optical Society of America B* **19**: 2331–40. (Cited on pages 54, 55 and 94.)

Kumar, V. V. R. K., George, A. K., Reeves, W. H., Knight, J. C., Russell, P. S. J., Omenetto, F. G. and Taylor, A. J. [2002]. Extruded soft glass photonic crystal fiber for ultra-broad supercontinuum generation, *Physical Review Special Topics - Accelerators and Beams* **10**(25): 1520–5. (Cited on page 26.)

Kuriki, K., Shapira, O., Hart, S. D., Benoit, G., Kuriki, Y., Viens, J. F., Bayindir, M., Joannopoulos, J. D. and Fink, Y. [2004]. Hollow multilayer photonic bandgap fibers for nir applications, *Optics Express* **12**(8): 1510–17.
URL: `http://www.opticsexpress.org/abstract.cfm?URI=OPEX-12-8-1510` (Cited on page 27.)

Kuzyk, M. G. [2003]. An overview of dye-doped polymer optical fibers: Fabrication characterization and applications, *Proceedings of the Plastic Optical Fibers conference*, Seattle, USA, pp. 73–6. (Cited on page 28.)

Limpert, J., Schreiber, T., Liem, A., Nolte, S., Zellmer, H., Peschel, T., Guyenot, V. and Tünnermann, A. [2003]. Thermo-optical properties of air-clad photonic crystal fiber lasers in high power operation, *Optics Express* **11**(22): 2982–90.
URL: `http://www.opticsexpress.org/abstract.cfm?URI=OPEX-11-22-2982` (Cited on pages 26, 113 and 126.)

Lin, X. E. [2001]. Photonic band gap fiber accelerator, *Physical Review Special Topics - Accelerators and Beams* **4**: 051301. (Cited on page 27.)

Litchinitser, N. M., Abeeluck, A. K., Headley, C. and Eggleton, B. J. [2002]. Antiresonant reflecting photonic crystal optical waveguides, *Optics Letters* **27**(18): 1592–1594. (Cited on page 27.)

Litchinitser, N. M., Dunn, S. C., Usner, B., Eggleton, B. J., White, T. P., McPhedran, R. C. and Martijn de Sterke, C. [2003]. Resonances in microstructured optical waveguides, *Optics Express* **11**(10): 1243–51.
URL: `http://www.opticsexpress.org/abstract.cfm?URI=OPEX-11-10-1243` (Cited on page 25.)

Lyytikäinen, K., Canning, J., Digweed, J. and Zagari, J. [2003]. Geometry control of air-silica structured optical fibres using pressurisation, *Proceedings of the International Microwave and Optoelectronics Conference*, Parana, Brazil. (Cited on page 97.)

MacChesney, J. B. and DiGiovanni, D. J. [1990]. Materials development of optical fiber, *Journal of the American Ceramic Society* **73**(12): 3537–56. (Cited on page 23.)

MacChesney, J. B., O'Connor, P. B. and Presby, H. M. [1974]. A new technique for preparation of low-loss and graded index optical fibers, *Proceedings of the IEEE* **62**: 1278–9. (Cited on page 23.)

Mangan, B. J., Arriaga, J., Birks, T. A., Knight, J. C. and Russell, P. S. J. [2001]. Fundamental-mode cutoff in a photonic crystal fiber with a depressed-index core, *Optics Letters* **26**(19): 1469–71. (Cited on page 103.)

Mangan, B. J., Farr, L., Langford, A., Roberts, P. J., Williams, D. P., Couny, F., Lawman, M., Mason, M., Coupland, S., Flea, R., Sabert, H., Birks, T. A., Knight, J. C. and Russell, P. S. J. [2004]. Low loss (1.7db/km) hollow core photonic bandgap fiber, *Postdeadline of the Optical Fibre Communication conference*, Los Angeles, USA, p. 24. (Cited on page 26.)

Mangan, B. J., Knight, J. C., Birks, T. A., Russell, P. S. J. and Greenaway, A. H. [2000]. Experimental study of dual-core photonic crystal fibre, *Electronics Letters* **36**: 1358–9. (Cited on page 26.)

Marcatili, E. A. J. [1973]. Air clad optical fiber waveguide, *US patent 3,712,705* . (Cited on pages 23 and 112.)

Marcatili, E. A. J. and Schmeltzer, R. A. [1964]. Hollow metallic and dielectric waveguides for long distance optical transmission and lasers, *Bell System Technical Journal* **43**: 1783–809. (Cited on pages 104, 106 and 110.)

McIsaac, P. R. [1975a]. Symmetry-induced modal characteristics of uniform waveguides - I: Summary of results, *IEEE Transactions Microwave Theory and Techniques* **MTT-23**(5): 421–29. (Cited on pages 30, 31, 32 and 44.)

McIsaac, P. R. [1975b]. Symmetry-induced modal characteristics of uniform waveguides - II: Theory, *IEEE Transactions Microwave Theory and Techniques* **MTT-23**(5): 429–33. (Cited on pages 30, 31 and 32.)

Mediavilla, E., Arribas, S. and Watson, F. [1998]. *Fiber optics in astronomy Vol 3*, Astronomical Society of the Pacific, San Francisco, USA. (Cited on page 112.)

Michie, A., Canning, J., Lyytikäinen, K., Åslund, M. and Digweed, J. [2004]. Temperature independent highly birefringent photonic crystal fibre, *Optics Express* **12**(21): 5160–5. **URL:** `http://www.opticsexpress.org/abstract.cfm?URI=OPEX-12-21-5160` (Cited on page 102.)

Mogilevtsev, D., Broeng, J., Barkou, S. E. and Bjarklev, A. [2001]. Design of polarization-preserving photonic crystal fibers with elliptical pores, *Journal of Optics A* **3**: S141–3. (Cited on page 96.)

Monro, T. M., Belardi, W., Furusawa, K., Baggett, J. C., Broderick, N. G. R. and Richardson, D. J. [2001]. Sensing with microstructured optical fibres, *Measurement Science Technology* **12**: 854–8. (Cited on page 103.)

Monro, T. M., Bennett, P. J., Broderick, N. G. R. and Richardson, D. J. [2000]. Holey fibers with random cladding distributions, *Optics Letters* **25**(4): 206–8. (Cited on page 25.)

Monro, T. M., Richardson, D. J., Broderick, N. G. R. and Bennet, P. J. [1999]. Holey optical fibres: An efficient modal method, *Journal of Lightwave Technology* **17**: 1093–102. (Cited on pages 54 and 55.)

Mortensen, N. A., Folken, J. R., Skovgaard, P. M. W. and Broeng, J. [2002]. Numerical aperture of single-mode photonic crystal fibers, *IEEE Photonics Technology Letters* **14**: 1094–6. (Cited on pages 26 and 113.)

Mortensen, N. A., Folkenberg, J. R., Nielsen, M. D. and Hansen, K. P. [2003b]. Modal cutoff and the v parameter in photonic crystal fibers, *Optics Letters* **28**(20): 1879–81. (Cited on page 25.)

Mortensen, N. A. and Nielsen, M. D. [2004b]. Modeling of realistic cladding structures for air-core photonic bandgap fibers, *Optics Letters* **29**(4): 349–51. (Cited on page 109.)

Mortensen, N. A., Nielsen, M. D., Folkenberg, J. R., Jakobsen, C. and Simonsen, H. R. [2004]. Photonic crystal fiber with a hybrid honeycomb cladding, *Optics Express* **12**(3): 468–72. (Cited on page 26.)

Mortensen, N. A., Nielsen, M. D., Folkenberg, J. R., Petersson, A. and Simonsen, H. R. [2003c]. Improved large-mode-area endlessly single-mode photonic crystal fibers, *Optics Letters* **28**(6): 393–5. (Cited on page 26.)

Mortensen, N. A., Stach, M., Broeng, J., Petersson, A., Simonsen, H. R. and Michalzik, R. [2003a]. Multi-mode photonic crystal fibers for VCSEL based data transmission, *Optics Express* **11**(17): 1953–9.
URL: `http://www.opticsexpress.org/abstract.cfm?URI=OPEX-11-17-1953` (Cited on page 112.)

Nielsen, M. D., Folkenberg, J. R., Mortensen, N. A. and Bjarklev, A. [2004b]. Bandwidth comparison of photonic crystal fibers and conventional single-mode fibers, *Optics Express* **12**(3): 430–5.
URL: `http://www.opticsexpress.org/abstract.cfm?URI=OPEX-12-3-430` (Cited on page 26.)

Nielsen, M. D., Jacobsen, C., Mortensen, N. A., Folkenberg, J. R. and Simonsen, H. R. [2003a]. Low-loss photonic crystal fibers for transmission systems and their dispersion properties, *Optics Express* **12**(7): 1372–6.
URL: `http://www.opticsexpress.org/abstract.cfm?URI=OPEX-12-7-1372` (Cited on pages 25 and 26.)

Nielsen, M. D. and Mortensen, N. A. [2003b]. Photonic crystal fiber design based on the v-parameter, *Optics Express* **11**(21): 2762–8.
URL: `http://www.opticsexpress.org/abstract.cfm?URI=OPEX-11-21-2762` (Cited on page 25.)

Nielsen, M. D., Mortensen, N. A., Albertsen, M., Folkenberg, J. R., Bjarklev, A. and Bonacinni, D. [2004a]. Predicting macrobending loss for large-mode area photonic crystal fibers, *Optics Express* **12**(8): 1775–9.
URL: `http://www.opticsexpress.org/abstract.cfm?URI=OPEX-12-8-1775` (Cited on page 25.)

Ortigosa-Blanch, A., Knight, J. C., Wadsworth, W. J., Arriaga, J., Mangan, B. J., Birks, T. A. and Russell, P. S. J. [2000]. Highly birefringent photonic crystal fibers, *Optics Letters* **25**: 1325–27. (Cited on pages 26, 96 and 100.)

Padden, W. E., van Eijkelenborg, M. A., Argyros, A. and Issa, N. A. [2004]. Coupling in a twin-core microstructured polymer optical fibre, *Applied Physics Letters* **84**(10): 1689–91. (Cited on page 26.)

Park, J. H., Shin, B. G. and Kim, J. J. [2002]. Fabrication of plastic holey fibers, *Proceedings of the Plastic Optical Fibers conference*, Tokyo, Japan, pp. 9–11. (Cited on page 28.)

Poladian, L., Issa, N. A. and Monro, T. M. [2002]. Fourier decomposition algorithm for leaky modes of fibres with arbitrary geometry, *Optics Express* **10**(10): 449–54.
URL: `http://www.opticsexpress.org/abstract.cfm?URI=OPEX-10-10-449` (Cited on pages 19, 32, 54 and 56.)

Potter, R. J. [1961]. Transmission properties of optical fibers, *Journal of the Optical Society of America* **51**: 1079–89. (Cited on pages 113 and 116.)

Qiu, M. and He, S. [1999]. Large complete band gap in two dimensional photonic crystals with elliptical air holes, *Physical Review B* **60**: 10610–12. (Cited on page 96.)

Ritari, T., Tuominen, J., Ludvigsen, H., Petersen, J. C., Sørensen, T., Hansen, T. P. and Simonsen, H. R. [2004]. Gas sensing using air-guiding photonic bandgap fibers, *Physical Review B* **12**(17): 4080–7.
URL: `http://www.opticsexpress.org/abstract.cfm?URI=OPEX-12-17-4080` (Cited on page 27.)

Russell, P. S. J. [2003]. Photonic crystal fibers, *Science* **299**: 358–62. (Cited on pages 18 and 27.)

Sahu, J. K., Renaud, C. C., Furusawa, K., Selvas, R., Alvarez-Chavez, J. A., Richardson, D. J. and Nilsson, J. [2001]. Jacketed air-clad cladding pumped ytterbium-doped fiber laser with wide tuning range, *Electronics Letters* **37**: 1116–7. (Cited on pages 112 and 113.)

Saitoh, K. and Koshiba, M. [2002]. Full-vectorial imaginary-distance beam propagation method based on a finite element scheme: application to photonic crystal fibers, *Journal of Quantum Electronics* **38**: 927–33. (Cited on pages 54 and 56.)

Saitoh, K., Koshiba, M., Hasegawa, T. and Sasaoka, E. [2003]. Chromatic dispersion control in photonic crystal fibers: application to ultra-flattened dispersion, *Optics Express* **11**(8): 843–52. (Cited on page 26.)

Saitoh, K., Mortensen, N. A. and Koshiba, M. [2004]. Air-core photonic band-gap fibers: the impact of surface modes, *Optics Express* **12**(3): 394–400.
URL: `http://www.opticsexpress.org/abstract.cfm?URI=OPEX-12-3-394` (Cited on page 109.)

Sakoda, K. [2001]. *Optical properties of photonic crystals*, Springer, Berlin, Germany. (Cited on pages 100, 120 and 129.)

Sammut, R. [1975]. *The theory of unbound modes on circular dielectric waveguides*, PhD dissertation, Australian National University, Canberra, Australia. (Cited on pages 37 and 39.)

Sammut, R. and Snyder, A. W. [1976]. Leaky modes on circular optical waveguides, *Applied optics* **15**(2): 477–82. (Cited on page 37.)

Sammut, R. and Snyder, A. W. [1976a]. Leaky modes on a dielectric waveguide: Orthogonality and excitation, *Applied Optics* **15**(4): 1040–44. (Cited on pages 37, 39, 40, 86 and 114.)

Shephard, J. D., Jones, J. D. C., Hand, D. P., Bouwmans, G., Knight, J. C., Russell, P. S. J. and Mangan, B. J. [2004]. High energy nanosecond laser pulses delivered single-mode through hollow-core PBG fibers, *Optics Express* **12**(4): 717–23.
URL: `http://www.opticsexpress.org/abstract.cfm?URI=OPEX-12-4-717` (Cited on page 27.)

Shevchenko, V. V. [1971]. The expansion of the fields of open waveguides into proper and improper modes, *Izvestiya vysshikh uchebnykh zavedenii radiofizika (Institute of radio engineering and electronics, acadamy of sciences of the* USSR*)* **14**(8): 1242–9. (Cited on pages 37 and 39.)

Silvestre, E., Andrés, M. V. and Andrés, P. [1998]. Biorthogonal-basis method for the vector description of optical fiber modes, *Journal of Lightwave Technology* **16**(5): 923–8. (Cited on page 61.)

Snyder, A. W. and Love, J. D. [1974]. Tunnelling leaky modes on optical waveguides, *Optics Communications* **12**(3): 326–8. (Cited on page 37.)

Snyder, A. W. and Love, J. D. [1983]. *Optical waveguide theory*, Chapman and Hall, New York. (Cited on pages 37, 38, 39, 42, 45, 46, 48, 58, 59, 91, 106, 116, 122, 123, 126, 130, 150 and 152.)

Sørensen, T., Broeng, J., Bjarklev, A., Knudsen, E. and Libori, S. E. B. [2001]. Macrobending loss properties of photonic crystal fibre, *Electronics Letters* **37**(5): 287–9. (Cited on page 25.)

Steel, M. J., White, T. P., Martijn de Sterke, C., McPhedran, R. C. and Botten, L. C. [2001b]. Symmetry and degeneracy in microstructured optical fibers, *Optics Letters* **26**(8): 488–90. (Cited on page 30.)

Steel, M. and Osgood, R. M. [2001a]. Polarization and dispersive properties of elliptical-hole photonic crystal fibers, *Journal of Lightwave Technology* **19**: 495–503. (Cited on pages 55 and 96.)

Suzuki, K., Kubota, H., Kawanishi, S., Tanaka, M. and Fujita, M. [2001]. Optical properties of low-loss polarization-maintaining photonic crystal fiber, *Optics Express* **9**(13): 676–80.

URL: `http://www.opticsexpress.org/abstract.cfm?URI=OPEX-9-13-676` (Cited on pages 26, 96 and 100.)

Szpulak, M., Martynkien, T., Urbanczyk, W., Wójcik, J. and Bock, W. J. [2002]. Influence of temperature on birefringence and polarization mode dispersion in photonic crystal holey fiber, *Proceedings of the 1st European Symposium on Photonic Crystals*, Vol. 2, Warsaw, Poland, pp. 89–92. (Cited on page 102.)

Temelkuran, B., Hart, S. D., Benoit, G., Joannopoulos, J. D. and Fink, Y. [2002]. Wavelength-scalable hollow optical fibres with large photonic bandgaps for co2 laser transmission, *Nature* **420**: 650–3. (Cited on pages 27 and 103.)

Tinkham, M. [1964]. *Group theory and quantum mechanics*, McGraw-Hill book company, New York, USA. (Cited on pages 31, 32 and 34.)

Uranus, H. P. and Hoekstra, H. J. W. M. [2004]. Modelling of microstructured waveguides using a finite-element-based vectorial mode solver with transparent boundary conditions, *Optics Express* **12**(12): 2795–809.

URL: `http://www.opticsexpress.org/abstract.cfm?URI=OPEX-12-12-2795` (Cited on pages 54 and 56.)

van Eijkelenborg, M. A. [2004b]. Imaging with microstructured polymer fibre, *Optics Express* **12**(2): 342–6. (Cited on page 29.)

van Eijkelenborg, M. A., Argyros, A., Bachmann, A., Barton, G. W., Large, M. C. J., Henry, G., Issa, N. A., Klein, K. F., Poisel, H., Pok, W., Poladian, L., Manos, S. and Zagari, J. [2004a]. Bandwidth and loss measurements of graded-index microstructured polymer optical fibre, *Electronics Letters* **40**(10): 592–3. (Cited on page 29.)

van Eijkelenborg, M. A., Argyros, A., Barton, G. W., Bassett, I. M., Fellew, M., Henry, G., Issa, N. A., Large, M. C. J., Manos, S., Padden, W. E., Poladian, L. and Zagari, J. [2003]. Recent progress in microstructured polymer optical fibre fabrication and characterization, *Optical Fiber Technology* **9**(4): 199–209. (Cited on pages 18, 53, 96 and 138.)

van Eijkelenborg, M. A., Canning, J., Ryan, T. and Lyytikäinen, K. [2000]. Bending-induced colouring in a photonic crystal fibre, *Optics Express* **7**(2): 88–94.
URL: `http://www.opticsexpress.org/abstract.cfm?URI=OPEX-7-2-88` (Cited on page 103.)

van Eijkelenborg, M. A., Large, M. C. J., Argyros, A., Bassett, I. and Zagari, J. [2002]. Photonic band gap guiding in microstructured polymer optical fibres, *Proceedings of the International Quantum Electronics Conference, IQEC*, Moscow, Russia, p. QThH3. (Cited on pages 103 and 104.)

van Eijkelenborg, M. A., Large, M. C. J., Argyros, A., Zagari, J., Manos, S., Issa, N. A., Bassett, I., Fleming, S., McPhedran, R. C., Martijn de Sterke, C. and Nicorovici, N. A. P. [2001]. Microstructured polymer optical fibre, *Optics Express* **9**(7): 319–27.
URL: `http://www.opticsexpress.org/abstract.cfm?URI=OPEX-9-7-319` (Cited on pages 26, 28 and 103.)

Vassallo, C. [1990]. Circular fourier analysis of full maxwell equations for arbitrary shaped dielectric waveguides - application of gain factors of semiconductor laser waveguides, *Journal of Lightwave Technology* **8**(11): 1723–9. (Cited on pages 32 and 61.)

Vassallo, C. [1991]. *Optical waveguide concepts*, Elsevier, Amsterdam. (Cited on pages 39, 42 and 48.)

Venkataraman, N., Gallagher, M. T., Smith, C., Müller, D., West, J. A., Koch, K. W., Fajardo, J. C. and Park, S. [2002]. Low loss (13db/km) air core photonic band gap fibre, *Post-deadline of the European Conference on Optical Communication.* (Cited on page 104.)

Vienne, G., Xu, Y., Jakobsen, C., Deyerl, H. J., Jensen, J. B., Sorensen, T., Hansen, T. P., Huang, Y., Terrel, M., Lee, R. K., Mortensen, N. A., Broeng, J., Simonsen, H., Bjarklev, A. and Yariv, A. [2004]. Ultra-large bandwidth hollow-core guiding in all-silica bragg fibers with nano-supports, *Optics Express* **12**(15): 3500–8.
URL: `http://www.opticsexpress.org/abstract.cfm?URI=OPEX-12-15-3500` (Cited on page 27.)

Wadsworth, W. J., Percival, R. M., Bouwmans, G., Knight, J. C., Birks, T. A., Hedley, T. D. and Russell, P. S. J. [2004]. Very high numerical aperture fibers, *IEEE Photonics Technology Letters* **16**: 843–5. (Cited on pages 114, 126 and 129.)

Wadsworth, W. J., Percival, R. M., Bouwmans, G., Knight, J. C. and Russell, P. S. J. [2003]. High power air-clad photonic crystal fibre laser, *Optics Express* **11**(1): 48–53.
URL: `http://www.opticsexpress.org/abstract.cfm?URI=OPEX-11-1-48` (Cited on pages 113 and 126.)

Wang, X., Lou, J., Lu, C., Zhao, C. and Ang, W. T. [2004]. Modeling of pcf with multiple reciprocity boundary element method, *Optics Express* **12**(5): 961–6.
URL: `http://www.opticsexpress.org/abstract.cfm?URI=OPEX-12-5-961` (Cited on page 54.)

West, J. A. and Allan, D. C. [2002]. Effect of disorder on photonic band-gap fibers, *Proceedings of the European Conference on Optical Communication*, pp. L–5719–MAN. (Cited on pages 104 and 109.)

West, J. A., Fajardo, J. C., Gallagher, M. T., Koch, K. W., Borrelli, N. F. and Allan, D. C. [2000]. Demonstration of an ir-optimized air-core photonic band-gap fiber, *Proceedings of the 26th European Conference on Optical Communication ECOC*, Vol. 4, Berlin, Germany, pp. 41–2. (Cited on page 103.)

West, J. A., Smith, C. M., Borrelli, N. F., Allan, D. C. and Koch, K. W. [2004]. Surface modes in air-core photonic band-gap fibers, *Optics Express* **12**(8): 1485–96.
URL: `http://www.opticsexpress.org/abstract.cfm?URI=OPEX-12-8-1485` (Cited on pages 109 and 110.)

White, T. P., Kuhlmey, B. T., McPhedran, R. C., Maystre, D., Renversez, G., Martijn de Sterke, C. and Botton, L. C. [2002b]. Multipole method for microstructured optical fibers i: Formulation, *Journal of the Optical Society of America B* **19**: 2322–30. (Cited on pages 54, 55 and 94.)

White, T. P., McPhedran, R. C., Martijn de Sterke, C., Botten, L. C. and Steel, M. J. [2001]. Confinement losses in microstructured optical fibers, *Optics Letters* **26**(21): 1660–2. (Cited on pages 26, 61 and 64.)

White, T. P., McPhedran, R. C., Martijn de Sterke, C., Lichinitser, N. M. and Eggleton, B. J. [2002a]. Resonance and scattering in microstructured optical fibres, *Optics Letters* **27**(22): 1977–9. (Cited on pages 25, 27 and 103.)

Yeh, P., Yariv, A. and Marom, E. [1978]. Theory of bragg fiber, *Journal of the Optical Society of America* **68**: 1196–1201. (Cited on page 27.)

Yoshida, K. and Morikawa, T. [1996]. Fabrication and characterization of side-hole single-mode optical fibers, *Optical Fiber Technology* **2**: 285–90. (Cited on page 97.)

Yu, C. P. and Chang, H. C. [2004]. Applications of the finite difference mode solution method to photonic crystal structures, *Journal of Quantum Electronics* **36**: 145–63. (Cited on page 54.)

Zagari, J., Argyros, A., Barton, G. W., Henry, G., Large, M. C. J., Issa, N. A., Poladian, L. and van Eijkelenborg, M. A. [2004]. Small-core single-mode microstructured polymer optical fibre with large external diameter, *Optics Letters* **29**(8): 818–20. (Cited on page 26.)

Zhi, W., Guobin, R., Shuqin, L. and Shuisheng, J. [2003a]. Dependence of mode characteristics on the central defect in elliptical hole photonic crystal fibers, *Optics Express* **11**(17): 1966–79.
URL: `http://www.opticsexpress.org/abstract.cfm?URI=OPEX-11-17-1966` (Cited on page 96.)

Zhi, W., Guobin, R., Shuqin, L. and Shuisheng, J. [2003b]. Supercell lattice method for photonic crystal fibers, *Optics Express* **11**(9): 980–91.
URL: `http://www.opticsexpress.org/abstract.cfm?URI=OPEX-11-9-980` (Cited on pages 54 and 55.)

Zhu, Z. and Brown, T. G. [2002]. Full-vectorial finite-difference analysis of microstructured optical fibers, *Optics Express* **10**(17): 853–64.
URL: `http://www.opticsexpress.org/abstract.cfm?URI=OPEX-10-17-853` (Cited on page 54.)